



HAL
open science

Numerical modeling of the adhesive contact at the bone-implant interface

Katharina Immel

► **To cite this version:**

Katharina Immel. Numerical modeling of the adhesive contact at the bone-implant interface. Biophysics. Université Paris-Est; Rheinisch-westfälische technische Hochschule (Aix-la-Chapelle, Allemagne), 2021. English. NNT : 2021PESC0066 . tel-03856158

HAL Id: tel-03856158

<https://theses.hal.science/tel-03856158>

Submitted on 16 Nov 2022

HAL is a multi-disciplinary open access archive for the deposit and dissemination of scientific research documents, whether they are published or not. The documents may come from teaching and research institutions in France or abroad, or from public or private research centers.

L'archive ouverte pluridisciplinaire **HAL**, est destinée au dépôt et à la diffusion de documents scientifiques de niveau recherche, publiés ou non, émanant des établissements d'enseignement et de recherche français ou étrangers, des laboratoires publics ou privés.

UNIVERSITÉ PARIS-EST
École doctorale SIE : Sciences, Ingénierie et Environnement
in joint supervision with
RWTH AACHEN UNIVERSITY
Faculty of Mechanical Engineering

Thesis submitted for the grade of Doctor of Philosophy
Major: Biomechanics

Numerical Modeling of the Adhesive Contact at the Bone-Implant Interface

by

Katharina Immel

supervised by Guillaume HAIAT and Roger A. SAUER

defended on December 17, 2021

in front of the following board of examiners:

M. Guillaume Haiat Directeur de recherche (CNRS - Université Paris-Est)	PhD Supervisor
M. Roger A. Sauer Professor (Gdańsk University of Technology)	PhD Supervisor
M. Vu-Hieu Nguyen Maitre de conférences (Université Paris-Est)	PhD Co-Supervisor
M. Marek Behr Professor (RWTH Aachen University)	President of the Jury
Mme. Stéphanie Chaillat-Loseille Chargée de recherche (CNRS - ENSTA ParisTech)	Rapporteur
M. Mikhail Itskov Professor (RWTH Aachen University)	Rapporteur
Mme. Sophie LeCann Chargée de recherche (CNRS - Université Paris-Est)	Examiner

Abstract

Cementless implants have become more and more common for joint replacement and dental surgery. Initial stability is obtained during the surgery through a press fit process in the host bone, while long-term stability is obtained by bone growing around and into the porous surface of the implant, a process called osseointegration. As debonding of the bone-implant interface due to aseptic loosening and insufficient osseointegration still occur and may have dramatic consequences, predicting implant stability and failure is one of the major goals in modern implant research.

This work presents different 3D FE modeling approaches to model contact and initial and long-term stability of cementless implants using the example of a cylindrical implant (CSI) and an acetabular cup implant (ACI).

First, an approach to assess the initial stability of an ACI considering a realistic geometry of a patient's hip, based on Coulomb's friction contact and standard FE, is presented. The influence of different patient and implant-specific parameters is analyzed in order to determine optimal stability for different configurations and thus obtain the optimal combination of the implant's surface roughness and the press-fit, based on a patient's bone quality.

Second, a phenomenological model for the frictional contact behavior of debonding osseointegrated implants is developed. The classical Coulomb's law is extended from a constant to a varying friction coefficient, that models the transition from an unbroken (osseointegrated) to a broken (debonded) state, based on a state variable depending on the deformation of the bone-implant interface. This model can account for the higher tangential forces observed in osseointegrated implants compared to unbonded implants. In addition, a NURBS-enrichment approach for 3D contact elements is used for an efficient modeling of the geometries and their contact. This model is applied to the torsional debonding of CSI and the results are compared to experimental data and to a previous analytical model.

Third, the modified Coulomb's law model is extended in normal direction considering a cohesive zone model, to account for debonding in normal direction and allow for adhesive friction. This model is applied to simulate secondary stability and debonding of an ACI in different removal tests, and to determine the relevance of osseointegration and biomechanical factors for long-term stability. The results are compared with the purely tangential model to identify the relevance of normal adhesion in the debonding of ACI.

Last, three simple evolution laws for osseointegration based on initial stability to account for realistic and time-dependent osseointegration, are presented.

Due to their generality, all models presented herein can be applied to all kinds of endosseous implants or imperfectly bonded interfaces in general. Furthermore, the models can be coupled with remodeling algorithms or realistic loading data, to make simulations and prognoses for the whole life cycle of an implant from the surgery, through osseointegration and bone remodeling, to long-term stability under cyclic loading.

Zusammenfassung

Unzementierte Implantate werden immer häufiger als Gelenkersatz und in der Zahnchirurgie eingesetzt. Da eine Ablösung des Implantats vom Knochen aufgrund von Lockerung und einer unzureichenden Knochenintegration immer noch auftritt und dramatische Folgen haben kann, ist die Vorhersage der Implantatstabilität und des Versagens des Knochen–Implantat–Verbunds eines der Hauptziele in der Implantatforschung.

In dieser Arbeit werden verschiedene dreidimensionale finite Elemente Methoden zur Modellierung des Kontakts zwischen Knochen und Implantat, sowie der simulation der primären und Langzeitstabilität von unzementierten Implantaten vorgestellt.

Zunächst wird ein Ansatz zur quantifizierung der primären Stabilität einer Hüftpfanne in einer realistischen Geometrie der Hüfte eines Patienten vorgestellt. Der Einfluss verschiedener patienten- und implantatspezifischer Parameter wird analysiert, um die optimale Stabilität, basierend auf der Kombination der Oberflächenrauheit und der Presspassung des Implantats, unter der Berücksichtigung der Knochenqualität eines Patienten, zu erhalten.

Anschließend wird ein phänomenologisches Modell für das reibungsbehaftete Kontaktverhalten von sich lösenden, osseointegrierten Implantaten vorgestellt. Das klassische Coulombsche Reibungsgesetz wird von einem konstanten auf einen variablen Reibungskoeffizienten erweitert, der auf einer Zustandsvariable basiert, die von der Verformung der Grenzfläche zwischen Knochen und Implantat abhängt. So kann der Übergang von einem osseointegrierten zu einem völlig abgelösten Zustand modelliert werden. Dieses Modell wird auf die Ablösung durch Torsion von zylindrischen Implantaten angewendet und die Ergebnisse werden mit experimentellen Daten und einem bestehenden analytischen Modell verglichen.

Dieses Reibungsmodell wird anschließend in normalen Richtung um ein Adhäsionsmodell erweitert um Haftreibung zu ermöglichen. Dieses Modell wird angewendet, um die Langzeitstabilität und das Ablösen einer Hüftpfanne in verschiedenen Belastungstests zu simulieren und die Relevanz der Osseointegration, Adhäsion in Normalenrichtung und der biomechanischen Faktoren für die Langzeitstabilität zu bestimmen. Die Ergebnisse werden mit dem rein tangentialen Modell verglichen, um die Relevanz der normalen Adhäsion für das Ablösen von Hüftimplantaten zu ermitteln.

Schließlich werden drei einfache Evolutionsgesetze für die Osseointegration basierend auf der primären Stabilität vorgestellt, um eine realistische und zeitabhängige Osseointegration berücksichtigen zu können.

Aufgrund ihrer Allgemeinheit können alle hier vorgestellten Modelle auf alle Arten von Knochenimplantaten oder unvollständig gebundenen Grenzflächen im Allgemeinen angewendet werden. Darüber hinaus können die Modelle z.B. mit Algorithmen für Knochenumbau oder realistischen Belastungszyklen gekoppelt werden, um Simulationen und Prognosen für den gesamten Lebenszyklus eines Implantats von der Operation über Osseointegration und Knochenumbau, bis hin zur Langzeitstabilität unter zyklischer Belastung zu erstellen.

Résumé

Les implants osseux constituent actuellement l'approche thérapeutique la plus utilisée pour réparer les articulations et les os endommagés. La stabilité initiale est obtenue pendant la chirurgie grâce à un processus d'ajustement serré dans l'os hôte, tandis que la stabilité à long terme est obtenue par la croissance osseuse autour et dans la surface poreuse de l'implant, un processus appelé ostéointégration. Comme le décollement de l'interface os-implant dû à un descellement aseptique et à une ostéointégration insuffisante se produit toujours et peut avoir des conséquences dramatiques, prédire la stabilité et l'échec de l'implant est l'un des objectifs majeurs de la recherche implantaire moderne.

L'objectif de ce travail est de proposer plusieurs modélisations complémentaires du contact adhésif à l'interface os-implant pendant et après la chirurgie.

Premièrement, les déterminants biomécaniques de la stabilité primaire d'une cupule acétabulaire (ACI) sont présentés. Pour quantifier la stabilité primaire, l'insertion de l'ACI dans un hémibassin humain et le retrait ultérieur sont simulés. L'influence de différents paramètres spécifiques au patient et à l'implant sur la stabilité primaire est discutée. Sur la base de la rigidité osseuse d'un patient, des combinaisons optimales de l'ajustement serré et du coefficient de frottement peuvent être identifiées pour assurer une stabilité initiale optimale.

Deuxièmement, un modèle phénoménologique du comportement de contact frictionnel des implants ostéointégrés décollés est développé. La loi de Coulomb classique est étendue d'un coefficient de frottement constant à un coefficient de frottement variable, qui modélise la transition d'un état ininterrompu (ostéo-intégré) à un état cassé (délié), basé sur une variable d'état dépendant de la déformation de l'interface os-implant. Ce modèle est appliqué au décollement en torsion des implants de forme cylindrique et les résultats sont comparés aux données expérimentales et à un modèle analytique précédent.

Troisièmement, le modèle de loi de Coulomb modifié est étendu dans la direction normale en considérant un modèle de zone cohésive, pour tenir compte du décollement dans la direction normale et tenir compte du frottement adhésif. Ce modèle est appliqué pour simuler la stabilité secondaire et le décollement d'un ACI dans différents tests de retrait, et pour déterminer la pertinence de l'ostéointégration et des facteurs biomécaniques pour la stabilité à long terme.

Enfin, trois lois d'évolution simples pour l'ostéointégration basée sur la stabilité initiale sont présentées pour rendre compte d'une ostéointégration réaliste et dépendante du temps.

En raison de leur généralité, tous les modèles présentés dans ce travail peuvent être appliqués à toutes sortes d'implants osseux ou plus généralement d'interfaces imparfaitement collées. De plus, les modèles peuvent être couplés à des algorithmes de remodelage ou à des données de chargement réalistes, pour mener à bien des simulations et des pronostics pour tout le cycle de vie d'un implant depuis la chirurgie, en passant par le remodelage osseux et l'ostéointégration, jusqu'à la stabilité à long terme sous chargement cyclique.

Prior publications

This thesis is based in part on research performed by the author during her time at the Aachen Institute for Advanced Studies in Computational Engineering Science (AICES) at RWTH Aachen University, Germany, and the Laboratoire Modélisation et Simulation Multi Echelle (MSME) at Université Paris-Est Créteil, France, between April 2017 and December 2021. Major parts of this thesis have appeared in previous publications and are reproduced here, in restructured, modified and/or extended form. In particular, mayor parts of Chapter 5 are derived from [Immel et al. \(2021a\)](#); [Raffa et al. \(2019\)](#), Chapter 6 is reproduced from [Immel et al. \(2019, 2020\)](#), and Chapter 7 is reproduced from [Immel et al. \(2021b,c\)](#). Mayor parts of Chapter 2 are derived from the introductions of all publications listed below. Figures and Tables reproduced from these publications are referenced accordingly.

- Immel, K., Duong, T. X., Nguyen, V.-H., Haiät, G., and Sauer, R. A. A Frictional and Adhesive Contact Model for Debonding of the Bone–Implant interface Based on State Variable Friction Laws. *Proceedings of 8th GACM Colloquium on Computational Mechanics, August 28th – 30th, 2019, University of Kassel, Germany* (2019)
- Raffa, M., Nguyen, V.-H., Tabor, E., Immel, K., Housset, V., Flouzat-Lachaniette, C.-H., and Haiät, G. Dependence of the primary stability of cementless acetabular cup implants on the biomechanical environment. *Proceedings of the Institution of Mechanical Engineers, Part H: Journal of Engineering in Medicine*, **233**(12):1237–1249 (2019)
- Immel, K., Duong, T. X., Nguyen, V.-H., Haiät, G., and Sauer, R. A. A modified Coulomb’s law for the tangential debonding of osseointegrated implants. *Biomechanics and Modeling in Mechanobiology*, **19**:1091–1108 (2020)
- Immel, K., Nguyen, V.-H., Dubory, A., Flouzat-Lachaniette, C.-H., Sauer, R. A., and Haiät, G. Determinants of the primary stability of cementless acetabular cup implants: A 3D finite element study. *Computers in Biology and Medicine*, **135**:104607 (2021)
- Immel, K., V.-H., Haiät, G., and Sauer, R. A. Long–Term Stability and Debonding of Cementless Implants. *Proceedings in Applied Mathematics and Mechanics*, **21**: e202100118. <https://doi.org/10.1002/pamm.202100118> (2021)
- Immel, K., Nguyen, V.-H., Haiät, G., and Sauer, R. A. Modeling the debonding process of osseointegrated implants due to coupled adhesion and friction. *arXiv preprint arXiv:2112.06793* (2021)

Furthermore, mayor parts of Chapter 8 are in preparation for publication:

- Sauer, R. A. and Immel, K. A fully coupled chemo–thermo–mechanical contact model and its application to bonding and debonding. *in preparation* (2022)

Acknowledgments

First and foremost, I would like to express my deepest gratitude towards my supervisors Guillaume Haïat and Roger A. Sauer. Their expertise, their approachable nature and literally open door, their guidance and patience but also the freedom they gave me, made this work possible.

I am also grateful for the support of Vu-Hieu Nguyen and Bo N. J. Persson.

Another thank you goes to Marek Behr, Stéphanie Chaillat-Loseille, Mikhail Itskov, and Sophie LeCann for participating in my defense committee and reviewing my thesis.

During my PhD, I had the privilege and pleasure to work at two different institutes with many international colleagues. Although, I had to split my time at those institutes, I was always welcomed warmly and felt integrated. The many experiences and fruitful discussions with my colleagues found their way into this work one way or the other. For this, I would like to thank Ali, Anne-Sophie, Christopher, Elisabeth, Eshwar, Fakhraddin, Farzad, Giuseppe, Florian, Karsten, Léo, Lucie, Manon, Maria, Mathieu, Maximilian, Michał, Nicolas, Olivier, Reza, Sophie, Thang, Yoann, and Yunsang. The same goes for my colleagues from the SIAM Student Chapter Aachen, namely Ankit, Anna, Christian, and Nicole.

I would also like to thank the administrative teams and IT supports at MSME and AICES who were always a great help and support for my work, especially during my time in France. I am also grateful for Linda's support in navigating administrative matters regarding the co-tutelle at RWTH Aachen University.

Another big thank you goes to my former supervisor Lutz H. Pauli who let me look over his shoulder for almost 5 years, which also contributed to this thesis.

While having scientific, administrative, and technical support certainly is essential for a successful PhD thesis, the emotional support of my friends also contributed to this work. Therefore, I would also like to thank especially but not exclusively: Alexander, Christine, Daniel, Eric, Hatim, Iljana, Kai, Lukas, Michelle, and Till.

I am also grateful to my family. They raised me to be independent and self-sufficient, and gave me the freedom to pursue my own goals.

Nomenclature

Acronyms

Symbol	Description	Page
ACI	acetabular cup implant	2
BIC	bone-to-implant contact	14
BII	bone-implant interface	1
BVP	boundary value problem	27
CAD	computer aided design	33
CAE	computer aided engineering	34
CAM	computer aided manufacturing	34
CSI	coin-shaped implant	3
CZM	cohesive zone model	24
FE	finite element	15
FEA	finite element analysis	15
FEM	finite element method	28
IGA	isogeometric analysis	33
MMA	methylmetacrylate	7
MC	modified Coulomb's friction law	83
EMC	extended modified Coulomb's friction law	83
NURBS	non-uniform rational basis splines	32
PDE	partial differential equation	28
PMMA	polymethylmethacrylate	7
PTFE	polytetrafluorethylen	68
QUS	quantitative ultrasound	14
RFA	resonance frequency analysis	14
vdW	van der Waals	24
THA	total hip arthroplasty	10
μ CT	microcomputed tomography	15

Latin Symbols

In general, upright symbols denote their respective discretized vectors and matrices, i.e., vectors and matrices associated with finite element nodes, and are not listed here.

Symbol	Description	Unit	Equation	Page
a_s	sliding threshold	[m]	(6.5)	67
$a_{\alpha\beta}$	surface metric tensor components		(3.23)	23
\mathbf{a}_α^p	co-variant tangent vector	[1] or [m]	(3.22)	23
\mathbf{a}_p^α	contra-variant tangent vector	[1] or [m]	(3.23)	23
$A_{\alpha\beta}$	surface metric tensor components			23
\mathbf{A}_α^p	co-variant tangent vector	[1] or [m]		23
\mathbf{A}_p^α	contra-variant tangent vector	[1] or [m]		23
b_s	transition factor		(6.5)	67
\mathbf{b}	left Cauchy-Green tensor		(3.9)	20
$\bar{\mathbf{b}}$	prescribed body force	[N/kg]	(3.43)	27
\mathbf{B}^e	Bernstein polynomials		(4.21)	35
\mathcal{B}	set of points defining a body			19
$\partial\mathcal{B}$	set of points defining a surface on body \mathcal{B}			19
c	critical/crack radius	[m]	(6.7)	68
C	effective shear stiffness		(6.16)	70
\mathbf{C}	right Cauchy-Green tensor		(3.9)	20
\mathbf{C}^e	Bézier extraction operator		(4.21)	35
\mathfrak{c}	spatial elasticity tensor		(3.14)	21
d	displacement	[m]	(5.1)	49
da	area element in current configuration	[m ²]	(3.7)	20
dA	area element in reference configuration	[m ²]	(3.7)	20
dv	volume element in current configuration	[m ³]	(3.6)	20
dV	volume element in reference configuration	[m ³]	(3.6)	20
\mathbf{D}	rate of deformation tensor	[1/s]	(3.15)	22
e	error	[%]	(6.24)	72
\mathbf{E}	Green-Lagrange strain tensor		(3.8)	20
E	Young's modulus	[N/m ²]	(3.13)	21
E_{adh}	adhesion energy	[J]	(6.7)	69
f_s	slip criterion		(3.35)	25
\mathbf{f}	tensor function		(3.58)	29
\mathbf{f}	virtual force vector		(4.23)	37
F	force	[N]		49
\mathbf{F}	deformation gradient		(3.3)	19
g	gap	[m]	(3.28)	23
\mathbf{g}	gap vector	[m]	(3.26)	23
h_e	element size	[m]		47
G	shear modulus	[N/m ²]	(3.12)	21
H^e	Hermite polynomial			36
H	constant height	[m]		47

\mathbf{I}	identity tensor		(3.8)	20
\mathbb{I}	fourth-order symmetric tensor		(3.14)	21
IF	interference fit	[m]		46
J	change of volume		(3.4)	19
J_s	change of area		(3.5)	19
\mathbf{k}	stiffness/tangent matrix		(4.36)	38
\overrightarrow{k}	bone apposition rate		(8.2)	110
\overleftarrow{k}	bone resorption rate		(8.2)	110
k_r	reaction rate	[1/day]	(8.2)	110
ls	load step		(5.1)	49
Δls	load step increment		(5.1)	49
L	linearization		(3.58)	29
L	constant length	[m]		24
m	mass	[kg]		24
M	torque	[N m]	(6.10)	69
n	number/amount		(4.1)	31
\mathbf{n}	surface normal		(3.10)	21
N, M	shape function		(4.4)	32
\mathbf{N}	array of shape functions		(4.4)	32
p, q	polynomial order		(4.20)	35
p_c	contact pressure	[N/m ²]	(3.31)	23
\bar{p}	average contact pressure	[N/m ²]		74
\mathbf{P}	control point vector		(4.17)	34
\mathcal{P}	parameter space		(3.40)	26
r_{res}	residual		(3.50)	28
r	radius (coordinate)	[m]	(6.8)	69
R^e	rational basis function		(4.21)	35
R	constant radius	[m]		47
\mathbf{S}	second Piola-Kirchhoff stress tensor	[N/m ²]	(3.11)	21
t	time	[s]		42
t_0	reference traction	[N/m ²]	(7.1)	83
\mathbf{t}	surface traction	[N/m ²]	(3.10)	21
$\bar{\mathbf{t}}$	prescribed surface load	[N/m ²]	(3.43)	27
\mathbf{u}	displacement vector	[m]	(3.2)	19
\mathbf{v}	discretized virtual displacement		(4.7)	32
\mathcal{V}	function space		(3.51)	28
W^e	weighting function		(4.21)	35
W	energy	[J]	(6.25)	77
\mathbf{W}	spin tensor		(3.16)	22
\mathbf{W}^e	weights		(4.21)	35
\mathbf{x}	current position of a material point	[m]	(3.1)	19
\mathbf{X}	initial position of a material point	[m]	(3.1)	19
x, y, z	coordinate	[m]	(6.8)	69

Greek Symbols

Symbol	Description	Unit	Equation	Page
Γ	surface element		(4.1)	31
ε	infinitesimal strain tensor		(3.12)	21
ϵ	penalty parameter	[N/m ²]	(4.44)	40
θ	rotation angle	[deg]	(6.7)	68
Λ	first Lamé parameter		(3.12)	21
μ	friction coefficient		(3.38)	25
ν	Poisson ratio		(3.13)	21
ξ, η, ζ	parametric coordinates		(4.9)	32
ξ	vector of parametric coordinates		(3.22)	23
Ξ	knot vector		(4.14)	34
Π	potential energy	[J]	(3.54)	29
$\delta\Pi$	variation of the potential energy	[J]	(3.54)	29
ρ	mass density	[kg/m ³]	(3.41)	26
σ	stress (component)	[N/m ²]	(6.9)	69
$\boldsymbol{\sigma}$	Cauchy stress tensor	[N/m ²]	(3.10)	21
$\dot{\boldsymbol{\sigma}}$	Jaumann rate of the Cauchy stress tensor	[N/m ² s]	(3.17)	22
$\boldsymbol{\tau}$	tangential sliding direction		(3.37)	25
ϕ	(de)bonding state		(6.1)	66
$\hat{\phi}$	bonding state (during osseointegration)		(8.1)	110
ϕ_0	initial degree of osseointegration		(6.5)	67
$\bar{\phi}_0$	average percentage of initially osseointegrated area		(6.26)	77
φ	deformation mapping		(3.1)	19
$\delta\varphi$	variation/test function/virtual displacement		(3.51)	28
Ω	bulk element		(4.1)	31

Mathematical Operators

$\mathbf{a} \cdot \mathbf{b}$	scalar product (vector): $\sum_i a_i b_i$
$\mathbf{A} : \mathbf{B}$	scalar product (tensor): $\sum_{i,j} A_{ij} B_{ij}$
$\mathbf{a} \otimes \mathbf{b}$	tensor product: $[\mathbf{a} \otimes \mathbf{b}]_{ij} = a_i b_j$
$\dot{\bullet}$	temporal derivative: $\partial \bullet / \partial t$

Subscripts and Superscripts

The position of a symbol as a subscript or superscript has no particular meaning and is chosen based on convenience.

Symbol	Description	Symbol	Description
∞	infinite/steady state	SR	short range
*	reference value	stick	sticking
0	initial/reference state	t	tangential
A	ancillary	tb	trabecular bone
adh	adhesion	\bar{t}	Neumann boundary
b	broken	ub	unbroken
c	contact	vdW	van der Waals
cb	cortical bone	α, β	$\in\{1,2\}$ surface coordinate index
cp	control point	θ	degree (coordinate)
CZ	cohesive zone	\square	parent element
e	elastic		
e	element-wise		
el	element		
ext	external		
gp	Gauss-point		
h	discretized variable		
i	inelastic		
i	load increment		
I	implant		
in	inertia		
int	internal		
k	$\in\{1,2\}$ body index		
ℓ	$\in\{2,1\}$ body index		
lim	limit		
lin	linear		
max	maximum		
mp	mean percentage		
n	normal		
n	load/time step		
opt	optimal		
p	projection point		
r	reaction (chemical)		
s, slide	sliding		
s	surface		

Contents

1	Introduction	1
2	Background	5
2.1	Bone	5
2.1.1	Bone Tissue	5
2.1.2	Bone Remodeling	6
2.2	Endosseous Implants	7
2.2.1	Coin-Shaped Implants	9
2.2.2	Acetabular Cup Implants	10
2.2.3	The Bone-Implant Interface	11
2.3	Determining Biomechanical Properties and Behavior of the Bone-Implant Interface	13
2.3.1	Non-Invasive Experimental Methods	13
2.3.2	Invasive Experimental Methods	14
2.3.3	Numerical Methods	15
2.4	Further Challenges	17
3	Nonlinear Continuum Mechanics	19
3.1	Kinematics	19
3.1.1	Strain Measures	20
3.1.2	Stress Measures	20
3.2	Constitutive Equations	21
3.2.1	Linear Material Model	21
3.2.2	Hypoelastic Material Model	22
3.2.3	Compressible Neo-Hookean Material Model	22
3.3	Contact Mechanics	22
3.3.1	Contact Surface Description and Kinematics	22
3.3.2	Adhesion	24
3.3.3	Friction	25
3.4	Balance Laws	26
3.4.1	Balance of Mass	26
3.4.2	Balance of Linear Momentum	27
3.4.3	Balance of Angular Momentum	27
3.4.4	Strong Form of the Mechanical Contact Boundary Value Problem	27
3.4.5	Weak Form of the Mechanical Contact Boundary Value Problem	28
3.5	Linearization	29

4	Finite Element Discretization and Algorithmic Contact Treatment	31
4.1	Spatial Discretization	31
4.1.1	Lagrangian Elements and Lagrangian Enrichment	32
4.1.2	Isogeometric Analysis	33
4.1.3	NURBS-enriched Contact Elements	35
4.1.4	Discretized Weak Form	36
4.1.5	Element Mapping	37
4.2	Solution Procedure	38
4.3	Contact Projection Approaches	39
4.4	The Penalty Method for Frictional Contact	40
4.5	Predictor-Corrector Algorithms	41
4.5.1	Elastoplasticity Based Formulation	41
4.5.2	Surface Potential Based Formulation	42
4.6	Solution Algorithm	44
5	Determinants of Initial Stability of Cementless Implants	45
5.1	Motivation	45
5.2	Setup	46
5.2.1	Geometry and Mesh	46
5.2.2	Material Properties and Varied Parameters	48
5.2.3	Boundary and Loading Conditions	48
5.2.4	Quantifying Primary Stability	49
5.3	Results	50
5.3.1	Reference Case	50
5.3.2	Stress Distribution	51
5.3.3	Effect of Variations of the Young's Modulus of Bone	52
5.3.4	Effect of variations of the Friction Coefficient and the Interference Fit	53
5.3.5	Optimal Conditions	56
5.4	Discussion and Limitations	57
5.4.1	Pull-Out Force	58
5.4.2	Polar Gap	59
5.4.3	Contact Stresses	59
5.4.4	Optimal Conditions for Primary Stability	60
5.4.5	Limitations	61
5.4.6	Conclusion	62
6	Tangential Debonding of Partially Osseointegrated Implants	65
6.1	Motivation	65
6.2	State Variable Friction Laws	66
6.3	Modified Coulomb's Friction Law	66
6.4	Application to Coin-Shaped Implants	68
6.4.1	Experimental Setup	68
6.4.2	Analytical Model of Mathieu et al. (2012a)	68
6.4.3	New Analytical Model	69
6.4.4	Numerical Setup	71

6.4.5	Results	72
6.4.6	Discussion and Limitations	80
6.4.7	Conclusion	82
7	Normal and Tangential Debonding of Partially Osseointegrated Implants	83
7.1	Adhesive Friction and Debonding	83
7.2	Application to Coin-Shaped Implants	85
7.2.1	Setup	85
7.2.2	Results	87
7.3	Application to Acetabular Cup Implants	92
7.3.1	Setup	92
7.3.2	Debonding without Adhesion in Normal Direction	95
7.3.3	Debonding with Adhesion in Normal Direction and Adhesive Friction	99
7.4	Discussion	103
7.4.1	Comparison of the Modified and Extended Coulomb's Law with Respect to their Biomechanical Relevance	103
7.4.2	Comparison with Similar Studies	105
7.4.3	Numerical Stability	105
7.4.4	Perspectives and Guidelines for Future Work	105
7.5	Conclusion	108
8	Evolution Laws for Osseointegration Based on Initial Stability	109
8.1	Simple Evolution Laws for Osseointegration	109
8.1.1	Model A	110
8.1.2	Model B	112
8.1.3	Model C	113
8.2	Application to Coin-Shaped Implants	114
8.2.1	Setup	114
8.2.2	Results	116
8.2.3	Discussion and Limitations	117
8.2.4	Conclusion	118
9	Conclusion	119
9.1	Summary	119
9.2	Perspective	121
9.2.1	Coupled Models	121
9.2.2	Additive Manufacturing and Shape Optimization	121
9.2.3	Experimental Measurement Techniques	121
	Résumé substantiel	i
	A Linearization	v
A.1	Tangent Matrix for the Modified Coulomb's Friction Law	v
	B Convergence Studies	ix
B.1	Acetabular Cup Implant in Human Hemi-Pelvis	ix

B.2 Modified Coulomb's Friction Law on Coin-Shaped Implants	x
B.3 Modified Coulomb's Friction Law on Acetabular Cup Implants	xi
Bibliography	xiii

List of Figures

2.1	Schematic illustration of the hierarchical structure of bone tissue.	6
2.2	Examples of different endosseous implants.	8
2.3	Different images of a CSI.	9
2.4	Total hip replacement.	10
2.5	A variety of ACI with different surface treatments and with and without screw holes.	10
2.6	Schematic illustration of the different stages of osseointegration and examples of osseointegration failure.	12
3.1	Reference configuration, current configuration and their respective surfaces.	20
3.2	Schematic illustrations of the basic surface description and contact kinematics.	24
3.3	Illustration of adhesive contact models.	25
3.4	Frictional, tangential traction for a single point for constant pressure, defined by Coulomb's law, as a function of the tangential gap.	26
3.5	Mechanical contact boundary value problem.	28
4.1	Example of a spatial discretization of a 2D body with quadrilateral, linear finite elements.	32
4.2	Example of linear Lagrangian bulk discretization with different surface-enriched contact elements in 2D with corresponding parent element.	36
4.3	Mappings of the parent bulk and surface element to their respective reference and current configurations.	38
4.4	Contact projection approaches.	40
4.5	Penalty contact traction.	40
4.6	Comparison of formulations for the tangential sliding direction.	41
5.1	Images of the pelvis geometry with the ACI and ancillary and the corresponding FE mesh	47
5.2	Variation of the reaction force applied to the ancillary as a function of the load step for the 2D and 3D model for the reference case.	50
5.3	Distribution of the von Mises stress in the hip cavity for the reference case and the optimal case.	51
5.4	Variation of the reaction force applied to the ancillary for different bone Young's moduli.	52
5.5	Variation of the pull-out force and the polar gap as a function of the Young's moduli of bone.	53

5.6	Variation of the reaction force applied to the ancillary for different friction coefficients and interference fit.	54
5.7	Variation of the pull-out force and the polar gap as a function of the friction coefficient, the interference fit and trabecular Young's modulus.	55
5.8	Variation of the pull-out force as a function of the interference fit and the friction coefficient.	56
5.9	Variation of the maximal pull-out force obtained for the optimal interference fit as a function of the friction coefficient w.r.t. trabecular bone Young's modulus.	56
5.10	Variation of the optimal interference fit as a function of the friction coefficient w.r.t. trabecular bone Young's modulus.	57
6.1	Modified Coulomb's law.	68
6.2	Illustrations for the analytical and numerical setup.	69
6.3	New analytical model: critical radius.	70
6.4	New analytical model: normalized tangential traction.	71
6.5	Variation of the torque as a function of the imposed rotation angle.	75
6.6	Evolution of the debonding of the BII: Value of the friction coefficient and the sliding distance.	76
6.7	Evolution of the debonding of the BII: Behavior of the friction coefficient and the transition zone for the first data set.	76
6.8	Original and constructed osseointegration patterns with average osseointegration of 55 %.	78
6.9	Variation of the friction coefficient at the BII for different angles of rotation for different patterns of partial osseointegration of 55 %.	79
6.10	Partial osseointegration: Variation of the torque for different patterns of partial osseointegration of 55 %.	79
6.11	Variation of the friction coefficient at the BII for different angles of rotation for different patterns of partial osseointegration of 55 %.	80
7.1	Illustration of (a) the cohesive zone model and (b) the extended modified Coulomb's law with adhesive friction for $\phi_0 > 0$. Adopted from Immel et al. (2021c)	84
7.3	CSI debonding: Sliding under constant pressure or tension.	87
7.4	CSI debonding: Torsion under constant pressure or tension.	88
7.5	CSI debonding: Variation of the normal and tangential reaction force as a function of the tangential displacement for angled debonding, starting from an initial contact pressure.	89
7.6	CSI debonding: Variation of the normal and tangential reaction force as a function of the tangential displacement for angled debonding, starting from zero contact force.	89
7.7	CSI debonding: Variation of the normal and tangential reaction force as a function of the tangential displacement for angled debonding and varying CZM parameter, starting from an initial contact pressure.	90
7.8	CSI debonding: Variation of the normal and tangential reaction force as a function of the tangential displacement for angled debonding and varying CZM parameter, starting from zero contact force.	90

7.9	CSI debonding: Variation of the normal and tangential reaction force as a function of the tangential displacement for angled debonding and different degree of osseointegration, starting from an initial contact pressure.	91
7.10	CSI debonding: Variation of the normal and tangential reaction force as a function of the tangential displacement for angled debonding and different degree of osseointegration, starting from zero contact force.	91
7.11	ACI debonding: Illustration of the FE mesh and the boundary conditions for the ACI.	92
7.12	ACI debonding: Illustration of the simulation stages and removal tests.	94
7.13	ACI debonding: Normal debonding without adhesion.	95
7.14	ACI debonding: Variation of MC parameters.	96
7.15	ACI debonding: Pull-out forces for normal debonding without adhesion.	96
7.16	ACI debonding: Tangential debonding without adhesion.	97
7.17	ACI debonding: Pull-out forces for tangential debonding without adhesion.	98
7.18	ACI debonding: Torsional debonding without adhesion.	98
7.19	ACI debonding: Removal torque for torsional debonding without adhesion.	99
7.20	ACI debonding: Normal debonding with adhesive friction.	100
7.21	ACI debonding: Pull-out forces for normal debonding with adhesive friction.	100
7.22	ACI debonding: Tangential debonding with adhesive friction.	101
7.23	ACI debonding: Pull-out forces for tangential debonding with adhesive friction.	101
7.24	ACI debonding: Torsional debonding with adhesive friction.	102
7.25	ACI debonding: Removal torque for torsional debonding with adhesive friction.	102
7.26	ACI debonding: Ratio between the maximum removal forces/torque obtained for perfect initial osseointegration and no initial osseointegration.	104
8.1	Illustration of the reaction rates for truly touching and short range contact of model A.	112
8.2	Illustration of the reaction rates for truly touching and short range contact for model B.	113
8.3	Illustration of the reaction rate model C.	114
8.4	Example of the evolution of osseointegration at a certain point on the BII over time .	114
8.5	NURBS-enriched FE mesh of the rough bone block.	115
8.6	Osseointegration of the CSI with respect to the healing time.	116
8.7	Average degree of osseointegration over time for model A, B, and C.	117
8.8	Variation of the torque as a function of the imposed rotation angle for model A	117
B.1	Mesh sensitivity: Normal pull-out force and corresponding computing time.	ix
B.2	Mesh sensitivity: mean relative error for different configurations of data set 1.	x
B.3	Mesh sensitivity: Normal pull-out force and corresponding computing time with respect to number of contact elements on the bone block.	xi

List of Tables

- 5.1 Material properties of the four subdomains considered in the numerical model as well as ranges and reference values of the studied parameters. 48
- 5.2 Optimal values of the of interference fit and friction coefficient with respect to trabecular bone stiffness with fixed cortical bone stiffness. 57
- 6.1 Parameters of the finite element mesh. 72
- 6.2 Data sets used for the parameter estimation. 73
- 6.3 Results for the parameter estimation of the two data sets or values independent of the friction coefficient. 74
- 6.4 Results for the parameter estimation of the two data sets. 74
- 6.5 Total debonding energy, frictional energy, work of adhesion, and corresponding area-specific works of adhesion and for the different models and data sets. 77
- 6.6 Change in model parameters and results for implants with partial initial bonding compared to homogeneous bonding. 80
- 7.1 ACI debonding: Parameters of the finite element mesh. 93
- 7.2 ACI debonding: Average percentage increase in the maximum pull-out force and torque for perfect osseointegration. 104
- 8.1 Parameters of the finite element mesh. 115
- 8.2 Parameters of the evolution laws for osseointegration and the contact law. 115
- B.1 Mesh sensitivity: mean percentage error for different configurations of data set 1. x
- B.2 Number of elements of the finite element meshes. xi
- B.3 Average computing time, average number of Newton-Raphson steps, and corresponding number of load steps for the MC and EMC. xii

Chapter 1

Introduction

Endosseous implants, which are implants that partially or completely replace or support biological structures, are currently the most applied therapy for worn out, damaged, or destroyed joints, bones or teeth. Severe cases require the total replacement of the damaged joint or tooth, such as total hip or knee arthroplasty or dental implants. These replacements are the most commonly performed type of orthopedic surgery, with over 1 million replacements annually in the USA alone (Lee and Goodman, 2008). With the ever increasing life expectancy, there is a rapid increase in patients with musculoskeletal conditions and diseases such as fractures, osteoporosis, and bone metastases, which require partial or total replacement of joints (Kurtz et al., 2007, 2014; Wengler et al., 2014). The increase of joint replacements leads to an increase in aseptic loosening and debonding-related implant failure (Cram et al., 2012), which are difficult to anticipate, as the responsible phenomena of bone remodeling and bone apposition are complex and remain poorly understood.

One of the most important factors for the success of an endosseous implant is mechanical stability (Huja et al., 1999). Good initial contact between bone and implant, good bone quality, and an appropriate amount of micro-motion at the bone-implant interface (BII) govern the growth of new bone and therefore, the adaptation of the implant inside the patient's body. Poor initial stability, incorrect load distribution, and large micro-motions can lead to maladaptation of the implant. In turn, maladaptation of the implant can lead to loosening, malapposition of bone tissue, and bone loss. These conditions can increase friction at the BII, which in turn may lead to wear and failure of the implant (Huiskes, 1993).

Two types of implant stability can be distinguished: (i) primary (or initial) stability during surgery, which is mainly governed by mechanical factors, such as interlocking phenomena and bone quality (Viceconti et al., 2000) and (ii) secondary (or long-term) stability, that is achieved several weeks or months after surgery, through the formation and maturation of newly formed bone tissue at the BII, a process called *osseointegration* (Albrektsson et al., 1981). While the evolution of secondary implant stability is governed by complex biochemical processes, the mechanical behavior of the BII remains crucial for the surgical outcome (Gao et al., 2019). Therefore, a thorough understanding of the contact mechanisms that govern and inhibit the adaptation of implants is necessary. The application of these new insights during the design and testing phase of implants, can lead to improved implants with a longer life expectancy, fewer implant failures and therefore, fewer revisions of artificial joints. In addition, advanced numerical

prediction of implant behavior *in vivo*¹ could reduce the amount of animal experiments and clinical patient trials, which are necessary for the evaluation of endoprosthetics. Furthermore, these tools could help surgeons make informed decisions of the optimal implant and implantation technique for a specific patient.

In most mechanical engineering disciplines and industries, computational modeling, e.g. computational fluid dynamics or structural mechanics, is already a well established tool to design, simulate, and optimize procedures, machinery, and biological and chemical processes. However, adhesive contact between bones and implants is a highly complex multi-physics and multi-scale problem that still lacks a holistic computational model that addresses all relevant phenomena and is able to predict correct results for the whole life cycle of an implant. As implant stability includes phenomena on different time- and length-scales, tissue mechanics, structure and contact mechanics, and biochemistry, it presents a number of unique challenges absent in more traditional computational modeling applications. Furthermore, due to the size and shape of common joint replacements and the reliance on bone remodeling and osseointegration, experimental data on long-term stability is scarce, making validation of numerical models difficult. Most numerical analyses of orthopedic devices are performed to: (i) model bone remodeling and osseointegration, (ii) gain a fundamental understanding of the (mechanical) behavior of the BII, and (iii) assist the design and pre-clinical testing of new implants and to compare their performance with existing designs. While there are many numerical studies concerning these aspects (Pankaj, 2013; Taylor et al., 2013; Haiat et al., 2014; Murakami and Wakabayashi, 2014; Taylor and Prendergast, 2015), the specific modeling and prediction of debonding due to imperfect osseointegration is still lacking in the literature.

The objective of this thesis is to propose several computational models for the adhesive contact at the BII during the surgery and after osseointegration. The contact models consider non-linear material behavior, large deformation, adhesive friction, osseointegration, and debonding. Bone and implant are assumed to be deformable solids. The models are applied to coin-shaped implants for verification and validation and then applied to simulate initial and long-term stability of an acetabular cup implant (ACI). The new contributions of this work comprise four complementary studies on primary and long-term stability and debonding of osseointegrated implants.

First, determinants of the primary stability of cementless ACI are presented. To quantify primary stability, the insertion of an ACI into a human hemi-pelvis and subsequent pull-out are simulated. Primary stability is quantified by the remaining gap between hip cavity and implant after insertion, and the maximum pull-out force. The influence of the interference fit, the interfacial friction coefficient, and the stiffness of the cortical and trabecular bone tissue on primary stability is discussed. Based on the patient's bone stiffness, optimal combinations of the interference fit and the friction coefficient (i.e. implant surface roughness) can be identified to ensure optimal initial stability.

Second, a phenomenological model for the frictional contact behavior of debonding osseointegrated implants is developed. The classical Coulomb's law (see Section 3.3.3) is extended from a constant to a varying friction coefficient, that models the transition from an unbroken to a broken state, based on a state variable depending on the total sliding distance of the implant.

1. Latin for "within the living"; *in vivo* studies are performed inside a living organisms.

While the unbroken state denotes osseointegration and thus the presence of adhesive bonds and a higher friction coefficient, the broken state denotes pure frictional contact behavior of the interface with a lower friction coefficient. Thus, this model can account for the higher tangential shear forces observed in osseointegrated implants compared to unbonded implants. This model is applied to the torsional debonding of coin-shaped implants (CSI) and the results are compared to experimental data and a previous analytical model.

Third, the modified Coulomb's law for tangential debonding is applied to simulate secondary stability of an ACI and determine relevant factors. Furthermore, the model is extended in normal direction by a cohesive zone model (see Section 3.3.2), to account for debonding in normal direction and allow for adhesive friction. This contact model is applied to simulate the debonding of a 3D, osseointegrated ACI in different removal tests. The implant stability is quantified by the removal force/torque and the biomechanical determinants of long-term stability, such as primary stability and degree of osseointegration are assessed. The results are compared with the purely tangential model to identify the relevance of normal adhesion in the debonding of ACI.

Last, two simple evolution laws for osseointegration are presented, which are based on initial stability, in terms of contact pressure and contact gap. They are used to compute realistic and time-dependent osseointegration of implants and can be coupled with models of initial and long-term stability to provide a complete workflow for implant assessment.

Due to their generality all models presented herein can be applied to various kinds of endosseous implants or imperfectly bonded interfaces in general. Furthermore, the presented models can be coupled with more advanced bone remodeling algorithms or realistic loading data, to make qualitative simulations and prognoses for the whole life cycle of an implant from the surgery, through bone remodeling and osseointegration, to long-term stability under cyclic loading.

The remainder of this thesis is structured as follows: Chapter 2 provides an introduction into the biomedical and biomechanical background of this thesis. Furthermore, several experimental methods to analyze implant stability and the state of the art in numerical simulation of implant stability are summarized. In Chapter 3, the continuum mechanical equations required to generally describe nonlinear contact between two deformable bodies are summarized. Chapter 4 follows with an introduction into nonlinear finite element methods for solids and the resulting solution procedure for contact problems. A finite element study on the determinants of primary stability of an ACI is discussed in Chapter 5. An analytical and numerical model for tangential debonding of osseointegrated implants is derived and applied to simple implants in Chapter 6. This model is extended into normal direction and applied to model long-term stability of an ACI in Chapter 7. In Chapter 8, three simple evolution laws for osseointegration based on the initial stability of the implant are presented. These time-dependent evolution laws are used to compute the distribution and degree of osseointegration, based on the contact gaps and contact pressure distribution at the BII. Chapter 9 concludes this thesis and provides some perspective for future work.

Chapter 2

Background

This work introduces various computational contact models to analyze the primary and secondary stability and adhesive debonding of osseointegrated implants and identifies biomechanical determinants of implant stability. This chapter provides an introduction into the topic of bone implants, bone implant stability, and the necessary biomedical and biomechanical background. Furthermore, several experimental methods to analyze implant stability and the state of the art in numerical simulation of implant stability are summarized.

2.1 Bone

From a biomedical point of view, bones are rigid organs that form part of the skeleton of vertebrates. The main functions of bones are the support of the body structure, mobility, production of red and white blood cells, and storage of minerals. The adult human body consists of around 205 bones, which can be divided into groups of long and short bones, flat, sesamoid and irregular bones. Besides mineralized tissues, bones consist of bone marrow, nerves, blood vessels, and cartilage. From a biomechanical point of view, bone is a multiscale composite and heterogeneous medium ([Sansalone et al., 2010](#)).

2.1.1 Bone Tissue

Bone tissue is a mineralized tissue that appears in the human body in mainly two forms: cortical and trabecular bone. Both types have a hierarchical structure. At the macroscopic scale, bone tissue is governed by a rigid matrix that composes 30 % of the volume of the whole bone and is made up of collagen fibers, non-collageneous proteins, and lipids. The other 70 % are inorganic minerals, such as calcium carbonates and calcium phosphates (e.g., hydroxyapatite), in varying percentage ([Paschalis et al., 2001](#); [Olszta et al., 2007](#); [Gao and Sevostianov, 2016](#)). At the microscopic scale, bone tissue consists of different types of bone cells, e.g., osteoblasts and osteocytes, which are responsible for formation and mineralization of bone tissue, and osteoclasts, which are involved in the resorption and reformation of bone. An illustration of the hierarchical structure of bone tissue is shown in [Figure 2.1](#).

The exterior shell of bones is made up of cortical bone, also referred to as compact bone. It facilitates the main functions of bones, such as the support and protection of the whole body, provision of levers and attachment sites for muscles, sinews, and joints, and the storage and release of minerals, mainly calcium. Cortical bone is composed of concentric parallel

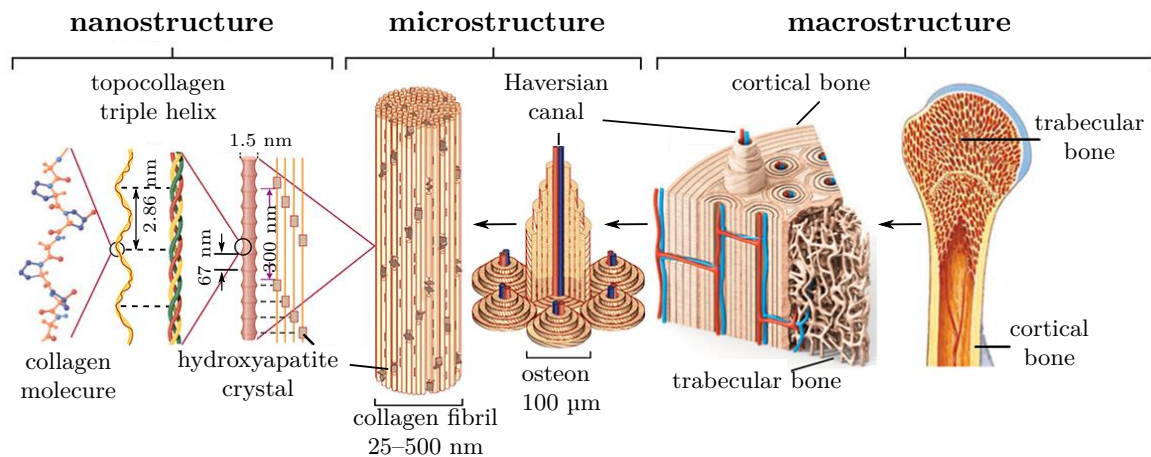


Figure 2.1 – Schematic illustration of the hierarchical structure of bone tissue. Adopted and modified from (Grandfield, 2015).

bone lamellae, which form base units called osteons or Haversian systems. Osteons are centered around Haversian canals, which contain blood vessels. Haversian canals communicate between the blood vessels, the medullary cavity, and the periosteum by transverse canals, called Volkmann’s canals.

Trabecular bone, which is also known as cancellous or spongy bone, is typically found at the ends of long bones, such as the femur (see Figure 2.4). It has a sponge like, porous structure made up by a network of trabeculae. The trabeculae are embedded in a medium composed of bone marrow, blood, and stem cells that produce blood cells. Trabeculae are aligned towards the mechanical load distribution, and thus trabecular bone is exposed to constant change as the bone adapts to new load cycles or damage. While having a larger specific surface area than cortical bone, trabecular bone is less dense and less stiff.

From a mechanical point of view, bone tissue is a multiscale composite and a heterogeneous medium and exhibits different mechanical properties: (i) anisotropy, i.e., it has different material properties in different directions, (ii) viscoelasticity, i.e., it exhibits both viscous and elastic characteristics when undergoing deformation, (iii) surface roughness and porosity on different length scales. Furthermore, bone properties vary according to the type of bone tissue and the observation scale but also from patient to patient (and species to species), due to, e.g., differences in sex, age, activity level, and health conditions (Whitehouse and Dyson, 1974; Goldstein, 1987; Bayraktar et al., 2004). Furthermore, bone properties evolve constantly due to bone remodeling processes, that allow bone to heal and to adapt its structure and loading capabilities to new loading conditions.

2.1.2 Bone Remodeling

Healthy bone remodels constantly and adapts its structure to the loads it is subjected to, in order to optimize load distribution inside the bone as well as to improve stability and to prevent and heal fractures (Wolff, 1892). During this process, bone tissue is resorbed by osteoclasts, which remove the mineralized matrix and break up organic bone components. Then, new bone tissue is created by osteoblasts where needed. Osteoblasts are responsible for bone synthesis and mineralization, renewal and repair. Once trapped inside the bone matrix, they become inactive

and are transformed into osteocytes, which are mature bone cells that constitute the osteons.

Bone healing can be divided into two mechanisms: direct bone growth and indirect bone growth after callous formation (Agarwal and García, 2015). The first mechanism involves the growth of bone from the broken ends at a fracture site without forming fibrous tissue and this is the mechanism that is exploited by cementless implants (see Section 2.2 and 2.2.3.2). The second mechanism involves inflammation, leading to a callous formation that needs to be resorbed so that healthy bone growth can take place.

2.2 Endosseous Implants

Endosseous implants are used to support or replace joints, bones, or teeth by directly inserting the implants into the bone structure. Some examples of commercially used endosseous implants are shown in Figure 2.2. Essentially, endosseous implants can be divided into two groups: cemented and uncemented implants.

Cemented implants use acrylic cement (polymethylmethacrylate (PMMA) copolymer and methylmethacrylate (MMA) monomer) to quickly establish a solid attachment to the bone, which allows for mobility immediately after surgery. Cemented joint replacements have been in clinical use for many decades and a successful implant may last more than 20 years. A successful joint replacement has a stable boundary between the implant and the cement and a durable mechanical connection between the cement and the bone. However, over time the cement can crack or wear out, loosening the connection between the implant and adjacent bone, making a revision surgery necessary (Herberts and Malchau, 1997, 2000). Loosening is more likely to occur in patients who are very active or very heavy, as the implants are put under more frequent and higher loads. For this reason, cemented joint replacements are more commonly recommended for patients who are older, have conditions such as rheumatoid arthritis, or are younger but have compromised health or poor bone quality and density. While cemented implants can be loaded immediately after surgery, the introduction of bone-cement and cement-implant interfaces increases the risk of debonding and wear. Furthermore, the bone cement can cause thermal damage due to the polymerization reaction (Charnley, 1964; Hailer et al., 2010) and can become problematic in case of revision surgery, as it needs to be removed (Charnley, 1964; Galasso et al., 2011). The widespread use of uncemented implants has shown that some implants experience a better fixation through osseointegration than by cementing the interface, e.g. the acetabular component (see Figure 2.4 and 2.5) (Widmer et al., 2002).

Nowadays, uncemented implants have become more and more common (Grimberg et al., 2019). Uncemented implants establish initial stability during surgery by a press-fit, which is mainly governed by mechanical factors, such as interlocking phenomena (Swami et al., 2016). Long-term stability is achieved several weeks or months after surgery, through osseointegration. The contact surfaces of such implants are rough or semi-porous, to allow bone to grow into and around the implant surface and to form a solid attachment, due to mechanical interlocking and chemical bonding between the calcium of the bone and the alloy or coating of the implant (Barriere et al., 2004; Baril et al., 2011; Sul et al., 2013). Cementless implants are mostly used in younger, more active patients with good bone quality (Drexler et al., 2012). Younger bone is more prone to grow into the implant as expected, and thus facilitates the fixation of the implant.

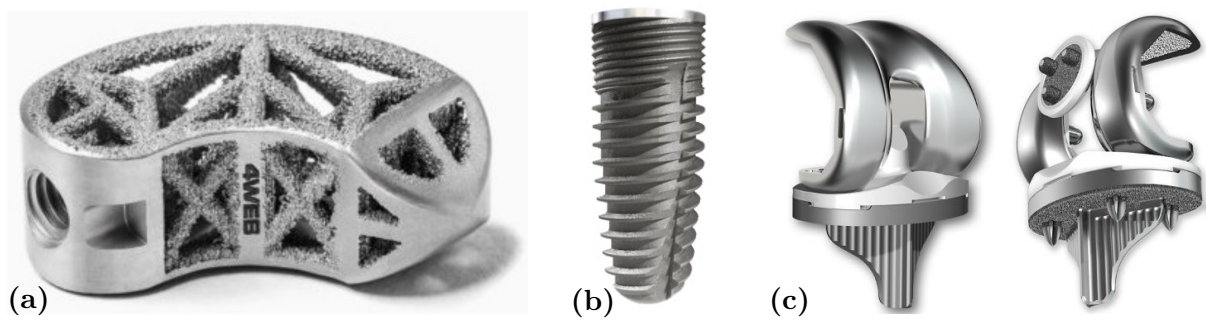


Figure 2.2 – Examples of different endosseous implants: (a) Spinal implant (4web medical, 2021). (b) Dental implant (biotech-dental). (c) Knee implants (strykerCTKS).

For some joint implants, e.g., total knee or hip replacements, a combination of both methods is applied where one component is cemented while the other part is left to osseointegrate. In evaluating cementless knee prostheses, physicians have found that better attachment to the bone occurs with the femur than with the kneecap or lower leg (Robertsson et al., 2014; Wyatt et al., 2014). Accordingly, some physicians use a cementless attachment to the femur and cement the other portions of the implant, an approach called hybrid or mixed total knee replacement.

While stainless steel has been used as implant material for over a century, titanium and titanium alloys (e.g., Ti-6Al-4V) have gained more and more attention, as they have been shown to form a closer contact to bone, due to chemical bonding with the bone tissue (Albrektsson et al., 1985, 1986). In addition, titanium has a similar tensile strength as stainless steel but is much lighter.

Not only the material, but also the surface properties play a significant role in the success and quality of the integration of an implant. In general, rough surfaces are preferred for implant parts in contact with bone as they have a larger available area for host proteins and cells and have been shown to promote mineralization (Shalabi et al., 2006; Novaes et al., 2010). The typical surface roughness of implants varies from 0.5 to 10 μm (Albrektsson et al., 1986; Jemat et al., 2015; De Bruyn et al., 2017). Common surface treatments are acid etching, sand blasting, oxidation, and mechanical polishing. In addition to surface treatment, the application of hydroxyapatite or other bioactive coatings has shown to be promising and led to improved bone ingrowth in several studies (Cook et al., 1992; Søballe, 1993; Barrere et al., 2003). With the recent development of laser beam melting, 3D printing, and topology optimization, titanium implants and implant surfaces can now be printed with complex topography and topology (Palmquist et al., 2010; Baril et al., 2011). In the context of implants, surface topography refers to the surface roughness, including the waviness, asperity, and surface finish, while topology refers to the macroscopic geometry and structure of the implant (see Figure 2.2, left).

Despite recent advances in implant technology and the optimization of surgical procedures, debonding and failure of endosseous implants of both types still occur and may have dramatic consequences. Aseptic loosening due to, e.g., wear and osteolysis, is the main cause (75 %) of implant revisions worldwide (Crawford and Murray, 1997; Drexler et al., 2012). Up to 25 % of patients have to undergo revision surgery and approximately 7 % within the first 8 years of implantation. Revision surgery is usually more invasive than the first surgery and the reported 15-year survival rate of revision surgery is only 69 % (Ulrich et al., 2008). Therefore, there is a high demand in reliable models that can assess and predict the behavior of the BII, to aid in

implant conception and optimizing surgical procedures.

The methods developed in this work will be applied to two different types of cementless implants: coin-shaped implants and acetabular cup implants.

2.2.1 Coin-Shaped Implants

Most studies on bone attachment to implants have used push-in or pull-out *in vitro*¹ tests (Bishop et al., 2014; Wennerberg et al., 2014; Berahmani et al., 2015; Damm et al., 2015). The implant geometry influences the test results (Brånemark et al., 1998) and leads to spatially complex, non-uniform, multi-axial stress fields (Shirazi-Adl, 1992) and unstable crack propagation. Therefore, using realistic implant geometries makes it difficult to estimate a physically meaningful value for the interfacial mechanical strength. As a consequence, models with a planar BII were designed to minimize the effects of friction and mechanical forces introduced by the geometry (Skripitz and Aspenberg, 1999).

A frequently used group of models are coin-shaped implants (CSI) These small, cylindrical implants can be implanted into rabbits in order to study determinants of implant stability and the healing process (Rønold and Ellingsen, 2002; Rønold et al., 2003). They can be used for different kinds of analyses, such as histology and histomorphometry, spectroscopy, and experimental testing. The planar bottom surface allows the study of the BII in a controlled manner (Mathieu et al., 2012a; Vayron et al., 2014; Fraulob et al., 2020b). Initial gaps between implant and bone allow the study of newly formed bone (Fraulob et al., 2020b), while Polytetrafluoroethylene (PTFE) caps on the side wall ensure that only the bottom surface is osseointegrated, which is essential for some types of mechanical testing, e.g., torsion (Mathieu et al., 2012a). Figure 2.3 shows two images of a freshly implanted CSI in a rabbit tibia and a histological image of an osseointegrated CSI.

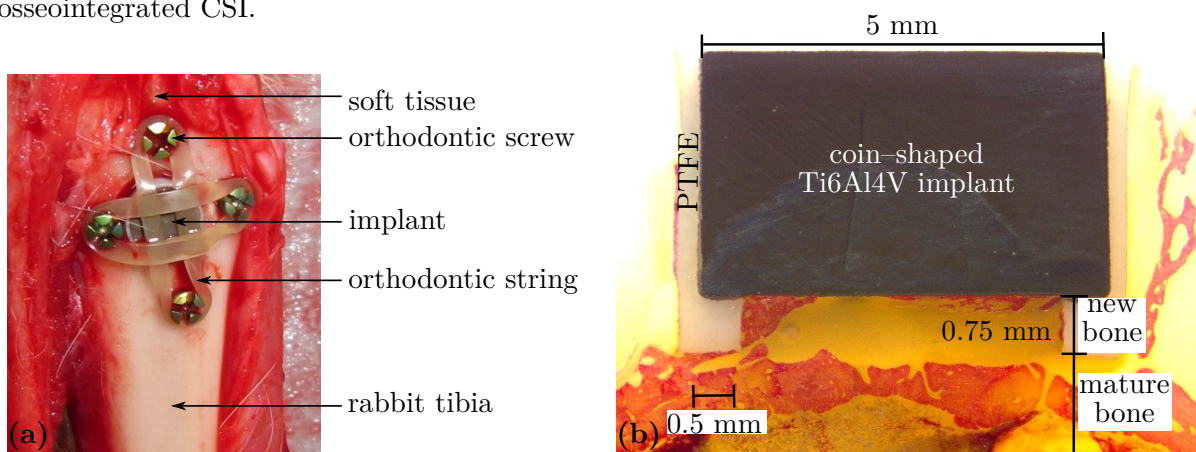


Figure 2.3 – Different images of a CSI: (a) CSI after implantation in a rabbit tibia. (b) Histological image of an osseointegrated and cut CSI after a healing time of 10 weeks. Adopted and modified from Vayron et al. (2014); Fraulob et al. (2020b).

1. Latin for "within the glass"; *in vitro* studies are experimental studies that are performed outside a living organism in a controlled environment.

2.2.2 Acetabular Cup Implants

One of the most common orthopedic surgery is hemi- or total hip arthroplasty (THA) (Lee and Goodman, 2008; Grimberg et al., 2019). The femoral head and, if necessary, the acetabulum are replaced with an artificial implant. A total replacement implant consists of three parts: (i) an ACI, (ii) a liner, and (iii) a femoral stem, which are depicted in Figure 2.4. An ACI is usually a hemispherically shaped implant, covered with an alloy or a bioactive coating, such as hydroxyapatite. The outer surface of the implant is usually rough, porous, or has a complex surface structure. Some examples of commercially used ACI are shown in Figure 2.5. During surgery, a hemispherical cavity is drilled into the pelvis. In the case of cementless implants, this cavity is often under-reamed to produce an interference fit between bone and implant. This interference fit is defined as the difference in diameter between the cavity and the ACI.

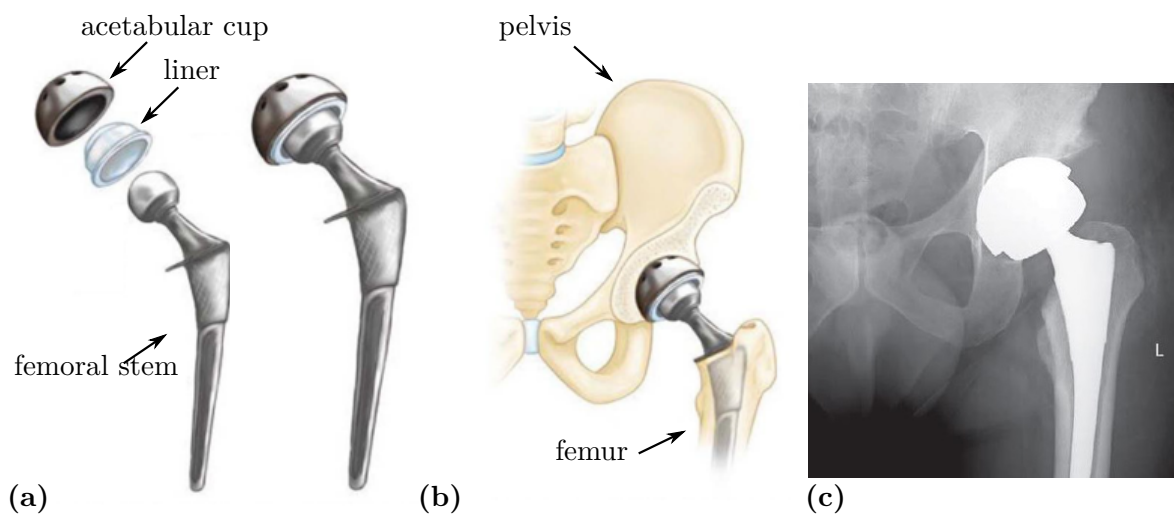


Figure 2.4 – Total hip replacement: (a) Schematic illustration of the components and the final system of a total hip replacement. (b) Implant position inside the patient. (c) X-ray of a total hip replacement inside a patient. Adopted and modified from AAOS; Learmonth et al. (2007).



Figure 2.5 – A variety of ACI with different surface treatments and with and without screw holes (b.braun; strykerTridentII).

During the surgery, an ancillary is attached to the ACI. The ACI is then inserted into the cavity through hammer blows onto the ancillary (Michel et al., 2014). The interference fit produces a press-fit of the implant and ensures initial stability. For patients with poor bone

quality or mass or for revision surgeries, ACI can also be fixated by using screws. Long-term stability is then achieved by bone growing around and into the surface of the implant.

2.2.3 The Bone-Implant Interface

The BII is a complex system governed by biochemical and biomechanical processes, occurring at nano- and micro-scales (molecular level biochemistry and surface roughness) as well as the macro-scale (organ level load application). Here, the definitions of primary and secondary stability are given, and relevant biological and mechanical factors are discussed.

2.2.3.1 Primary Stability

Primary stability of a cementless implant is defined as the initial fixation of the implant in the host bone and is achieved during surgery. It is governed by patient- and implant-specific factors, as well as by the surgical protocol.

The patient's bone quality and quantity are essential to ensure that initial fixation takes place (Swami et al., 2016). If bone stiffness or bone mass is insufficient, some implants, like the ACI, can be additionally fixed with screws, to avoid excessive micro-motion and displacement.

While the implant geometry has an effect on the load distribution from implant to bone, the surface properties (e.g., roughness, porosity, surface treatment) affect the seating of the implant (Curtis et al., 1992; Hadjari et al., 1994; Ries et al., 1997; Markel et al., 2002). A certain roughness and porosity is needed to ensure osseointegration later on. However, highly rough surfaces can inhibit the proper seating of the implant.

From a mechanical point of view, the key elements of the surgical protocol of uncemented implants can be reduced to interference fit, implantation angle, insertion load, and bone stiffness. While a certain interference fit and insertion load is needed to properly insert and fixate the implant, excessive interference fit and insertion load can lead to bone damage and bone resorption.

2.2.3.2 Osseointegration and Secondary Stability

Secondary stability is achieved several weeks after surgery, through osseointegration phenomena. The process of osseointegration is based on bone remodeling and healing. An implant is considered as osseointegrated (and therefore secondarily stable) if there is no relative motion between the bone and the implant. Thus, it is rather measured in terms of stability and not in terms of contact area.

Osseointegration can be divided into three stages, which are shown in Figure 2.6: In the insertion stage, a cavity is drilled into the host bone, resulting in destroyed bone. Then, the implant is inserted by screwing (e.g., for dental implants) or hammering it into the cavity. The space between implant and bone is initially filled with fluids, blood clots, and bone fragments (see Figure 2.6, 1.). In the healing phase, blood clots and wound fluid are absorbed and replaced by a collagen matrix that is mineralized progressively by the action of osteoblasts (see Figure 2.6, 2a.). In addition, the new tissue is vascularized. During this phase, the implant temporarily loosens, while new bone grows onto and into the implant. Therefore, the implant should not be loaded fully for several weeks to ensure proper stability. The newly formed bone matures in up to 16 weeks (Roberts et al., 1992).

After healing, the new bone tissue has fully mineralized. A steady state is established where the implant is fully integrated into the bone and the bone tissue remodels to given loads and stresses (see Figure 2.6, 3a.).

However, osseointegration can fail at any stage. An example of an initial failure is that the wound fluid is not replaced by a mineralized collagen matrix but rather by non-mineralized connective tissue that does not support the implant and can increase further bone loss (Huiskes, 1993), as it does not distribute loads onto the remaining bone properly (see Figure 2.6, 2b.). A failure later on is usually due to insufficient bone-to-implant contact. This can lead to suboptimal load distribution between implant and bone, which may lead to debonding of the interface, interface motion, debris, and wear (see Figure 2.6, 3b.).

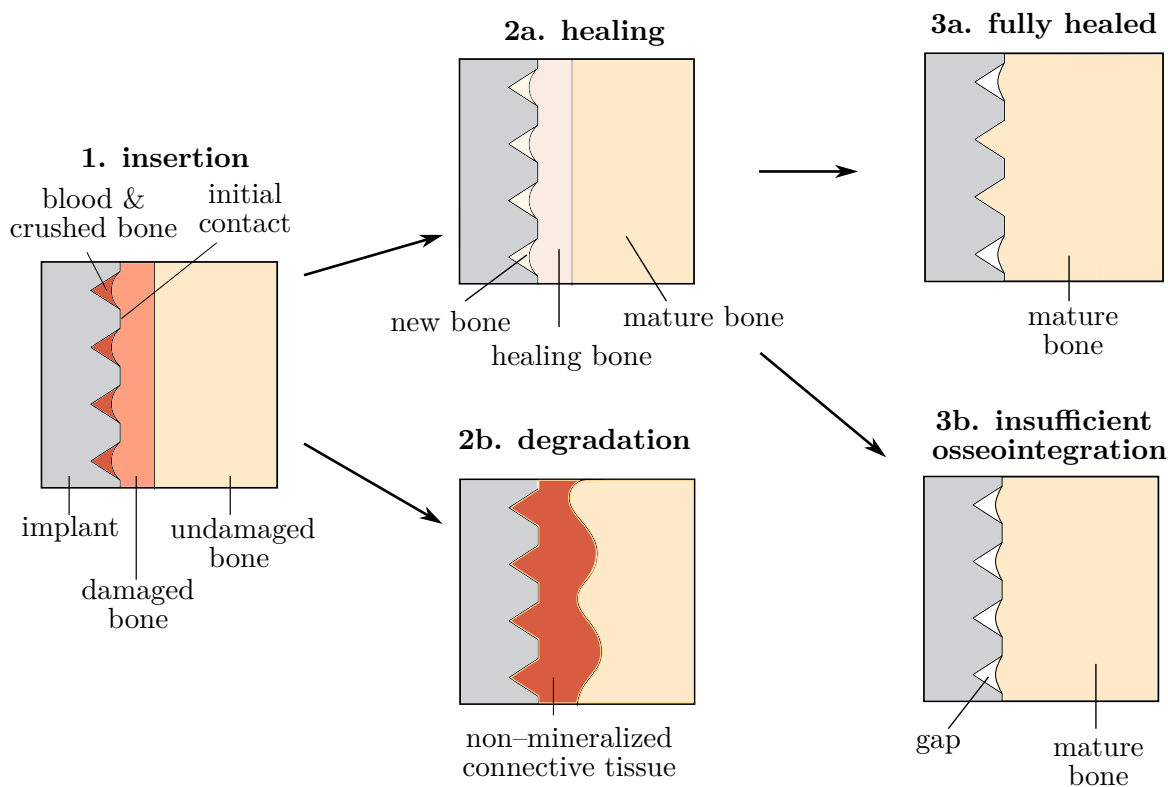


Figure 2.6 – Schematic illustration of the different stages of osseointegration and examples of osseointegration failure.

Biological factors that inhibit proper osseointegration are, e.g., poor bone quantity and mineral density. In addition, many biological mechanisms of the BII are stimulated or inhibited by the mechanical behavior of the interface, depending on the intensity of the mechanical stimulation.

The implant's surface material, roughness, and coating are not only important factors for primary but also secondary stability. An appropriate degree of surface roughness ensures the implant fixation through new bone growing into the surface (Schwarz et al., 2009) and by minimizing micro-motion during the healing phase, due to higher interfacial friction (Gao et al., 2019). Different surface treatments and coatings, such as hydroxyapatite coatings have been shown to promote bone healing (Le Guéhennec et al., 2007). The contact surface area of the implant is also important, as a larger initial contact with bone also increases the possible sites for bone ingrowth.

Another important factor is the implant geometry, which is responsible for the stress distribution. Excessive compressive stresses created during the implant insertion can lead to bone necrosis and ischemia (Sotto-Maior et al., 2010). Although the implant may be in contact with trabecular and cortical bone, the latter plays the governing role in experimental and numerical analyses, as the highest stresses occur in cortical bone around the neck of the implant (Sütpideler et al., 2004). Improper load distribution after osseointegration can have a negative impact on bone remodeling, as bone may grow away from the implant, leading to implant loosening. Furthermore, the load cases and the load distribution influence the interface micro-motion. While there is still some disagreement about how much micro-motion is really necessary to stimulate bone growth, usually a value of up to 50 μm is stated (Bragdon et al., 1996; Fitzpatrick et al., 2014). Micro-motion that exceeds a value of 150 μm has been shown to inhibit bone growth and promote bone loss (Pilliar et al., 1986; Jasty et al., 1997). Loading conditions vary not only with the implant geometry but also with the patient's height, weight, age, sex, and vitality (Kutzner et al., 2010). Therefore, the determination of biomechanical properties and mechanical phenomena is essential to understand the behavior of the BII.

2.3 Determining Biomechanical Properties and Behavior of the Bone-Implant Interface

There are different methods to assess the properties of the BII and implant stability. They can be divided into invasive and non-invasive experimental methods, and numerical methods. Often, multimodal approaches are used to gain as much insight out of a sample as possible, e.g, histological analysis and quantitative ultrasound techniques (Fraulob et al., 2020c) or nanoindentation and Raman spectroscopy (Fraulob et al., 2020b). This section summarizes the most common approaches found in the literature.

2.3.1 Non-Invasive Experimental Methods

There exist several non-invasive methods to monitor osseointegration that can be applied during the surgery and at different stages of the healing process.

In orthopedic surgery, the surgeons mostly rely on their experience, perception, and proprioception to determine the proper seating and initial stability of the implant. For certain implants (e.g., a femoral stem) the proper seating during insertion can be identified by changes in (i) the sound and (ii) the physical sensation during the impacts with a surgical hammer (Trisi and Rao, 1999).

A simple method is the percussion test, where the implant is struck with a metallic instrument to induce a sound (Atsumi et al., 2007). A "dull" sound may indicate no or poor osseointegration while a "crystal" sound indicates good osseointegration (Swami et al., 2016). This technique was used to develop Periotest (Medizintechnik Gulden, Bensheim, Germany), which is a commercially available tool that uses an electro-magnetically driven and controlled tapping metallic rod. The mobility of the BII is measured by the reaction of the implant to the imposed impact load and the bone density can be derived. However, the reliability of this method has been questioned due to its sensibility to many factors, such as the striking height and handpiece angulation (Salvi and Lang, 2004). Furthermore, this method is deemed unsuitable for standardized testing, due to its dependence on the surgeon (Atsumi et al., 2007;

Bayarchimeg et al., 2013; Swami et al., 2016) and cannot be applied to every type of implant. In addition, this method only allows an assessment of initial stability but cannot predict the long-term outcome of the surgery.

Another measurable factor during the surgery is the cutting torque resistance while reaming or drilling the implantation site. Studies have shown that the cutting torque resistance is highly correlated with bone density (Friberg et al., 1995, 1999) and can be used as an indicator for bone quality.

Medical imaging, such as quantitative computer tomography and photon absorptiometry, can be used to assess bone quantity and density (e.g. before surgery) and can also monitor the progression of osseointegration and detect gaps in the BII. However, depending on the size and location of the implant, not all values can be quantified and gaps might not be visible due to restrictions in imaging perspective, resolution, and artifacts (Knott et al., 2010).

Resonance frequency analysis (RFA) uses the vibration of a transducer and structural analysis to measure implant stability and bone density. One part of the transducer is directly screwed onto the implant while the other part works as a receptor. The implant is perturbed by a sinusoidal input with increasing frequency until the implant resonates. Measurements after surgery provide a baseline reading. During and after the healing period, high frequency resonance indicates a strong BII. There exist different commercially available products on the market that use enhanced RFA, such as electronic technology RFA and magnetic technology RFA (Ostell, Integration Diagnostic AB, Goteborg, Sweden). However, RFA cannot be used to directly identify the properties of the BII and the orientation and fixation of the transducers were found to have significant effects on the measured implant stability (Vayron et al., 2018a,b).

Quantitative ultrasound (QUS) techniques are used to estimate bone quality and quantity and degree of bone-to-implant contact (Laugier and Haïat, 2011; Mathieu et al., 2011a, 2012b, 2011c). Ultrasonic waves are sensitive to the bone's elastic properties (Laugier and Haïat, 2011). As the bone-implant contact ratio (BIC), the elastic properties, and the mass density of periprosthetic bone tissue increase, the changes in the reflection of the ultrasonic waves can be measured and quantified. Recent studies have shown that QUS techniques are significantly more sensitive to changes of periprosthetic bone tissue compared to RFA (Vayron et al., 2018a,b).

2.3.2 Invasive Experimental Methods

There exist several invasive techniques to determine implant stability and evaluate osseointegration that are mainly used in research and implant testing.

In histomorphometric analysis, the osseointegrated implant is removed including the surrounding bone and sliced into specimens and often dyed to differentiate between tissues (see Figure 2.3). These specimens can be probed, e.g., by nanoindentation (Anchieta et al., 2014; Kim et al., 2016a,b; Anchieta et al., 2018) and observed under a microscope. With this method, the bone-implant contact ratio and bone microarchitecture (Trisi and Rao, 1999) and mineral density (Artzi et al., 2003a,b), can be assessed. Histomorphometric analysis is also used after different healing periods to assess the change in bone structure and composition. However, this method cannot quantify the fixation of the implant and only provides 2D information. Furthermore, this technique is mainly used for small implants, like dental implants and CSI.

Raman spectroscopy uses a specific Raman interferometer with an infrared laser. The scattered light reflects compositions of mineral and collagen phases due to the difference in molecule

and ion vibrations. This can be used to evaluate the local biochemical composition of bone tissue at the nanoscale, which includes the mineral and organic components. Raman spectroscopy has been used to investigate the remodeling process of healing bone tissues in general (Ahmed et al., 2018; Shah et al., 2019) and for titanium implants (Lopes et al., 2007; Shah et al., 2016). As with histomorphometry, this method cannot quantify the stability of the BII.

Removal tests, such as pull-out, push-out, lever-out, and torsional tests, are widely used to evaluate the implant fixation by recording the force-displacement curve, the maximum removal force, micro-motion, or the shear strength of the BII (Søballe, 1993; Brunski et al., 2000; Chang et al., 2010; Trisi et al., 2011; Mathieu et al., 2012a), which has been correlated with histological assessments in animal studies (Johansson and Albrektsson, 1991; Haiat et al., 2014). These techniques are used to quantify primary and secondary stability of implants *in vitro* and *ex vivo*². Most experimental studies on secondary stability are performed on dental implants and CSI. The influence of biological as well as mechanical factors on the long-term stability, and the implant topology make experimental testing of cementless implants difficult and at present, such studies are lacking in the literature (Viceconti et al., 2004; Helgason et al., 2008). Therefore, there is a high demand in reliable numerical models that can model and quantify the behavior of the BII during the surgery, through osseointegration, up to cyclic loading, bone remodeling, and debonding.

2.3.3 Numerical Methods

Finite element analysis (FEA) has been applied to the whole spectrum of endosseous implants, modeling their behavior *in vivo*, *ex vivo*, and *in vitro*, and assessing determinants of initial and long-term stability, as well as bone remodeling. It has significantly improved the understanding of the mechanical behavior of bone implants and the BII. There exist a number of thorough reviews on numerical models for bone implants and the BII (Pankaj, 2013; Taylor et al., 2013; Haiat et al., 2014; Murakami and Wakabayashi, 2014; Taylor and Prendergast, 2015). Therefore, this section is limited to (i) the primary stability of ACI (ii) osseointegration algorithms, and (iii) macroscopic models of long-term stability, partial osseointegration, and debonding of uncemented implants in general.

2.3.3.1 Primary Stability of ACI

Initially, finite element (FE) modeling of orthopedic implants was mainly used to gain a qualitative insight into the behavior of the bone-implant system inside the patient and to determine relevant patient-, implant- and surgery-specific parameters affecting implant performance (Taylor and Prendergast, 2015), as most of these factors cannot be observed or measured experimentally. Nowadays, numerical modeling is also used in the design phase of implants and studies are carried out to assess the impact on performance of, e.g., changes in implant design and surface treatment (Viceconti et al., 2009; Taylor et al., 2013). Due to the progress of medical imaging (e.g. microcomputed tomography (μ CT)) and its use as geometrical input for FE models, case-specific modeling (Hsu et al., 2006) and multi-factorial studies (Anderson et al., 2005; Hsu et al., 2007; Janssen et al., 2010; Amirouche et al., 2014; Rourke and Taylor, 2020) with realistic bone geometries are carried out to assess patient-related factors on the surgical

2. Latin for "out of the living"; *ex vivo* experiments are either performed on dead organisms (cadaveric studies) or with tissue extracted from a living organism and not grown artificially

outcome, such as bone geometry, bone quality, and loading cycles. A case-specific model is usually used to investigate a unique situation, e.g., a specific condition or geometrical anomaly, whereas a multi-factorial study aims to generate various cases representative of a population and may require a large number of analyses (Clarke et al., 2013). Furthermore, there is a growing potential in FE models to provide patient specific models that can guide the decision making process of orthopedic surgeons in terms of choice of implant and surgical protocol.

2.3.3.2 Predicting Osseointegration

Mathematical and numerical models that can predict osseointegration and bone remodeling are mostly based on continuum damage mechanics (Prendergast and Taylor, 1994; Doblaré and Garcia, 2002; Moreo et al., 2007; Caouette et al., 2013) and mechanoregulatory algorithms (Huiskes et al., 1987; Weinans et al., 1992; Huiskes et al., 1997; Prendergast, 1997; Fernandes et al., 2002; Andreykiv et al., 2005; Dickinson et al., 2012).

These models often incorporate cell differentiation rules based on mechanical stimulus to simulate the creation and maturation of bone tissue by changes in material properties, such as bone density and stiffness. For the mechanical stimulation or threshold of bone growth, strain energy density (Huiskes et al., 1987; Weinans et al., 1993; Andreykiv et al., 2005; Lutz and Nackenhurst, 2012; Chanda et al., 2020), micromotion (Caouette et al., 2013; Tarala et al., 2013; Chanda et al., 2020), interface gap size (Tarala et al., 2013; Chanda et al., 2020) and interface stress (Chanda et al., 2020) are used.

Biological factors that are considered are, e.g. platelet reactions, growth factors, cell density (Andreykiv et al., 2005) and cell differentiation (Andreykiv et al., 2005; Dickinson et al., 2012; Mukherjee and Gupta, 2017; Chanda et al., 2020). Intermediate bonding can be characterized by applying spring elements (Chanda et al., 2020) or change in material parameters (Andreykiv et al., 2005; Dickinson et al., 2012; Tarala et al., 2013; Mukherjee and Gupta, 2017) such as interfacial stiffness. The successful bonding is then modeled by, e.g., setting the osseointegrated contact region to bonded contact (Spears et al., 2000; Fernandes et al., 2002; Viceconti et al., 2004; Andreykiv et al., 2005; Chanda et al., 2020), by means of spring elements (Tarala et al., 2013) or interface elements (Lutz and Nackenhurst, 2012; Caouette et al., 2013).

Some works combine osseointegration estimations with simultaneous or subsequent bone remodeling (Dickinson et al., 2012; Tarala et al., 2013; Mukherjee and Gupta, 2017; Chanda et al., 2020). However, due to the iterative nature and the complexity of the algorithms, they are computationally expensive and can often only be applied to 2D geometries (Andreykiv et al., 2005) or small portions of the FE mesh (Mukherjee and Gupta, 2017).

While these models provide detailed osseointegration states for different types of implants, to the author's knowledge, none of them have been used as input for simulating the debonding of the BII so far.

2.3.3.3 Debonding of Partially Osseointegrated Implants

Most finite element models that study secondary stability and implant failure assume the BII to be either perfectly bonded or fully sliding (Gupta et al., 2010; Tomaszewski et al., 2010; Galloway et al., 2013; Chou et al., 2014; Demenko et al., 2016; Rittel et al., 2017; Mondal and Ghosh, 2019). While perfectly bonded contact conditions do not allow for debonding to occur, interface behavior that is modeled as frictionless or by Coulomb's friction cannot fully represent

the nonlinear interface behavior of the BII even before osseointegration occurs (Dammak et al., 1997b; Viceconti et al., 2004). Furthermore, it was shown that implants are typically never fully osseointegrated and only show a 30-70% bone-to-implant contact after healing (Brånemark et al., 1997; Marin et al., 2010). Therefore, imperfect osseointegration and its influence on stability must be considered.

A common approach is to model imperfect osseointegration by setting osseointegrated contact elements to be perfectly bonded while non-integrated contact elements follow frictionless or Coulomb's friction contact (Spears et al., 2001; Viceconti et al., 2004; Helgason et al., 2009; Galloway et al., 2013). Another approach to account for varying degree of osseointegration is to adjust material properties of the BII, while keeping the interface fully bonded (Kurniawan et al., 2012) or by varying the friction coefficient of the BII from zero for unbonded to infinity for perfectly osseointegrated surfaces (Korabi et al., 2017). However, these models cannot represent the adaptive changes of the bone-implant interface and debonding. Furthermore, they usually determine failure by excessive stress or strain at the BII or the bone, without modeling the actual separation between bone and implant and local changes of contact conditions. So far, only very few FE studies model contact and failure of partially osseointegrated implants. Rittel et al. (2018) studied the influence of partial osseointegration on dental implant stability and cohesive failure. There, a tie constraint was applied to the BII, such that bone-implant debonding occurs in the bone tissue around the interface. Partial osseointegration was model by defining a relative osseointegrated area with random distribution and setting non-integrated areas to frictional contact. To address the lack of numerical models that model partial osseointegration and explicit debonding of the BII, this work puts a special focus on developing and applying such models.

2.4 Further Challenges

Difficulties concerning the modeling of short and long-term stability of endosseous implants arise at many levels. First of all, there is a lack of consistent experimental data, especially on long-term stability. Besides few well documented patient trials, most experiments are performed on animals. Unfortunately, animals have different bone properties and experience different loading cycles than humans, making adaptation of *in vivo* data to humans difficult. Furthermore, even within humans the material parameters differ greatly, requiring multi-factorial studies. Another drawback is that, except for dental implants, there currently exists no effective, non-invasive way to assess implant stability, requiring complicated and ethically difficult animal experiments. In addition, the normal life expectancy of animals is too short for long-term studies, as implants have a life expectancy of 15 years and beyond.

Apart from the available data, bones and bone tissue are complex biological compounds. Bone tissue is a viscoelastic and anisotropic material with nonlinear stress-strain behavior, and therefore is difficult to model realistically and efficiently at the same time. In addition, the load distribution onto bones is not fully understood yet, as many aspects like muscle activity and interaction, posture, and type of movement have to be taken into account. Furthermore, bone-implant contact is a multi-scale problem including chemical binding between bone and implant, motion over the whole contact surface, reaction to external loads, and biochemical remodeling of bone tissue due to mechanical stimulation which all lead to inhomogeneous, time-dependent

2. BACKGROUND

contact. Concerning the stability of implants, some factors like the bone quality of the patients and the skill of the surgeon are factors that cannot be determined beforehand and are hard to quantify.

Chapter 3

Nonlinear Continuum Mechanics

In the previous chapter, the biomedical and biomechanical background of the present work was introduced. This chapter gives an introduction on the basics of nonlinear continuum mechanics of deformable bodies in contact, which are necessary to describe the mechanical behavior of the BII. In this work, nonlinearity occurs due to the stress-strain behavior of the materials and the geometrical variations that significantly affect the load-deformation behavior. A more detailed introduction to nonlinear continuum mechanics of solids can be found in [Holzapfel \(2000\)](#). Contact mechanics involving large deformation and friction is discussed in detail in [Laursen \(2013\)](#) and [Wriggers \(2006\)](#). This work follows the standard notation of nonlinear solid mechanics: lower case letters denote the current (spatial) configuration and upper case letters denote the reference (material) configuration. Bold letters denote vectors and tensors, while standard font denotes scalar quantities.

3.1 Kinematics

Consider a deformable body \mathcal{B}_{0k} ($k = 1$) and its surface $\partial\mathcal{B}_{0k}$ as shown in Figure 3.1. In its reference (material) configuration \mathcal{B}_{0k} , a material point in or on the body has the coordinates \mathbf{X}_k . As this point undergoes large deformation, it obtains the coordinates $\mathbf{x}_k(\mathbf{X}_k)$ in the deformed (or current or spatial) configuration \mathcal{B}_k , defined by

$$\mathbf{x}_k := \boldsymbol{\varphi}_k(\mathbf{X}_k), \quad (3.1)$$

where $\boldsymbol{\varphi}_k$ is the mapping from the reference to the current configuration. The deformation within the body is characterized by the displacement \mathbf{u}_k and the deformation gradient \mathbf{F}_k as

$$\mathbf{u}_k = \boldsymbol{\varphi}_k(\mathbf{X}_k) - \mathbf{X}_k, \quad (3.2)$$

$$\mathbf{F}_k = \frac{\partial \boldsymbol{\varphi}_k}{\partial \mathbf{X}_k}. \quad (3.3)$$

From the deformation gradient \mathbf{F}_k follow the volume change J_k and surface area change J_{sk} defined by

$$J_k := \det \mathbf{F}_k > 0, \quad (3.4)$$

$$J_{sk} := \det_s \mathbf{F}_k > 0, \quad (3.5)$$

which govern the local volume change and surface area change between the reference and the current configuration:

$$dv_k = J_k dV_k \quad \forall \mathbf{x}_k \in \mathcal{B}_k, \quad (3.6)$$

$$da_k = J_{sk} dA_k \quad \forall \mathbf{x}_k \in \partial\mathcal{B}_k. \quad (3.7)$$

Here $\det_s(\bullet)$ is the surface determinant on $\partial\mathcal{B}_k$, see, e.g., [Sauer et al. \(2019\)](#).

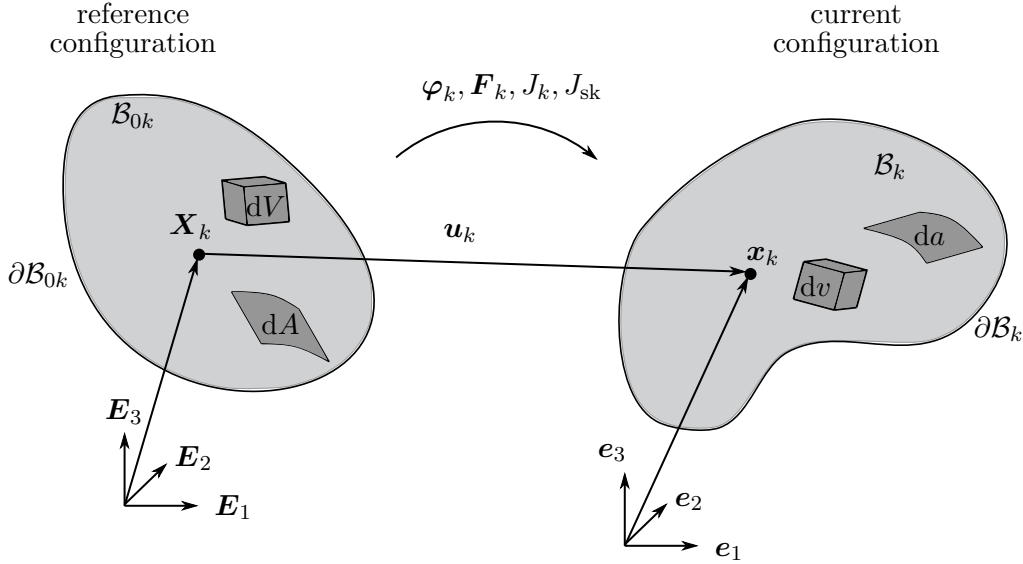


Figure 3.1 – Reference configuration \mathcal{B}_{0k} , current configuration \mathcal{B}_k and their respective surfaces $\partial\mathcal{B}_{0k}$ and $\partial\mathcal{B}_k$.

3.1.1 Strain Measures

Strain describes the change in shape of a body due to external forces (excluding rigid body motion). This change in shape can be exhibited as, e.g. dilatation or shear. Different equivalent choices for the expression of a strain tensor can be made, depending on whether it is defined with respect to the reference or the current configuration and on whether finite or infinitesimal deformation is considered. As the applications in this thesis involve large deformation, a finite strain tensor in material configuration is chosen. Based on the deformation gradient \mathbf{F}_k the Green-Lagrangian strain tensor

$$\mathbf{E}_k = \frac{1}{2} \left(\mathbf{F}_k^T \mathbf{F}_k - \mathbf{I} \right), \quad (3.8)$$

can be defined, where \mathbf{I} is the identity tensor. The corresponding right and left Cauchy-Green deformation tensors are defined as

$$\mathbf{C}_k = \mathbf{F}_k^T \mathbf{F}_k, \quad \mathbf{b}_k = \mathbf{F}_k \mathbf{F}_k^T, \quad (3.9)$$

where \mathbf{C}_k is a material tensor and \mathbf{b}_k is a spatial tensor.

3.1.2 Stress Measures

Stress describes the internal response of a body to external loads. A body can exhibit stress due to external forces, e.g., change in pressure or temperature, or due to internal forces, e.g., the pre-stress of blood vessels.

If we intersect the body \mathcal{B}_k at a point \mathbf{x}_k by a plane with unit normal \mathbf{n}_k , we can determine the traction \mathbf{t}_k acting at this point from

$$\mathbf{t}_k = \boldsymbol{\sigma}_k \mathbf{n}_k, \quad (3.10)$$

where $\boldsymbol{\sigma}_k$ is usually referred to as the Cauchy or true stress tensor. The Cauchy stress tensor $\boldsymbol{\sigma}_k$ completely describes the stress state of a uniformly stressed body. Another common stress measure is the second Piola-Kirchhoff stress tensor \mathbf{S}_k , which is defined by

$$\mathbf{S}_k = J_k \mathbf{F}_k^{-1} \boldsymbol{\sigma}_k \mathbf{F}_k^{-T}. \quad (3.11)$$

This stress tensor relates forces in the reference configuration to areas in the reference configuration. The concrete definition of these stress measures depends on the chosen constitutive (material) behavior.

3.2 Constitutive Equations

Constitutive theory describes the (microscopic or macroscopic) behavior of a material. In the purely mechanical case for deformable solids, constitutive theory formulates relationships between the deformation and the inner forces of a body, also referred to as stress-strain relations. More generally, these relationships are extended by density, temperature, and entropy.

In this work, all materials are modeled as homogeneous (i.e., they have the same properties at every material point) and isotropic (i.e., they exhibit the same behavior in every loading direction). Furthermore, all materials are either linear elastic, linear hypoelastic, or non-linear hyperelastic, which are explained in the following.

3.2.1 Linear Material Model

A Cauchy elastic or linear elastic material does not depend on the past history of the deformation. Consequently, the stress depends only on the current deformation gradient \mathbf{F}_k . The stress-strain relation of a linear elastic body is thus linear and is given by Hooke's law:

$$\boldsymbol{\sigma}_k = 2G_k \boldsymbol{\varepsilon}_k + \Lambda_k \text{tr}(\boldsymbol{\varepsilon}_k) \mathbf{I}, \quad (3.12)$$

where $\boldsymbol{\varepsilon}_k = \frac{1}{2}(\nabla \mathbf{u}_k + \nabla \mathbf{u}_k^T)$ is the infinitesimal strain tensor. Λ_k and G_k are commonly referred to as the first and second Lamé parameters¹, and for a homogeneous, isotropic material defined as

$$\Lambda_k = \frac{E_k \nu_k}{(1 + \nu_k)(1 - 2\nu_k)}, \quad G_k = \frac{E_k}{2(1 + \nu_k)}, \quad (3.13)$$

where E_k is the Young's modulus and ν_k is the Poisson ratio. The corresponding spatial elasticity tensor \mathbb{c}_k is given by

$$\mathbb{c}_k = \Lambda_k \mathbf{I} \otimes \mathbf{I} + 2G_k \mathbb{I}_4, \quad (3.14)$$

where \mathbb{I}_4 is the fourth-order symmetric identity tensor.

Constitutive behavior of elastic materials is a function of only the current state of deformation. This model cannot describe, e.g., hysteresis, stress softening, residual strains, and other inelastic effects. If a deformable body goes through a large deformation or if a material does not behave linearly, a more accurate material model is required.

1. In terms of the Lamé parameters, the shear modulus G_k is often denoted μ . To avoid confusion with the friction coefficient μ the shear modulus is denoted G_k throughout this work.

3.2.2 Hypoelastic Material Model

Hypoelastic material models are also referred to as incremental material models since they are expressed in rate form. In order to derive meaningful material models for finite deformations, objective rates should be used. Material objectivity states that the constitutive laws must not depend on the chosen external reference frame. An objective strain rate is given e.g., by the rate of deformation tensor \mathbf{D}_k and the spin tensor \mathbf{W}_k , defined by

$$\mathbf{D}_k = \frac{1}{2} \left(\dot{\mathbf{F}}_k \mathbf{F}_k^{-1} + \mathbf{F}_k^{-\text{T}} \dot{\mathbf{F}}_k^{\text{T}} \right), \quad (3.15)$$

$$\mathbf{W}_k = \frac{1}{2} \left(\dot{\mathbf{F}}_k \mathbf{F}_k^{-1} - \mathbf{F}_k^{-\text{T}} \dot{\mathbf{F}}_k^{\text{T}} \right). \quad (3.16)$$

As an objective stress rate, one can use the *Jaumann* rate of the Cauchy stress tensor

$$\check{\boldsymbol{\sigma}}_k = \dot{\boldsymbol{\sigma}}_k + \boldsymbol{\sigma}_k \cdot \mathbf{W}_k - \mathbf{W}_k \cdot \boldsymbol{\sigma}_k. \quad (3.17)$$

The stress-strain relationship of a linear hypoelastic material model is then defined by

$$\check{\boldsymbol{\sigma}}_k = \Lambda_k \text{tr}(\mathbf{D}_k) \mathbf{I} + 2G_k \mathbf{D}_k, \quad (3.18)$$

together with the spatial elasticity tensor \mathbb{c}_k from Eq. (3.14).

3.2.3 Compressible Neo-Hookean Material Model

In the particular case of hyperelasticity, the material behavior does not depend on the deformation path. Thus, the work done by stresses only depends on the initial state in the reference configuration and current state in the deformed configuration. A material is defined as Green elastic or hyperelastic, if the stress-strain relationship derives from a strain energy density function W . A special case of the hyperelastic material models is the compressible Neo-Hookean model that also includes a nonlinear stress-strain dependence, such as

$$\boldsymbol{\sigma} = \frac{\Lambda_k}{J_k} (\ln J_k)^2 \mathbf{I} + \frac{G_k}{J_k} (\mathbf{B}_k - \mathbf{I}), \quad (3.19)$$

$$\mathbb{c}_k = \frac{\Lambda_k}{J_k} \mathbf{I} \otimes \mathbf{I} + 2 \frac{G_k - \Lambda_k \ln J_k}{J_k} \mathbb{I}_4. \quad (3.20)$$

3.3 Contact Mechanics

This work focuses on contact problems that arise from surface effects, including friction and adhesion. This section introduces the basic contact surface description, kinematics, and general descriptions of friction and adhesion.

3.3.1 Contact Surface Description and Kinematics

Consider two 3D bodies \mathcal{B}_k , $k = 1, 2$, their boundaries $\partial\mathcal{B}_k$, and their contact surfaces $\partial_c\mathcal{B}_k$, as shown in Figure 3.2(a). In this work, a contact surface denotes the whole potential surface area where contact between two bodies can occur. A 3D surface of body \mathcal{B}_k can be described by the mapping

$$\mathbf{x}_k = \mathbf{x}_k(\boldsymbol{\xi}), \quad \boldsymbol{\xi} \in \mathcal{P}_k, \quad (3.21)$$

which maps a point $\boldsymbol{\xi} = \{\xi^1, \xi^2\}$ lying in the 2D parameter space \mathcal{P}_k to the surface point $\mathbf{x}_k \in \partial_c \mathcal{B}_k$. For a given surface point \mathbf{x}_k one can determine the point that minimizes the distance between \mathbf{x}_k and the neighboring contact surface $\partial_c \mathcal{B}_\ell$, which is denoted by the closest point projection $\mathbf{x}_p = \mathbf{x}_\ell(\boldsymbol{\xi}_p) \in \partial_c \mathcal{B}_\ell$ ($\ell = 2, 1$). At the unknown point \mathbf{x}_p , the surface $\partial_c \mathcal{B}_\ell$ can be characterized by the co-variant and contra-variant tangent vectors \mathbf{a}_α^p and \mathbf{a}_p^α ($\alpha = 1, 2$) and by its surface normal \mathbf{n}_p . Then, a set of tangent vectors on $\partial_c \mathcal{B}_k$ can be defined as

$$\mathbf{a}_\alpha^p := \frac{\partial \mathbf{x}_\ell(\boldsymbol{\xi})}{\partial \xi^\alpha} \Big|_{\boldsymbol{\xi}_p}, \quad (3.22)$$

$$\mathbf{a}_p^\alpha := a_p^{\alpha\beta} \mathbf{a}_\beta^p, \quad [a_p^{\alpha\beta}] = [a_{\alpha\beta}^p]^{-1}, \quad a_{\alpha\beta}^p = \mathbf{a}_\alpha^p \cdot \mathbf{a}_\beta^p, \quad (3.23)$$

$$\mathbf{n}_p := \frac{\mathbf{a}_1^p \times \mathbf{a}_2^p}{\|\mathbf{a}_1^p \times \mathbf{a}_2^p\|}. \quad (3.24)$$

In the reference configuration $\partial_c \mathcal{B}_{0k}$ the tangent vectors $\mathbf{A}_\alpha^p, \mathbf{A}_p^\alpha$ and the surface metric tensor components $A_{\alpha\beta}^p$ can be defined similarly as in Eqs. (3.22)-(3.23). The coordinates $\boldsymbol{\xi}_p$ of the projection point \mathbf{x}_p can be determined by solving

$$(\mathbf{x}_p - \mathbf{x}_k) \cdot \mathbf{a}_\alpha^p = 0, \quad \alpha = 1, 2. \quad (3.25)$$

This equation is nonlinear in general and thus has to be solved using, e.g., Newton's method (Sauer and De Lorenzis, 2013). Once the coordinates of the projection point are determined, one can define the contact gap vector

$$\mathbf{g}_c := \mathbf{x}_k - \mathbf{x}_p, \quad (3.26)$$

which can be decomposed into a normal and tangential component

$$\mathbf{g}_c = \mathbf{g}_n + \mathbf{g}_t. \quad (3.27)$$

The signed normal gap g_n is defined by

$$g_n := \begin{cases} \|\mathbf{g}_n\|, & \mathbf{x}_k \notin \mathcal{B}_\ell, \\ -\|\mathbf{g}_n\|, & \mathbf{x}_k \in \mathcal{B}_\ell \end{cases}. \quad (3.28)$$

To capture tangential sticking and sliding, one has to define a tangential slip

$$\mathbf{g}_t = \mathbf{g}_e + \mathbf{g}_s. \quad (3.29)$$

The tangential slip \mathbf{g}_t can be decomposed into a reversible/elastic part \mathbf{g}_e that is associated with sticking, and an irreversible/inelastic part \mathbf{g}_s , associated with sliding. A schematic representation of the different components is given in Figure 3.2(b). Given the contact surfaces, the contact traction \mathbf{t}_c can be decomposed into a normal and tangential component, i.e.

$$\mathbf{t}_c = \mathbf{t}_n + \mathbf{t}_t. \quad (3.30)$$

In the case of no adhesion and no friction, these components are defined as

$$\mathbf{t}_n = p_c \mathbf{n}_p \quad p_c \geq 0, \quad (3.31)$$

$$\mathbf{t}_t = \mathbf{0}, \quad (3.32)$$

where p_c is the contact pressure.

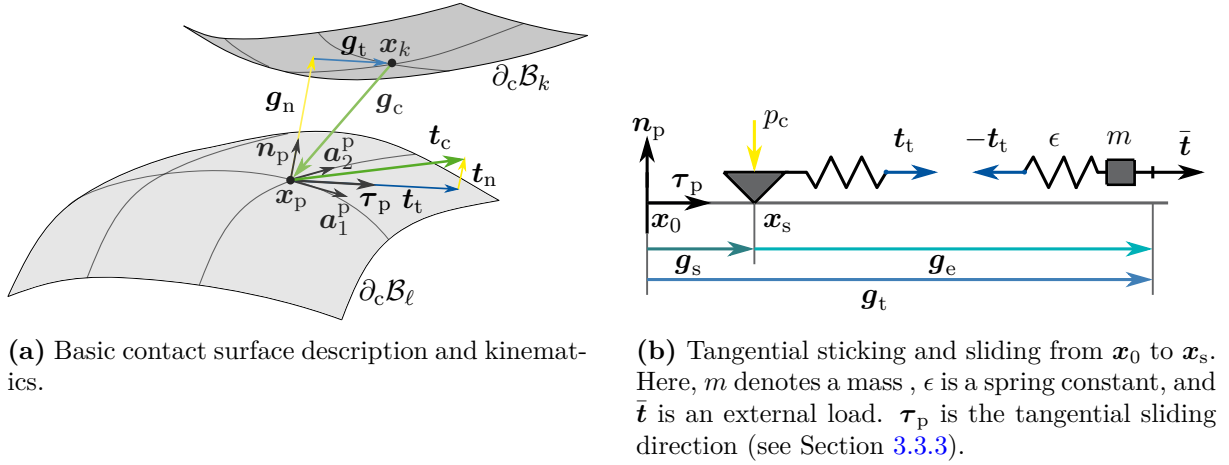


Figure 3.2 – Schematic illustrations of the basic surface description and contact kinematics. Adopted and modified from [Duong and Sauer \(2019\)](#).

3.3.2 Adhesion

Adhesion describes the clinging of two different surfaces to each other, such as velcro, glue, or the feet of a gecko that stick to a glass plane. It can be caused on the microscopic or macroscopic level by different mechanisms, such as chemical bonding and van der Waals forces, electrostatic and magnetic forces, but also mechanical effects, such as capillary interaction, mechanical interlocking, suction forces, and diffusion.

In this work adhesion at the BII occurs due to mechanical interlocking between the porous implant surface and the newly formed bone tissue and a chemical bond between the titanium alloy of the implant and the calcium of the bone. Both are forms of dry adhesion, as opposed to wet adhesion, which includes a lubricant. The macroscopic adhesion at the BII is still poorly understood and no agreed upon model exists. In this work for the adhesion in normal direction, a simple cohesive zone model (CZM) is chosen; even though cohesion usually describes the clinging of the molecules of one material to each other, which is governed by electrical attraction. Cohesive zone models are fracture mechanics models, where the separation of the contact surfaces takes place across an extended crack tip, or cohesive zone (CZ), and is resisted by cohesive tractions ([Dugdale, 1960](#); [Barenblatt, 1962](#)). A simple example is the exponential CZM

$$\mathbf{t}_{cz} = \frac{t_{cz}}{g_{cz}} e^{\left(1 - \frac{\|\mathbf{g}_n\|}{g_{cz}}\right)} \mathbf{g}_n \quad \text{for } \mathbf{g}_n \geq \mathbf{0} \quad (3.33)$$

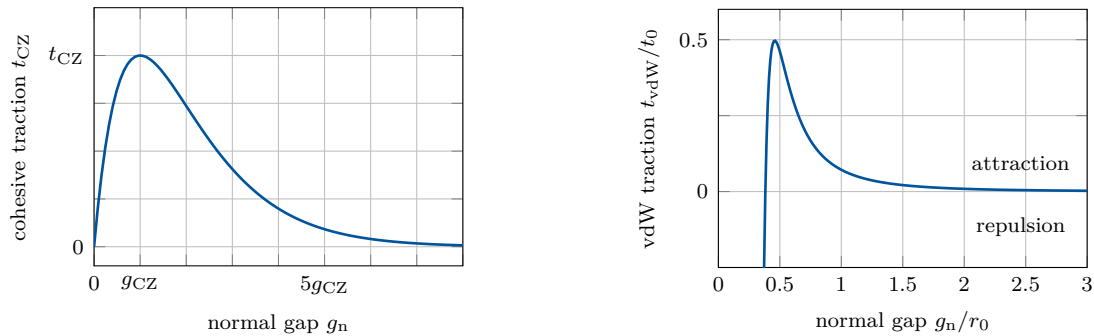
by [Xu and Needleman \(1993\)](#) depicted in [Figure 3.3\(a\)](#). t_{cz} denotes the largest amount of cohesive traction and g_{cz} is its location.

Another possibility is to model adhesion due to van der Waals (vdW) forces, which describe adhesion and repulsion between molecules. This model is mostly used for particle simulation but can also be applied to continuum mechanics, according to [Sauer \(2011\)](#), as

$$\mathbf{t}_{vdW} = t_{vdW} \mathbf{n}_p, \quad t_{vdW} = \frac{A_H}{2\pi r_0^3} \left[\frac{1}{45} \left(\frac{r_0}{g_n}\right)^9 - \frac{1}{3} \left(\frac{r_0}{g_n}\right)^3 \right]. \quad (3.34)$$

A_H denotes the *Hamaker constant*, whose magnitude reflects the strength of the van der Waals force between two particles, or between a particle and a substrate (Hamaker, 1937). Here, r_0 denotes the equilibrium spacing of the *Lennard-Jones potential* (Jones, 1924a,b).

Figure 3.3(b) shows the van der Waals traction t_{vdW} as a function of the normal gap g_n , where g_n is normalized by r_0 and t_{vdW} is normalized by the traction t_0 .



(a) Exponential cohesive zone model based on the normal gap g_n with maximum traction t_{CZ} occurring at $g_n = g_{CZ}$.

(b) Van der Waals adhesion model based on the normal gap g_n .

Figure 3.3 – Illustration of adhesive contact models.

3.3.3 Friction

In general, friction denotes the force resisting the relative motion of solid surfaces, fluid layers, and material elements. In this work, only dry friction is considered, which is the force that opposes the relative tangential motion of two solid surfaces in contact. Dry friction generally arises from the surface roughness and surface deformation, but also from adhesion and debris.

For frictional contact, the tangential traction t_t is determined by the behavior during sticking and sliding. The distinction between these two states is based on a slip criterion of the form

$$f_s \begin{cases} < 0, & \text{sticking,} \\ \geq 0, & \text{sliding.} \end{cases} \quad (3.35)$$

An example of the slip criterion f_s is

$$f_s = \|\mathbf{t}_t\| - t_t^{\text{slide}}. \quad (3.36)$$

During sticking, the traction t_t is defined by the constraint that no relative tangential motion occurs. During sliding, the traction

$$\mathbf{t}_t = t_t^{\text{slide}} \boldsymbol{\tau}_p \quad (3.37)$$

is characterized by a sliding law, where $\boldsymbol{\tau}_p$ is the tangential sliding direction. One of the simplest but most commonly used friction laws is Coulomb's law, shown in Figure 3.4, which is stated as

$$t_t^{\text{slide}} = \mu t_n, \quad (3.38)$$

where μ is a constant friction coefficient and $t_n = \|\mathbf{t}_n\|$. The tangential sliding direction $\boldsymbol{\tau}_p$ usually cannot be computed analytically and therefore, needs to be approximated. Two different approaches, one based on elastoplasticity theory (Wriggers, 2006; Laursen, 2013; Sauer and

De Lorenzis, 2015)) and one based on surface potentials (Sauer and De Lorenzis, 2013; Duong and Sauer, 2019) are explained in Section 4.3.

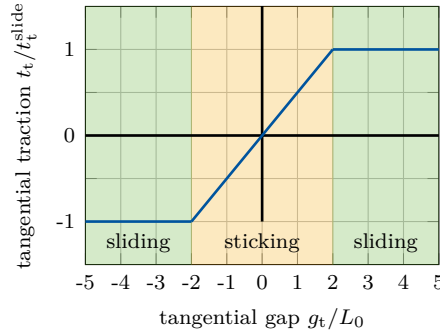


Figure 3.4 – Frictional, tangential traction for a single point for constant pressure, defined by Coulomb’s law (3.38), as a function of the tangential gap $g_t = \|\mathbf{g}_t\|$. Here, L_0 is a reference length.

3.4 Balance Laws

When considering deformable solids as continua, their deformation and interaction can be described by balance laws. These equations can be formulated with respect to the reference configuration (material form) or the current configuration (spatial form) and in global and local form. In this work, only the quasi-static case is considered, in which case the balance laws become conservation equations. Furthermore, the balance of mechanical energy requires that the internal energy of the bodies remains constant. This condition is automatically satisfied by the material models introduced in Section 3.2 and thus, is not discussed further.

The derivations of the balance laws are based on the following mathematical theorems: The divergence theorem is stated as

$$\int_{\partial\mathcal{B}_k} \bullet \cdot \mathbf{n}_k \, da_k = \int_{\mathcal{B}_k} \text{div}(\bullet) \, dv_k, \quad (3.39)$$

where \mathbf{n}_k is the outward normal vector of boundary $\partial\mathcal{B}_k$. The other theorem is the localization theorem

$$\int_{\mathcal{P}_k} \bullet \, dv = 0 \quad \mathcal{P}_k \subset \mathcal{B}_k \quad \Leftrightarrow \quad \bullet = 0 \quad \forall \mathbf{x}_k \in \mathcal{B}_k, \quad (3.40)$$

which can equally be applied to surface integrals.

3.4.1 Balance of Mass

Assuming that a body cannot lose or gain mass, the mass density can only change due to change of volume J_k in Eq. (3.4). The global conservation of mass is defined by

$$\int_{\mathcal{B}_k} \rho_k \, dv_k = 0, \quad \forall \mathbf{x}_k \in \mathcal{B}_k \quad (3.41)$$

where ρ_k is the density. The local form of the conservation of mass is given by

$$\rho_{0k} = J_k \rho_k \quad \forall \mathbf{x}_k \in \mathcal{B}_k, \quad (3.42)$$

where ρ_{0k} is the density in the reference configuration.

3.4.2 Balance of Linear Momentum

Linear momentum is changed by the action of external forces. Excluding forces due to inertia, the global linear momentum balance states that

$$\sum_{k=1}^2 \left[\int_{\mathcal{B}_k} \rho_k \bar{\mathbf{b}}_k \, dv + \int_{\partial_{\bar{\mathbf{t}}}\mathcal{B}_k} \bar{\mathbf{t}}_k \, da \right] = 0, \quad (3.43)$$

where $\bar{\mathbf{b}}_k$ denotes the external body forces and $\bar{\mathbf{t}}_k$ are the surface forces with the *Neumann* boundary $\partial_{\bar{\mathbf{t}}}\mathcal{B}_k \subseteq \partial\mathcal{B}_k$. Taking into account local mass conservation (3.42) and Cauchy's theorem (3.10) and applying the divergence theorem (3.39), one can obtain the local form of the linear momentum balance as

$$\operatorname{div}\boldsymbol{\sigma}_k + \rho_k \bar{\mathbf{b}}_k = 0 \quad \forall \mathbf{x}_k \in \mathcal{B}_k. \quad (3.44)$$

3.4.3 Balance of Angular Momentum

The balance of angular momentum requires that the Cauchy stress tensor (3.10) is symmetric (Belytschko et al., 2000):

$$\boldsymbol{\sigma}_k = \boldsymbol{\sigma}_k^T \quad \forall \mathbf{x}_k \in \mathcal{B}_k. \quad (3.45)$$

Hence, the second Piola-Kirchhoff stress tensor (3.11) must also be symmetric.

3.4.4 Strong Form of the Mechanical Contact Boundary Value Problem

Due to the addition of contact in the system, the balance equations have to be amended. In this work, no mass and heat sources are assumed, hence the mass balance (3.42) remains unchanged for contact contributions. When considering contact between two deformable bodies \mathcal{B}_1 and \mathcal{B}_2 , their boundaries are decomposed into

$$\partial\mathcal{B}_k = \partial_{\varphi}\mathcal{B}_k \cup \partial_{\bar{\mathbf{t}}}\mathcal{B}_k \cup \partial_c\mathcal{B}_k, \quad k = 1, 2, \quad (3.46)$$

and are assumed to be pairwise disjoint (see Figure 3.5). ∂_{φ} denotes the Dirichlet boundary, $\partial_{\bar{\mathbf{t}}}\mathcal{B}_k$ denotes the Neumann boundary, and $\partial_c\mathcal{B}_k$ is the contact boundary. When including contact phenomena, the definition of the Cauchy stress tensor (3.10) is extended to

$$\boldsymbol{\sigma}_k \mathbf{n}_k = \bar{\mathbf{t}}_k + \mathbf{t}_{ck}, \quad (3.47)$$

leading to an additional boundary condition

$$\boldsymbol{\sigma}_k \mathbf{n}_k = \mathbf{t}_{ck} \quad \text{on } \partial_c\mathcal{B}_k, \quad (3.48)$$

with $\mathbf{t}_{ck} = \mathbf{t}_{nk} - \mathbf{t}_{tk}$. The mechanical contact boundary value problem (BVP) can then be formulated as follows: for each of the two bodies \mathcal{B}_k ($k = 1, 2$), find the current positions $\mathbf{x}_k(\mathbf{X}_k)$, $\forall \mathbf{x}_k \in \mathcal{B}_k$, s.t.

$$\begin{aligned} \operatorname{div}\boldsymbol{\sigma}_k + \rho_k \bar{\mathbf{b}}_k &= \mathbf{0} && \text{in } \mathcal{B}_k, \\ \boldsymbol{\sigma}_k \mathbf{n}_k &= \bar{\mathbf{t}}_k && \text{on } \partial_{\bar{\mathbf{t}}}\mathcal{B}_k, \\ \boldsymbol{\sigma}_k \mathbf{n}_k &= \mathbf{t}_{ck} && \text{on } \partial_c\mathcal{B}_k, \\ \mathbf{x}_k &= \bar{\boldsymbol{\varphi}}_k && \text{on } \partial_{\varphi}\mathcal{B}_k, \\ \mathbf{x}_k(t=0) &= \mathbf{X}_k. \end{aligned} \quad (3.49)$$

Equations (3.49) are also called the *strong form* of the partial differential equation (PDE) system, because all their components and their derivatives have to be continuously differentiable functions. However, many physical problems have no strong solution. Hence, discrete methods have to be used to derive a solvable PDE. In this work the finite element method (FEM) is used, which requires a *variational* or *weak* formulation of the BVP (3.49).

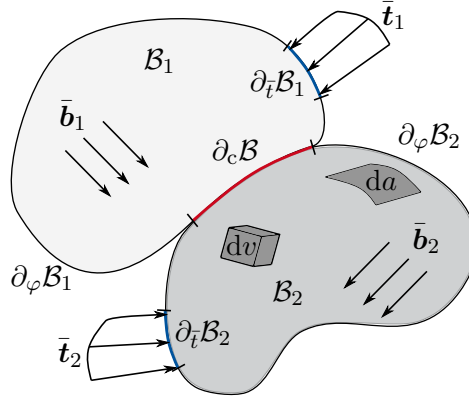


Figure 3.5 – Mechanical contact boundary value problem: Contact of two deformable bodies \mathcal{B}_1 , \mathcal{B}_2 , with Dirichlet boundaries $\partial_\varphi\mathcal{B}_1$, $\partial_\varphi\mathcal{B}_2$, Neumann boundaries $\partial_t\mathcal{B}_1$, $\partial_t\mathcal{B}_2$, contact boundary $\partial_c\mathcal{B}$, body forces $\bar{\mathbf{b}}_1$, $\bar{\mathbf{b}}_2$, and external tractions $\bar{\mathbf{t}}_1$, $\bar{\mathbf{t}}_2$.

3.4.5 Weak Form of the Mechanical Contact Boundary Value Problem

Instead of solving the BVP (3.49) analytically, one can use an approximate method, such as FEM. There, e.g., the deformation \mathbf{u}_k is approximated by \mathbf{u}_k^h , which is then inserted into the BVP (3.49)

$$\operatorname{div}\boldsymbol{\sigma}_k(\mathbf{u}_k^h) + \rho_k\bar{\mathbf{b}}_k = r^{\text{res}}. \quad (3.50)$$

The residual r^{res} represents the error between the exact solution and the approximated solution. This error can be reduced to zero in a weak sense, by multiplying the residual with a variation $\delta\boldsymbol{\varphi}_k$ (also called *test function* or *virtual displacement*) and integrating over the whole domain:

$$\sum_{k=1}^2 \left[\int_{\mathcal{B}_k} (\operatorname{div}\boldsymbol{\sigma}_k + \rho_k\bar{\mathbf{b}}_k) \cdot \delta\boldsymbol{\varphi}_k \, dv \right] = 0 \quad \forall \delta\boldsymbol{\varphi}_k \in \mathcal{V}, \quad (3.51)$$

where \mathcal{V} is a suitable function space for $\delta\boldsymbol{\varphi}_k$. After reformulation, application of the divergence theorem, and decomposition of the boundary $\partial\mathcal{B}_k$ into a Neumann part $\partial_t\mathcal{B}_k$ and a contact part $\partial_c\mathcal{B}_k$, the first term of Eq. (3.51) can be expressed as

$$\int_{\mathcal{B}_k} \operatorname{div}\boldsymbol{\sigma}_k \cdot \delta\boldsymbol{\varphi}_k \, dv_k = \int_{\partial_t\mathcal{B}_k} \bar{\mathbf{t}}_k \cdot \delta\boldsymbol{\varphi}_k \, da_k + \int_{\partial_c\mathcal{B}_k} \mathbf{t}_{ck} \cdot \delta\boldsymbol{\varphi}_k \, da_k - \int_{\mathcal{B}_k} \operatorname{grad}(\delta\boldsymbol{\varphi}_k) : \boldsymbol{\sigma}_k \, dv_k. \quad (3.52)$$

Finally, the weak form of the local linear momentum balance can be written as

$$\begin{aligned} \sum_{k=1}^2 \left[\underbrace{\int_{\mathcal{B}_k} \operatorname{grad}(\delta\boldsymbol{\varphi}_k) : \boldsymbol{\sigma}_k \, dv_k}_{\text{virtual internal work}} - \underbrace{\int_{\partial_c\mathcal{B}_k} \mathbf{t}_{ck} \cdot \delta\boldsymbol{\varphi}_k \, da_k}_{\text{virtual contact work}} \right. \\ \left. + \underbrace{\int_{\partial_t\mathcal{B}_k} \bar{\mathbf{t}}_k \cdot \delta\boldsymbol{\varphi}_k \, da_k + \int_{\mathcal{B}_k} \rho_k\bar{\mathbf{b}}_k \cdot \delta\boldsymbol{\varphi}_k \, dv_k}_{\text{virtual external work}} \right] = 0 \quad \forall \delta\boldsymbol{\varphi}_k \in \mathcal{V}. \end{aligned} \quad (3.53)$$

Equation (3.53) can also be expressed as the variation of the potential energy $\delta\Pi_k$ (*principle of virtual work*), as

$$\delta\Pi_k = \delta\Pi_{\text{int},k} + \delta\Pi_{c_k} - \delta\Pi_{\text{ext},k} = 0 \quad \forall \delta\boldsymbol{\varphi}_k \in \mathcal{V}, \quad (3.54)$$

with

$$\delta\Pi_{\text{int},k} = \int_{\mathcal{B}_k} \text{grad}(\delta\boldsymbol{\varphi}_k) : \boldsymbol{\sigma}_k \, dv_k, \quad (3.55)$$

$$\delta\Pi_{\text{ext},k} = \int_{\partial_{\bar{\mathbf{t}}}\mathcal{B}_k} \bar{\mathbf{t}}_k \cdot \delta\boldsymbol{\varphi}_k \, da_k + \int_{\mathcal{B}_k} \rho_k \bar{\mathbf{b}}_k \cdot \delta\boldsymbol{\varphi}_k \, dv_k, \quad (3.56)$$

$$\delta\Pi_{c_k} = - \int_{\partial_c \mathcal{B}_k} \mathbf{t}_{c_k} \cdot \delta\boldsymbol{\varphi}_k \, da_k. \quad (3.57)$$

In order to solve the generally nonlinear system of equations (3.54) numerically with the Newton-Raphson methods it must be linearized first.

3.5 Linearization

In continuum mechanics, nonlinearity can arise from the geometry due the use of nonlinear strain measures, such as the Green-Langrange strain tensor (3.8), from nonlinear constitutive behavior, such as hyperelastic materials (3.19), or from unilateral geometrical constraints, which are common in contact problems.

The linearization of a differentiable function $\mathbf{f}(\mathbf{x})$ is given by the function evaluation at a specific point $\bar{\mathbf{x}}$ and the directional derivative $\Delta\mathbf{f}(\bar{\mathbf{x}}, \Delta\mathbf{x})$, i.e.,

$$\mathbb{L}[\mathbf{f}, \Delta\mathbf{x}]_{\bar{\mathbf{x}}} = \mathbf{f}(\bar{\mathbf{x}}) + \Delta\mathbf{f}(\bar{\mathbf{x}}, \Delta\mathbf{x}). \quad (3.58)$$

The directional derivative $\Delta\mathbf{f}(\bar{\mathbf{x}}, \Delta\mathbf{x})$ at $\bar{\mathbf{x}}$ in the direction $\Delta\mathbf{x}$ is defined by

$$\begin{aligned} \Delta\mathbf{f}(\bar{\mathbf{x}}, \Delta\mathbf{x}) &= \Delta\mathbf{f}(\bar{\mathbf{x}})[\Delta\mathbf{x}] \\ &:= \lim_{\omega \rightarrow 0} \frac{\mathbf{f}(\bar{\mathbf{x}} + \omega\Delta\mathbf{x}) - \mathbf{f}(\bar{\mathbf{x}})}{\omega} \\ &= \left[\frac{d}{d\omega} \mathbf{f}(\bar{\mathbf{x}} + \omega\Delta\mathbf{x}) \right]_{\omega=0}. \end{aligned} \quad (3.59)$$

For the weak form of the mechanical problem (3.54) the corresponding linearization is given by

$$\Delta\delta\Pi_k^e = \frac{\partial\delta\Pi_k^e}{\partial\mathbf{x}_k} \Delta\mathbf{x}_k, \quad \Delta\delta\Pi_{\bullet,k}^e = \Delta_x \delta\Pi_{\bullet,k}^e, \quad \bullet = \text{int}, \text{ext}, \text{c}, \quad (3.60)$$

which allows the linearization to be done contribution-wise. The linearizations of Eqs. (3.55)–(3.57) depend on the applied constitutive and contact models and are presented in Appendix A.

Chapter 4

Finite Element Discretization and Algorithmic Contact Treatment

Now that the mechanical foundations of the contact of two deformable bodies have been introduced, the numerical formulation and implementation of contact problems can be formulated. In this chapter, the basic concepts of FEM and its application to contact problems are outlined. In this work, FEM is used to compute numerical solutions of partial differential equations, such as Eqs. (3.53). As this work only considers quasi-static simulations, Eqs. (3.53) only have to be discretized in space. In the following, upright symbols denote vectors and matrices that are associated with FE nodes.

4.1 Spatial Discretization

For FEM it is necessary to discretize the geometry of the bodies \mathcal{B}_k , $k = 1, 2$ in space. Hence, both interacting bodies \mathcal{B}_k and their surfaces $\partial\mathcal{B}_k$ are decomposed into $n_{\text{el},k}$ smaller subdomains, or *elements*. Depending on the type and amount of elements, this results in an approximation of the original geometry, i.e.,

$$\mathcal{B}_{0k} \approx \mathcal{B}_{0k}^h = \bigcup_{e=1}^{n_{\text{el},k}} \Omega_{0k}^e, \quad \partial\mathcal{B}_{0k}^h \approx \bigcup_{e=1}^{n_{\text{el},k}} \Gamma_{0k}^e, \quad (4.1)$$

$$\mathcal{B}_k \approx \mathcal{B}_k^h = \bigcup_{e=1}^{n_{\text{el},k}} \Omega_k^e, \quad \Omega_k^e \approx \varphi_k(\Omega_{0k}^e), \quad \partial\mathcal{B}_k^h \approx \bigcup_{e=1}^{n_{\text{el},k}} \Gamma_k^e, \quad \Gamma_k^e \approx \varphi_k(\Gamma_{0k}^e), \quad (4.2)$$

in material and spatial configuration, respectively. The superscript h indicates the spatial approximation of the continuous variable. The surface elements correspond to the bulk elements and together, are referred to as *finite elements*. Often, the surface elements are chosen as the faces of the bulk elements which lie on the surface. An example of a spatial discretization in 2D is shown in Figure 4.1. For each finite element in the reference configuration, a point \mathbf{X}_k (or \mathbf{x}_k) is approximated by $n_{\text{ne},k}$ *nodes*, which are weighted by $n_{\text{ne},k}$ shape functions. By storing the positions of these nodes in the vectors

$$\mathbf{X}_k^e = \begin{bmatrix} \mathbf{X}_1^e \\ \vdots \\ \mathbf{X}_{n_{\text{ne},k}}^e \end{bmatrix}, \quad \mathbf{x}_k^e = \begin{bmatrix} \mathbf{x}_1^e \\ \vdots \\ \mathbf{x}_{n_{\text{ne},k}}^e \end{bmatrix}, \quad (4.3)$$

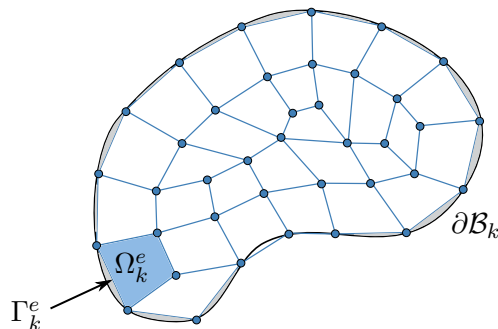


Figure 4.1 – Example of a spatial discretization of a 2D body \mathcal{B}_k with quadrilateral, linear finite elements Ω_k^e, Γ_k^e . Blue dots represent the element nodes.

and introducing the array of shape function $\mathbf{N}_k = [N_1 \mathbf{I}, \dots, N_{n_{ne,k}} \mathbf{I}]$ we can deduce a shorter notation, namely

$$\mathbf{X}_k \approx \mathbf{X}_k^h = \mathbf{N}_k \mathbf{X}_k^e \quad \text{for } \mathbf{X}_k \in \Omega_{0k}^e, \quad (4.4)$$

$$\mathbf{x}_k \approx \mathbf{x}_k^h = \mathbf{N}_k \mathbf{x}_k^e \quad \text{for } \mathbf{x}_k \in \Omega_k^e. \quad (4.5)$$

The most commonly used method in spatial discretization is the isoparametric concept; it has been proven to be very practical for nonlinear problems (Zienkiewicz and Taylor, 2005; Wriggers, 2008). It uses the same shape functions for the geometry and the field variables. The displacement \mathbf{u}_k , for instance, can be discretized as

$$\mathbf{u}_k \approx \mathbf{u}_k^h = \mathbf{N}_k \mathbf{u}_k^e \quad \text{in } \Omega_k^e. \quad (4.6)$$

Using the same set of shape functions, one can approximate the test functions $\delta\varphi_k$ for the weak form (3.53), by

$$\delta\varphi_k \approx \delta\varphi_k^h = \mathbf{N}_k \mathbf{v}_k^e \quad \text{in } \Omega_k^e. \quad (4.7)$$

The shape functions \mathbf{N}_k depend on the interpolation functions used. In the following, the Lagrangian interpolation basis functions and the Lagrangian surface enrichment are introduced, as well as the non-uniform rational basis splines (NURBS) enriched discretization, that is used for the contact surfaces in Chapters 6-8.

4.1.1 Lagrangian Elements and Lagrangian Enrichment

The standard FEM uses Lagrangian polynomials as shape functions. In the one-dimensional case, a general Lagrange element of order $n - 1$ can be written as (Wriggers, 2008)

$$\mathbf{N}_k(\xi) = \prod_{j=1, j \neq k}^n \frac{\xi_j - \xi}{\xi_j - \xi_k}, \quad (4.8)$$

For higher-dimensional cases, the shape functions can be constructed by tensor products of the one-dimensional shape functions, namely

$$\mathbf{N}_k(\xi, \eta) = \mathbf{N}_j(\xi) \mathbf{N}_m(\eta), \quad (4.9)$$

$$\mathbf{N}_k(\xi, \eta, \zeta) = \mathbf{N}_j(\xi) \otimes \mathbf{N}_m(\eta) \otimes \mathbf{N}_o(\zeta), \quad j, m, o = 1, \dots, n, \quad (4.10)$$

in the 2D quadrilateral and 3D hexahedral case, respectively, yielding

$$N_I^{2D} = \frac{1}{4}(1 \pm \xi)(1 \pm \eta), \quad N_I^{3D} = \frac{1}{8}(1 \pm \xi)(1 \pm \eta)(1 \pm \zeta), \quad (4.11)$$

with the parametric coordinates ξ, η, ζ .

In order to increase the accuracy of the geometrical approximation, one can increase the density and decrease the size of the FE at the contact surfaces; or one can use FE with higher-order shape functions. However, this increases the computational cost and not all solvers are suitable to solve meshes with higher-order elements. Furthermore, higher-order Lagrangian interpolation is prone to oscillate.

Another, usually less costly strategy, is to enrich both the contact surface and the solution variables by shape functions of higher order, e.g., second-order Lagrangian elements (Zienkiewicz and Taylor, 2005) (see Figure 4.2). As an example, the shape functions for a 2D quadrilateral element with quadratic Lagrangian enrichment (Sauer, 2011) are

$$\begin{aligned} N_1(\xi, \eta) &= \frac{1}{4}(\xi^2 - \xi)(1 - \eta), & N_4(\xi, \eta) &= \frac{1}{4}(1 - \xi)(1 + \eta), \\ N_2(\xi, \eta) &= \frac{1}{4}(\xi^2 + \xi)(1 - \eta), & N_5(\xi, \eta) &= \frac{1}{2}(1 - \xi^2)(1 - \eta), \\ N_3(\xi, \eta) &= \frac{1}{4}(1 + \xi)(1 + \eta), \end{aligned} \quad (4.12)$$

and for a 3D hexahedral element

$$\begin{aligned} N_1 &= \frac{1}{4}(\xi^2 - \xi)(\eta^2 - \eta)(1 - \zeta), & N_8 &= \frac{1}{8}(1 - \xi)(1 + \eta)(1 + \zeta), \\ N_2 &= \frac{1}{4}(\xi^2 + \xi)(\eta^2 - \eta)(1 - \zeta), & N_9 &= \frac{1}{4}(1 - \xi^2)(\eta^2 - \eta)(1 - \zeta), \\ N_3 &= \frac{1}{4}(\xi^2 + \xi)(\eta^2 + \eta)(1 - \zeta), & N_{10} &= \frac{1}{4}(\xi^2 + \xi)(1 - \eta^2)(1 - \zeta), \\ N_4 &= \frac{1}{4}(\xi^2 - \xi)(\eta^2 + \eta)(1 - \zeta), & N_{11} &= \frac{1}{4}(1 - \xi^2)(\eta^2 + \eta)(1 - \zeta), \\ N_5 &= \frac{1}{8}(1 - \xi)(1 - \eta)(1 + \zeta), & N_{12} &= \frac{1}{4}(\xi^2 - \xi)(1 - \eta^2)(1 - \zeta), \\ N_6 &= \frac{1}{8}(1 + \xi)(1 - \eta)(1 + \zeta), & N_{13} &= \frac{1}{4}(1 - \xi^2)(1 - \eta^2)(1 - \zeta), \\ N_7 &= \frac{1}{8}(1 + \xi)(1 + \eta)(1 + \zeta). \end{aligned} \quad (4.13)$$

While enriched elements of this type are at least C^1 -continuous¹ almost everywhere on the contact surface, they are still only C^0 -continuous at their element boundaries. These discontinuities can cause problems during the contact projection (see Section 4.3), especially for non-planar contact surfaces. As it remains crucial to ensure C^1 -continuity for the entire contact surface, especially for curved and complex geometries such as implants, a enrichment approach based on isogeometric analysis (IGA) is used in parts of this work.

4.1.2 Isogeometric Analysis

IGA was proposed by Hughes et al. (2005) to bridge the gap between computer aided design (CAD), which is generally used to create virtual geometries, and FEA, that requires a FE mesh.

1. C denotes the smoothness of a function in terms of the number of continuous derivatives it has in a specific domain. Hence, C^0 -continuity refers to a function that is continuous, but its derivatives are not. A function with C^1 -continuity is at least once continuously differentiable.

In CAD, computed manufacturing (CAM) and engineering (CAE), basis splines (B-splines) and non-uniform rational B-splines (NURBS) are used to represent the often curved and complex geometries. However, traditional FEA requires the generation of a suitable FE mesh from the geometry, where the geometry is usually discretized by Lagrangian FE. In addition to the loss of accuracy in geometry representation and the limited smoothness at the element boundaries, the creation of a FE mesh from a CAD geometry consumes the majority of the total time of a FEA project (Cottrell et al., 2009). To ensure an accurate geometry representation and increase efficiency, IGA aims at using the same geometric representation for design and analysis.

One of the basic ingredients are B-splines. B-splines are piece-wise polynomial functions defined by their polynomial order p and a *knot vector* Ξ . A knot vector is a set of non-decreasing parametric coordinates

$$\Xi = [\xi_1, \xi_2, \dots, \xi_{n+p+1}]. \quad (4.14)$$

Here, n is the number of basis functions defined by the knot vector. The interval between two adjacent knot values $[\xi_i, \xi_{i+1}] \geq 0$ is called *knot span*. Each of these knot spans partitions the parameter space into elements which are mapped to the physical domain. The basis function only depends on the relative size of the knot spans, which can be used to classify B-splines. In a *uniform* B-spline the knots in the knot vector are equally spaced, whereas in a *non-uniform* B-spline, the size of the knot spans can differ.

Using the definition in Eq. (4.14), a B-spline basis function can be defined recursively with the Cox-de Boor recursion formula (Cox, 1972; De Boor, 1972), where piece-wise constant basis functions are obtained on each knot span, as

$$N_{i,0}(\xi) = \begin{cases} 1 & \text{if } \xi_i \leq \xi < \xi_{i+1}, \\ 0 & \text{otherwise,} \end{cases} \quad \text{for } p = 0, \quad (4.15)$$

$$N_{i,p}(\xi) = \frac{\xi - \xi_i}{\xi_{i+p} - \xi} N_{i,p-1}(\xi) + \frac{\xi_{i+p+1} - \xi}{\xi_{i+p+1} - \xi_{i+1}} N_{i+1,p-1}(\xi), \quad \text{for } p > 0. \quad (4.16)$$

A B-spline curve is then obtained by multiplying the basis functions $N_{i,p}$ with the *control points* $\mathbf{P}_i, i = 1, 2, \dots, n$, i.e.

$$C(\xi) = \sum_{i=1}^n N_{i,p}(\xi) \mathbf{P}_i = \mathbf{N}_p(\xi) \mathbf{P}. \quad (4.17)$$

The control points \mathbf{P}_i span the so-called *control polygon*, which is the piece-wise linear interpolation of the control points.

To define a B-spline surface, knot vectors in two parametric directions are required, resulting in shape functions $N_{i,p}$ and $M_{j,q}, j = 1, 2, \dots, m$, and a grid of control points \mathbf{P}_{ij} . The B-spline surface can then be expressed by

$$S(\xi, \eta) = \sum_{i=1}^n \sum_{j=1}^m N_{i,p}(\xi) M_{j,q}(\eta) \mathbf{P}_{ij}. \quad (4.18)$$

NURBS are an extension of B-splines. In contrast to B-splines, NURBS can represent conic sections, such as circles and ellipses exactly, as their basis functions are rational. NURBS geometries in \mathbb{R}^d can be imagined as B-spline geometries in \mathbb{R}^{d+1} projected onto \mathbb{R}^d . The additional coordinate of each NURBS control point \mathbf{P}_i^w is the NURBS weight w_i . The NURBS

control points are obtained by dividing the components $1, \dots, d$ of the control points \mathbf{P}_i^w by their corresponding weight w_i , i.e.

$$\begin{aligned} (\mathbf{P}_i)_j &= \frac{(\mathbf{P}_i^w)_j}{w_i}, \quad \text{for } j = 1, \dots, d, \\ w_i &= (\mathbf{P}_i^w)_{d+1}. \end{aligned} \quad (4.19)$$

A detailed introduction into NURBS and isogeometric analysis can be found in [Cottrell et al. \(2009\)](#).

4.1.3 NURBS-enriched Contact Elements

When using surface-enriched FE, the bulk of the bodies \mathcal{B}_k and their surfaces other than the contact surfaces are discretized with standard (linear) Lagrangian elements. The contact surfaces $\partial_c \mathcal{B}_k$ can be enriched, e.g., by a higher-order Lagrangian discretization, by a polynomial interpolation (e.g., Hermite polynomials H^e ([Sauer, 2011](#))), or a spline. In parts of this work NURBS-enriched contact FE are used ([Corbett and Sauer, 2014, 2015](#)).

A 2D NURBS-enriched element has three linear faces in 2D and one NURBS curve. Such an element is defined by $p + 3$ nodes, with $p + 1$ control points on the NURBS curve and 2 in the bulk part (see [Figure 4.2](#)). The basis functions of such a (quadrilateral) element are given by

$$\begin{aligned} N_1(\xi, \eta) &= R_1^e(\xi) \frac{1}{2}(1 - \eta), & N_{p+2}(\xi, \eta) &= \frac{1}{4}(\xi + 1)(1 + \eta), \\ &\vdots & & \\ N_{p+1}(\xi, \eta) &= R_{p+1}^e(\xi) \frac{1}{2}(1 - \eta), & N_{p+3}(\xi, \eta) &= \frac{1}{4}(\xi - 1)(1 + \eta), \end{aligned} \quad (4.20)$$

with the rational basis functions R^e given by

$$R^e(\xi) = \frac{\mathbf{W}^e \mathbf{C}^e \mathbf{B}^e(\xi)}{W^e(\xi)}, \quad (4.21)$$

with the weighting functions $W^e(\xi)$, the weights \mathbf{W}^e , localized Bézier extraction operator \mathbf{C}^e ([Borden et al., 2011](#)), and the Bernstein polynomials $\mathbf{B}^e(\xi)$. This results in a continuous normal vector used in finding the closest point projection \mathbf{x}_p on the contact surface (for straight or curved surfaces; not for sharp edges and kinks). For a three dimensional body, the surface is enriched by a NURBS surface of order p and q . One element then consists of $(p + 1)(q + 1) + 4$ nodes, $n_{cp} = (p + 1)(q + 1)$ control points on the contact surface and four in the bulk domain. The basis functions and approximations follow in an analogous manner:

$$\begin{aligned} N_1(\xi, \eta) &= R_1^e(\xi, \eta) \frac{1}{2}(1 - \zeta), & N_{n_{cp}+1} &= \frac{1}{8}(1 - \xi)(1 - \eta)(1 + \zeta), \\ &\vdots & & \\ N_{n_{cp}}(\xi, \eta) &= R_{n_{cp}}^e(\xi, \eta) \frac{1}{2}(1 - \zeta), & N_{n_{cp}+2} &= \frac{1}{8}(1 + \xi)(1 - \eta)(1 + \zeta), \\ & & & \\ & & N_{n_{cp}+3} &= \frac{1}{8}(1 + \xi)(1 + \eta)(1 + \zeta). \\ & & N_{n_{cp}+4} &= \frac{1}{8}(1 - \xi)(1 + \eta)(1 + \zeta). \end{aligned} \quad (4.22)$$

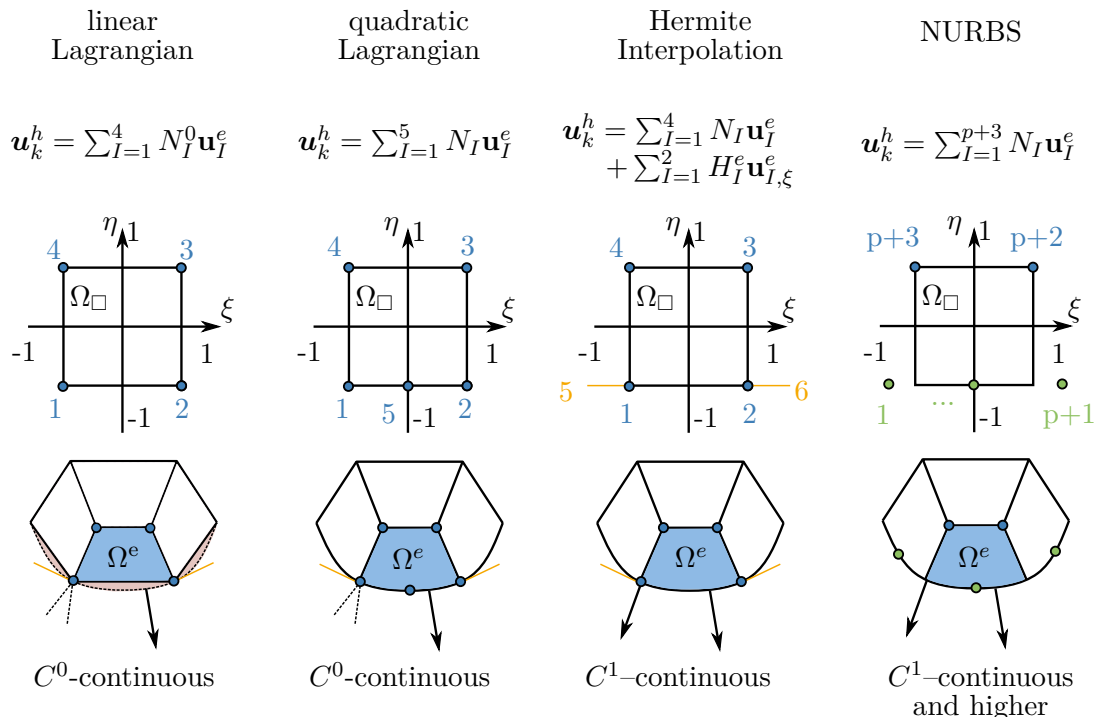


Figure 4.2 – Example of linear Lagrangian bulk discretization with different surface-enriched contact elements in 2D (Sauer, 2011; Sauer and De Lorenzis, 2013; Corbett and Sauer, 2014, 2015) with corresponding parent element Ω_\square (see Section 4.1.5).

NURBS-enriched contact elements are accurate, robust and efficient, especially for problems dominated by surface effects, such as frictional and adhesive contact. The isogeometric surface elements provide accuracy, smoothness, and at least C^1 -continuity over the element boundaries, while the Lagrangian finite elements in the bulk are simple and efficient. A more detailed explanation and derivation is provided in Corbett and Sauer (2014, 2015). The Lagrangian bulk discretization and several surface-enrichment approaches are pictured in Figure 4.2.

Apart from the shape functions exist two general types of meshes: structured and unstructured meshes. In structured meshes, the finite elements within a body are aligned in a regular, predictable pattern, while in unstructured grids they are distributed in an irregular pattern. In this work, mainly structured hexahedral grids are used. While irregular meshes are, in general, more suitable to discretize complex and curved shapes, the usage of NURBS-enriched structured hexahedral grids at the contact boundary outperforms the quality of spatial discretization by unstructured grids. Furthermore, structured grids use a predictable numbering of the nodes and elements. On the one hand, the storage of element connectivity becomes unnecessary in general, and on the other hand, it facilitates the debugging of grids that have to be created by hand.

4.1.4 Discretized Weak Form

Now, the weak form (3.55)–(3.57) can be discretized in space. First, the variations of the potential energy $\delta\Pi_k$ are expressed in terms of the contribution of a single FE by using the

approximation (4.7):

$$\delta\Pi_{\text{int},k} = (\mathbf{v}_k^e)^\top \mathbf{f}_{\text{int},k}^e, \quad \mathbf{f}_{\text{int},k}^e = \int_{\Omega_k^e} \mathbf{B}_k^\top \boldsymbol{\sigma}_k \, dv_k, \quad (4.23)$$

$$\delta\Pi_{\text{ext},k} = (\mathbf{v}_k^e)^\top \mathbf{f}_{\text{ext},k}^e, \quad \mathbf{f}_{\text{ext},k}^e = \int_{\Gamma_k^e} \mathbf{N}_k^\top \bar{\mathbf{t}}_k \, da_k + \int_{\Omega_k^e} \rho_k \mathbf{N}_k^\top \bar{\mathbf{b}}_k \, dv_k, \quad (4.24)$$

$$\delta\Pi_{\text{ck}} = (\mathbf{v}_k^e)^\top \mathbf{f}_{\text{ck}}^e, \quad \mathbf{f}_{\text{ck}}^e = - \int_{\Gamma_{\text{ck}}^e} \mathbf{N}_k^\top \mathbf{t}_{\text{ck}} \, da_k. \quad (4.25)$$

The spatially discrete weak form of the system is then obtained by assembling all elemental contributions

$$(\mathbf{v})^\top [\mathbf{f}_{\text{int}} + \mathbf{f}_{\text{c}} - \mathbf{f}_{\text{ext}}] = \mathbf{0}, \quad (4.26)$$

where $\mathbf{f}_{\text{int}}, \mathbf{f}_{\text{ext}}, \mathbf{f}_{\text{c}}$ denote global force vectors. This implies, that at those nodes for which \mathbf{v} is arbitrary, the force equilibrium condition

$$\mathbf{f}(\mathbf{u}) = \mathbf{f}_{\text{int}}(\mathbf{u}) + \mathbf{f}_{\text{c}}(\mathbf{u}) - \mathbf{f}_{\text{ext}}(\mathbf{u}) = \mathbf{0} \quad (4.27)$$

must be satisfied. This equation system can now be solved by numerical integration.

4.1.5 Element Mapping

The elemental force vectors \mathbf{f}^e contain integrals over the corresponding bulk or surface elements Ω_k^e and Γ_k^e . Most of these integrals cannot be solved analytically and thus have to be computed numerically by, e.g., a quadrature rule. In order to efficiently evaluate both, the integrals and the shape function array \mathbf{N}_k , in either the reference or current configuration, it is useful to consider a so-called *parent element* Ω_\square . For quadrilateral and hexahedral elements, which are mainly used in this work, Ω_\square corresponds to a square (or cube) with edge length 2 and is described in terms of a local coordinate $\boldsymbol{\xi}^* \in [-1, 1]^d$ on the parent element, where d is the space dimension. Then, one can define the shape functions in \mathbf{N}_k with respect to this coordinate, as

$$N_I = N_I(\boldsymbol{\xi}^*), \quad I = 1, \dots, n_{\text{ne},k}. \quad (4.28)$$

With respect to the local derivatives of the shape functions $\partial N_I / \partial \boldsymbol{\xi}^*$, one can define a *mapping* from the parent element to the actual reference or current element as

$$\mathbf{j}_k^e = \frac{\partial \mathbf{x}_k^h}{\partial \boldsymbol{\xi}^*} \approx \sum_{I=1}^{n_{\text{ne},k}} \mathbf{x}_I^e \otimes \frac{\partial N_I}{\partial \boldsymbol{\xi}^*}, \quad \mathbf{J}_k^e = \frac{\partial \mathbf{X}_k^h}{\partial \boldsymbol{\xi}^*} \approx \sum_{I=1}^{n_{\text{ne},k}} \mathbf{X}_I^e \otimes \frac{\partial N_I}{\partial \boldsymbol{\xi}^*}, \quad (4.29)$$

which are denoted the *elemental Jacobians*. These expressions can be used to determine, e.g., the deformation gradient \mathbf{F}_k^e and its determinant

$$\mathbf{F}_k^e = \mathbf{j}_k^e (\mathbf{J}_k^e)^{-1}, \quad J_k^e = \det \mathbf{F}_k^e = \frac{\det \mathbf{j}_k^e}{\det \mathbf{J}_k^e}. \quad (4.30)$$

Since the local derivatives of the shape functions $\partial N_I / \partial \boldsymbol{\xi}^*$ do not change during the computation, they only need to be evaluated once at the beginning. The derivatives with respect to the global coordinates are then given by

$$\frac{\partial N_I}{\partial \mathbf{x}_k^h} = (\mathbf{j}_k^e)^{-\top} \frac{\partial N_I}{\partial \boldsymbol{\xi}^*}, \quad \frac{\partial N_I}{\partial \mathbf{X}_k^h} = (\mathbf{J}_k^e)^{-\top} \frac{\partial N_I}{\partial \boldsymbol{\xi}^*}. \quad (4.31)$$

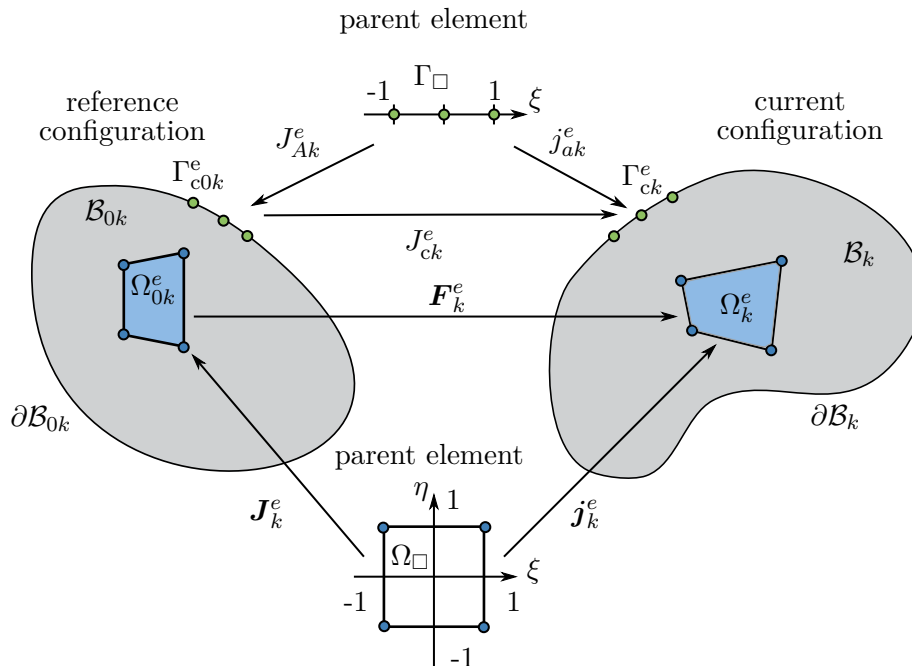


Figure 4.3 – Mappings of the parent bulk and surface element Ω_{\square} and Γ_{\square} to their respective reference and current configurations.

Similarly, one can define a parent element Γ_{\square} with coordinates $\xi \in [-1, 1]^d$ for the surface elements, as well as a scalar representing the surface stretch

$$j_{ak}^e = \sqrt{\det a_{\alpha\beta}^k}, \quad J_{Ak}^e = \sqrt{\det A_{\alpha\beta}^k}, \quad J_{ck}^e = \frac{j_{ak}^e}{J_{Ak}^e}. \quad (4.32)$$

The volume and the surface integrals in terms of the parent elements Ω_{\square} and Γ_{\square} can then be reformulated as

$$dv_k = \det \mathbf{j}_k^e d\xi^*, \quad dV_k = \det \mathbf{J}_k^e d\xi^*, \quad (4.33)$$

$$da_k = j_{ak}^e d\xi, \quad dA_k = J_{Ak}^e d\xi. \quad (4.34)$$

An illustration of the mapping and the mapped components is shown in Figure 4.3.

4.2 Solution Procedure

Once the elemental force vectors are evaluated and assembled according to Eq. (4.27), the system of equations must be solved. As both, the internal forces and the contact forces in Eq. (4.27) are nonlinear with respect to the displacement \mathbf{u} , the entire system of equations must first be linearized (as shown in Section 3.5), so that it can be solved with the Newton-Raphson method (Wriggers, 2008). This method solves a nonlinear equation system by repeatedly solving its linearization around the current solution \mathbf{u}_i in load increment i and updating the solution

$$\mathbf{u}_{i+1} = \mathbf{u}_i + \Delta \mathbf{u}_{i+1}, \quad i = 0, 1, \dots \quad (4.35)$$

for the next load increment. The update $\Delta \mathbf{u}_{i+1}$ is obtained by solving the linear equation system

$$\mathbf{k} \Delta \mathbf{u}_{i+1} + \mathbf{f}(\mathbf{u}_i) = \mathbf{0}, \quad \mathbf{k} := \frac{\partial \mathbf{f}(\mathbf{u}_i)}{\partial \mathbf{u}_i}. \quad (4.36)$$

The tangent or stiffness matrix \mathbf{k} is composed of the internal stiffness \mathbf{k}_{int} , external stiffness \mathbf{k}_{ext} , and the contact stiffness \mathbf{k}_c :

$$\mathbf{k} = \mathbf{k}_{\text{int}} + \mathbf{k}_{\text{ext}} + \mathbf{k}_c, \quad \mathbf{k}_{\text{int}} := \frac{\partial \mathbf{f}_{\text{int}}(\mathbf{u})}{\partial \mathbf{u}}, \quad \mathbf{k}_c := \frac{\partial \mathbf{f}_c(\mathbf{u})}{\partial \mathbf{u}}, \quad \mathbf{k}_{\text{ext}} := \frac{\partial \mathbf{f}_{\text{ext}}(\mathbf{u})}{\partial \mathbf{u}}. \quad (4.37)$$

In analogy to the global force vectors these are assembled from the contributions of each single FE. To solve the linear system, one starts with an initial guess $\mathbf{u}_i = 0$ and iterates until a certain convergence criterion, e.g.,

$$r_i^{\text{res}} := \mathbf{f}(\mathbf{u}_i) \cdot \Delta \mathbf{u}_{i+1} < \varepsilon_{\text{tol}}, \quad (4.38)$$

is satisfied, where ε_{tol} is a pre-defined tolerance.

4.3 Contact Projection Approaches

Traditional contact algorithms require the definition of a *master* surface $\partial_c \mathcal{B}_\ell$ and a *slave* surface $\partial_c \mathcal{B}_k$. Then, the contact traction \mathbf{t}_c is only evaluated on the slave surface $\partial_c \mathcal{B}_k$, by

$$\delta \Pi_c \approx \delta \Pi_c^h = \sum_{e=1}^{n_k} (\delta \mathbf{x}_k^e \cdot \mathbf{f}_{ck}^e + \delta \mathbf{x}_\ell^e \cdot \mathbf{f}_{c\ell}^e), \quad (4.39)$$

where n_k denotes the number of elements of the slave surface. The elemental contact force vectors

$$\mathbf{f}_{ck}^e = - \int_{\Gamma_k^e} \mathbf{N}_k^T \mathbf{t}_{ck} \, da_k, \quad \mathbf{f}_{c\ell}^e = - \int_{\Gamma_k^e} \mathbf{N}_\ell^T(\boldsymbol{\xi}) \mathbf{t}_{ck} \, da_k, \quad (4.40)$$

act on element $\Gamma_k^e \subset \partial_c \mathcal{B}_k^h$ and partially on some elements $\Gamma_\ell^e \subset \partial_c \mathcal{B}_\ell^h$ ($\ell \neq k$). The contact traction is carried over to the master surface as $-\mathbf{t}_{ck}$. Although the so-called master-slave or full-pass approach is widely used for contact between two deformable bodies, it introduces a bias into the formulation and requires additional effort to integrate the quantities of the neighboring surfaces (Sauer and De Lorenzis, 2013). To overcome these issues, one can use an unbiased *two-half-pass* approach for contact (Sauer and De Lorenzis, 2013; Sauer and De Lorenzis, 2015). There, the original weak formulation of the virtual contact work is considered and the contact tractions \mathbf{t}_{ck} are evaluated on each contact surface $\partial_c \mathcal{B}_k$ ($k = 1$ and $k = 2$) separately:

$$\delta \Pi_c \approx \delta \Pi_c^h = \sum_{k=1}^2 \sum_{e=1}^{n_k} \delta \mathbf{x}_k^e \cdot \mathbf{f}_{ck}^e, \quad (4.41)$$

$$\mathbf{f}_{ck}^e = \int_{\Gamma_k^e} \mathbf{N}_k^T \mathbf{t}_{ck} \, da_k. \quad (4.42)$$

Although this formulation solves the drawback of the full-pass algorithm it introduces some other drawbacks. The first issue is that this formulation does not fulfill the equilibrium of the contact tractions exactly. However, the resulting error is of the same order as those errors stemming, e.g., from the finite element discretization and decreases to zero with further mesh refinement (Sauer and De Lorenzis, 2013). The other important issue concerns over-constraining, which may occur for the penalty method (introduced in Section 4.4) when used with many quadrature points (Sauer and De Lorenzis, 2015). This can be circumvented by mesh refinement or the choice of moderate penalty parameters. Both contact projection approaches are sketched in Figure 4.4.

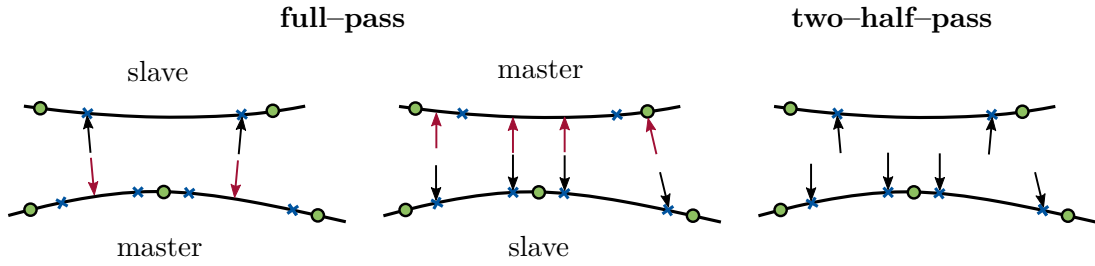


Figure 4.4 – Contact projection approaches. Green dots denote FE nodes while blue crosses represent the Gauss points. Black arrows denote quadrature point entries in \mathbf{f}_{ck}^e and red arrows denote quadrature point entries in \mathbf{f}_{cl}^e . Adopted and modified from [Sauer and De Lorenzis \(2015\)](#).

4.4 The Penalty Method for Frictional Contact

The exact treatment of normal contact (without adhesion) requires that the normal contact pressure p_c is zero when the bodies \mathcal{B}_k are not in contact ($g_n > 0$) and that contact ($g_n = 0$) results in a negative contact pressure ($p_c < 0$). These conditions are known as the *Karush-Kuhn-Tucker* or *Hertz-Signorini-Moreau* conditions and are summarized as

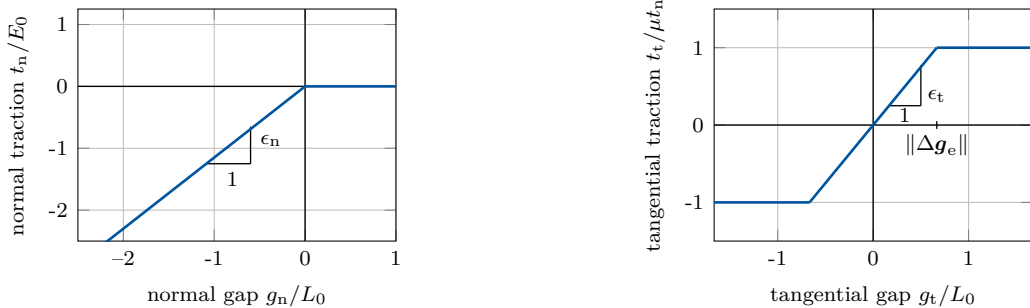
$$g_n \geq 0, \quad p_c \leq 0, \quad g_n p_c = 0. \quad (4.43)$$

To simplify the numerical treatment, one can allow for small interpenetrations $g_n < 0$ and a small reversible tangential gap $\Delta \mathbf{g}_e$, that are penalized by means of *penalty parameters* ϵ_n, ϵ_t . The normal traction \mathbf{t}_n is then given by

$$\mathbf{t}_n = \begin{cases} \epsilon_n g_n \mathbf{n}_k, & g_n < 0, \\ \mathbf{0}, & g_n \geq 0, \end{cases} \quad (4.44)$$

while the tangential traction becomes

$$\|\mathbf{t}_t\| = \min(\epsilon_t \|\Delta \mathbf{g}_e\|, t_t^{\text{slide}}). \quad (4.45)$$



(a) Normal traction of a single point for pure pressure as a function of the normal gap g_n (4.44).

(b) Tangential traction for a single point for constant pressure, defined by Coulomb's law (3.38) as a function of the tangential gap $g_t = \|\mathbf{g}_t\|$.

Figure 4.5 – Penalty contact traction. Here, L_0 is a reference length and E_0 is a reference stiffness.

An example for both traction components is shown in Figure 4.5. As the penalty parameters approach infinity, the penetration g_n approaches zero, thus converging to the exact solution. However, the penalty parameters have to be chosen appropriately, as high values can lead to ill-conditioning of the stiffness matrix \mathbf{k} (4.36).

4.5 Predictor-Corrector Algorithms

One common strategy to distinguish between frictional sticking and sliding is a predictor-corrector approach similar to those used in computational plasticity. This approach uses a so-called *trial* traction $\mathbf{t}_{\text{trial}}^{n+1}$. First, sticking is assumed, such that

$$\mathbf{t}_{\text{trial}}^{n+1} = \mathbf{t}_{\text{stick}}^{n+1}. \quad (4.46)$$

This trial traction can then be inserted into the slip criterion (3.36) to check the current contact state:

1. If $f_s(\mathbf{t}_{\text{trial}}^{n+1}, t_{\text{slide}}^{n+1}) < 0$, the point \mathbf{x}_p^{n+1} is sticking tangentially; in this case

$$\mathbf{t}_t^{n+1} = \mathbf{t}_{\text{trial}}^{n+1}, \quad (4.47)$$

2. If $f_s(\mathbf{t}_{\text{trial}}^{n+1}, t_{\text{slide}}^{n+1}) \geq 0$, the point \mathbf{x}_p^{n+1} is sliding; in this case a corrector step has to be performed to determine the actual traction \mathbf{t}_t^{n+1} satisfying $f_s(\mathbf{t}_t^{n+1}, t_{\text{slide}}^{n+1}) = 0$.

For the formulation of the sliding traction $\mathbf{t}_{\text{slide}}^{n+1}$ and the sliding direction $\boldsymbol{\tau}_p$ from Eq. (3.37), one can use elastoplasticity theory in order to incorporate a friction response in tangential direction (see e.g. Wriggers (2006); Laursen (2013); Sauer and De Lorenzis (2015)). In the context of this work, another approach is also used that is based on the surface potential-based contact formulations of Duong and Sauer (2019) and Sauer and De Lorenzis (2013). Both concepts will be summarized and explained based on Coulomb's friction (3.38) and are sketched in Figure 4.6.

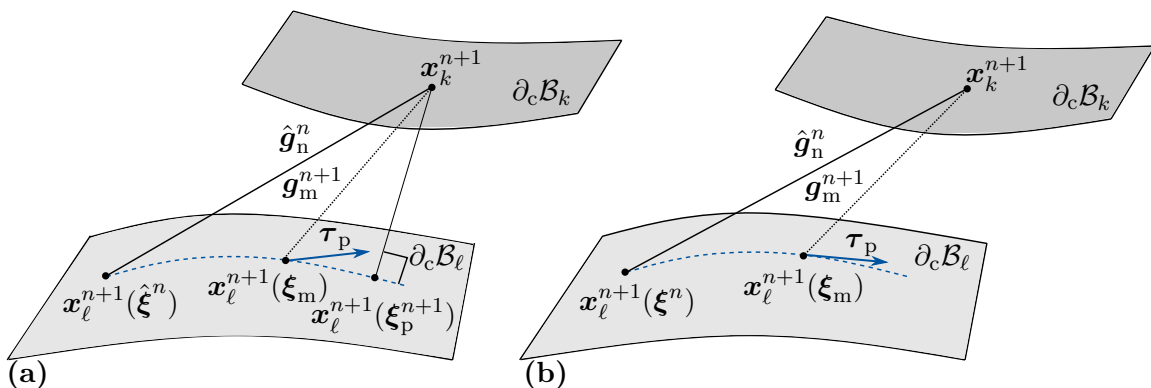


Figure 4.6 – Comparison of formulations for the tangential sliding direction $\boldsymbol{\tau}_p$: (a) $\boldsymbol{\tau}_p$ as the secant direction (Sauer and De Lorenzis, 2015). (b) $\boldsymbol{\tau}_p$ as the tangent direction (Duong and Sauer, 2019). Adopted and modified from Duong and Sauer (2019).

4.5.1 Elastoplasticity Based Formulation

Following Sauer and De Lorenzis (2015), the tangential contact traction during sticking is defined by

$$\mathbf{t}_t^n = \epsilon_t \left(\mathbf{x}_\ell^n(\boldsymbol{\xi}_p^n) - \mathbf{x}_\ell^n(\boldsymbol{\xi}_s^n) \right). \quad (4.48)$$

At the new pseudo-time t^{n+1} the following trial traction is considered, which is associated to sticking (predictor step)

$$\mathbf{t}_{\text{trial}}^{n+1} = \epsilon_t \left(\mathbf{x}_\ell^{n+1}(\boldsymbol{\xi}_p^{n+1}) - \mathbf{x}_\ell^{n+1}(\boldsymbol{\xi}_s^n) \right), \quad \xi_{s_{n+1}}^\alpha = \xi_{s_n}^\alpha. \quad (4.49)$$

In case of sliding, the implicit Euler method is used to discretize $\xi_{s_{n+1}}^\alpha$ in time:

$$\xi_{s_{n+1}}^\alpha \approx \xi_{s_n}^\alpha + \Delta\gamma_{n+1} \boldsymbol{\tau}_p^{n+1} \cdot \mathbf{a}_{s_{n+1}}^\alpha, \quad (4.50)$$

and thus

$$\mathbf{x}_\ell^{n+1}(\boldsymbol{\xi}_s^{n+1}) = \mathbf{x}_\ell^{n+1}(\boldsymbol{\xi}_s^n) + \Delta\gamma_{n+1} \boldsymbol{\tau}_p^{n+1}. \quad (4.51)$$

The scalar $\Delta\gamma_{n+1}$ can then be determined by assuming

$$\boldsymbol{\tau}_p^{n+1} = \frac{\mathbf{t}_{\text{trial}}^{n+1}}{\|\mathbf{t}_{\text{trial}}^{n+1}\|}, \quad \mathbf{a}_{p_{n+1}}^\alpha \approx \mathbf{a}_{s_{n+1}}^\alpha = \boldsymbol{\tau}_p^{n+1}, \quad (4.52)$$

and inserting Eq. (4.51) into the traction at pseudo-time t_{n+1} (4.49) and enforcing the slip criterion (3.36). This yields

$$\Delta\gamma_{n+1} = \frac{f_s(t_{\text{trial}}^{n+1}, t_{\text{slide}}^{n+1})}{\epsilon_t}, \quad (4.53)$$

$$\xi_{s_{n+1}}^\alpha \approx \xi_{s_n}^\alpha + \Delta\gamma_{n+1} \boldsymbol{\tau}_p^{n+1} \cdot \boldsymbol{\tau}_p^{n+1}, \quad (4.54)$$

$$\mathbf{t}_t^{n+1} = \mathbf{t}_{\text{trial}}^{n+1} - \epsilon_t \Delta\gamma_{n+1} \boldsymbol{\tau}_p^{n+1}. \quad (4.55)$$

For a more detailed derivation the reader is referred to [Sauer and De Lorenzis \(2015\)](#).

4.5.2 Surface Potential Based Formulation

In order to determine the contact traction at the current time step, according to the contact formulation of [Duong and Sauer \(2019\)](#), a so-called interacting (elastic) gap vector $\mathbf{g}_e(\hat{\boldsymbol{\xi}})$ is introduced. This gap vector is defined between the current slave point \mathbf{x}_k and the so-called current interacting point $\mathbf{x}_\ell(\hat{\boldsymbol{\xi}})$ on the master surface $\partial_c \mathcal{B}_\ell$ (defined below), i.e.

$$\mathbf{g}_e(\hat{\boldsymbol{\xi}}) := \mathbf{x}_k - \mathbf{x}_\ell(\hat{\boldsymbol{\xi}}). \quad (4.56)$$

The current gap vector can be further decomposed into a tangential and a normal component $\mathbf{g}_e(\hat{\boldsymbol{\xi}}) = \mathbf{g}_{\text{en}} + \mathbf{g}_{\text{et}}$, with

$$\mathbf{g}_{\text{en}}(\hat{\boldsymbol{\xi}}) := (\mathbf{n} \otimes \mathbf{n}) \mathbf{g}_e, \quad \mathbf{g}_{\text{et}}(\hat{\boldsymbol{\xi}}) := (\mathbf{a}_\alpha \otimes \mathbf{a}^\alpha) \mathbf{g}_e. \quad (4.57)$$

According to the penalty formulation, the total frictional contact traction is proportional to the interacting gap vector $\mathbf{g}_e(\hat{\boldsymbol{\xi}})$, according to

$$\mathbf{t}_c = \epsilon \mathbf{g}_e, \quad (4.58)$$

which follows from using the contact potential $W := \frac{1}{2} \epsilon \mathbf{g}_e \cdot \mathbf{g}_e$. At initial contact, the interacting point $\mathbf{x}_\ell(\hat{\boldsymbol{\xi}})$ is equal to the closest projection point of \mathbf{x}_k . During sticking, the current interacting point is equal to the previous interacting point $\hat{\boldsymbol{\xi}}^n$. Therefore, for sticking, the current contact

gap vector \mathbf{g}_e is determined from Eq. (4.56) with $\hat{\boldsymbol{\xi}} = \hat{\boldsymbol{\xi}}^n$. During sliding, the current interacting point $\hat{\boldsymbol{\xi}}$ is the solution of the kinematic constraint equation,

$$\mathbf{f}_g(\hat{\boldsymbol{\xi}}) := \mathbf{g}_{\text{et}} - \mathbf{g}_{\text{et}}^{\text{max}} = \mathbf{0}, \quad (4.59)$$

in the current configuration. \mathbf{g}_e then follows from Eq. (4.56). The critical value during sliding $\mathbf{g}_{\text{et}}^{\text{max}}$ is defined by the chosen friction law. For example, for Coulomb's friction, it is defined as

$$\mathbf{g}_{\text{et}}^{\text{max}} = \mu \|\mathbf{g}_{\text{en}}\| \boldsymbol{\tau}_p, \quad (4.60)$$

where $\boldsymbol{\tau}_p$ can be computed by projecting the previous interacting gap \mathbf{g}_e^n onto the tangent plane at the current interaction point $\mathbf{x}_\ell(\hat{\boldsymbol{\xi}})$:

$$\boldsymbol{\tau}_p = \frac{(\mathbf{a}_\alpha \otimes \mathbf{a}^\alpha) \mathbf{g}_e^n}{\|(\mathbf{a}_\beta \otimes \mathbf{a}^\beta) \mathbf{g}_e^n\|}, \quad (4.61)$$

where $\mathbf{a}_\alpha, \mathbf{a}^\alpha$ are evaluated at $\mathbf{x}_\ell(\hat{\boldsymbol{\xi}})$.

4.6 Solution Algorithm

Finally, the complete contact FE solution algorithm for frictional contact without adhesion with the full-pass approach can be assembled and is sketched below. For the two-half-pass approach the contact loop is performed for both contact surfaces $\partial_c \mathcal{B}_k$ and $\partial_c \mathcal{B}_\ell$. For the contact formulations and osseointegration models presented in Chapters 6-8 the code in the blue box needs to be adjusted.

loading loop: at each quadrature point

- apply load step: $n \rightarrow n + 1$
- provide initial guess for the nodal displacement \mathbf{u}_0 and the current contact surface configuration $\partial_c \mathcal{B}_\ell^{n+1}$

global Newton-Raphson loop: iterate for $i \rightarrow i + 1$ until converged

1. loop over the bulk elements Ω^e and their quadrature points

- compute and assemble the internal forces \mathbf{f}_{int} and tangent matrices \mathbf{k}_{int}

contact loop: loop over the slave contact elements Γ_k^e and their quadrature point

- 2.1 determine current position \mathbf{x}_k^{n+1} of the quadrature point

- 2.2 closest point projection:

- solve Eq. (3.25) with Newton's method to obtain the coordinates ξ_p of the closest projection point $\mathbf{x}_p \in \partial_c \mathcal{B}_\ell$ of \mathbf{x}_k^{n+1}

2.3 contact computation: evaluate the normal contact distance g_n and corresponding direction \mathbf{n}_p :

- if $g_n \geq 0$: set \mathbf{t}_c and corresponding gradients to zero; set $\xi_s = \xi_p$
- if $g_n < 0$:
 - evaluate the normal contact traction $\mathbf{t}_n = p_c \mathbf{n}_p$ based on Eq. (4.44)
 - evaluate the tangential contact traction \mathbf{t}_t :
 - elastic predictor step: assume sticking (4.47)
 - check slip criterion (3.36): if $f_s > 0$ perform inelastic corrector step $\mathbf{t}_t = \mathbf{t}_t^{\text{slide}} \boldsymbol{\tau}_p$
 - compute the gradients $\partial \mathbf{t}_c / \partial \mathbf{u}_k^e, \partial \mathbf{t}_c / \partial \mathbf{u}_\ell^e$, according to Appendix A
 - assemble tangent matrices \mathbf{k}_c

2. apply boundary conditions

3. solve $\mathbf{k} \Delta \mathbf{u} = -\mathbf{f}$

4. update $\mathbf{u}_{i+1} = \mathbf{u}_i + \Delta \mathbf{u}$ and evaluate error norm

5. check the convergence of the global Newton-Raphson loop

Chapter 5

Determinants of Initial Stability of Cementless Implants

In the previous chapters, the required foundations in nonlinear mechanics, finite element methods, and computational contact mechanics were introduced. In the following, the new contributions of this work are presented, beginning with the assessment of the determinants of primary stability of a cementless ACI.

Major parts of this chapter have been published in [Immel et al. \(2021a\)](#). The 2D results in Sections [5.3.1](#), [5.3.3–5.3.5](#) were adopted from [Raffa et al. \(2019\)](#). Figures [5.3](#) (b)–(d), [5.4](#) and [5.6](#), as well as the data for $E_{tb} = 0.1, 0.5$ GPa in Figures [5.9](#) and [5.10](#) and their discussion were not part of these publications and have been added here.

5.1 Motivation

Cementless ACI have become more and more common for THA surgery ([Toossi et al., 2013](#)). Initial stability is obtained during the surgical intervention through a diameter interference fit, by reaming the host bone cavity ([MacKenzie et al., 1994](#); [Kim et al., 1995](#); [Macdonald et al., 1999](#)). The ACI is inserted into the bone cavity using impacts and the initial fixation is achieved through residual stresses, localized mostly at the ACI rim ([Hothi et al., 2011](#); [Mukherjee and Gupta, 2014](#)). To achieve an optimal primary stability, a compromise should be found between: 1. reducing the relative micro-motions at the bone-implant interface (BII), and avoiding large gaps between bone and implant, which may lead to the formation of fibrous tissue in the peri-implant region ([Brånemark, 1977](#)), the formation of low-quality bone tissue or even inhibit bone growth ([Jasty et al., 1988](#); [Sandborn et al., 1988](#); [Mukherjee and Gupta, 2014](#)), and 2. avoiding excessive stresses in peri-implant bone tissue, which may lead to bone necrosis or local ischemia ([Sotto-Maior et al., 2010](#)). All these phenomena may jeopardize osseointegration processes ([Jasty et al., 1988](#); [Schmalzried et al., 1992](#); [Raffa et al., 2019](#)), and can lead to implant loosening. It remains difficult to predict ACI loosening because of its multi-factorial causes related to the implant properties, the cavity geometry (e.g., its diameter), and to the patient's bone quality ([Kwong et al., 1994](#); [Hsu et al., 2007](#); [Amirouche et al., 2014](#)). Different pull-out tests have been carried out *in vitro* and *ex vivo* to assess the ACI primary stability ([Le Cann et al., 2014](#); [Goldman et al., 2016](#)), with several studies focusing on the effect of bone quality on the biomechanical behavior of the ACI ([Hsu et al., 2007](#); [Janssen et al., 2010](#)). However,

such biomechanical testing cannot be applied during surgery. It remains difficult to carry out a systematic *in vitro* investigation of the multifactorial determinants of ACI stability because of the difficulty to precisely control all parameters when using bone tissue.

For these reasons, several numerical models have been developed to assess the biomechanical behavior of the cementless ACI with simplified bone geometries (Yew et al., 2006; Hothi et al., 2011; Souffrant et al., 2012; Raffa et al., 2019). While such models offer some initial insight on the biomechanical parameters and the contact behavior of the BII in a controlled environment, their simplified geometry constitutes a strong limitation because it does not properly capture 3D effects that have an important influence on the structural behavior of the pelvis. In particular, Cilingir et al. (2007) investigated the influence of the bone geometry on the contact pressure and stress distribution by comparing the performance of a 2D axisymmetric, 3D axisymmetric, and 3D hemi-pelvis model. They showed that, while all models predicted a similar contact pressure distribution in the acetabular cavity, the maximum von Mises stress within the bone tissue differed significantly. As the insertion of the ACI into the reamed cavity produces considerable stresses at the bone cavity rim, anatomic 3D models must be considered to achieve more reliable results. Consequently, more accurate models of the human pelvis have been developed to model the contact behavior of the ACI (Anderson et al., 2005; Hsu et al., 2007; Janssen et al., 2010; Amirouche et al., 2014; Rourke and Taylor, 2020). However, none of the aforementioned studies analyzed both the insertion and the stability of the ACI, which are highly interdependent. Moreover, only a small range of biomechanical parameters were analyzed so far.

The aim of this work is to provide a better understanding of the determinants of the primary stability of cementless ACI in the human pelvis. The ACI primary stability is assessed through the estimation of the pull-out force (Olory et al., 2004) and the polar gap (MacKenzie et al., 1994; Amirouche et al., 2014). Therefore, geometrically nonlinear FE analyses are performed to simulate the quasi-static insertion and subsequent pull-out of the ACI in a patient's hemi-pelvis. The influence of a broad range of different implant- and patient-specific parameters on the ACI primary stability, such as the friction coefficient at the BII μ , the bone quality in terms of cortical and trabecular bone Young's moduli E_{cb} , E_{tb} , and the diametric interference fit IF , are analyzed and compared to a previous 2D study (Raffa et al., 2019).

5.2 Setup

The choice of the input parameters and geometrical properties of the present FE model are based on the study of Raffa et al. (2019). In contrast to their work, the geometry of a 3D human pelvis is used here, instead of a simplified 2D trabecular bone block. Finite element meshing and numerical analyses were carried out using ANSYS Workbench software (v.14, ANSYS, Inc., Canonsburg, PA, USA).

5.2.1 Geometry and Mesh

The geometry for the human hemi-pelvis is obtained from a free online data base ([hipSTL](#)). The points comprising the contours of the hip are triangulated, decimated, and smoothed in MeshLab (Cignoni et al., 2008). The thickness of the cortical bone layer may vary and its limit with the trabecular bone is blurred because the properties of the bone change gradually, which is not taken into account in the present model. Instead, a uniform thickness of the cortical bone

tissue of 1 mm (Spears et al., 1999) is assumed. The corresponding cortical layer is created by extrusion with Meshmixer (Autodesk, San Rafael, CA, USA). A hemi-spherical cavity is created in the acetabula, using ANSYS Workbench. The cavity diameter is varied between 48.5 and 50.9 mm, which corresponds to different values of the diametric interference fit IF (0–2.5 mm), according to values found in the literature (Kwong et al., 1994; Macdonald et al., 1999; Spears et al., 1999; Yew et al., 2006; Hothi et al., 2011). The resulting pelvis geometry is shown in Figure 5.1(a) and (b).

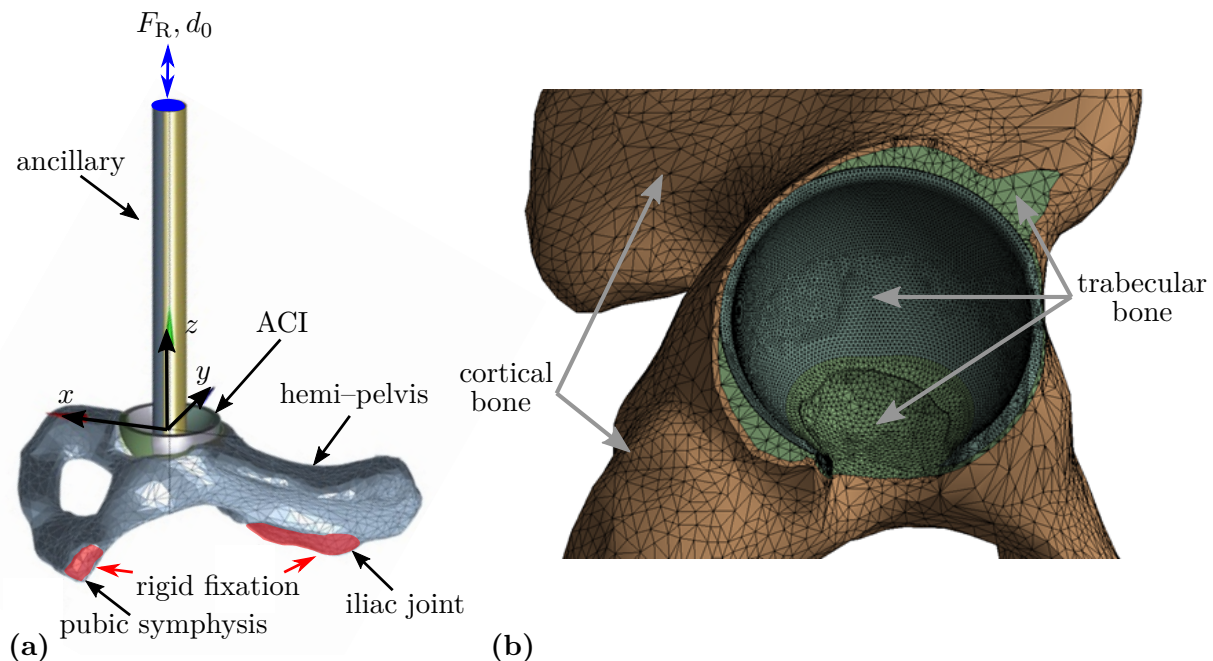


Figure 5.1 – (a) Image of the pelvis geometry with the ACI and ancillary. Red elements indicate fixed rigid boundary conditions. Blue elements indicate the region where the displacement is applied. (b) Enlargement of the FE mesh at the cavity. Brown elements indicate cortical bone and green elements represent trabecular bone. Adopted from Immel et al. (2021a).

The ACI is modeled after the Cotyle Cerafit (Ceraver, Roissy, France) and has an outer radius of $R_I = 25.5$ mm. Its thickness varies linearly as a function of the polar angle, with values between 2.9 mm at the cup dome and 3.7 mm at the cup rim, similarly as what is used in previous studies (Michel et al., 2017; Raffa et al., 2019). Moreover, a cylindrical ancillary, with a radius and height of $R_A = 8.5$ mm and $H_A = 190$ mm, is rigidly attached to the ACI, as it is done in the clinic during insertion. The complete model is shown in Figure 5.1(a).

The FE mesh is generated with ANSYS Workbench and it slightly varies for every value of the interference fit IF . It typically contains approximately 125,000 tetrahedral and hexahedral, quadratic Lagrangian elements, leading to a global system with approximately 615,000 degrees of freedom. The mesh size is finer around the bone cavity surface (average size 0.8 mm) to provide a sufficiently accurate geometrical approximation of the curved contact surface. An enlargement of the mesh at the cavity is shown in Figure 5.1(b). A standard convergence study concerning the element size h_e and the load step increment Δl_s is performed for the reference case (see Section 5.2.2), with the pull-out force (see Section 5.2.4) as the convergence criteria. The mesh and load step increment are refined until the relative change in the pull-out force was below 1 % and quadratic Newton-Raphson convergence within 2 steps was ensured (see Appendix B.1). In

	Material	Symbol	Range	Ref. value
Ancillary	Stainless steel	–	–	210 GPa
Implant	Titanium alloy	–	–	133 GPa
Outer bone	Cortical bone	E_{cb}	15–25 GPa (1993; 2011)	18 GPa (1993)
Inner bone	Trabecular bone	E_{tb}	0.1–1 GPa (2010; 2017)	0.2 GPa (2017)
Interference fit		IF	0.1–2.5 mm (1994; 1999; 1999)	1 mm (1994)
Friction coeff.		μ	0.1–1 (1997a; 1999)	0.3 (1999)

Table 5.1 – Material properties of the four subdomains considered in the numerical model as well as ranges and reference values of the studied parameters: interference fit IF , friction coefficient μ , Young’s modulus of cortical bone E_{cb} and Young’s modulus of trabecular bone E_{tb} . Adopted from [Immel et al. \(2021a\)](#).

cases where parameter combinations with high stiffness or interference fit do not converge for the determined load step increment, the load step increment is further decreased.

5.2.2 Material Properties and Varied Parameters

The ancillary and the ACI are made of stainless steel and titanium alloy (Ti-Al6-V4), respectively. The pelvis is assumed to be composed of a uniform thin outer layer of cortical bone (1 mm) and trabecular bone inside. However, due to the simulated reaming, no cortical bone remains on the contact surface of the hip cavity (see Figure 5.1(b)). All materials are assumed to be homogeneous, isotropic, and hypoelastic (3.2.2). The Poisson ratio for all materials is set to $\nu = 0.3$. Table 5.1 shows the elastic properties of the different materials used in this study.

Friction is modeled with a standard Coulomb’s law (3.38), with constant friction coefficient μ . A wide range of values of μ (0–1) was considered in order to simulate the physiological range of friction for various types of implant surfaces in contact with bone and for different clinical situations of the BII ([Dammak et al., 1997a](#); [Spears et al., 1999](#); [Novitskaya et al., 2011](#)). $\mu^* = 0.3$ is taken as the reference value ([Dammak et al., 1997a](#)). Variations of the Young’s moduli of cortical bone E_{cb} and trabecular bone E_{tb} are considered within their physiological range ([Shirazi-Adl et al., 1993](#); [Phillips et al., 2007](#); [Janssen et al., 2010](#); [Watson et al., 2017](#)) and for some extreme cases: E_{tb} between 0.1 and 2 GPa and E_{cb} between 0.2 and 25 GPa. The bone’s elastic modulus in the cavity provides an indication of the bone quality and has been previously investigated in FE studies ([Hsu et al., 2007](#); [Janssen et al., 2010](#)). The reference values are $E_{cb}^* = 18$ GPa ([Shirazi-Adl et al., 1993](#)) and $E_{tb}^* = 0.2$ GPa ([Phillips et al., 2007](#)), respectively.

A broad range of the diametric interference fit IF (0–2.5 mm) is considered, to cover most commonly used configurations, as well as extreme cases. The corresponding reference value is $IF^* = 1$ mm, which is a standard value used in clinical practice ([Kwong et al., 1994](#)). Throughout this study, the parameter set of $E_{cb}^* = 18$ GPa, $E_{tb}^* = 0.2$ GPa, $\mu^* = 0.3$, and $IF^* = 1.0$ mm is referred to as the *reference case*. Table 5.1 lists the analyzed parameters with their corresponding range and reference value.

5.2.3 Boundary and Loading Conditions

All simulations are performed with quasi-static analysis setting (i.e., excluding inertia and viscosity) and considering large deformation effects. Frictional contact with the augmented

Lagrange method is used. The hip cavity is set as the slave surface and the ACI is set as the master surface.

The pelvis is rigidly fixed in all directions at the pubic symphysis and the iliac joint (see Figure 5.1(a), red), following the literature (Shirazi-Adl et al., 1993; Anderson et al., 2005; Clarke et al., 2013; Henyš and Čapek, 2017). All other location corresponding to bone tissue are free. At the initial state (load step) $ls_0 = 0$, the outer boundary of the ACI and the internal boundary of the hip cavity are close but not in contact.

To simulate the insertion process, a uniform displacement d_0 is applied to the ancillary. The implant is displaced by d_0 until the normal reaction force reaches $F_z = F_0 = -2500$ N. The reaction force F_0 is chosen based on experimental measurements from Raffa et al. (2019) and is similar to values found in the literature (Sotto-Maior et al., 2010; Souffrant et al., 2012; Le Cann et al., 2014). The displacement d_0 depends on the studied parameters and is not known a priori. It is computed for each parameter combination individually by performing an initial insertion simulation first to determine $d_0(\mu, IF, E_{cb}, E_{tb}, F_0)$, s.t. $F_z(d_0) = F_0$.

To simulate the push-in and removal of the implant into and from the pelvis, the simulation is divided into three stages: First, the displacement d_0 is applied to the top surface of the ancillary (see Figure 5.1(a), blue) in order to insert the implant into the hip until the normal reaction force F_0 is reached at load step ls_1 . Second, the implant and the ancillary are held in place until load step ls_2 . This is done only for illustrative purposes; the actual holding time has no influence in quasi-static simulations. Third, the uniform pull-out displacement $-d_0$ is applied to the top surface of the ancillary, until the implant is completely detached from the bone (load step ls_3). The quasi-static displacement u_z in axial direction z can then be described by

$$u_z = \begin{cases} d_0 \cdot \Delta l s / l s_1 & \text{for } l s_0 \leq l s < l s_1, \\ d_0 & \text{for } l s_1 \leq l s < l s_2, \\ d_0 \cdot (l s_3 - \Delta l s) / l s_1 & \text{for } l s_2 \leq l s \leq l s_3. \end{cases} \quad (5.1)$$

In most cases the load step size of $\Delta l s = d_0/200$ is used during the insertion and the extraction phases (resulting in 440 load steps). For high friction coefficients (0.6–1.0) and a critical interference fit (1.0–1.8 mm), a smaller load step size, such as $\Delta l s = d_0/5000$ is needed to ensure Newton-Raphson convergence.

5.2.4 Quantifying Primary Stability

In this chapter, the primary stability is quantified by the size of the polar gap after insertion and by the values of the pull-out force. The pull-out force F_z^{\max} is defined by the positive maximum normal reaction force F_z obtained at the upper surface of the ancillary during the pull-out phase. The polar gap is determined as the distance between the pole of the ACI and the pole of the hip cavity during the holding phase (load step $l s = 220$). The pull-out force has already been used in previous works in order to assess the ACI primary stability (Spears et al., 1999; Olory et al., 2004; Bishop et al., 2014; Le Cann et al., 2014; Raffa et al., 2019). The pull-out force is a clinically relevant quantity because after inserting the ACI in the pelvis, surgeons usually attempt to pull or lever-out the ACI to check manually for the stability and motion of the ACI. Furthermore, it is commonly used as a determinant of primary stability in *in vitro* studies (Hsu et al., 2007; Janssen et al., 2010; Le Cann et al., 2014; Goldman et al., 2016). Moreover, the polar gap between the ACI and the hip is also frequently used in clinical

studies (Janssen et al., 2010; Michel et al., 2017; Rourke and Taylor, 2020) in order to assess the ACI stability. Large gaps indicate improper seating of the ACI and can affect the quality of long-term fixation due to the formation of fibrous tissue in the peri-implant region (Brånemark, 1977), the formation of low-quality bone tissue or even inhibit bone growth (Jasty et al., 1988; Sandborn et al., 1988; Mukherjee and Gupta, 2014). The polar gap is evaluated based on values found in the literature (Jasty et al., 1988; Schmalzried et al., 1992; MacKenzie et al., 1994; Udomkiat et al., 2002), where gaps below 500 μm (indicated in green in Figures 5.5(b),(d) and 5.7(b),(d)) are considered optimal, gaps between 500 μm and 1 mm are considered acceptable (indicated in yellow), and gaps above 1 mm (indicated in red) are considered to be critical.

5.3 Results

The results obtained with the FE model are presented and compared to a previous 2D study (Raffa et al., 2019). First, the main differences between the results obtained in the previous 2D axisymmetric study and in the present study for the reference case are discussed. Second, the structural response of the pelvis and the implant in terms of stress distribution is analyzed. Last, the parametric study on the influence of the bone Young's moduli E_{tb} and E_{cb} , the friction coefficient μ , and the interference fit IF on primary stability as well as optimal combinations of these parameters are discussed.

5.3.1 Reference Case

Figure 5.2 shows the variation of the vertical reaction force F_z at the upper surface of the ancillary as a function of time for the reference case.

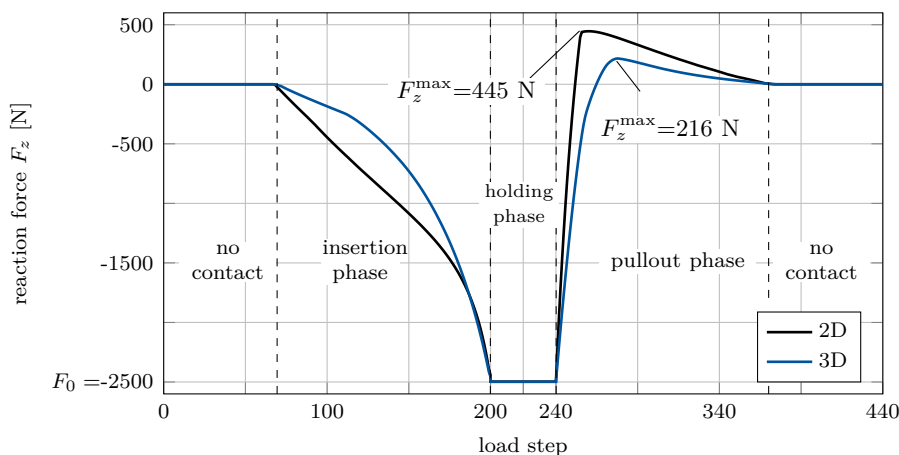


Figure 5.2 – Variation of the reaction force F_z applied to the ancillary as a function of load step ls for the 2D and 3D model for the reference case. Adopted from (Immel et al., 2021a; Raffa et al., 2019).

Three phases of the controlled displacement can be identified: 1) an insertion phase from $ls_0 = 0$ to $ls_1 = 200$. As soon as contact is established, the reaction force decreases as a function of the displacement until the predefined value $F_0 = -2500$ N is reached. During the insertion phase, the slope of F_z is first constant, which corresponds to constant stiffness of the bone-implant system. 2) a holding phase from $ls_1 = 201$ to $ls_2 = 240$, where the implant is held in

place. Here, the reaction force is constant with $F_z = F_0$. 3) a pull-out phase from $l_2 = 241$ to $l_3 = 440$, until the ACI is completely removed, and no contact remains. The reaction force increases up to a positive maximum F_{po} , and then decreases to 0.

5.3.2 Stress Distribution

Figure 5.3 shows the distribution of the von Mises stress σ_M in the hip cavity for the reference case and the optimal case for E_{tb}^* (E_{cb}^* , $IF = 0.8$ mm, $\mu = 0.6$, see Section 5.3.5) during the holding phase at $l_s = 220$ and at $F_z = F_z^{\max}$.

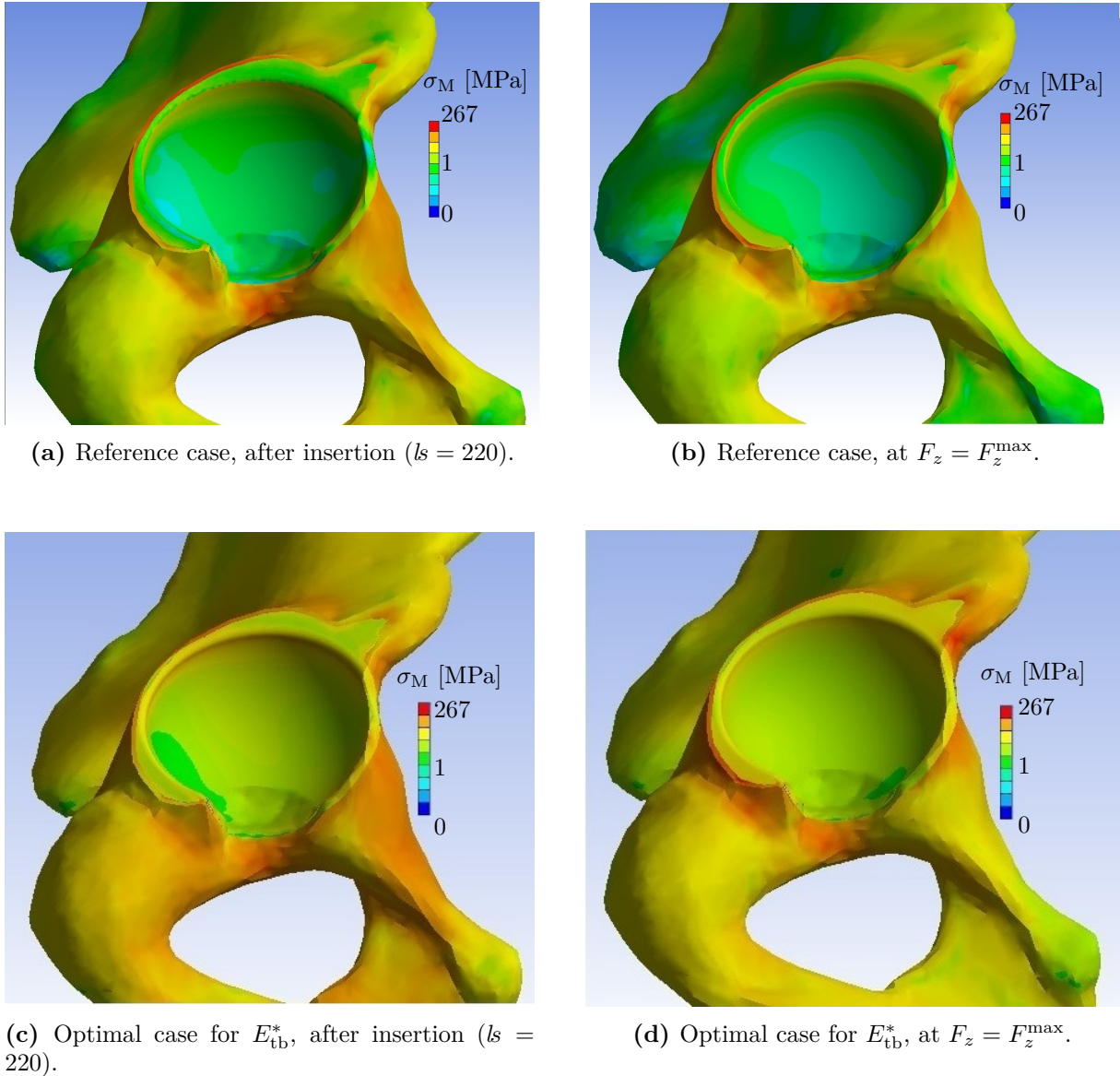


Figure 5.3 – Distribution of the von Mises stress σ_M in the hip cavity for the reference case and the optimal case for E_{tb}^* , after insertion ($l_s = 220$) and at $F_z = F_z^{\max}$. Adopted and extended from [Immel et al. \(2021a\)](#).

For the reference case, the maximal von Mises equivalent stress of 407 MPa is reached after full insertion and is localized in several elements of the cortical shell around the acetabulum. The von Mises equivalent stress inside the trabecular bone of the cavity is significantly lower

than in the cortical shell. Inside the contact area, the highest stresses are found in the equatorial rim with approximately 10 MPa. The stress distribution at the time where the maximal pull-out force is reached remains similar to the holding phase. However, the maximum stress only reaches 267 MPa during pull-out. For the optimal case for E_{tb}^* no sharp stress peaks and a more homogeneous stress distribution are observed. The maximum stress after insertion and at pullout are 226 MPa and 134 MPa, respectively. Similarly to the reference case, the highest stresses are located in the cortical shell around the cavity. Although the pullout force of 426 N is higher than in the reference case, the overall von Mises stress is considerably lower. However, a higher stress is observed in the cavity with up to 20 MPa at the equatorial rim. As expected, a higher pullout force corresponds to a higher stress in the cavity and thus a higher initial stability of the implant.

5.3.3 Effect of Variations of the Young's Modulus of Bone

Figure 5.4 shows the reaction force F_z as a function of the load step Δl_s for various bone Young's moduli E_{tb} and E_{cb} . For all values of E_{tb} and E_{cb} , F_z first decreases linearly at the beginning of the insertion phase, which corresponds to the macroscopic rigidity of the bone-implant system. For increasing E_{tb} , the duration of this linear phase and the pull-out force increase.

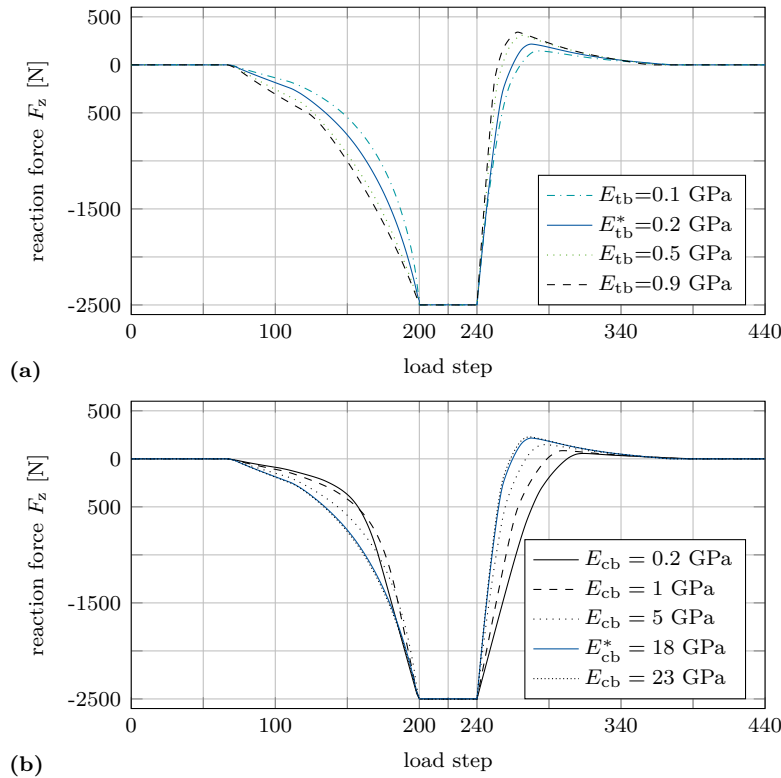


Figure 5.4 – Variation of the reaction force F_z applied to the ancillary as a function of the load step l_s for (a) different trabecular bone Young's modulus E_{tb} and (b) cortical bone Young's modulus E_{cb} . Results are shown for E_{tb}^* , E_{cb}^* , μ^* , IF^* , respectively.

Figure 5.5 shows the variation of the pull-out force F_z^{\max} (a) and the polar gap (b) as a function of the trabecular bone Young's modulus E_{tb} for the 2D and the 3D model. While the

results of the 2D model show a distinct peak of the pull-out force at $F_z^{\max} = 667$ N for $E_{\text{tb}} \approx 0.375$ GPa, the 3D hemi-pelvis model behaves differently since the pull-out force is an increasing function of E_{tb} . A similar behavior can be observed for the polar gap (b), which increases as a function of E_{tb} . Note that the variation of the polar gap was not investigated in the 2D case, so no comparison is possible with the 3D case.

A variation of the Young's modulus of cortical bone E_{cb} within the physiological range (15–23 GPa (Shirazi-Adl et al., 1993; Watson et al., 2017)) only has a negligible effect on the pull-out force (207–219 N). The pull-out force only decreases for extreme cases with very low cortical bone Young's modulus (< 10 GPa). Up to $E_{\text{cb}} = 8$ GPa, the polar gap increases only slightly and is less than several micrometers and may therefore be considered as negligible. In contrast to E_{tb} , all tested values of E_{cb} result in acceptable polar gaps (< 500 μm). Therefore, the influence of E_{cb} within its physiological range is deemed negligible here and only different values of E_{tb} will be considered in what follows.

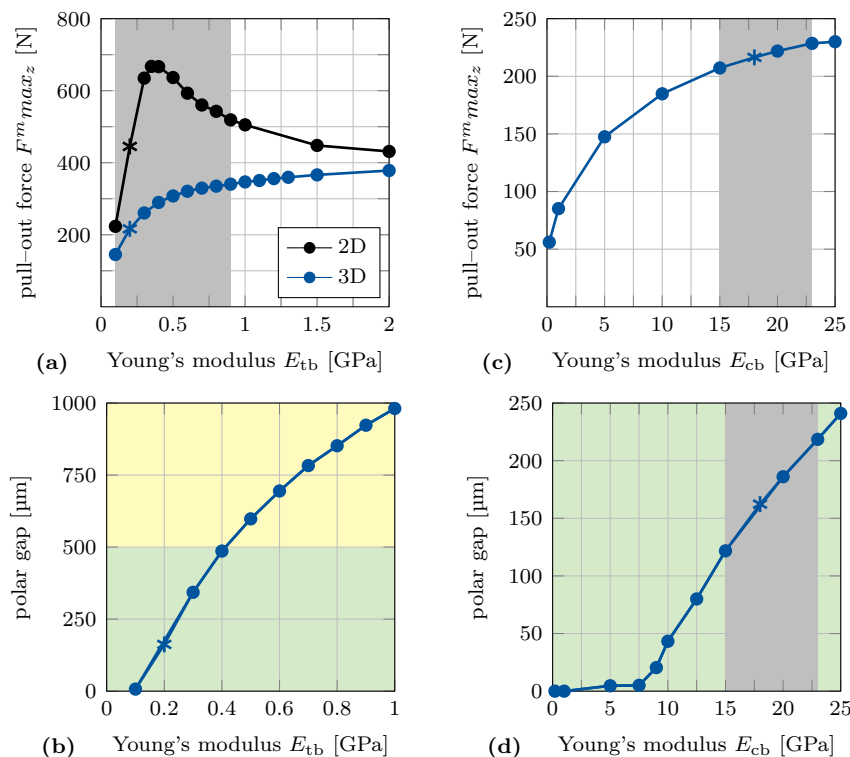


Figure 5.5 – Variation of the pull-out force F_z^{\max} (left) and the polar gap (right) as a function of the Young's modulus of trabecular bone E_{tb} (top) and cortical bone E_{cb} (bottom). Results are shown for E_{tb}^* , E_{cb}^* , μ^* , IF^* , respectively. The physiological range for E_{tb} and E_{cb} is indicated in gray. The polar gap is classified as optimal (< 500 μm , green), acceptable (< 1 mm, yellow), or critical (> 1 mm, red). The reference case is marked with a star. Adopted from Raffa et al. (2019); Immel et al. (2021a).

5.3.4 Effect of variations of the Friction Coefficient and the Interference Fit

Figure 5.6 shows the reaction force F_z as a function of the load step Δl_s for various values of the friction coefficient μ and the interference fit IF . A similar behavior of the reaction force as for the bone's Young's moduli can be observed. For all values of, F_z first decreases linearly at

the beginning of the insertion phase, which corresponds to the macroscopic rigidity of the bone-implant system. For increasing values of μ , the duration of this linear phase increases, while for increasing IF this linear response phase becomes shorter. In contrast to the previous 2D study (Raffa et al., 2019), the macroscopic rigidity for higher friction coefficients does not stay constant during the entire insertion phase. Increasing μ does not necessarily lead to an increase in pull-out force, as F_z^{\max} is visibly lower for $\mu = 1$ than for $\mu = 0.6$. Similar, increasing IF does not necessarily increase the pull-out force. Instead, a peak value is found between $IF = 1 - 1.5$ mm.

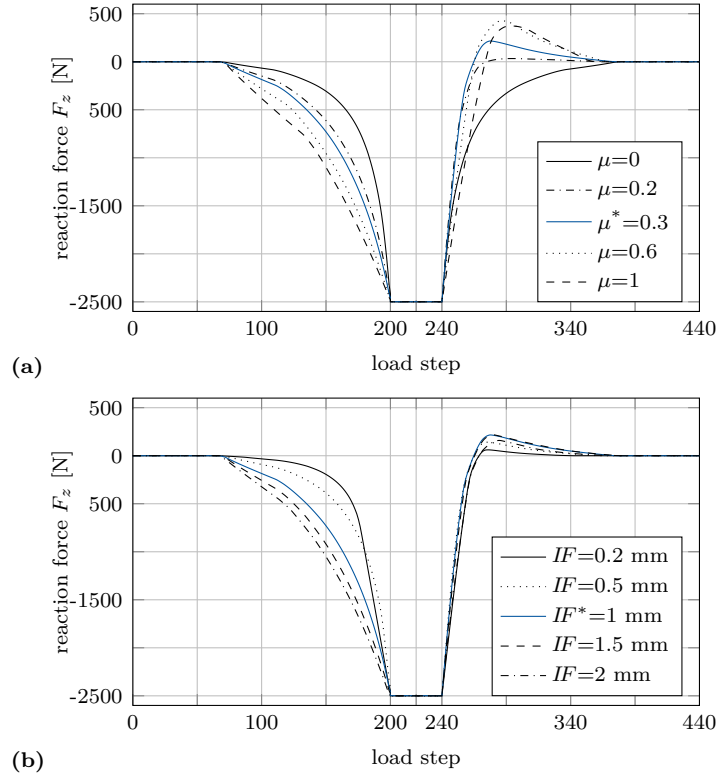


Figure 5.6 – Variation of the reaction force F_z applied to the ancillary as a function of the load step ls for (a) different friction coefficients μ and (b) interference fit IF . The results are shown for E_{cb}^* , E_{tb}^* , IF^* , μ^* , respectively.

Figure 5.7 shows the variation of the pull-out force F_z^{\max} (a),(c) and the polar gap (b),(d) as a function of the friction coefficient μ and interference fit IF for different values of E_{tb} . F_z^{\max} increases for low values of μ , reaches a maximum at around $\mu = 0.6$, and then slowly decreases for all models and chosen values of E_{tb} . The pull-out forces obtained with the present 3D model are approximately halved, compared to the results of the 2D study. For $\mu < 0.17$ the pull-out force is zero for all values of E_{tb} . F_z^{\max} increases as a function of the trabecular bone stiffness, while maintaining a similar behavior for various friction coefficients. The polar gap increases almost linearly as a function of the friction coefficient when a constant insertion force is considered, which can be explained by the fact that a high value of the friction coefficient inhibits the insertion process. Increasing the value of μ from 0.3 to 0.6 leads to an increase of the polar gap from 162 μm and 614 μm , which is above the maximum recommended gap of 500 μm (Schmalzried et al., 1992; Cochran et al., 1998). In the present case, all values of $\mu > 0.5$

lead to polar gaps higher than 500 μm and values of $\mu > 0.8$ lead to values of the polar gap exceeding the commonly reported limit of 1 mm (Jasty et al., 1988; MacKenzie et al., 1994). For $E_{\text{tb}} = 0.1$ GPa, polar gaps below 500 μm are achieved with $\mu < 0.9$, while for $E_{\text{tb}} = 0.5$ GPa only $\mu < 0.3$ results in sufficiently small polar gaps when an interference fit of $IF = 1$ mm is considered.

A non-linear behavior of F_z^{max} as a function of IF is obtained, similarly to the behavior of F_z^{max} as a function of μ . For both, the 2D axisymmetric model and the 3D geometry, F_z^{max} reaches a maximum value for an optimal interference fit of $IF = 1.2\text{--}1.4$ mm for E_{tb}^* . The pull-out force behaves similarly for different bone stiffness with a maximum value of 174 N for $E_{\text{tb}} = 0.1$ GPa and 361 N for $E_{\text{tb}} = 0.5$ GPa. Moreover, the polar gap increases as a function of the interference fit for all values of E_{tb} . A polar gap equal to 162 μm is obtained for the reference case and for $IF = 1.4$ mm, the polar gap is equal to 493 μm . In the reference case, $IF > 1.4$ mm lead to polar gaps values higher than 500 μm and $IF > 1.8$ mm lead to polar gaps higher than 1 mm. For $E_{\text{tb}} = 0.1$ GPa, acceptable gaps are achieved with $IF < 2$ mm, and for $E_{\text{tb}} = 0.5$ GPa with $IF < 1$ mm.

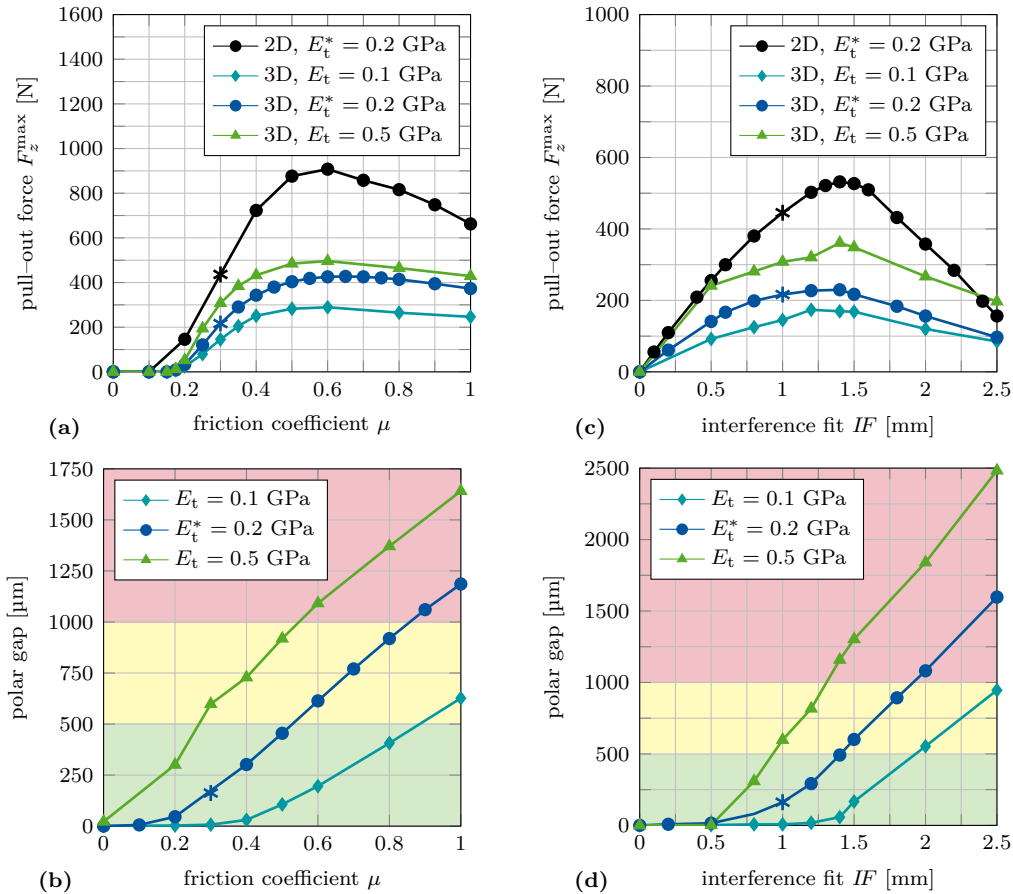


Figure 5.7 – Variation of the pull-out force F_z^{max} and the polar gap as a function of the friction coefficient μ (top) and the interference fit IF (bottom) for different trabecular Young's modulus E_{tb} . The results are shown for E_{cb}^* , IF^* , μ^* , respectively. The polar gap is classified as optimal (< 500 μm , green), acceptable (< 1 mm, yellow), or critical (> 1 mm, red). The reference case is marked with a star. Adopted from Raffa et al. (2019); Immel et al. (2021a).

5.3.5 Optimal Conditions

In what follows, the optimal combinations of μ and IF for primary stability of the ACI are discussed. Values or parameter sets that maximize the pull-out force while maintaining a polar gap lower than 500 μm for a given bone stiffness are denoted optimal. Figure 5.8 shows the variation of the pull-out force as a function of the interference fit IF and the friction coefficient μ for E_{tb}^* , E_{cb}^* for the 3D model. The optimal interference fit IF_{opt} for each value of μ is marked with a diamond. The variation of the maximum pull-out force F_z^{max} obtained for IF_{opt} as a function of μ is shown in Figure 5.9 and the variation of the optimal interference fit IF_{opt} as a function of μ is shown in Figure 5.10.

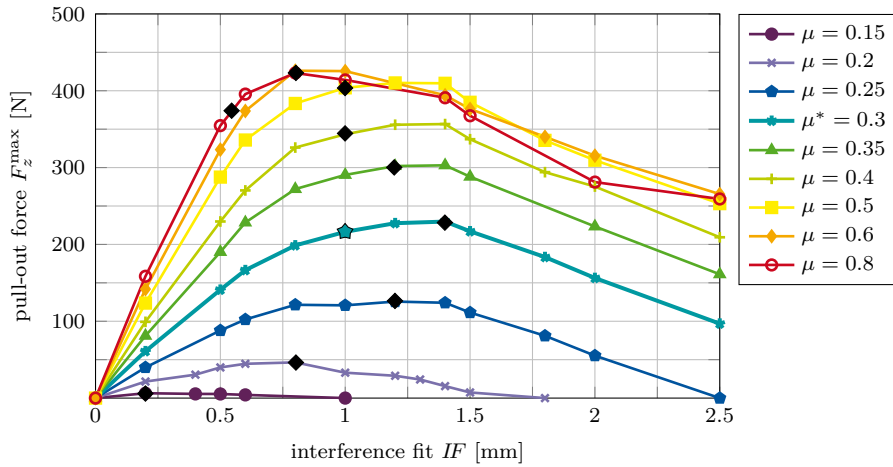


Figure 5.8 – Variation of the pull-out force F_z^{max} as a function of the interference fit IF and the friction coefficient μ . Results are shown for E_{cb}^* , E_{tb}^* . The optimal interference fit IF_{opt} for each constellation is marked with a diamond. The reference case is marked with a star. Adopted from [Immel et al. \(2021a\)](#).

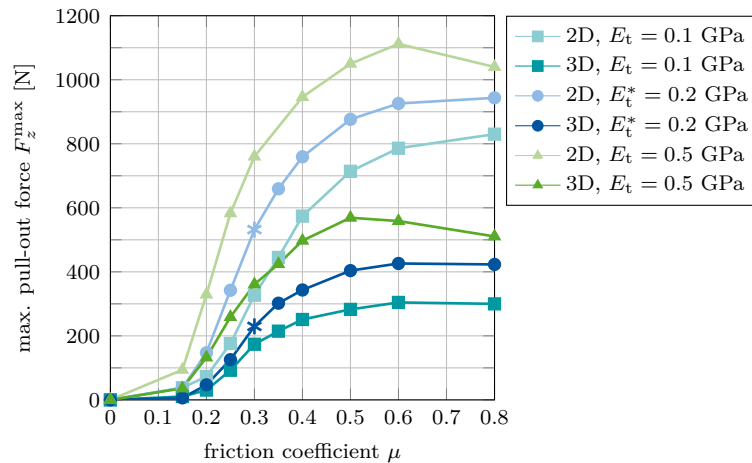


Figure 5.9 – Variation of the maximal pull-out force F_{max_z} obtained for the optimal interference fit IF_{opt} as a function of the friction coefficient μ w.r.t. trabecular bone Young's modulus E_{tb} for constant Young's modulus E_{cb}^* . Adopted and extended from ([Raffa et al., 2019](#); [Immel et al., 2021a](#)).

The lowest value is $IF_{\text{opt}} = 0.2$ for $\mu = 0.15$ and the highest is $IF_{\text{opt}} = 1.4$ mm for μ^* in the 3D model. The variation of the optimal interference fit IF_{opt} as a function of μ is qualitatively similar in the 2D and the 3D case. However, the maximum pull-out force obtained with the determined IF_{opt} for the 3D case are consistently lower than in the 2D case.

Figure 5.9 shows that increasing μ higher than 0.6 does not lead to a higher pull-out force, which is consistent with the results shown in Figure 5.7(a). Similar computations have also been done for $E_{\text{tb}} = 0.1$ and 0.5 GPa and the results show that an optimal case is also reached between $\mu_{\text{opt}} = 0.5 - 0.6$. Overall, the optimal parameter sets with respect to the three values of trabecular bone stiffness E_{tb} are shown in Table 5.2.

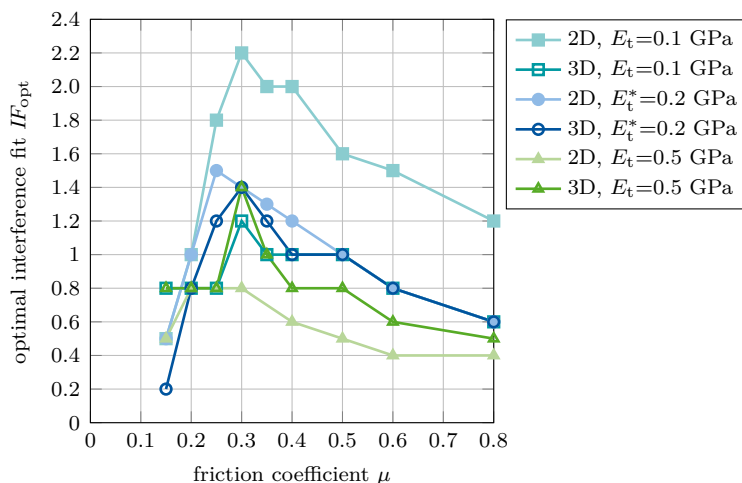


Figure 5.10 – Variation of the optimal interference fit IF_{opt} as a function of the friction coefficient μ w.r.t. trabecular bone Young’s modulus E_{tb} for constant Young’s modulus E_{cb}^* . Adopted and extended from (Raffa et al., 2019; Immel et al., 2021a).

E_{tb} [GPa]	IF_{opt} [mm]	μ_{opt}	F_z^{max} [N]	polar gap [μm]
0.1	0.8	0.6	304	190
0.2	0.8	0.6	426	304
0.5	0.8	0.5	569	475

Table 5.2 – Optimal values of the interference fit IF_{opt} and friction coefficient μ_{opt} with respect to trabecular bone stiffness E_{tb} with fixed cortical bone stiffness E_{cb}^* . Adopted from (Immel et al., 2021a).

5.4 Discussion and Limitations

This work aims to provide more insight into the biomechanical determinants of the primary stability of an ACI, which is estimated through the assessment of the pull-out force and the polar gap. The ACI primary stability is shown to depend on the elastic properties of the different bone tissues (E_{tb} and E_{cb}), on the friction coefficient μ , and on the interference fit IF . The influence of these four parameters on the ACI primary stability was investigated within their respective physiological range (see Table 5.1). For each parameter set, the insertion of an ACI into a hip is simulated using a realistic FE model. When considering variations within their

physiological ranges, E_{tb} is shown to have a stronger influence on the pull-out force and the polar gap than E_{cb} , which can be explained by the fact that no cortical bone is present in the cavity. The results show that a maximum value of the pull-out force is obtained for specific combinations of μ and IF (which depend on E_{tb}), while the polar gap increases as a function of all parameters. Based on these findings, optimal conditions for different bone stiffness can be determined and related to μ and to IF .

5.4.1 Pull-Out Force

The pull-out forces for E_{tb}^* are found to be comprised between 0 and 496 N in this study, which agrees with the results found in the literature (Spears et al., 1999; Le Cann et al., 2014; Raffa et al., 2019). The pull-out force increases along with the friction coefficient up to $\mu = 0.6$, which can be explained by an increase of the tangential contact stresses at the equatorial rim, and then decreases because higher values of the friction coefficient inhibit sufficient seating of the cup and thus removal becomes easier (Spears et al., 1999). From the point of view of implant manufacturers, the results shown in Figure 5.7(a) indicate that increasing the friction coefficient beyond 0.6 may weaken the ACI primary stability. However, rough surfaces may enhance osseointegration phenomena (Cochran et al., 1998) and thus long-term stability, which is another constraint that should be taken into account. It has been shown that the pull-out force cannot be taken as the sole determinant of implant stability, as a parameter set with a maximal pull-out force can lead to excessive values of the polar gap, which can inhibit bone ingrowth and thus long-term implant stability (Sandborn et al., 1988; Mukherjee and Gupta, 2014).

The pull-out forces predicted in the present study are significantly lower than the ones found in comparable 2D axisymmetric studies (Spears et al., 1999; Raffa et al., 2019). Moreover, while the results of the 2D model showed that the pull-out force reaches a maximum value of $F_z^{\max} = 667$ N for $E_{tb} \approx 0.375$ GPa, the behavior of the pull-out force predicted by the 3D hemi-pelvis model is different (see Figure 5.5(a)) since the pull-out force monotonically increases as a function of E_{tb} . Since in our study and in e.g., Spears et al. (1999) (Spears et al., 1999), a 1 mm thick cortical layer is present, the difference in the magnitude of the pull-out force obtained with the 2D models (Spears et al., 1999; Raffa et al., 2019) and with the present 3D model might be explained by the differences in the geometry of the acetabulum, the boundary conditions, and the corresponding structural stiffness. Both 2D studies (Spears et al., 1999; Raffa et al., 2019) used axisymmetric, simplified models of the pelvis with 1) a lower surface fixed in all directions and 2) a perfectly hemi-spherical cavity. In contrast, the present work considered a 3D hemi-pelvis model, which is fixed at the pubic symphysis and the iliac joint only. The cavity is not perfectly hemispherical since the acetabular wall is not present everywhere (see Figure 5.1(b)), similarly to what is obtained in the clinic. Moreover, the wall thickness of the cavity rim is much lower and non-uniform in the 3D model, implying lower wall stiffness, and hence lower contact pressures and pull-out forces, as shown in Figure 5.2. In particular, for the 3D model 1) the linear response during the insertion phase is considerably shorter, 2) the reaction force rises more slowly during the insertion and the pull-out phase, and 3) the pull-out force is much smaller than in the 2D model (Raffa et al., 2019). However, the present study shows that the 3D hemi-pelvis geometry does not influence the overall response of the pull-out force to different friction coefficients and interference fit when compared to a

2D axisymmetric setup (Raffa et al., 2019) (see Figure 5.7(a), (c)). Nonetheless, the real 3D geometry is shown to have a significant effect on the response of the pull-out force to trabecular bone stiffness (see Figure 5.5(a)). Therefore, when analyzing the implant stability in terms of the pull-out force and the polar gap, modeling a realistic pelvis geometry is necessary, which is consistent with previous studies (Kim et al., 1995).

5.4.2 Polar Gap

While bone ingrowth has been shown for polar gaps up to 5 mm (Mukherjee and Gupta, 2014), the potential osteocyte jumping distance is deemed to be no greater than 1 mm (Jasty et al., 1988; MacKenzie et al., 1994). Several studies agree that the initial polar gap should not exceed 500 μm , as higher gaps can promote the growth of weaker bone tissue (Sandborn et al., 1988; Mukherjee and Gupta, 2014) or inhibit bone growth completely, and thus jeopardize long-term stability (Jasty et al., 1988; Schmalzried et al., 1992). Polar gaps observed in the clinic are usually referred to being "lower than 500 μm and never higher than 1 mm" (Schmalzried et al., 1992; Udomkiat et al., 2002). In this study, high pull-out forces often coincide with large polar gaps ($> 500 \mu\text{m}$) and thus, a balance between maximizing the pull-out force and minimizing the polar gap should be targeted.

As shown in Figures 5.5(b), (d), and 5.7(b), (d), the polar gap increases as a function of E_{cb} , E_{tb} , μ , IF . While assuming the reference values for all other parameters, values of E_{tb} higher than 0.4 GPa lead to polar gaps above 500 μm . Therefore, and as shown in Figure 5.7, to balance out the pull-out force and the size of the polar gap, high friction coefficients and a large interference fit should be avoided for patients with stiffer bone. Since low interfacial friction may destabilize the implant (Janssen et al., 2010), a reduction of the interference fit might be favorable in such cases.

Polar gaps values are found to be between 0 and 2483 μm in this study, which is in agreement with the findings of other clinical (Schmalzried et al., 1992; Udomkiat et al., 2002; Mukherjee and Gupta, 2014), experimental (Kwong et al., 1994; MacKenzie et al., 1994) and FE studies (Yew et al., 2006; Amirouche et al., 2014; Rourke and Taylor, 2020). The polar gap is found to increase with larger interference fit (MacKenzie et al., 1994), as well as with bone stiffness and friction coefficient. In our study, the best compromise between a high pull-out force and a polar gap $\leq 500 \mu\text{m}$ for an interference fit of 1 mm is obtained for $\mu_{\text{opt}} = 0.5$ for E_{tb}^* and for $\mu_{\text{opt}} = 0.6$ for $E_{\text{tb}} = 0.1 \text{ GPa}$. For $E_{\text{tb}} = 0.5 \text{ GPa}$, only friction coefficients $\mu \leq 0.2$ lead to values of polar gaps below 500 μm but in this case, an insufficient pull-out force is obtained. Accepting a polar gap of up to 1 mm leads to $\mu = 0.5$ as the optimal choice. In general, polar gaps predicted in this study are significantly lower than in comparable 2D axisymmetric studies (Spears et al., 1999; Raffa et al., 2019), which may be explained by the fact that 2D configurations are much stiffer compared to the 3D case (see above). Optimal friction coefficients are found to be higher in our study, compared to e.g., Spears et al. (1999) (Spears et al., 1999) ($\mu = 0.2 - 0.3$), while Raffa et al. (2019) Raffa et al. (2019) found an optimum for $\mu = 0.6$, as only the pull-out force was considered as a determinant of primary stability.

5.4.3 Contact Stresses

The maximal value of the contact stresses on the cavity surface is found to be localized at the equatorial rim, which is in good agreement with previous works by several authors (Spears et al.,

1999; Janssen et al., 2010; Hothi et al., 2011; Amirouche et al., 2014; Le Cann et al., 2014) who established that the contact between the ACI and the surrounding bone tissue mostly occurs around the equatorial rim. As shown in Figure 5.3, the maximum value of the contact pressure for the reference configuration is found to be around 10 MPa, which is in good agreement with similar studies (Widmer et al., 2002; Raffa et al., 2019). The maximal contact stress observed in the optimal case for E_{tb} is twice as high as in the reference case, which corresponds to the increased pull-out force observed for the optimal case. However, excessive stresses can lead to bone damage during the implantation or to bone resorption later and thus should be monitored carefully.

5.4.4 Optimal Conditions for Primary Stability

Several studies suggest that the interference fit is one of the most important factors in order to achieve adequate fixation (Curtis et al., 1992; Macdonald et al., 1999; Spears et al., 1999) and that increased under-reaming can compensate low bone stiffness (Janssen et al., 2010; Rourke and Taylor, 2020). As low interfacial friction may destabilize the implant (Janssen et al., 2010) and thus has to be avoided, an adequate interference fit according to the bone quality must be chosen instead.

While it was shown that higher interference fit values are required for softer bone ($E_{tb} = 0.1$ GPa) to achieve similar pull-out forces as in the reference case E_{tb}^* , common interference fit values (between 1 and 2 mm) lead to excessive gaps for stiffer bone ($E_{tb} = 0.5$ GPa) and thus should be avoided. However, our findings suggest that the interference fit should not be increased to more than around 1.3 mm, because it leads to a concomitant decrease of the pull-out force and increase of the polar gap. For both, the 2D axisymmetric and 3D cases, an optimal interference fit of $IF = 1.4$ mm for E_{tb}^* and μ^* is found, when only considering maximizing the pull-out force, which is in agreement with other studies (Kwong et al., 1994; Macdonald et al., 1999).

Previous studies confirm our findings concerning the existence of an optimal primary stability condition linking press-fitting and friction (Kwong et al., 1994; Spears et al., 1999; Le Cann et al., 2014; Raffa et al., 2019). In our study an interference fit of around 1.3 mm is found to be optimal in terms of maximal pull-out force for friction coefficients ranging between $\mu = 0.25$ – 0.5 and E_{tb}^* , while a mean interference fit of 1.1 mm is found optimal when considering a polar gap less than 500 μm as well, similar to comparable studies (Kwong et al., 1994; Spears et al., 1999; Le Cann et al., 2014; Raffa et al., 2019). However, there are also studies that suggest a larger interference fit of $IF = 2 - 3$ mm (Le Cann et al., 2014).

The optimal values of IF and μ in terms of maximal pull-out force and minimal polar gap for the different values of trabecular bone stiffness are listed in Table 5.2. As the optimal friction coefficient is higher than in the reference case, while the interference fit is lower, the determined optimal cases suggest that a higher friction coefficient (up to $\mu = 0.6$) enhances primary stability more than an increased interference fit. While being optimal in terms of the polar gap and the pull-out force, the determined optimal cases exhibit a higher stress in the equatorial rim of the cavity compared to the reference configuration. Excessive stresses in the cavity can become critical because they can cause bone damage during the insertion and bone resorption during the healing phase (Sotto-Maior et al., 2010). Therefore, future analyses of optimal primary stability should also include and classify the hoop stress in the cavity.

5.4.5 Limitations

This study has several limitations. First, only a single pelvis geometry of unknown sex and age was considered. Moreover, in the context of hip replacements, pathological degeneration of the bone structure and damage often need to be considered. Due to the numerous parameters considered and to the considerable computation time, different patient geometries and implantation angles could not be taken into account here and the impact of changes of the anatomy should be considered in future work, since bone geometry and stiffness have an effect on implant stability (Clarke et al., 2013). Several recent studies analyzed the influence of different patient geometries and bone stiffness (Phillips et al., 2007; Clarke et al., 2013), as well as the influence of different implantation angles (Janssen et al., 2010; Goldman et al., 2016). Second, all materials were assumed to be homogeneous and isotropic as is mostly done in the literature (Cilingir et al., 2007; Janssen et al., 2010; Clarke et al., 2013). This assumption allows to assess the influence of a small number of parameters in a controlled manner.

Furthermore, the observed stress in the contact area was below the yield stress of human bone (Bayraktar et al., 2004; Morgan et al., 2018). Therefore, it may be assumed that no bone damage took place for the simulated insertion and pull-out tests, allowing to consider a hypoelastic material model as a valid simplification. While trabecular bone damage may occur during the insertion process, an experimental study showed that bone damage has no impact on the pull-out force (Bishop et al., 2014). As our study focuses on initial stability in terms of the pull-out force, bone damage was neglected as well.

Several studies consider the inhomogeneous (Clarke et al., 2013; Rourke and Taylor, 2020), an-isotropic (Nguyen et al., 2017), and plastic (Souffrant et al., 2012) nature of bone tissues, by using data obtained from CT scans or experiments with sawbones. Other studies have also considered elasto-plastic effects (Janssen et al., 2010; Le Cann et al., 2014; Ovesy et al., 2020), debonding (Immel et al., 2020, 2021b,c), and damage of the interface (Rittel et al., 2018; Ovesy et al., 2020). While some studies point out the need to explicitly model the nonuniform thickness of the cortical layer (Hsu et al., 2006; Clarke et al., 2013), realistic results have also been achieved with a uniform cortical thickness around 0.9–1.5 mm (Anderson et al., 2005; Phillips et al., 2007; Watson et al., 2017). Due to the simulated reaming in our study, there is no cortical bone remaining in the contact area for any interference fit value (see Figure 5.1(b)) so the ACI only comes into contact with trabecular bone. As shown in Figure 5.5, the influence of the cortical bone stiffness on the pull-out force and on the polar gap in our model is relatively small compared to other studied parameters. Thus, we assumed that the effect of the cortical bone thickness was negligible compared to the effect of other parameter, which is in agreement with the literature (Anderson et al., 2005; Phillips et al., 2007; Watson et al., 2017). However, when considering the stress and deformation distributions over the whole pelvis, the cortical bone thickness must be taken into account.

Third, as this study focuses on primary stability during surgery, only a pull-out test and no cyclic loading (e.g., walking) was simulated. Thus, the influence of muscle tissue and ligaments on the deformation behavior and load response was neglected, which is in agreement with what is done in the literature (Hao et al., 2011; Clarke et al., 2013). However, it has been shown that muscles and ligaments have to be taken into account when analyzing the stress distribution inside the acetabulum (Shirazi-Adl et al., 1993). To draw comparisons to a previous study (Raffa et al., 2019), a normal pull-out test was chosen, although lever-out tests have also been used in

the literature (Macdonald et al., 1999).

Fourth, a quasi-static configuration was considered, and all dynamic aspects were neglected, similarly to what was done in some comparable works (Spears et al., 1999; Le Cann et al., 2014; Raffa et al., 2019). Note that a previous study precisely focuses on the insertion process of an ACI by considering dynamic modeling (Michel et al., 2017), which is important when modeling the insertion by hammer impacts. However, using dynamic modeling would not modify the pull-out test performed in this study.

Fifth, only the pull-out force and the polar gap have been chosen as determinants of the ACI primary stability and the detailed stress distribution at the BII for each parameter set was not studied specifically. The stress distribution especially at the equatorial rim of the cavity should be analyzed and classified as well, as is done in other works (Janssen et al., 2010; Rourke and Taylor, 2020). Micromotion at the BII, as well as contact area are other determinants of initial stability used in the literature (Janssen et al., 2010; Rourke and Taylor, 2020). Furthermore, the polar gap was obtained at a given insertion force, which is the same for all cases considered in this work. However, when the insertion force is removed once the implant is inserted, the polar gap can increase due to relaxation (Michel et al., 2017). Although this situation is clinically relevant, it is out of the scope of this work but will be considered in future studies. In addition, a mathematical relationship for the trends of the relationship between bone stiffness, interference fit, and friction coefficient (shown in Figures 5.7(a) and (c), and 5.9) should be established. Including the aforementioned factors in future works could provide a more complete picture on implant primary stability and facilitate the choice of an implant configuration for a specific patient and provide a basis for modeling osseointegration.

Eventually, the proposed model should be validated experimentally as is partially done in the 2D case (Raffa et al., 2019). However, drawing comparisons to e.g., clinical studies is difficult, due to all the assumptions described above. Moreover, it remains difficult to measure the actual friction coefficient of the BII (Gao et al., 2019), as well as the elastic bone modulus (bone being heterogeneous, viscoelastic, and anisotropic) experimentally. Furthermore, as the hip cavity is reamed by hand, it is difficult to achieve a perfectly hemispherical cavity and it has been shown that the actual interference fit differs from what is determined by the implant and the last reamer size used (Kim et al., 1995; Macdonald et al., 1999).

5.4.6 Conclusion

All studied parameters E_{tb} , E_{cb} , IF , and μ significantly influence the ACI primary stability. Quadratic regression analyses were used for the dependence of the pull-out force on the different parameters and linear regression analyses were performed to analyze the dependence of the polar gap on the same parameters. All p-values were $p < 0.01$ (where p is the probability that the null hypothesis is true). An optimal combination of μ and IF was determined. For $E_{tb} = 0.1$ GPa, the optimal configuration corresponds to $IF = 0.8$ mm and $\mu = 0.6$, while for $E_{tb} = 0.2$ GPa, it corresponds to $IF = 0.8$ mm and $\mu = 0.6$ and for $E_{tb} = 0.5$ GPa, it is $IF = 0.8$ mm and $\mu = 0.5$. The strong correlation between the aforementioned parameters may therefore require particular attention of implant manufacturers and of surgeons in order to maximize the ACI primary stability. The numerical results are found to be consistent with previous experimental and numerical studies and can help surgeons select the optimal interference fit in a patient-specific manner, based on the patient's bone quality and the chosen implant. The results also

show that increasing IF above 1.4 mm and μ above 0.6 has no benefit on ACI primary stability, which can aid in ACI implant conception and selection of appropriate surface treatments. In addition, this study provides detailed knowledge of the local contact state and the influence of implant- and patient-specific parameters and hence, is an important step towards modeling and understanding osseointegration. The results presented in this work can be used as a basis for modeling long-term stability, e.g., for stress-, strain- or micro-motion-dependent osseointegration models and the subsequent debonding of osseointegrated implants (Rittel et al., 2018; Immel et al., 2020, 2021b), as is done in the following chapters. This model can also be applied to hip geometries with osseous defects to provide suggestions for ensuring primary stability for these challenging and clinically relevant cases. However, the proposed *in silico* model needs to be improved to better match the clinical conditions, e.g., by simulating lever-out tests or including different hip geometries and inhomogeneous bone stiffness. As the problem is characterized by multi-parameter optimization, a rigorous determination of optimal parameter combinations requires corresponding optimization algorithms, which should be considered in future works.

Chapter 6

Tangential Debonding of Partially Osseointegrated Implants

In the previous chapter, the determinants of primary stability of a cementless ACI were identified and discussed. Based on these findings, different models for the secondary stability of osseointegrated implants are introduced in the following chapters. This chapter presents a phenomenological model for the frictional contact behavior of tangentially debonding, osseointegrated implants, to model and assess long-term implant stability. The classical Coulomb's law is extended from a constant to a varying friction coefficient, that models the transition from an unbroken to a broken state, based on a state variable depending on the total sliding distance of the BII. While the unbroken state denotes osseointegration and thus the presence of adhesive bonds and a higher friction coefficient, the broken state denotes pure frictional contact behavior of the interface with a lower friction coefficient. Thus, this model can account for the higher tangential forces observed in osseointegrated implants compared to unbonded implants.

The content of this chapter has been published in restructured form in [Immel et al. \(2019, 2020\)](#).

6.1 Motivation

Most studies on bone attachment to implants have used push-in or pull-out *in vitro* tests ([Bishop et al., 2014](#); [Wennerberg et al., 2014](#); [Berahmani et al., 2015](#); [Damm et al., 2015](#)). As the implant geometry influences the test results ([Brånemark et al., 1998](#)) and leads to spatially complex, non-uniform, multiaxial stress fields ([Shirazi-Adl, 1992](#)) and instantaneous, unstable crack propagation, using realistic implant geometries makes it difficult to estimate a physically meaningful value for the interfacial mechanical strength. Therefore, models with a planar BII were designed to minimize the effects of friction and mechanical forces introduced by the geometry ([Skripitz and Aspenberg, 1999](#); [Rønold and Ellingsen, 2002](#); [Rønold et al., 2003](#)). However, the measured pull-out force in these experiments cannot be used to retrieve information about the strength of the interface. More recently, mode III cleavage experiments applied to CSI have been proposed by [Mathieu et al. \(2012a\)](#). A rotation of the implant with respect to the bone was imposed and the resulting moment was recorded. This resulted in stable crack propagation, which allows to assess the adhesion energy. However, the agreement between the analytical and experimental results was only moderate and significant discrepancies were obtained.

The tangential load-displacement behavior at the BII was found to be nonlinear (Rancourt et al., 1990; Shirazi-Adl et al., 1993; Dammak et al., 1997b). However, numerical analyses of implant stability still only consider either fully bonded, frictionless contact or pure Coulomb's friction (Pettersen et al., 2009; Chong et al., 2010; Ghosh and Gupta, 2014). While such assumptions may be valid for the assessment of initial stability, prediction of failure of osseointegrated implants requires a more accurate description of the contact behavior and the inclusion of frictional and adhesive effects (Castellani et al., 2011; Tschegg et al., 2011).

A simple way to model macroscopic friction phenomena that are related to different states of the BII are *state variable friction laws*, introduced by Rice and Ruina (1983); Ruina (1983), which were motivated by the experimental findings of Dieterich (1978, 1979a). These laws focus on the observed phenomena of (i) fading memory and steady state, (ii) positive dependence on the instantaneous slip rate, and (iii) negative dependence on past slip rates. In general, it is assumed that at any given time, the contact surface has a certain state and the frictional stress only depends on that state, the slip rate and the contact pressure. Similarly, the rate of change for the state only depends on the current state, the slip rate, and the pressure at the analyzed point. Although these laws have so far been mainly applied in geology and geophysics, one can also interpret the state variable as the degree of osseointegration and current debonding state of the BII.

6.2 State Variable Friction Laws

In so called *rate-state* or *state variable* friction laws (Rice and Ruina, 1983; Ruina, 1983) it is assumed, that at any given time, any point \boldsymbol{x} on the contact surface has a state $\phi = \phi(\boldsymbol{x}, t)$. The tangential contact traction then depends in general on the contact pressure p_c , the sliding rate $\dot{g}_s = \|\dot{\boldsymbol{g}}_s\|$, and the state variable ϕ , i.e.,

$$\boldsymbol{t}_t = \boldsymbol{t}_t(p_c, \dot{g}_s, \phi). \quad (6.1)$$

For a given \boldsymbol{x} , the state ϕ is assumed to be a continuous function of $\dot{g}_s(t)$. Moreover, the rate of change of ϕ at \boldsymbol{x} generally only depends on the pressure, the sliding rate and the instantaneous state of this point, i.e.,

$$\dot{\phi} = F(p_c, \dot{g}_s, \phi). \quad (6.2)$$

Since ϕ does not depend on the state at other points, Eq. (6.2) is a local evolution law. State variable friction laws are able to model a change in the frictional contact traction due to past states (referred to as *memory* (Rice and Ruina, 1983; Ruina, 1983)). They are also able to model an asymptotic approach to steady state sliding when \dot{g}_s becomes constant (Rice and Ruina, 1983).

6.3 Modified Coulomb's Friction Law

In contrast to a constant friction coefficient as is used in the classical Coulomb's law (3.38), we propose to model μ as a function of the scalar state variable ϕ , as

$$\mu := \mu(\phi) = \phi \mu_{ub} + (1 - \phi) \mu_b, \quad (6.3)$$

where μ_{ub} and μ_{b} are the friction coefficient for the unbroken (initial) and broken state, respectively, that are weighted according to the state variable ϕ . As this is a local friction model, where ϕ and thus μ can change pointwise, it allows for the description of locally varying bonding states, such as occur in crack propagation and partial osseointegration.

According to Eq. (6.3), the state variable ϕ determines whether a point is in an unbroken, partially broken or fully broken state. Here, ϕ is considered to depend on the accumulated sliding distance

$$g_s = \int_0^t \dot{g}_s dt \quad (6.4)$$

at a certain point \mathbf{x} , according to the smooth function

$$\phi(g_s) = \phi_0 \cdot \begin{cases} 1 & \text{if } \frac{g_s}{a_s} < 1, \\ \frac{1}{2} - \frac{1}{2} \sin\left(\frac{\pi}{2b_s} \left(\frac{g_s}{a_s} - b_s - 1\right)\right) & \text{if } 1 \leq \frac{g_s}{a_s} \leq 1 + 2b_s, \\ 0 & \text{if } \frac{g_s}{a_s} > 1 + 2b_s. \end{cases} \quad (6.5)$$

The parameter a_s represents the sliding threshold up to which tangential adhesion takes effect ($\mu = \mu_{\text{b}}$ for $g_s \leq a_s$), while b_s defines the size of the transition zone between the two friction coefficients. This implies, that up to a sliding length of $g_s = a_s$ we have a higher resistance to tangential displacement, similar to the effect of adhesion. After the sliding distance a_s is reached, the friction coefficient starts to decrease to $\mu = \mu_{\text{b}}$, corresponding to the sliding of a fully debonded body. The sliding distance needed for a certain point on the contact surface to fully debond is then controlled by the parameter b_s .

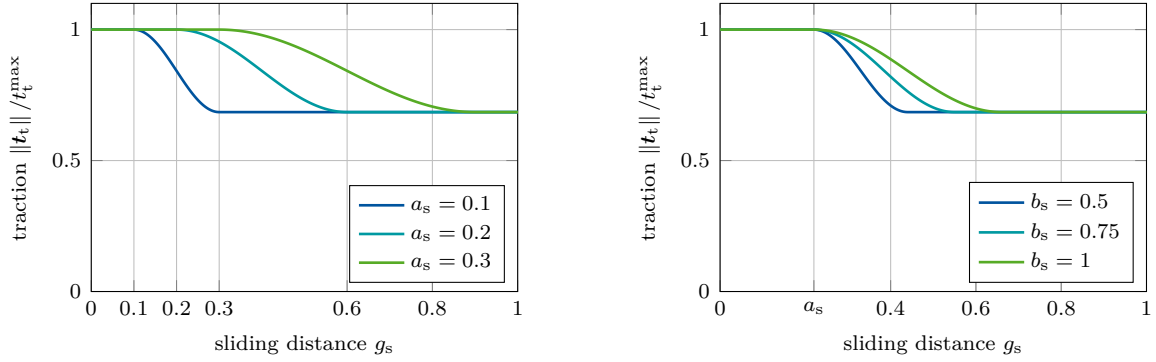
Eq. (6.5) was designed such that it captures the experimental behavior shown in Section 6.4.5.2 (see Figure 6.5). Equation (6.5) depends on the initial bonding state $\phi_0 = [0, 1]$, where $\phi_0(\mathbf{x}) = 0$ denotes no initial bonding and $\phi_0(\mathbf{x}) = 1$ represents full initial bonding.¹ The bonding state variable indicates that for $\phi(\mathbf{x}) > 0$ tangential contact at \mathbf{x} is governed by the proposed friction law (6.3), while for $\phi(\mathbf{x}) = 0$ it is governed by classical Coulomb's law (3.38) with $\mu = \mu_{\text{b}}$. This definition results in three possible states for every point on the contact surface: fully bonded ($\phi = 1$), debonding ($0 < \phi < 1$) and fully debonded/sliding ($\phi = 0$), which is illustrated in Figures 6.1(a) and 6.1(b).

The computation of the friction coefficient μ in Eq. (6.3) requires the knowledge of the accumulated sliding distance g_s . Here, we approximate Eq. (6.4) by accumulating the distance from the initial interacting point to the current interacting point, i.e.,

$$g_s^{n+1} \approx \sum_{i=1}^{n+1} \left\| \mathbf{x}_\ell(\hat{\boldsymbol{\xi}}^i) - \mathbf{x}_\ell(\hat{\boldsymbol{\xi}}^{i-1}) \right\|. \quad (6.6)$$

For simple cases, this model can be solved analytically, as presented in Section 6.4.3. However, for the complex geometries of endosseous implants, the nonlinear and anisotropic behavior of bone tissue and loading conditions inside the human body may require a numerical solution. This becomes particularly important when considering inhomogeneous initial bonding (where $\phi_0(\mathbf{x}) \neq \text{const} \forall \mathbf{x}$), due to imperfect or partial osseointegration, as presented in Section 6.4.5.4.

1. In principle Eq. (6.5) can be brought into the form of Eq. (6.2) if a dot is applied to Eq. (6.5) and then g_s is eliminated by the inverse function of (6.5). ϕ_0 follows from an evolution law that describes the healing/osseointegration process (ϕ_0 increasing from 0 to 1). However, this is not considered here. Here, only the (further) evolution of ϕ during debonding (ϕ decreasing from 1 to 0) is studied.



(a) Variation of the sliding threshold a_s for $b_s = 1$. (b) Variation of the transition factor b_s for $a_s = 0.22$.

Figure 6.1 – Modified Coulomb’s law: Tangential contact traction $\|\mathbf{t}_t\|/t_t^{\max}$ as a function of the sliding distance g_s for varying sliding threshold a_s and transition factor b_s for $\phi_0 = 1$. Adopted from [Immel et al. \(2020\)](#).

6.4 Application to Coin-Shaped Implants

To calibrate the friction model described above, it is applied to the mode III debonding of an osseointegrated implant. The test case is originally presented by [Mathieu et al. \(2012a\)](#) (in the following also referred to as the reference study).

6.4.1 Experimental Setup

In [Mathieu et al. \(2012a\)](#), two CSI made of titanium alloy (Ti-6Al-4V), with a radius $R_I = 2.5$ mm and a height $H_I = 3$ mm, were implanted into the tibiae of a rabbit and left *in vivo* during seven weeks. Polytetrafluoroethylene (PTFE) caps were placed around the implants, to ensure that bone in-growth only occurred at the bottom of the cylindrical implants. After seven weeks, the rabbit was sacrificed and the bone samples including the implants were extracted and conserved. Then, mode III cleavage experiments were carried out. The bone specimen was rigidly fixed to minimize the remaining normal force. The implant was fixed by a chuck screwed to a torque meter. Then, a 10° rotation with a constant rotation speed of $0.01^\circ \text{ s}^{-1}$ was imposed. Finally, the torque and rotation angle as a function of time were extracted via post processing.

6.4.2 Analytical Model of [Mathieu et al. \(2012a\)](#)

To explain the experimental results, [Mathieu et al. \(2012a\)](#) developed an analytical model that couples crack propagation with friction, based on [Chateauinois et al. \(2010\)](#). The model assumes that the crack starts from the outside and propagates purely in a circular manner and in mode III to the center of the contact surface, using a Dugdale crack model, without any normal force. In this description, the interfacial forces are supposed to be constant up to a given separation distance between the surfaces.

Let R be the radius of the implant and the initial contact area, then c defines the radius of the current crack (see [Figure 6.2\(a\)](#)), corresponding to the twisting angle

$$\theta = \sqrt{\frac{\pi E_{\text{adh}}}{4cG}} + \frac{\tau_0}{2G} \cosh^{-1} \left(\frac{R}{c} \right), \quad (6.7)$$

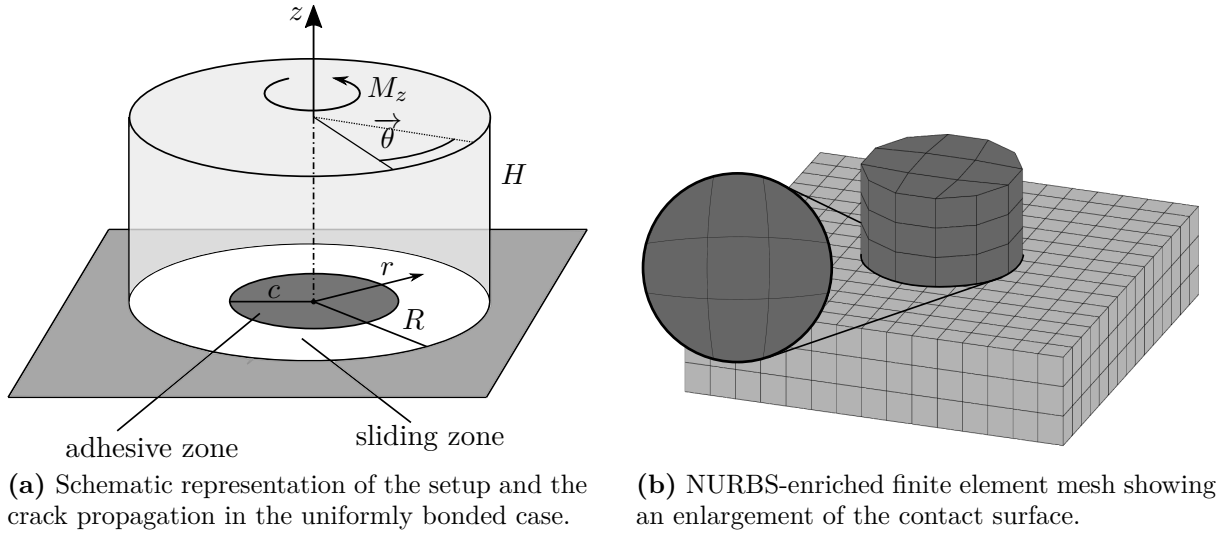


Figure 6.2 – Illustrations for the analytical and numerical setup. Adopted from [Immel et al. \(2020\)](#).

where E_{adh} denotes the adhesion energy. c separates the contact area into an adhering/sticking region for $r < c$ and a debonded/sliding region for $c < r < R$. In the sliding region, the orthoradial shear stress $\sigma_{\theta z}$ is assumed to be constant, according to

$$\sigma_{\theta z}(r) = \tau_0 \quad \text{for } c < r < R, \quad (6.8)$$

with constant $\tau_0 = 3M_z^\infty / 2\pi R^3$, where M_z^∞ corresponds to the torque for a rotation angle equal to infinity (i.e., where the surface is fully debonded), and z denotes the axial direction. In the sticking region, the orthoradial stress becomes

$$\sigma_{\theta z}(r) = \frac{2}{\pi} \left[\sqrt{\frac{\pi G E_{\text{adh}}}{c}} \frac{r}{\sqrt{c^2 - r^2}} + \tau_0 \sin^{-1} \left(\sqrt{\frac{\left(\frac{R}{c}\right)^2 - 1}{\left(\frac{R}{r}\right)^2 - 1}} \right) \right] \quad \text{for } r < c. \quad (6.9)$$

6.4.3 New Analytical Model

Given the modified Coulomb's law (6.3), a new analytical model can be derived. Due to symmetry, the tangential traction component $\sigma_{\theta z}$ is distributed radially symmetric along the BII, while the radial traction component σ_{zr} is zero (as in the model presented in Section 6.4.2).

In general, the torque M_z , as a function of the rotation angle θ , can be computed analytically, as

$$M_z(\theta) = 2\pi \int_r r^2 \cdot \sigma_{\theta z}(r, \theta, g_s) dr. \quad (6.10)$$

We assume both bodies to be linear elastic (see Section 3.2.1) and the normal contact pressure \bar{p}_c to be distributed homogeneously along the contact surface. We define the hyperbola

$$c(\theta) := \frac{\theta_{\text{lin}}}{\theta} R \quad (6.11)$$

to be the function of the critical radius for the stick/slip transition, such that $r < c$ denotes the sticking region and $c \geq r \geq R$ denotes the sliding region. Furthermore, we define θ_{lin} as the

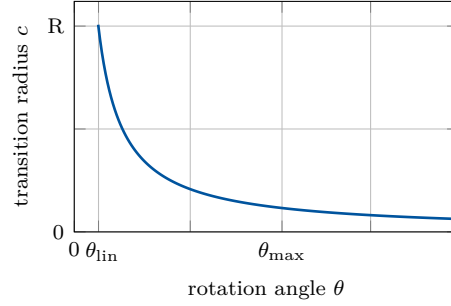


Figure 6.3 – New analytical model: Critical radius for stick/slip transition c as a function of the imposed rotation angle θ from Eq. (6.11). Adopted from [Immel et al. \(2020\)](#).

limit for which the tangential traction will be a linear function of the implant radius and θ_{\max} is the rotation angle for which the whole contact surface starts sliding (see Figure 6.3). It also marks the location of the maximal torque M_z^{\max} in the torque-angle-curve (see e.g. Figure 6.5). With the definition of the critical radius c from Eq. (6.11) we have $c(\theta_{\text{lin}}) = R$ and

$$\sigma_{\theta z}(\theta_{\text{lin}}, c(\theta_{\text{lin}})) := t_t^{\max}. \quad (6.12)$$

Assuming bone and implant to be linear elastic bodies, we know that for sticking, the tangential traction will be proportional to the applied rotation angle θ and the current radius r , i.e.,

$$\sigma_{\theta z}^{\text{stick}}(\theta, r) = \lambda \theta r, \quad \lambda = \text{const}, \quad (6.13)$$

where λ is a constant stress per length. Thus, the torque for the sticking region becomes

$$M_z(\theta) = 2\pi \int_0^R r^2 \cdot \lambda \theta r \, dr = \frac{1}{2} \pi R^4 \lambda \theta, \quad \text{for } \theta \leq \theta_{\text{lin}}. \quad (6.14)$$

If we calculate the slope of the torque at $\theta = \theta_{\text{lin}}$ and $c(\theta_{\text{lin}})$, we get

$$\frac{dM_z(\theta_{\text{lin}}, R)}{d\theta_{\text{lin}}} = \frac{1}{2} \pi R^4 \lambda. \quad (6.15)$$

We also know that for linear elasticity

$$\frac{dM_z(\theta)}{d\theta} = C, \quad \theta \leq \theta_{\text{lin}}, \quad (6.16)$$

where C is the effective shear stiffness of the system, that is approximately proportional to the shear modulus of bone. If we equate Eqs. (6.15) and (6.16), we obtain

$$\lambda = \frac{2C}{\pi R^4}, \quad (6.17)$$

and inserting λ into Eq. (6.13) yields

$$\sigma_{\theta z}^{\text{stick}}(\theta, r) = \frac{2C}{\pi R^4} \theta r. \quad (6.18)$$

Applying the definition in Eq. (6.12) to Eq. (6.18) yields

$$\sigma_{\theta z}^{\text{stick}}(\theta_{\text{lin}}, R) = \frac{2C}{\pi R^4} \theta_{\text{lin}} R = t_t^{\max} \rightarrow \frac{2C}{\pi R^3} = \frac{t_t^{\max}}{\theta_{\text{lin}}}. \quad (6.19)$$

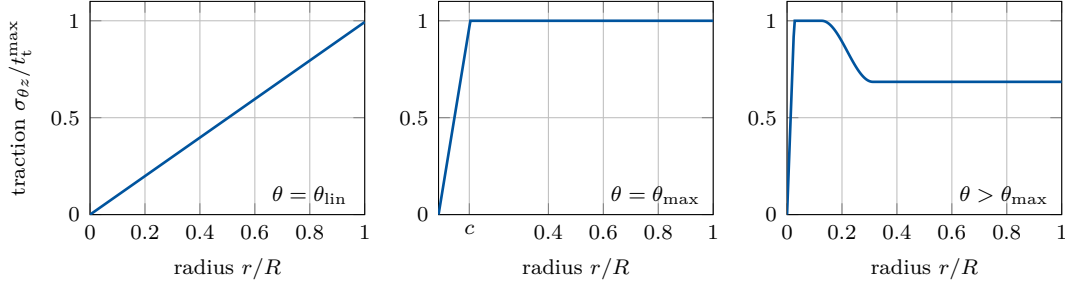


Figure 6.4 – New analytical model: normalized tangential traction $\sigma_{\theta z}/t_t^{\max}$ as a function of the radius r/R of the contact surface (see Eq. (6.23)) at different rotation angles. Adopted from [Immel et al. \(2020\)](#).

Together with Eq. (6.11) we obtain the tangential traction component for sticking

$$\sigma_{\theta z}^{\text{stick}}(\theta, r) = \theta r \frac{t_t^{\max}}{\theta_{\text{lin}} R} = \frac{r}{c(\theta)} t_t^{\max}. \quad (6.20)$$

In the sliding region $r \geq c$, the tangential traction follows the modified Coulomb's law

$$\sigma_{\theta z}^{\text{slide}} = \mu \bar{p}_c, \quad (6.21)$$

with $\mu = \mu(g_s)$ from Eq. (6.3). As long as a part of the interface remains sticking

$$g_s = 0, \quad \text{otherwise} \quad g_s = r(\theta - \theta_{\max} + \theta_{\text{lin}}). \quad (6.22)$$

The tangential contact traction as a function of the rotation angle can then be summarized by

$$\sigma_{\theta z}(\theta, r) = \begin{cases} t_t^{\max} \frac{r}{c(\theta)}, & \text{for } r < c \text{ (sticking),} \\ \mu \bar{p}_c, & \text{for } r \geq c \text{ (sliding),} \end{cases} \quad (6.23)$$

Figure 6.4 illustrates the variation of the tangential contact traction (6.23) for $\theta = \theta_{\text{lin}}$, $\theta = \theta_{\max}$, and some θ larger than θ_{\max} .

While the two analytical models presented in Sections 6.4.2 and 6.4.3 both assume circular crack propagation from outside to inside and determine the stick/slip transition by a critical (or crack) radius, the analytical model from the reference study imposes the crack radius and computes the corresponding rotation angle, while the new model directly imposes the rotation angle.

6.4.4 Numerical Setup

As in the experiments, we consider a CSI with the same dimensions $R_I = 2.5$ mm and $H_I = 3$ mm. The bone sample is modeled as a rectangular cuboid with dimensions $12.5 \times 12.5 \times 5$ mm. The implant is positioned at the center of the upper bone surface. The bodies are meshed according to the parameters given in Table 6.1, where n_e denotes the number of elements of the body/surface and n_{gp} denotes the number of Gauss-points per element. While the bulk is discretized with linear Lagrangian shape functions, the contact surfaces are discretized with quadratic NURBS (see Section 4.1.3). The FE mesh is pictured in Figure 6.2(b). To justify this coarse discretization, a refinement analysis of the mesh and the load step size is performed (see Appendix B.2).

body	n_e	type of shape fcts.	n_{gp}
implant bulk	18	linear Lagrange	$2 \times 2 \times 2$
bone bulk	450	linear Lagrange	$2 \times 2 \times 2$
lower implant surface	9	quadratic NURBS	5×5
upper bone surface	225	quadratic NURBS	5×5

Table 6.1 – Parameters of the finite element mesh: Number of elements n_e , type of shape functions and number of Gauss-points per element n_{gp} for the two bodies and their contact surfaces. Adopted from [Immel et al. \(2020\)](#).

Contact is computed with a penalty regularization (see Section 4.4), and the corresponding penalty parameter is set according to the Young’s modulus of bone to $\epsilon_t = \epsilon_n = E_{cb}/L_0$, with $L_0 = 0.01$ m. The full-pass approach (see Section 4.3) with the predictor-corrector algorithm from Section 4.5.2 are used.

The lower surface of the bone block is fixed in all directions, while the sides of the bone block are fixed in their corresponding normal direction. The modified Coulomb’s friction model requires a contact pressure during sliding, see Eqs. (3.38) and (6.23). We generate this pressure by applying a uniform vertical displacement d_0 at the upper surface of the implant. Then, the implant is rotated by 10° around its central axis with a constant load step size of 0.01° .

All computations in Sections 6.4.5.1–6.4.5.3 use homogeneous initial bonding ($\phi_0(\mathbf{x}) = 1, \forall \mathbf{x} \in \mathcal{S}_k$), while Section 6.4.5.4 presents cases with inhomogeneous initial bonding. For both bodies, the Neo-Hookean material model of Eq. (3.19) is used. The material properties for the implant are those of titanium alloy (Ti-6Al-4V: $E_i = 113$ GPa, $\nu_i = 0.3$). The material properties of the bone and the friction parameters μ_{ub} , μ_b , a_s , b_s , and the contact pressure p_c have to be determined by a parameter study and are presented in 6.4.5.1.

All simulations were performed with an in-house, MATLAB-based solver (R2018b, The MathWorks, Natick, MA, USA).

6.4.5 Results

In the following, the results obtained with the new analytical model and numerical study are presented and compared to the experimental and analytical results corresponding to the reference study. First, the parameter estimation and the subsequent error estimation for homogeneous osseointegration are presented. Second, the torque-per-angle curves corresponding to the different models are compared and the debonding behavior of the implant is discussed. Third, the work of adhesion and frictional energy loss of the models are compared. Last, several cases of partial osseointegration are presented and compared with the homogeneous case.

6.4.5.1 Parameter Calibration

During the parameter estimation stage, the Poisson ratio of bone is fixed to $\nu_b = 0.3$. The remaining parameters G_{cb} , d , μ_{ub} , a_s , b_s are determined by minimizing the mean relative error

$$e_{M_z}^{mp} = \text{mean}_{\theta \in [0^\circ, 10^\circ]} \left(\left\| \frac{M_z^{\text{exp}}(\theta) - M_z(\theta)}{M_z^{\text{exp}}(\theta)} \right\| \right), \quad (6.24)$$

where M_z^{exp} is defined as the torque over the rotation angle θ obtained from the corresponding experiment. The shear modulus G_{cb} is calibrated using the initial slope of the linear

part of the torque-per-angle curve (i.e., $M_z(\theta \leq \theta_{\text{lin}})$) (e.g. see Figure 6.5(a)). The other parameters depend on the friction coefficient μ_b , which is investigated at the fixed values $\mu_b = [0.2, 0.25, 0.3, 0.35, 0.4, 0.45, 0.5]$, which corresponds to the typical range found in the literature (Rancourt et al., 1990; Shirazi-Adl et al., 1993; Grant et al., 2007; Biemond et al., 2011). The vertical displacement d_0 is calibrated from steady state sliding, which is considered here to occur for $\theta > 9^\circ$. We thus minimize Eq. (6.24) for $\theta \in [9^\circ, 10^\circ]$ to calibrate d_0 . There, the implant is assumed to be fully debonded and thus, tangential sliding contact is governed by Coulomb's law (3.38) with $\mu = \mu_b$. Once d_0 is determined, it is considered constant for all rotation angles θ .

The initial friction coefficient μ_{ub} is calibrated using M_z^{max} (as $t_t^{\text{max}} = \mu_{\text{ub}} p_c$) (see Table 6.2). Finally, the parameters a_s and b_s are then determined by minimizing Eq. (6.24) for the whole torque-per-angle curve.

The bone shear modulus can be estimated from the new analytical model. Due to the non-homogeneous pressure distribution, the displacement d_0 and subsequently all other parameters are determined using the numerical model. However, adjusting d_0 for the new analytical model of Section 6.4.3 leads to the same estimated values for μ_{ub} , a_s , and b_s .

data set	M_z^{max} [N m]	M_z^∞ [N m]	θ_{lin}	θ_{max}
1	0.0538	0.0368	0.13°	1.13°
2	0.0595	0.0444	0.11°	2.02°

Table 6.2 – Data sets used for the parameter estimation. Data set 1 and 2 correspond to the data shown in Figure 4a and 4b of Mathieu et al. (2012a), respectively. θ_{lin} denotes the limit of the elastic part of the deformation, while θ_{max} is the location of the maximum torque M_z^{max} . M_z^∞ denotes the torque for a fully debonded implant and is taken at 10° . Adopted from Immel et al. (2020).

Table 6.3 shows the estimated shear moduli and the corresponding Young's moduli obtained from the numerical parameter estimation for the two data sets, compared to the computed shear moduli obtained in the reference study. The estimated shear moduli of 7 and 8 GPa are higher than the reported values of 2–6 GPa (Sharma et al., 2012; Tang et al., 2015)), while the corresponding Young's moduli of 18 and 21 GPa are in good agreement with experimental data from the literature (Rho et al., 1993; Novitskaya et al., 2011) and previous studies (Vayron et al., 2011, 2012). In the reference study the model was fit to match the peak and the decrease in torsion, which results in a considerable error for the shear modulus, as shown in Table 6.3 and Figure 6.5. As our proposed model allows for more control, it is possible to match more characteristics of the torque curve, such as the initial slope, the peak, the softening and the torque for complete debonding.

Table 6.4 shows the results of the numerical parameter estimation of the different data sets and the corresponding mean percentage error, for the chosen levels of friction coefficient μ_b . For the analyzed μ_b , the corresponding initial friction coefficient μ_{ub} lies between 0.29 and 0.73 and agrees well with the values of 0.28–1.1 reported in the literature (Rancourt et al., 1990; Shirazi-Adl et al., 1993; Zhang et al., 1999; Grant et al., 2007; Biemond et al., 2011; Damm et al., 2015). Increasing μ_b results in a smaller normal force and a higher μ_{ub} . Calibrating the parameters using M_z^{max} and M_z^∞ results in almost identical curves for all tested values of μ_b . Therefore, for the second data set only $\mu_b = 0.3$ (Rancourt et al., 1990) and $\mu_{\text{ub}} = 0.4$ (Shirazi-Adl et al.,

1993; Grant et al., 2007) are investigated, which are the values most commonly reported for the interface between cortical bone and polished metal implants.

As shown in Table 6.4, the parameters a_s and b_s only depend on the shear modulus and on the overall shape of the torque curve, i.e., the width of the peak and the slope of $M_z(\theta)$. The computed values for a_s indicate that adhesion takes effect for a sliding distance up to 22 and 26 μm , respectively. When these values are exceeded, the implant starts to debond, which is indicated by a decreasing friction coefficient (see 6.7(b)). This observation is in agreement with the reported threshold for micro-motion of the BII, where no deformation occurs. In most studies, a value of up to 50 μm is reported (Bragdon et al., 1996; Fitzpatrick et al., 2014), while values exceeding 150 μm have shown to inhibit bone growth and promote bone loss (Pilliar et al., 1986; Jasty et al., 1997). However, these values were only reported for normal displacement and may vary for tangential displacement.

data set	model	G_{cb} [GPa]	E_{cb} [GPa]
	literature (1993; 2011; 2011; 2012; 2012; 2015)	2–6	15–23
1	analytical solution from (2012a)	0.04	–
	present numerical solution	7	18
2	analytical solution from (2012a)	0.02	–
	present numerical solution	8	21

Table 6.3 – Results for the parameter estimation of the two data sets for values independent of the friction coefficient μ_b . Shown are results from the analytical model presented in Mathieu et al. (2012a) (see Eqs. (6.7),(6.9)) and the present numerical solution. The estimated parameter is the bone shear modulus G_{cb} . The Young’s modulus E_{cb} then follows from Eq. (3.13). Adopted from Immel et al. (2020).

data set	μ_b	d_0 [μm]	\bar{p}_c [MPa]	μ_{ub}	a_s [μm]	b_s	$e_{M_z}^{\text{mp}}$ [%]
	ana. (2012a)	–	–	–	–	–	7.7200
1	0.20	9.8	5.2	0.29			2.2390
	0.25	7.8	4.2	0.37			2.2395
	0.30	6.5	3.5	0.44			2.2397
	0.35	5.6	3.0	0.51	22	0.74	2.2399
	0.40	4.9	2.6	0.58			2.2400
	0.45	4.4	2.3	0.66			2.2401
	0.50	3.9	2.1	0.73			2.2401
	ana. (2012a)	–	–	–	–	–	11.6231
2	0.30	6.8	4.1	0.41	26	1.86	2.1499
	0.40	5.1	3.1	0.55			2.1500

Table 6.4 – Results for the parameter estimation of the two data sets. Shown are results from the analytical model presented in (Mathieu et al., 2012a) (see Eqs. (6.7),(6.9)) and the present numerical solution. The estimated parameters are the enforced normal displacement d_0 , corresponding average contact pressure \bar{p}_c , friction coefficient for the unbroken state μ_{ub} , sliding threshold a_s , and transition factor b_s . Adopted from Immel et al. (2020).

6.4.5.2 Torque Curves and Debonding Behavior

The corresponding curves representing the variation of the torque as a function of the angle of rotation are shown in Figure 6.5(a) and 6.5(b). The resulting torque obtained with the new analytical model described in Section 6.4.3 and the numerical solution of the proposed friction model of Section 6.3 (using $\mu_b = 0.4$) are very close. While the analytical solution shows a slightly closer fit to the experimental data before the peak in torque (resulting in an error of 2.18 % for the first data set and 2.83 % for the second data set), the numerical solution provides a better estimation of the behavior after debonding.

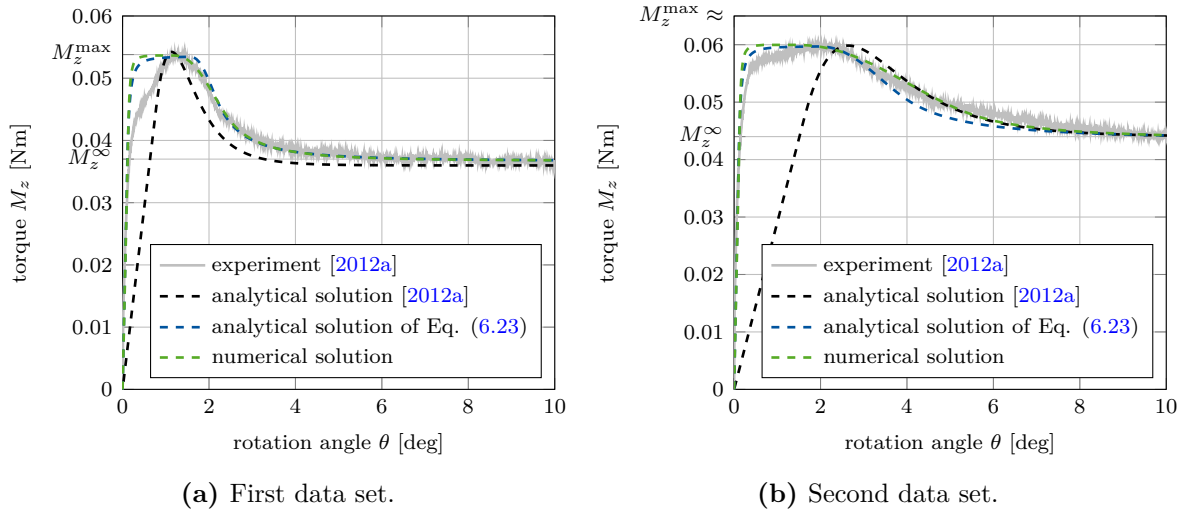


Figure 6.5 – Variation of the torque M_z as a function of the imposed rotation angle θ . Adopted from [Immel et al. \(2020\)](#).

The errors obtained with the numerical solution are given in Table 6.4 and are compared to the analytical model from the reference study. Overall, the numerical solutions yield the best agreement with the experimental data, especially concerning the initial slope (i.e. stiffness) of the torque and the decrease after its peak. The torque curves show a flat plateau at the peak, which comes from the behavior induced by the sliding threshold a_s . Increasing a_s induces an offset of the debonding process and thus, results in an elongated peak. Another difference is shown in Figure 6.5(b) for $\theta > 2.5^\circ$, where the decrease of the torque is not exactly reproduced. A different transition function ϕ may allow for a closer fit there.

The top row in Figure 6.6 shows the distribution of the friction coefficient μ in the contact area for different angles of rotation. A transition zone (characterized by $\mu_b < \mu < \mu_{ub}$), which may be understood as a crack front, cf. [Mathieu et al. \(2012a\)](#) and Figure 6.2(a), appears at 1.13° . The transition zone propagates inward in the radial direction from the external radius R into the center, which corresponds to the crack mode assumed by the analytical models. The transition zone can also be observed in Figure 6.7(a), which shows the value of the friction coefficient as a function of the implant radius for different angles of rotation. When the rotation angle increases, the width of the transition zone decreases. It becomes apparent, that for the numerical model no full debonding is achieved after a rotation of 10° , since for the nodes close to the center of the implant's contact surface the appropriate sliding distance to start the transitioning of μ has not been reached yet. In fact, under perfect twisting conditions, g_s

remains zero at the center of the implant. Thus the center of the implant will never debond for (perfect) twisting.

The bottom row of Figure 6.6 shows the distribution of the sliding distance over the contact surface for different angles of rotation. Although the body starts sliding before a twisting angle of 1° , the factor a_s prevents a change of the friction coefficient until a sliding distance of $22 \mu\text{m}$ is reached. This is also shown in Figure 6.7(b), which illustrates the variation of the friction coefficient as a function of the sliding distance g_s for $r = R$ and data set 1. The friction coefficient stays constant as $\mu = \mu_{\text{ub}}$ for $g_s \leq a_s$ and then decreases, until it reaches $\mu = \mu_{\text{b}}$ at $g_s = 66 \mu\text{m}$.

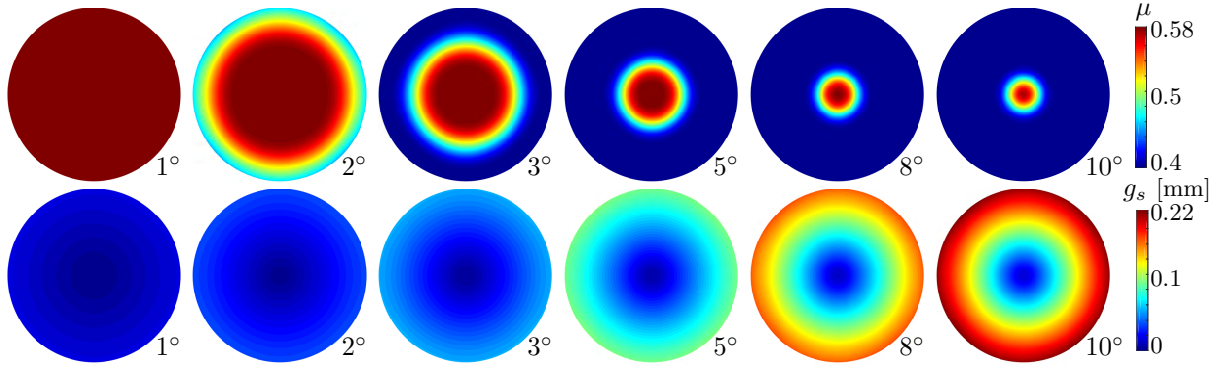
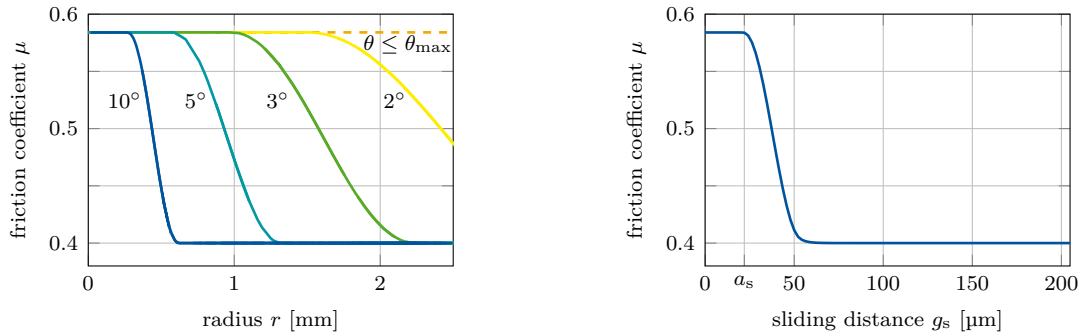


Figure 6.6 – Evolution of the debonding of the BII: Value of the friction coefficient μ (top) and the sliding distance g_s (bottom) on the contact area of the implant for different angles of rotation. Adopted from [Immel et al. \(2020\)](#).



(a) Variation of the friction coefficient μ as a function of the implant radius r for different angles of rotation.

(b) Variation of the friction coefficient μ as a function of the total sliding distance g_s at $r = R$.

Figure 6.7 – Evolution of the debonding of the BII: Behavior of the friction coefficient and the transition zone for the first data set. Adopted from [Immel et al. \(2020\)](#).

6.4.5.3 Work of Adhesion

Due to the poor agreement between the experimental results and the analytical model developed in [Mathieu et al. \(2012a\)](#), an energetic approach was proposed to determine the dissipated frictional energy W_{fric} , the work of adhesion W_{adh} , and the total energy necessary for debonding

W_{deb} ,² which are given by

$$W_{\text{deb}} = \int_{\theta=0^\circ}^{\theta=10^\circ} M_z(\theta) d\theta, \quad W_{\text{fric}} = \int_{\theta=\theta_{\text{max}}}^{\theta=10^\circ} M_z^\infty d\theta, \quad W_{\text{adh}} = W_{\text{deb}} - W_{\text{fric}}. \quad (6.25)$$

Based on the experimental results, $\theta = 10^\circ$ was chosen to be the angle of rotation where the implant was completely debonded from the bone, indicated by a constant torque M_z^∞ . The area-specific average work of adhesion E_{adh} is then given by

$$E_{\text{adh}} = \frac{W_{\text{adh}}}{\pi R^2 \bar{\phi}_0}, \quad (6.26)$$

where $\bar{\phi}_0$ is the average of the initially osseointegrated area, see also Section 6.4.5.4. A visual analysis of the implant surfaces after debonding yielded $\bar{\phi}_0 = 0.73$ for the first data set (see Figure 6.8(a)) and $\bar{\phi}_0 = 0.72$ for the second (Mathieu et al., 2012a).

Table 6.5 gives the results for the different energies with respect to the values of $\bar{\phi}_0$ determined by the surface analysis. In the cases presented here, the analytical and the numerical models use $\phi_0(\mathbf{x}) = 1 \forall \mathbf{x}$. Therefore, the true area-specific work of adhesion for these models E_{adh}^* was computed by using $\bar{\phi}_0 = 1$ in Eq. (6.26). Results for E_{adh} where $\bar{\phi}_0 \neq 1$ is used during the simulation are presented in Section 6.4.5.4.

For both data sets, the analytical solution by Mathieu et al. (2012a) underestimates the total debonding work and the area-specific adhesion work, while the numerical results with the modified Coulomb's law lead to very good agreement with the experimental data. The analytical solution with the modified Coulomb's law yields less accurate results for the second data set.

For simplicity, the results in the remaining part of this work were obtained based only on the estimated parameters for the first data set and $\mu_b = 0.4$ (see Table 6.4).

data set	model	W_{deb} [N m]	W_{fric} [N m]	W_{adh} [N m]	E_{adh} [N m ⁻¹]	E_{adh}^* [N m ⁻¹]
1	exp.	0.0070	0.0056	0.0014	98	71
	ana. (2012a)	0.0066	0.0056	0.0010	70	51
	ana. Eq. (6.23)	0.0071	0.0057	0.0014	98	72
	sim.	0.0071	0.0057	0.0014	98	72
2	exp.	0.0088	0.0060	0.0028	198	143
	ana. (2012a)	0.0080	0.0064	0.0016	120	81
	ana. Eq. (6.23)	0.0087	0.0067	0.0020	141	102
	sim.	0.0089	0.0062	0.0027	191	138

Table 6.5 – Total debonding energy W_{deb} , frictional energy W_{fric} , work of adhesion W_{adh} , and corresponding area-specific works of adhesion E_{adh} and E_{adh}^* for the different models and data sets. Adopted from Immel et al. (2020).

6.4.5.4 Partial Osseointegration

Mathieu et al. (2012a) showed that part of the limitations of their model lies in the assumption of a fully bonded surface at the beginning of the experiment. The analysis of the implants' surfaces after debonding indicated that most likely, full osseointegration was not achieved. This resulted in regions where no bone tissue was initially attached to the implant surface, as seen in Figure 6.8(a), and thus no adhesive or frictional effects can take place. This state of partial

2. The strain energy inside the bodies, which generally should also be accounted for, is negligible in this case.

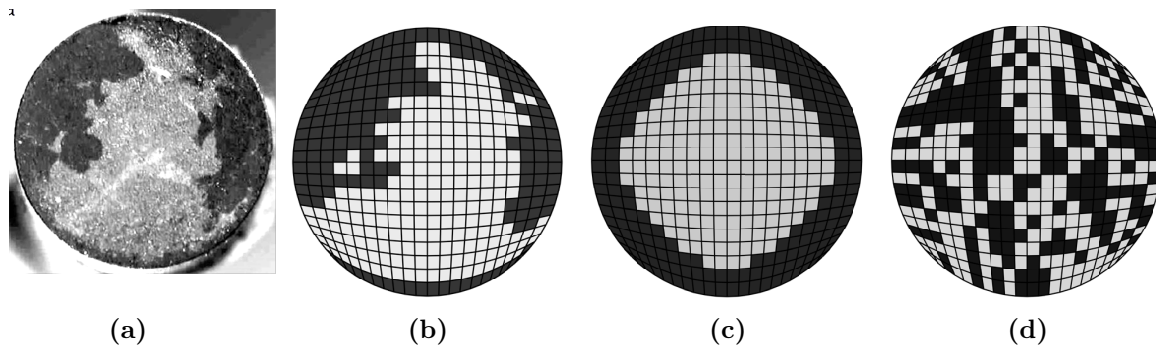


Figure 6.8 – Original and constructed osseointegration patterns with average osseointegration $\bar{\phi}_0 = 0.55$. (a) Original pattern (Mathieu et al., 2012a). (b) Reconstructed pattern. (c) Circular pattern. (d) Random pattern. Light areas represent full osseointegration ($\phi_0 = 1$), while dark areas represent no osseointegration ($\phi_0 = 0$). For the corresponding elements in the reconstructed and artificial patterns ϕ_0^e is set to 1. Adopted from Immel et al. (2020).

osseointegration can be readily investigated with the proposed numerical model. Therefore, an analysis assuming inhomogeneous initial bonding was performed, with various distributions $\phi_0(\mathbf{x})$ in model (6.5).

In order to analyze the debonding behavior of the BII and to determine the influence of the percentage and the distribution of osseointegration, different cases for a fine mesh with 400 contact elements on the implant surface were constructed: First, a bonding pattern based on Figure 6.8(a), assuming that light gray areas indicate osseointegration, was reconstructed. From a visual inspection of the photograph, the sample in Figure 6.8(a) is considered to have average osseointegration $\bar{\phi}_0 = 0.55$. Second, to compare the influence of osseointegration patterns, two other patterns with $\bar{\phi}_0 = 0.55$ were constructed. A simple circular pattern, where only the center part of the interface is integrated and last, a random distribution. For patterns (b)–(d), $\phi_0 = 1$ within the light gray surface elements. The corresponding osseointegration patterns are shown in Figure 6.8.

Partial Osseointegration for Different Material Parameters

When the model parameters are fitted for every pattern (see Table 6.6), the torque-angle curve only weakly depends on the various distributions of osseointegration, as seen in Figure 6.10, resulting in a minimum error of 1.95 % for the reconstructed pattern, 1.99 % for the circular pattern and 2.15 % for the random distribution, respectively. While the error is slightly larger compared to the reconstructed pattern, the circular pattern has a closer fit to the experimental data for $\theta < \theta_{\max}$, which leads to a small improvement of the prediction of E_{adh} . Since the model parameters are unknown, fitting the parameters to the experimental data leads to similar curves for every presented case. Out of the different osseointegration patterns, the random pattern is the closest to the results obtained with full initial bonding. The random pattern still has a balanced degree of osseointegration over the implant radius, while pattern (b) and (c) are only weakly (or not) bonded on the outer part of the implant and thus, a bigger difference is seen in the beginning of the torque curve. Overall, the aforementioned results lead to the conclusion that without knowing the friction coefficients, the torque-per-angle curve does not provide sufficient information on the degree and distribution of osseointegration of the BII.

As the state of an element does not depend on the states of neighboring elements, the total sliding distance is not affected by inhomogeneous initial bonding. Therefore, a similar propagation of the transition zone as in the homogeneous case can be seen in Figure 6.9. In contrast to the torque, partial osseointegration has a larger effect on the model parameters, as shown in Table 6.6. In general, partial osseointegration leads to the estimation of higher μ_{ub} , that are still well within the range of reported values in the literature. In addition, the transition time is notably lower and for the distinct patterns (b) and (c), the sliding threshold is lower, as well.

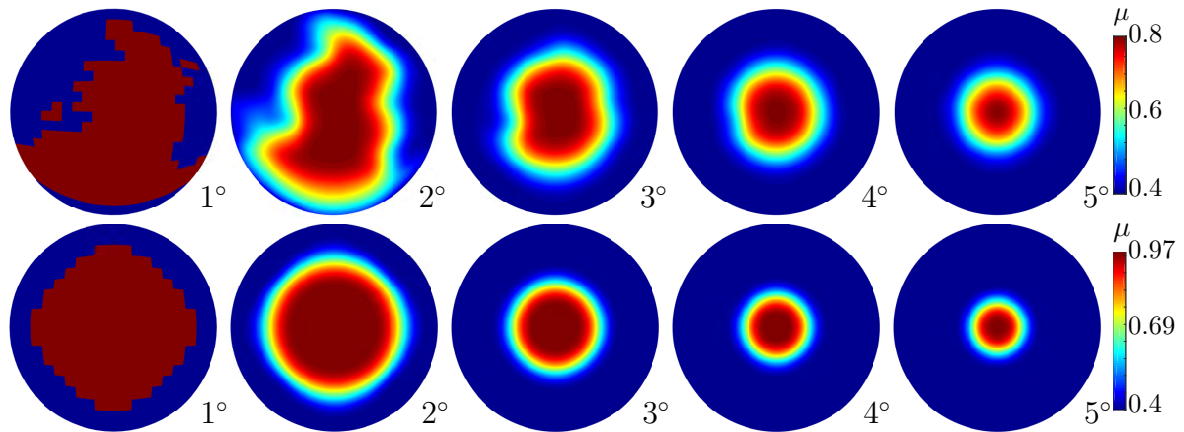


Figure 6.9 – Variation of the friction coefficient μ at the BII for different angles of rotation for different patterns of partial osseointegration. Adopted from [Immel et al. \(2020\)](#).

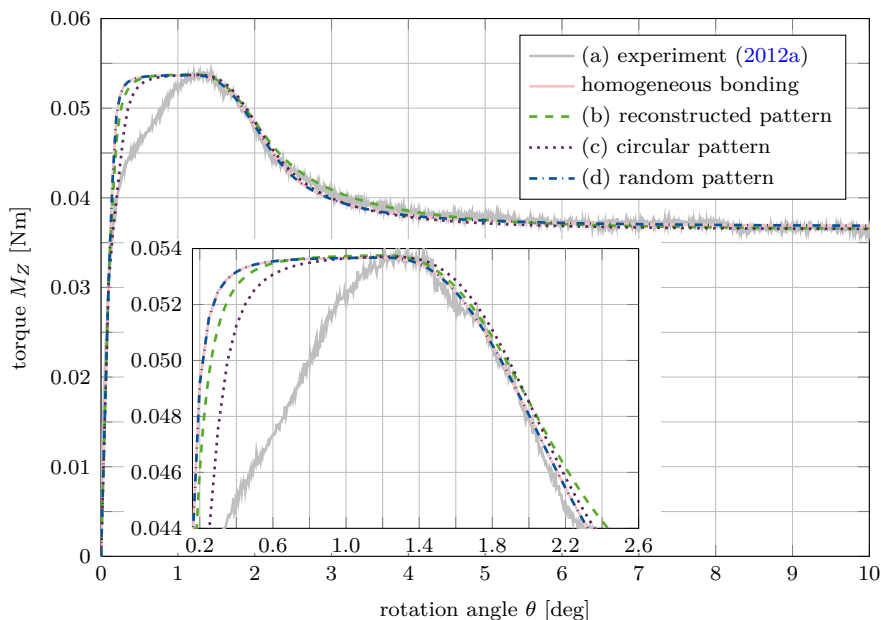


Figure 6.10 – Partial osseointegration: Variation of the torque M_z as a function of the imposed rotation angle θ for different cases of the initial bonding state of the interface with the material parameters shown in Table 6.6. Adopted from [Immel et al. \(2020\)](#).

bonding pattern	$\bar{\phi}_0$	d_0 [μm]	μ_{ub}	a_s [μm]	b_s	$e_{M_z}^{\text{mp}}$ [%]	W_{adh} [N m]	E_{adh} [N m^{-1}]
homog.	1	4.9	0.58	22	0.74	2.240	0.0014	130
(b)	0.55	4.8	0.80	21	0.63	1.949	0.0015	139
(c)	0.55	4.8	0.97	15	0.67	1.988	0.0014	130
(d)	0.55	4.9	0.73	22	0.66	2.152	0.0015	139

Table 6.6 – Change in model parameters and results for implants with partial initial bonding compared to homogeneous bonding (see Figure 6.8). Adopted from [Immel et al. \(2020\)](#).

Partial Osseointegration for Equal Material Parameters

The effect of the different osseointegration patterns becomes much more distinct when studying the results obtained for equal material parameters for bone tissue and the implant, as presented in Figure 6.11. Here, the parameters for the homogeneous case of the first data set ($\mu_b = 0.4$) were used (see Tables 6.3 and 6.4) with $\bar{\phi}_0 = 0.55$ for all four patterns. Using partial osseointegration only affects the part of the deformation where (tangential) adhesive forces are expected to play a mayor role, represented by the peak in the torque curve. In general, partial osseointegration patterns lead to a lower M_z^{max} and differences in the softening of the curve. The initial slope of the torque curve and M_z^∞ are not affected by the different osseointegration patterns. Applying $\phi_0 = 0.55$ to all contact elements in the homogeneous bonding case produces the same result as using a randomly distributed pattern with $\bar{\phi}_0 = 0.55$, where $\phi_0 = 1$ for the osseointegrated elements. The distinct patterns (b) and (c) with weak or no bonding on the outer part of the implant produce a lower peak and longer softening periods.

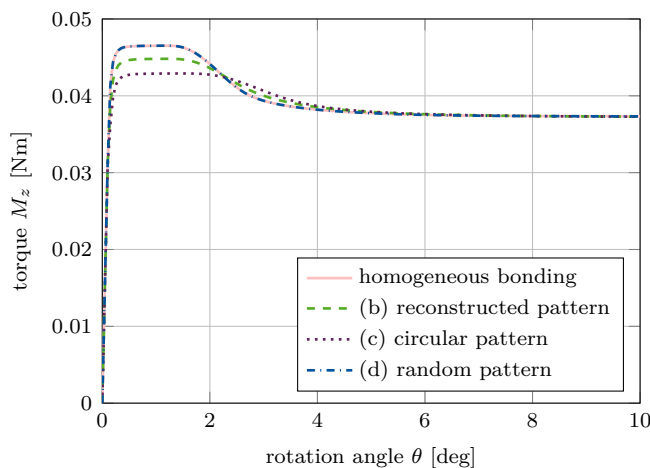


Figure 6.11 – Partial osseointegration: Variation of the torque M_z as a function of the imposed rotation angle θ for different patterns of the initial bonding state of the interface with $\bar{\phi}_0 = 0.55$ and the same material parameters for all patterns. $M_z^\infty = 0.0368 \text{ N m}$ according to data set 1 (see Table 6.2). Adopted from [Immel et al. \(2020\)](#).

6.4.6 Discussion and Limitations

This work aims to provide a simple friction law to model the debonding of the BII. The mechanical model is incorporated into an analytical model and is implemented into an accurate and efficient contact algorithm with NURBS-enriched finite elements and thus, allows to predict

the debonding of osseointegrated implants numerically. The model only depends on four physiological parameters (μ_{ub} , p , a_s , and b_s), that can be determined by a parameter study based on experimental results. Moreover, it allows for reasonable estimations of other parameters, such as the bone's Young's modulus and adhesion energy. However, due to the limited experimental data analyzed here, no *a-priori* determination of the input parameters can be made yet. While the analytical solution of the proposed friction law already leads to good estimates, the results obtained by the finite element simulation are more accurate as they can also account for non-linear material behavior, large deformations, and partial osseointegration.

One difficulty associated with the present study arises from the contact pressure, which is required to establish frictional contact. In Mathieu et al. (2012a), it was reported that although the experimental pressure was minimized, it could not be completely excluded nor measured. Since the experimental torque does not go to zero for fully debonded implants, a normal pressure is likely to remain applied to the implants. As friction coefficients and normal force are unknown, no statement can be made about the accuracy of the estimated contact pressure. Furthermore, in the beginning, p_c accounts for applied normal forces as well as adhesive forces due to chemical and mechanical bonding. The measurement or elimination of applied normal forces would clearly determine the friction coefficient for the broken state and thus also for the unbroken state of a certain sample. Therefore, an improvement of the testing machine used for the experimental measurements is needed and is currently under development.

While the estimated parameters are within a reasonable range compared to the literature (Shirazi-Adl et al., 1993; Novitskaya et al., 2011; Damm et al., 2015), and result in a good qualitative and quantitative representation of the torque-angle curve, there are still visible differences, in particular at the beginning of the peak. Following the argumentation of the reference study, these differences might be explained by the assumption of a full initial bonding between bone and implant, while an initial bonding of 30–70 % is reported in the literature (Brånemark et al., 1997; Marin et al., 2010). Accounting for inhomogeneous osseointegration in our model has shown an influence on the torque curves and the model parameters, such as the friction coefficient for the unbroken state. As these values were not or cannot be measured experimentally yet, it is assumed that the parameters obtained by incorporating imperfect osseointegration are more accurate than assuming a homogeneous distribution of osseointegration. Furthermore, a partial bonding will most likely lead to a more complex crack front and propagation than what is assumed by the analytical and numerical models.

Other factors that were not taken into account in the present work are the roughness of bone and implant surfaces, as well as wear and debris. Furthermore, only a healing time of 7 weeks was considered, while a comparison of different healing times in terms material parameters and of osseointegration would be interesting. Thus, a study on the influence of the surface roughness and healing time is planned for future work.

Another interesting aspect for future work is the application of the model to actual implant and bone geometries, for example in artificial hip joints and dental implants. The latter have been recently examined by Rittel et al. (2018) to study the influence of partial osseointegration on implant stability and cohesive failure. In addition, only torsional debonding was tested in this work while other loading conditions, such as push-in and pull-out of the implant are more commonly analyzed (Bishop et al., 2014; Wennerberg et al., 2014; Berahmani et al., 2015; Damm et al., 2015).

Although, bone is highly non-linear and anisotropic, the choice of an isotropic, non-linear

elastic Neo-Hookean material model here leads to reasonable results for the planar mode III debonding of titanium and cortical bone, due to the small deformation. It has to be investigated if this still holds for, e.g., pull-out tests and contact with trabecular bone, as is presented in Chapter 7. Especially for the modeling of cohesive failure of bone, a fracture model would be needed.

6.4.7 Conclusion

Overall it is shown, that assuming a smooth transition from an unbroken to a broken state, characterized by a decreasing friction coefficient during the debonding process leads to good agreement with experimental data with both, an analytical and a numerical approach. While the analytical model is simple, it is an efficient way to provide initial estimates for this kind of experiment. The numerical results on the other hand are more accurate and allow for more complex material behavior, stress distribution, and (partial) osseointegration. Both approaches enable the estimation of several parameters of the BII. The proposed friction model is expected to help in understanding the debonding phenomena at the BII. An extension to adhesive friction ([Mergel et al., 2019, 2021](#)) as well as application to hip implants is presented in the following chapter.

Chapter 7

Normal and Tangential Debonding of Partially Osseointegrated Implants

In the previous chapter, a contact model for the tangential debonding of partially osseointegrated implants was introduced. To increase the accuracy and applicability of this model, this chapter introduces the extension of the modified Coulomb's friction law (MC) in normal direction and to adhesive friction. Consequently, a CZM (see Section 3.3.2) is used to extend the normal traction for positive contact gaps and the tangential traction is shifted, accordingly. This extended model (EMC) is tested with the CSI model from Chapter 6 and is then applied to simulate the debonding of a 3D, osseointegrated ACI in different removal tests. The ACI stability is quantified by the removal force/torque and the biomechanical determinants of the long-term stability, such as primary stability and degree of osseointegration are assessed. The results of the formulations with and without the CZM extension are compared to assess the impact of adhesion and adhesive friction on the stability of osseointegrated implants.

Major parts of this chapter have been published as [Immel et al. \(2021b,c\)](#).

7.1 Adhesive Friction and Debonding

To account for normal adhesion and debonding in the extension of the modified Coulomb's law, the normal traction (3.31) is extended by an exponential CZM ([Xu and Needleman, 1992](#)) (see [Sauer \(2016\)](#)), i.e.

$$\mathbf{t}_n = \begin{cases} \mathbf{0} & g_b \geq g_n \text{ or } \phi = 0, \\ \phi_0 \frac{t_0}{g_0} g_n \exp\left(1 - \frac{g_n}{g_0}\right) \mathbf{n} & 0 \leq g_n < g_b \text{ and } \phi > 0, \\ -\epsilon_n \mathbf{g}_n & g_n < 0, \end{cases} \quad (7.1)$$

where t_0 is the maximum positive normal traction, g_0 is the contact distance, where the maximum traction t_0 occurs, and g_b is a cut-off distance, where contact is lost. The parameters t_0, g_0, g_b depend on the interface. The normal traction model (7.1) is illustrated in Figure 7.1(a).

Equation (7.1) implies that, when pulling the contact surfaces apart in normal direction, as long as the point remains fully or partially bonded ($\phi > 0$) the normal traction keeps increasing until $g_n = g_b$. As soon as the point is fully debonded ($\phi = 0$) or the normal gap is $g_n > g_b$, the contact is lost and the normal traction component becomes $\mathbf{t}_n = \mathbf{0}$. The sharp drop in the normal

traction at g_b is motivated by observations from experimental pull-out tests of osseointegrated, coin-shaped implants (Rønold and Ellingsen, 2002; Nonhoff et al., 2015).

To enable sliding for tensile normal traction in the present extension of the contact model, the tangential sliding limit (3.36) is shifted by

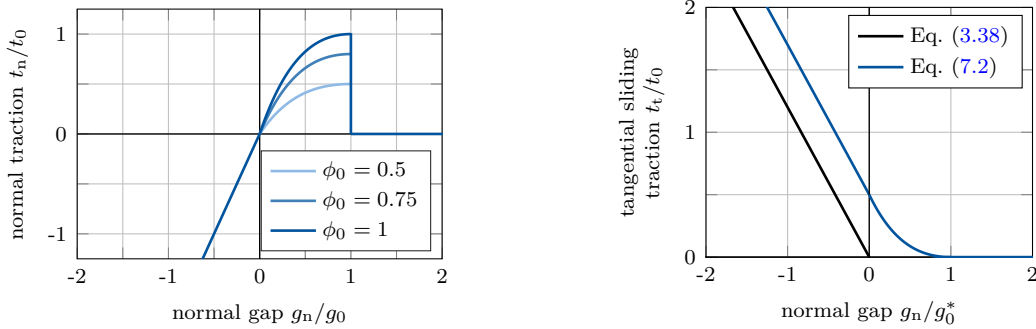
$$t_t^{\text{slide}} = \mu(\phi) (t_0 - t_n), \quad (7.2)$$

according to Mergel et al. (2019, 2021).

The slope of the function $t_n(g_n)$ and $t_t^{\text{slide}}(\mu)$ at $g_n = 0$ depends solely on the choice of the parameters. It is smooth when

$$\epsilon_n = \phi_0 e \frac{t_0}{g_0}, \quad (7.3)$$

(where e is Euler's number), otherwise it is discontinuous. A comparison of the standard Coulomb's law and the proposed extended modified Coulomb's law based on adhesive friction is shown in Figure 7.1.



(a) Exponential cohesive zone model based on the normal gap g_n for various ϕ_0 , $g_b = g_0$, and $t_n := t_n \cdot \mathbf{n}$.

(b) Tangential sliding traction t_t as a function of the normal gap g_n .

Figure 7.1 – Illustration of (a) the cohesive zone model and (b) the extended modified Coulomb's law with adhesive friction for $\phi_0 > 0$. Adopted from Immel et al. (2021c).

The damage parameter $g_d(\mathbf{x})$ is composed of an accumulated irreversible tangential slip g_s (see Section 6.3) and the accumulated normal gap g_{sn} , i.e. ¹

$$g_d = g_s + g_{sn}. \quad (7.4)$$

This implies that during sticking, g_d only increases if g_{sn} increases. Otherwise, there is no change in the debonding state. The irreversible normal slip g_{sn} is defined as

$$g_{sn} = \int_0^t \dot{g}_{sn} dt. \quad (7.5)$$

Here, we approximate g_{sn} as (see Figure 3.2(a))

$$g_{sn}^{n+1} \approx \sum_{i=1}^{n+1} \left\| \mathbf{g}_n^i - \mathbf{g}_n^{i-1} \right\|. \quad (7.6)$$

Only the magnitudes of the slip g_s and g_{sn} are accumulated, not their direction. Thus, a load-reversal in negative direction does not lead to a decrease in g_d .

1. More accurately, the damage parameter could also be computed as $g_d = \sqrt{g_s^2 + g_{sn}^2}$.

7.2 Application to Coin-Shaped Implants

To demonstrate the new contact formulation (7.1) and (7.2) a CSI model is used to simulate different debonding modes.

7.2.1 Setup

We consider the same basic setup as in Chapter 6.4.4. The parameters of the state function (6.5) are chosen to be $a_s = 22 \mu\text{m}$, $b_s = 0.74$, $\mu_{\text{ub}} = 0.44$, and $\mu_b = 0.3$, based on Section 6.4.5.1. The initial osseointegration is constant across the bone-implant interface and is set to be $\phi_0 = 1$ (perfectly integrated). Due to the lack of experimental data, the cohesive zone parameters g_0, g_b are set to $g_b = g_0 = 3a_s$, for simplicity.

The maximum traction of the cohesive zone model, $t_0^* = 1.8 \text{ MPa}$, is calibrated based on the results of Rønold and Ellingsen (2002) for polished, titanium CSI. In that experimental study, CSI with different surface roughness were implanted into rabbit tibiae and allowed to osseointegrate for 10 weeks. Then, the implants were removed together the surrounding bone. The bone and implant parts were fixed into a tensile test machine and the implant was pulled constantly in the normal direction until it was completely debonded from the bone. For the polished CSI an average degree of osseointegration of $\phi_0 = 0.26$ and an average maximum pull-out force of 9 N were determined, which results in an approximate 35 N for $\phi = 1$.

The boundary conditions and considered test configurations are shown in Figure 7.2. The lower surface of the bone block is fixed in all directions. In this work, only quasi-static conditions are considered. First, the implant is pressed into the bone block until a normal reaction force of -70 N is reached, as is done in Section 6.4.4. Then, for the first three test cases, full and homogeneous initial osseointegration ($\phi_0 = 1$) of the bone-implant interface is applied (Figure 7.2 (a) and (c)). For test cases with tension, the implant is then pulled in normal direction until an average normal reaction force of 20 N is reached (Figure 7.2(b)). Last, debonding with no initial pressure or tension is considered (Figure 7.2(d)).

Then, the new contact model is examined for five different debonding test cases:

1. mode II: the upper implant surface is moved in x -direction under constant compression (mode IIa) or tension (mode IIb).
2. mode III: the upper surface of the implant is rotated around its z -axis under constant compression (mode IIIa) or tension (mode IIIb).
3. mode I+II: the upper implant surface simultaneously pulled along the z -axis and in x -direction, corresponding to an angle $\alpha = 30, 45, \text{ or } 60^\circ$. This is performed with initial compression (mode I+IIci) and without initial contact force (mode IIIdi).
4. mode I+II: the upper implant surface is simultaneously pulled along the z -axis and in x -direction, corresponding to an angle of $\alpha = 45^\circ$ for different choices of $t_0 \in [t_0^*/2, t_0^*, 2t_0^*]$. This is performed with initial compression (mode I+IIcii) and without initial contact force (mode IIIdii).
5. mode I+II: the upper implant surface is simultaneously pulled along the z -axis and in x -direction, corresponding to an angle of $\alpha = 45^\circ$ for increasing degrees of initial osseointegration $\phi_0 \in [0, 0.25, 0.5, 0.75, 1]$. This is performed with initial compression (mode I+IIciii) and without initial contact force (mode IIIdiii).

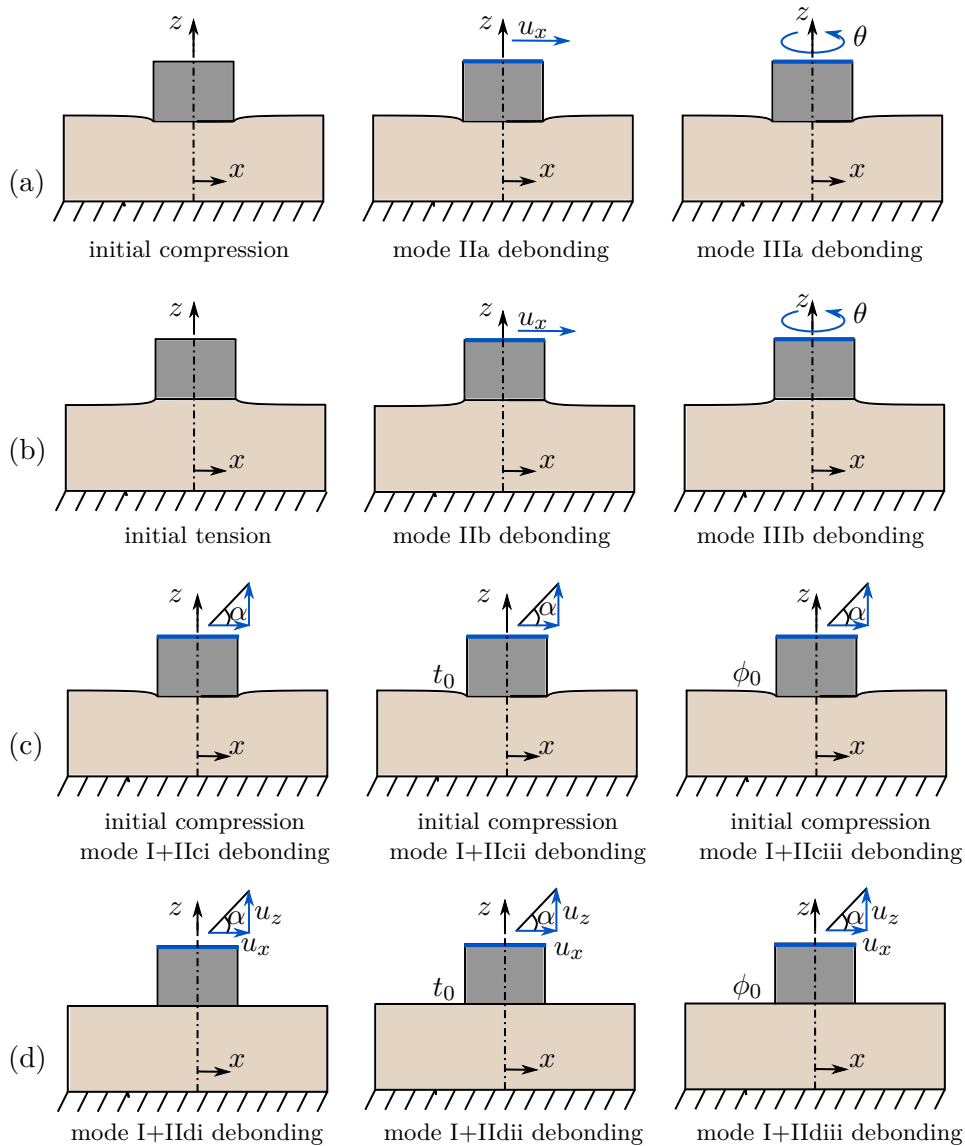


Figure 7.2 – CSI debonding: Illustrations of the boundary conditions for different debonding cases. (a) Debonding under an initial compression of -70 N, either in mode II or III. (b) Debonding under an initial tension of 20 N, either in mode II or III. Mixed mode debonding with initial compression of -70 N (ci) and without initial contact force (di), and under various loading angles α . Mixed mode debonding with initial compression of -70 N (cii) and without initial contact force (dii), under loading angle $\alpha = 45^\circ$ and various CZM parameter t_0 in Eq. (7.1). Mixed mode debonding with initial compression of -70 N (ciii) and without initial contact force (diii), under loading angle $\alpha = 45^\circ$ and various initial degrees of osseointegration ϕ_0 . Adopted from [Immel et al. \(2021c\)](#).

All simulations are performed with an in-house, MATLAB-based solver (R2019b, The MathWorks, Natick, MA, USA). Contact is computed with a penalty regularization, and the corresponding penalty parameter is set to $\epsilon_n = \epsilon_t = E_{tb}/L_0$, with $L_0 = 0.01$ m. The step size for all load cases is $\Delta u = 0.65$ μm (for applied displacement loads and $\Delta\theta = 0.1^\circ$ for applied rotations).

7.2.2 Results

In the following, the results of the debonding tests for the CSI, in terms of load-displacement curves, obtained with the MC and its new extension to adhesive friction (EMC) are presented and compared with each other.

7.2.2.1 Test 1: Mode II Debonding

Figure 7.3 shows the normal and tangential reaction forces F_z and F_x for debonding and possible subsequent sliding in (tangential) x -direction under prescribed constant compression or tension. For a constant compression of -70 N, the slope of the curve of the tangential reaction force is identical for the MC and the EMC. The maximum tangential reaction force increases from 30 N to 45 N for the EMC. For a constant tension of 20 N, the tangential reaction force reaches up to 6 N before decreasing and dropping to 0 because of the absence of contact. The maximum tangential reaction force under tension is smaller than under compression, due to the decrease in ϕ stemming from the accumulated deformation in normal direction before the debonding started (due to pulling the implant back up before sliding). The contact is lost abruptly after the limit for the accumulated deformation g_d is reached, due to the positive contact gap at the bone-implant interface.

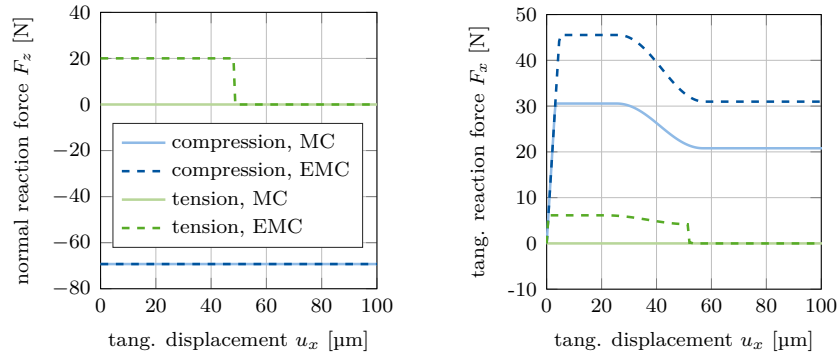


Figure 7.3 – CSI debonding: Variation of the normal reaction F_z (left) and the tangential reaction force F_x (right) as a function of the tangential displacement u_x for mode II debonding under constant compression (mode IIa) or constant tension (mode IIb). The results illustrate the difference between the modified Coulomb’s law (MC) and the new extension (EMC). Adopted from [Immel et al. \(2021c\)](#).

7.2.2.2 Test 2: Mode III Debonding

Figure 7.4 shows the normal reaction force F_z and the debonding torque M_z for mode III debonding due to rotation around the implant’s (normal) z -axis under prescribed constant compression or tension for the considered contact laws. For a constant compression of -70 N, the slope of the torque curve is identical for both contact laws. The maximal torque increases by 0.027 Nm (about 50%) when including normal adhesion (EMC). For a constant tension of 20 N the torque reaches 0.011 Nm and then decreases down to zero due to loss of contact. This loss is gradual, starting in the external region of the cylinder and propagating inward to its center. These results emphasize the fact that torque tests yield a stable crack propagation,

which is particularly interesting when it comes to assessing the effective adhesion energy of the bone-implant interface (Mathieu et al., 2012a).

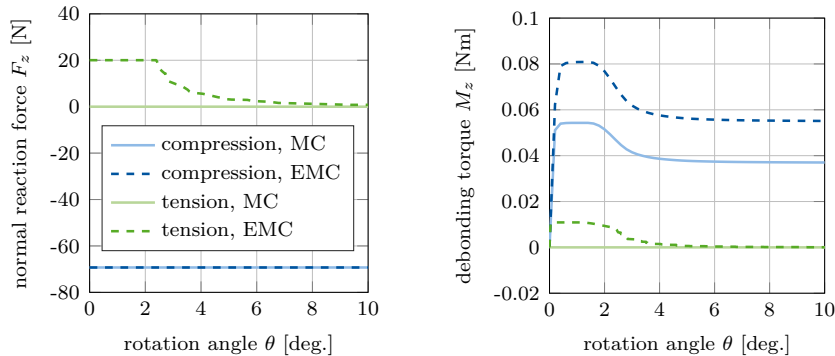


Figure 7.4 – CSI debonding: Variation of the normal reaction F_z (left) and the torque M_z (right) as a function of the rotation angle θ for mode III debonding under constant compression (IIIa) or constant tension (IIIb). The results illustrate the difference between the modified Coulomb’s law (MC) and its new extension (EMC). Adopted from Immel et al. (2021c).

7.2.2.3 Test 3: Mode I+II Debonding for Varying Angles

Figure 7.5 shows the normal and tangential reaction forces F_z and F_x for mixed mode debonding under different angles α (mode I+IIci) starting from an initial contact pressure, based on the MC and the EMC. The normal reaction force F_z increases linearly until it reaches zero. For each angle, the slope of the reaction force curve is identical for both considered contact laws, respectively. In case of the EMC, the reaction force becomes positive at some point and follows the debonding curve of cohesive zone model (7.1) seen in Fig. 7.1(a). In all presented cases, the debonding occurs because the maximal normal gap exceeds g_b , due to the prescribed upward movement. Therefore, increasing the debonding angle α decreases the amount of tangential deformation necessary for debonding, i.e. where contact is lost and the reaction force becomes zero.

The tangential reaction force F_x increases linearly until the respective sliding limit is reached. Then the implant starts sliding and the tangential reaction force decreases linearly, as long as the normal force F_z is still negative. When the normal reaction force reaches zero, the cases with the MC show zero tangential reaction force, as there is no contact anymore. For the cases with the EMC, the bone-implant interface has not fully debonded yet and thus, there is still a normal (adhesive) contact force building up. As a result, the tangential reaction force decreases nonlinearly until it reaches zero.

While the maximum normal reaction force is the same for all three tested angles, the maximum tangential reaction force decreases for an increasing debonding angle. The respective maximal tangential reaction force for each case is around 1.5 times higher for the EMC compared to the MC, due to the shift in tangential contact traction (7.2).

Figure 7.6 shows the normal and tangential reaction forces F_z and F_x for mixed mode debonding under different angles α (mode I+II di), with no initial contact force, based on the EMC. The different curves of the normal reaction force F_z are identical to the positive part of the curves in Figure 7.5. As there is no initial compression or tension in the beginning of this loading case, all curves begin at the origin. Similarly, the different curves for the tangential

reaction force F_x are identical to the exponential part of the curves in Figure 7.5 and are shifted by the same displacement towards the origin, respectively, as the normal reaction force.

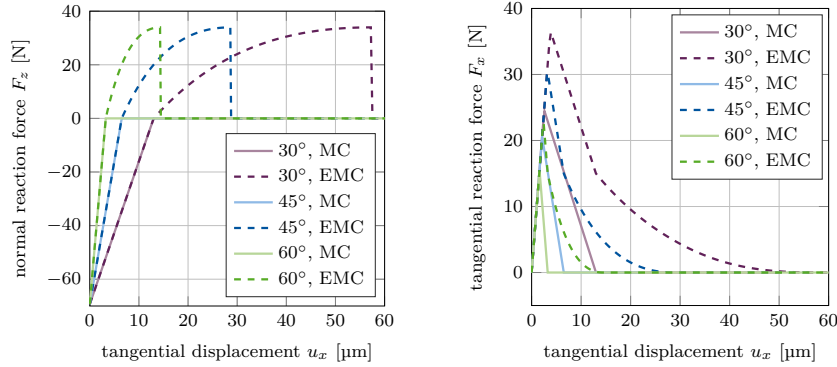


Figure 7.5 – CSI debonding: Variation of the normal reaction force F_z (left) and the tangential reaction force F_x (right) as a function of the tangential displacement u_x for mixed mode debonding, starting from an initial contact pressure (mode I+IIci). The results illustrate the difference between the modified Coulomb’s law (MC) and its new extension (EMC). Adopted from [Immel et al. \(2021c\)](#).

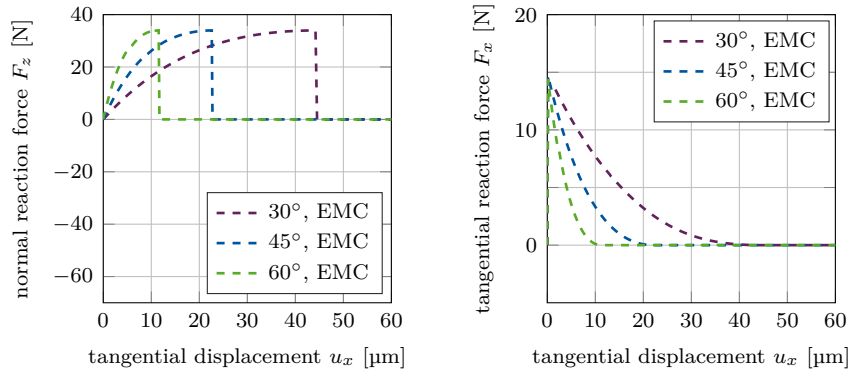


Figure 7.6 – CSI debonding: Variation of the normal reaction force F_z (left) and the tangential reaction force F_x (right) as a function of the tangential displacement u_x for mixed mode debonding, starting from zero contact force (mode I+II di). The results show the extended modified Coulomb’s law (EMC). Adopted from [Immel et al. \(2021c\)](#).

7.2.2.4 Test 4: Mode I+II Debonding for Varying CZM Parameter t_0

Figure 7.7 shows the normal and tangential reaction force F_z and F_x for mixed mode debonding under $\alpha = 45^\circ$ as a function of the tangential displacement with different values of the maximal CZM traction t_0 when considering adhesive friction (mode I+IIcii). As expected, the maximum normal and tangential reaction forces are proportional to t_0 (see Eqs. (7.1) and (7.2)). Furthermore, the slopes of F_z and F_x at the transition from compression to tension ($F_x = 0$, $u_x = 6.5$ mm) are smooth for about $t_0 = 2t_0^*$ (as $2t_0^* \approx \epsilon_n g_0 / \phi_0 e$ (see Eq. 7.3)).

Figure 7.8 shows the normal and tangential reaction forces F_z and F_x for mixed mode debonding under $\alpha = 45^\circ$, with no initial contact force, as a function of the tangential displacement for different values of the maximal CZM traction t_0 when considering adhesive friction (mode I+II dii). The different curves of the normal reaction force F_z are identical to the positive part

of the curves in Figure 7.7. As there is no initial contact force in the beginning of this loading case, all curves begin at the origin. Similarly, the different curves of the tangential reaction force F_x are identical to the exponential part of the curves in Figure 7.7 and are shifted by the same displacement towards the origin, respectively, as the normal reaction force.

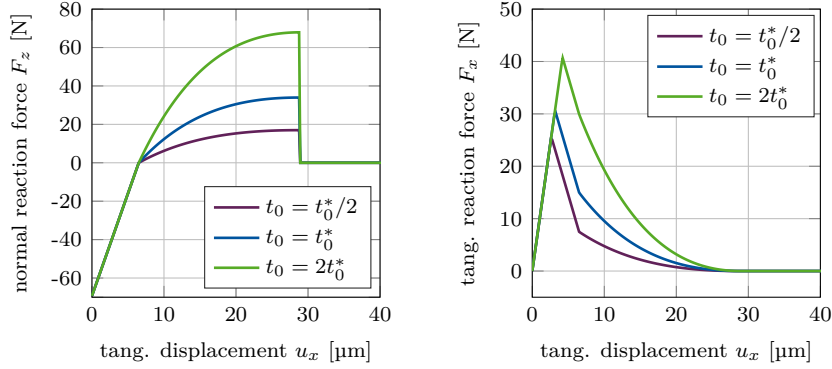


Figure 7.7 – CSI debonding: Variation of the normal reaction force F_z (left) and the tangential reaction force F_x (right) as a function of the tangential displacement for mixed mode debonding under $\alpha = 45^\circ$ and varying CZM parameter t_0 , starting from an initial contact pressure (mode I+IIciii). The results show the extended modified Coulomb’s law (EMC). Adopted from [Immel et al. \(2021c\)](#).

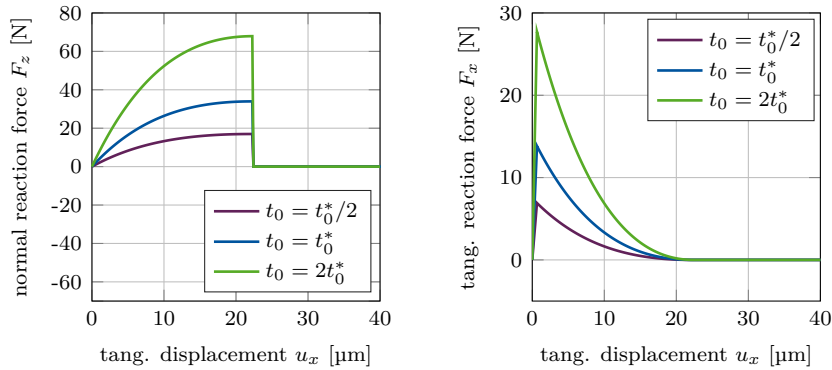


Figure 7.8 – CSI debonding: Variation of the normal reaction force F_z (left) and the tangential reaction force F_x (right) as a function of the tangential displacement for mixed mode debonding under $\alpha = 45^\circ$ and varying CZM parameter t_0 , starting from zero contact force (mode I+IIcii). The results show the extended modified Coulomb’s law (EMC). Adopted from [Immel et al. \(2021c\)](#).

7.2.2.5 Test 5: Mode I+II Debonding for Varying Degree of Osseointegration

Figure 7.9 shows the normal and tangential reaction force F_z and F_x for mixed mode debonding under 45° as a function of the tangential displacement with increasing degree of osseointegration ϕ_0 when considering adhesive friction (mode I+IIciii). Increasing the degree of initial osseointegration increases the peak magnitude in the normal and tangential reaction force. This is due to the fact that in this test case, debonding occurs first due to $g_n > g_b$ and not due to exceeding the limit of the deformation of the interface $g_d = a_s(1 + 2b_s)$ (see Eq. (6.5)). The

maximal normal and tangential reaction force increase proportionally with increasing ϕ_0 , while the tangential displacement necessary for debonding remains the same.

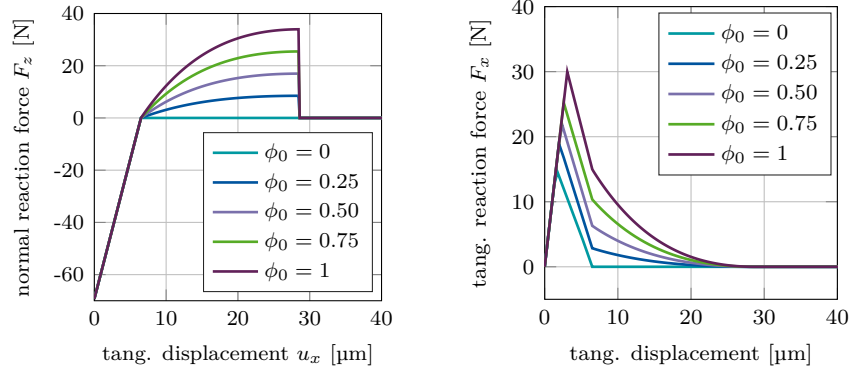


Figure 7.9 – CSI debonding: Variation of the normal reaction force F_z (left) and the tangential reaction force F_x (right) as a function of the tangential displacement for mixed mode debonding under $\alpha = 45^\circ$ and initial degree of osseointegration ϕ_0 , starting from an initial contact pressure (mode I+IIciii). The results show the extended modified Coulomb’s law (EMC). Adopted from [Immel et al. \(2021c\)](#).

Figure 7.10 shows the normal and tangential reaction forces F_z and F_x for mixed mode debonding under $\alpha = 45^\circ$, with no initial contact force, as a function of the tangential displacement with increasing degree of osseointegration ϕ_0 when considering adhesive friction (mode I+IIIdiii). The different curves of the normal reaction force F_z are identical to the positive part of the curves in Figure 7.9. As there is no initial contact force in the beginning of this loading case, all curves begin at the origin. Similarly, the different curves of the tangential reaction force F_x are identical to the exponential part of the curves in Figure 7.9 and are shifted by the same displacement towards the origin, respectively, as the normal reaction force.

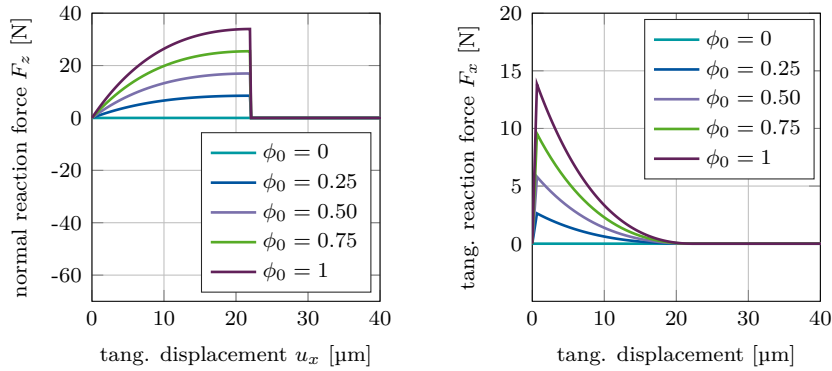


Figure 7.10 – CSI debonding: Variation of the normal reaction force F_z (left) and the tangential reaction force F_x (right) as a function of the tangential displacement for mixed mode debonding under $\alpha = 45^\circ$ and initial degree of osseointegration ϕ_0 , starting from zero contact force (mode I+IIIdiii). The results show the extended modified Coulomb’s law (EMC). Adopted from [Immel et al. \(2021c\)](#).

7.3 Application to Acetabular Cup Implants

Both, the MC and the EMC have been examined for a simple implant model in Section 7.2. Now, both models are applied to simulate the debonding of a 3D, osseointegrated ACI, under different removal conditions, similar to the simulations in [Raffa et al. \(2019\)](#) and Chapter 5. Here, the implant's secondary stability is considered and is quantified by assessing the removal force/torque. Furthermore, the biomechanical determinants of the long-term stability, such as primary stability and initial degree of osseointegration are assessed. The results of the MC and its extension to adhesive friction, EMC, are compared to assess the importance of adhesive effects for long-term stability because it allows to distinguish the influence of primary stability and osseointegration phenomena on the secondary stability.

7.3.1 Setup

A simple cylindrical block is considered, as it is a suitable simplification of the pelvis geometry that qualitatively captures the relevant contact conditions. The same geometry of the ACI including the ancillary used in [Raffa et al. \(2019\)](#) and Chapter 5 is considered herein and is briefly summarized in the following. An idealized bone block with the same properties as in [Raffa et al. \(2019\)](#) is used in order to calibrate the model and compare results. The bone block is modeled as a cylinder with a radius of 50 mm and a height of 40 mm. A hemi-spherical cavity is cut into the cylinder with a radius R_b based on the fixed radius of the implant R_i and the chosen interference fit IF , i.e., $R_b = R_i - IF/2$. The edge of the cavity has a fillet radius of 2 mm.

As in Section 7.2, the bodies are meshed with surface-enriched hexahedral elements according to the parameters given in Table 7.1. The finite element mesh is shown in Figure 7.11. A refinement analysis of the mesh and the load step size is performed to ascertain mesh convergence (see Appendix A) for the reference case (see Section 7.3.1.1).

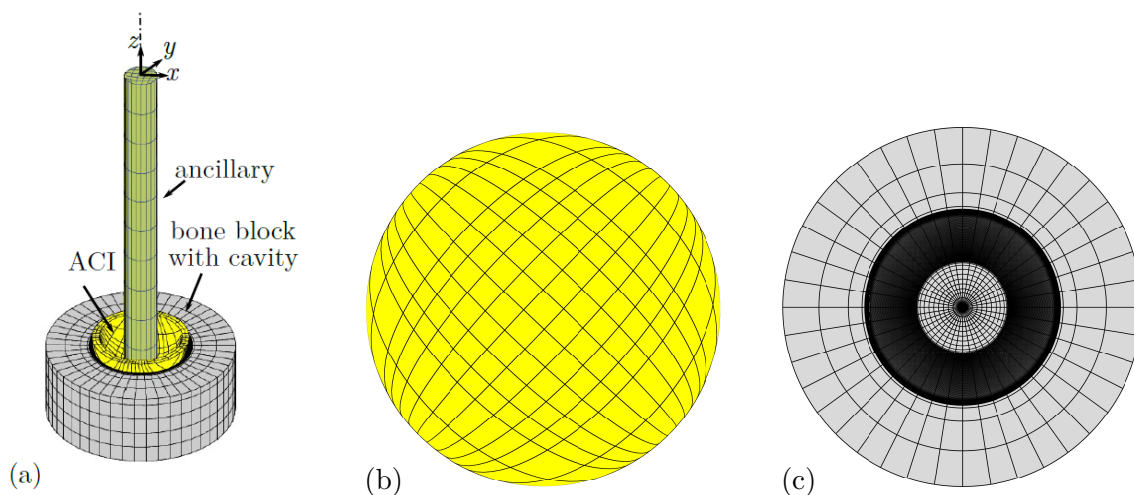


Figure 7.11 – (a) Finite element mesh of the ACI, bone block, and ancillary ([Immel et al., 2021b](#)). (b) Bottom view of the ACI implant. (c) Top view of the bone block. A very fine mesh is used around the rim of the cavity, as the contact forces are expected to vary most strongly there. Adopted from [Immel et al. \(2021c\)](#).

body	n_{el}	type of shape fcts.	n_{gp}
implant bulk	338	linear Lagrange	$2 \times 2 \times 2$
ancillary	250	linear Lagrange	$2 \times 2 \times 2$
bone bulk	20000	linear Lagrange	$2 \times 2 \times 2$
outer implant surface	169	quadratic NURBS	5×5
upper bone surface	4000	quadratic NURBS	5×5

Table 7.1 – ACI debonding: Number of finite elements n_{el} , type of shape functions and number of Gauss points per element n_{gp} for the two bodies and their contact surfaces. Adopted from [Immel et al. \(2021c\)](#).

7.3.1.1 Model Parameters

The ancillary and the ACI are assumed to be made of stainless steel ($E_a = 211$ GPa, $\nu_a = 0.3$) and titanium alloy (Ti-Al6-V4; $E_i = 113$ GPa, $\nu_i = 0.3$), respectively. The bone block is assumed to consist only of trabecular bone tissue ($\nu_b = 0.3$ ([Yew et al., 2006](#))), without an outer cortical layer. This is in accordance with the study presented in Chapter 5 and findings in the literature ([Anderson et al., 2005](#); [Phillips et al., 2007](#); [Watson et al., 2017](#)), that indicate that the reaming of the hip performed during surgery may completely remove cortical bone tissue from the contact area. For all bodies, the Neo-Hookean material model of Eq. (3.19) is used. Furthermore, all materials are assumed to be homogeneous and isotropic and both contact surfaces are assumed to be perfectly smooth.

In this work, the effect of various biomechanical properties of the bone-implant system on the ACI long-term stability is assessed. Therefore, different degrees of osseointegration from 0 – 100% are considered. Furthermore, the influence of varying bone stiffness $E_{tb} = 0.1 - 0.6$ GPa, interference fit $IF = 0 - 2.0$ mm, and friction coefficient $\mu_b = 0 - 0.7$ on the long-term stability are analyzed. The corresponding friction coefficient $\mu_{ub} = 0.15 - 1$ is taken from Table 4 from [Immel et al. \(2020\)](#) and is roughly 1.5 times higher than μ_b . Based on previous studies ([Raffa et al., 2019](#); [Immel et al., 2021a](#)) the parameter set of $E_{tb}^* = 0.2$ GPa, $IF^* = 1$ mm, and $\mu_b^* = 0.3$ is denoted as the reference case and marked with *. The parameters of the state function (6.5) are chosen to be $a_s = 128$ μm and $b_s = 1.84$, which does not affect the maximum of the removal force/torque. Due to the lack of experimental data, the values of a_s and b_s are chosen large enough so that the debonding process is visible and a removal force/torque can be identified (see Figure 7.14). The coefficients of the cohesive zone model $t_0 = t_0^* = 1.8$ MPa and $g_b = g_0 = 3a_s$ are calibrated based on the results of [Rønold and Ellingsen \(2002\)](#) for polished CSI, as was done in Section 7.2.

7.3.1.2 Boundary and Loading Conditions and Solver Settings

The bone block is fixed in all directions at the bottom surface. As before, only quasi-static conditions are considered. The simulations of implant insertion and subsequent removal are comprised of three stages (see Fig. 7.12):

1. insertion: the implant is inserted vertically into the cavity, by pushing the upper surface of the ancillary in negative z -direction, until the reaction force at the top of the ancillary reaches $F_0 = -2500$ N, similar to values found in the literature ([Sotto-Maior et al., 2010](#); [Souffrant et al., 2012](#); [Le Cann et al., 2014](#)) and to what was done in previous studies ([Raffa](#)

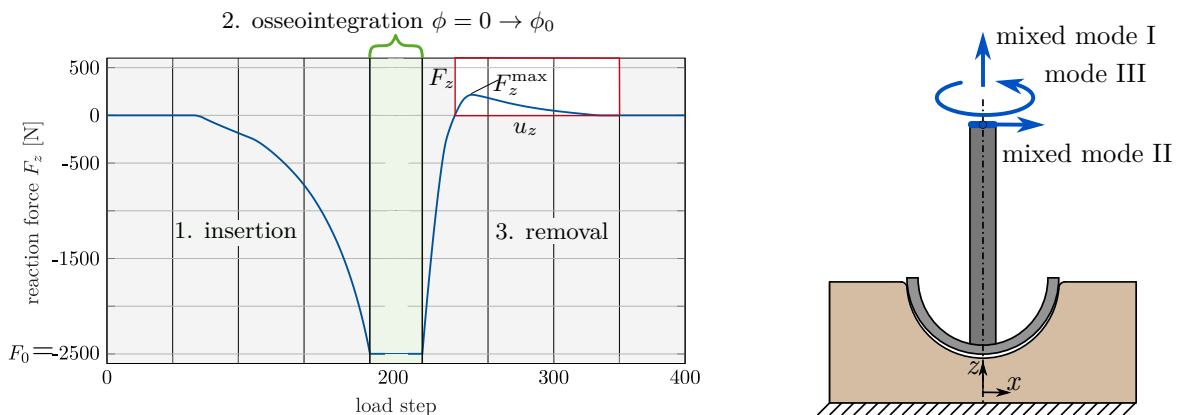
et al., 2019; Immel et al., 2021a). The downward displacement attained at the top of the ancillary for $F_0 = -2500$ N is denoted d_0 . It depends on the considered parameters E_{tb} , IF , and μ_b and thus changes for each case, i.e. $d_0 = d_0(\mu_b, IF, E_{tb}, F_0)$.

2. osseointegration: the contact surfaces are assumed to be homogeneously osseointegrated with an initial degree of osseointegration varying from $\phi_0 \in [0, 0.25, 0.5, 0.75, 1]$.
3. removal: the implant is removed either
 - mixed mode I: by displacing the upper surface of the ancillary in positive z -direction by $-d_0$,
 - mixed mode II: by displacing the center of the upper surface of the ancillary in positive x -direction by d_0 ,
 - mode III: by rotating the upper surface of the ancillary around its z -axis by $\theta = 10^\circ$.

The three simulation stages are shown in Figure 7.12(a) and the different removal cases are illustrated in Figure 7.12(b). The example of mode I debonding is shown, with the final output of the load-displacement curve inside the red square (cf. Fig. 7.13 (a)).

The stability of the configuration is then assessed by determining the maximum pull-out force in normal direction, F_z^{\max} , the maximum pull-out force in tangential direction, F_x^{\max} , or the maximum debonding torque M_z^{\max} .

Contact is computed with a penalty regularization, and the corresponding penalty parameter is chosen based on the Young's modulus of trabecular bone as $\epsilon_n = \epsilon_t = E_{tb}/L_0$, with $L_0 = R_1 = 0.0255$ m corresponding to the radius of the implant. The number of load steps for the different simulation stages are: $l_1 = l_{3,\text{modeI}} = l_{3,\text{modeIII}} = 100$ and $l_{3,\text{modeII}} = 1000$. All simulations were performed with an in-house, MATLAB-based solver (R2019b, The MathWorks, Natick, MA, USA) with MATLAB's own parallelization. Computations were performed on the RWTH Compute Cluster (Intel HNS2600BPB, Platinum 8160) with 20 cores. The average computing time for the different contact laws and loading cases is listed in Table B.3. The computing time is sensitive to the parameter combination. Parameter combinations that produce high pull-out forces/debonding torque have a longer computing time. The difference in computing time between the debonding tests and the contact models is discussed in Section 7.4.3.



(a) Illustration of the three simulation stages on the example of mode I debonding. The final output of the reaction force and maximum pull-out force is shown in red.

(b) Illustration of the three different removal tests.

Figure 7.12 – ACI debonding: (a) Illustration of the three simulation stages and (b) the three removal tests. Adopted from Immel et al. (2021c).

7.3.2 Debonding without Adhesion in Normal Direction

First, the results of the removal tests, in terms of load-displacement curves and pull-out force/ debonding torque, obtained with the MC are presented. The results with the EMC follow in Section 7.3.3, and a comparison is given in Section 7.4.1.

7.3.2.1 Mixed Mode I: Normal Pull-Out Test

Figure 7.13 (a) shows the normal reaction force F_z^* for the reference case, which increases and reaches a peak at a displacement of 0.25–0.32 mm and then slowly decreases to zero. This maximum coincides with the start of the decrease of the average degree of osseointegration of the bone-implant interface $\bar{\phi}$ (see Figure 7.13, (b)). At a displacement of 1.07 mm, the reaction force becomes independent from ϕ_0 . At this point, the bone-implant interface is completely debonded ($\bar{\phi} = 0$) and only pure Coulomb's friction is taking place until the contact at the bone-implant interface is lost completely at a displacement of about 4.25 mm. In this test, osseointegration only affects the magnitude of the peak, while the overall slope of the load-displacement curve remains unchanged when increasing the initial degree of osseointegration. The location of the peak does not change significantly with increasing ϕ_0 .

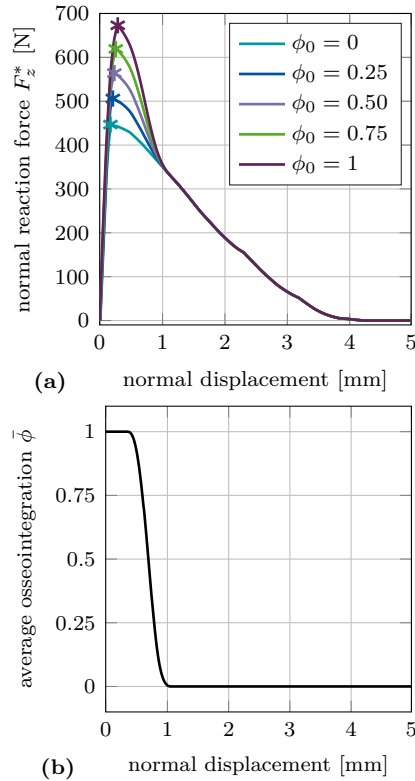


Figure 7.13 – Normal debonding without adhesion for the reference case: (a) Variation of the normal force F_z^* a function of the initial degree of osseointegration ϕ_0 . The maximum pull-out force $F_z^{\text{max}*}$ is marked with *. (b) Average degree of osseointegration of the bone-implant interface $\bar{\phi}$ for an initial degree of osseointegration $\phi_0 = 1$. Adopted from [Immel et al. \(2021c\)](#).

Due to the lack of experimental data for this work, the values of $a_s^* = 128 \mu\text{m}$ and $b_s^* = 1.84$ are chosen large enough so that the debonding process is visible and a removal force/torque can

be identified. The effect of changing the value of a_s and b_s on $F_z^*(\phi_0 = 1)$ is shown in Figure 7.14. Naturally, both parameters have no effect on the mechanical behavior before debonding and on the maximum pull-out force. Decreasing or increasing a_s and b_s decreases or increases the amount of deformation that is necessary for the interface to fully debond (about 0.7, 0.75, 1.1, 1.75, 1.9 mm, respectively, see Fig. 7.14). After debonding, only pure Coulomb's friction takes place until the contact between bone and implant is lost completely (after a displacement of about 4.25 mm).

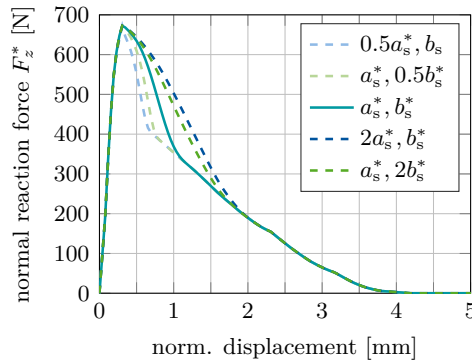


Figure 7.14 – Normal debonding without adhesion: Variation of the normal force F_z^* for $\phi_0 = 1$ as a function of the MC parameters a_s and b_s . Adopted from [Immel et al. \(2021c\)](#).

Figure 7.15(a)–(c) shows the maximum normal pull-out force F_z^{\max} as a function of the interference fit IF , trabecular bone stiffness E_{tb} , friction coefficient μ_b , for different values of the initial degree of osseointegration ϕ_0 . The results obtained for F_z^{\max} with $\phi_0 = 0$ are identical to the results from [Raffa et al. \(2019\)](#), which constitutes a validation of the model. First, the pull-out force increases as a function of IF , E_{tb} , μ_b , then reaches a peak, and eventually decreases. The maximum value of the pull-out force is obtained for around $IF = 1.4$ mm, $E_{tb} = 0.4$ GPa, and $\mu_b = 0.6$. For $\mu_b \leq 0.15$ the pull-out force is zero, for all degrees of osseointegration.

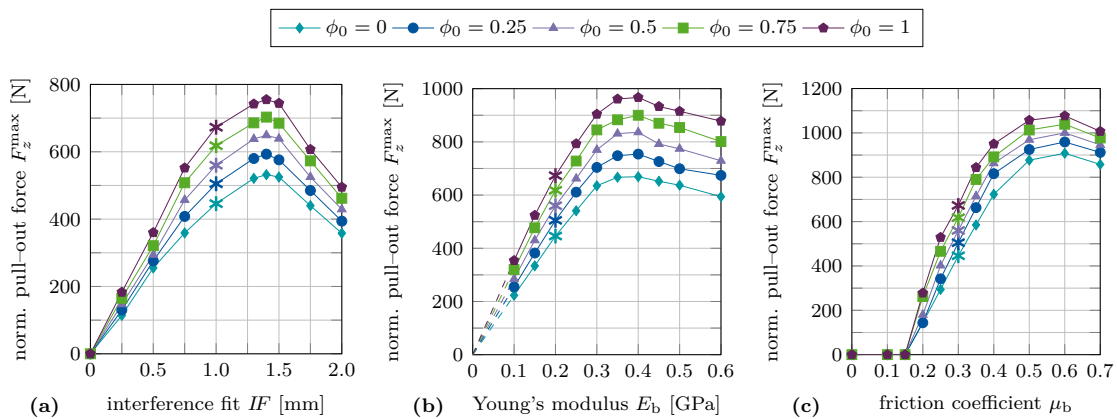


Figure 7.15 – Normal debonding without adhesion: Variation of the maximum normal pull-out force F_z^{\max} as a function of the initial degree of osseointegration ϕ_0 and (b) the interference fit IF , (c) the trabecular Young's modulus E_{tb} , and (d) the friction coefficient μ_b . The reference case is marked with *. Adopted from [Immel et al. \(2021c\)](#).

7.3.2.2 Mixed Mode II: Tangential Pull-out Test

The tangential reaction force F_x^* for the reference case increases and reaches a peak at a displacement of about 75 μm and then slowly decreases to zero (see Figure 7.16 (a)). The average degree of osseointegration of the bone-implant interface $\bar{\phi}$ starts to decrease already beyond 34 μm (Figure 7.16 (b)). At a displacement of about 0.3 mm, the reaction force becomes independent from ϕ_0 . Similarly to the normal pull-out test, increased osseointegration only affects the magnitude of the tangential pull-out force, while the location of the peaks and the initial slope of the curves for different degrees of osseointegration are very similar.

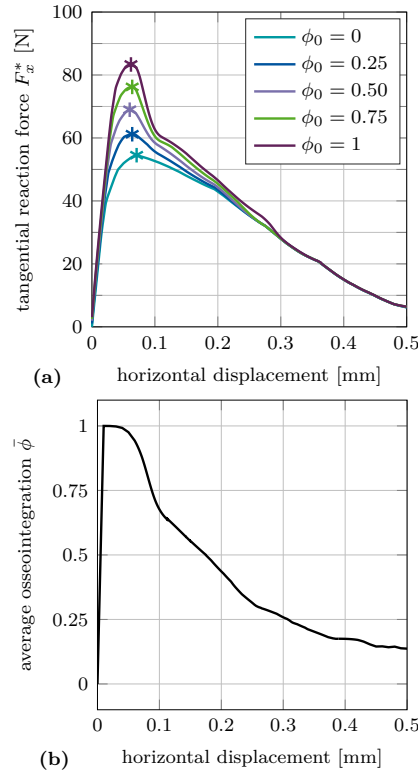


Figure 7.16 – Tangential debonding without adhesion for the reference case: (a) Variation of the tangential force F_x^* as a function of the initial degree of osseointegration ϕ_0 . The maximum pull-out force $F_x^{\text{max}*}$ is marked with *. (b) Average degree of osseointegration of the bone-implant interface $\bar{\phi}$ for an initial degree of osseointegration $\phi_0 = 1$. Adopted from [Immel et al. \(2021c\)](#).

Figure 7.17(a)–(c) shows the maximum tangential pull-out force F_x^{max} as a function of the interference fit IF , trabecular bone stiffness E_{tb} , friction coefficient μ_b , for different values of the initial degree of osseointegration ϕ_0 . First, the pull-out force increases as a function of IF , E_{tb} and μ_b , then reaches a peak, and eventually decreases. The maximum value of the pull-out force is obtained for around $IF = 1.4$ mm, $E_{\text{tb}} = 0.4$ GPa, and $\mu_b = 0.6$ – the same values as for the normal pull-out test. For $\mu_b \leq 0.15$ the pull-out force is zero for all degrees of osseointegration. Tangential pull-out forces are roughly one magnitude lower than the corresponding normal pull-out force, which agrees with observations from clinical practice. During surgery, after the insertion of the ACI, surgeons often attempt to lever out an acetabular cup to test the seating of the ACI. That is, the surgeon applies a tangential force, such as is considered here, instead

of a normal force since normal pull-out would require too much force.

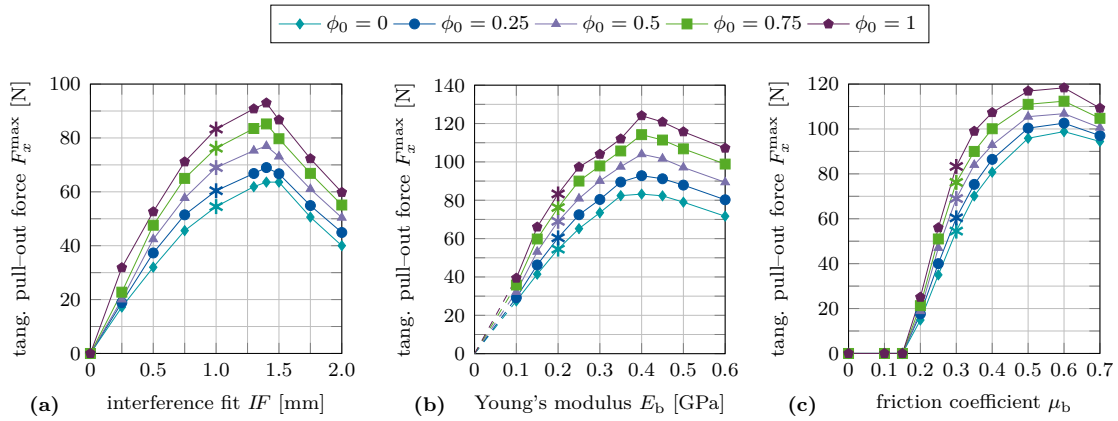


Figure 7.17 – Tangential debonding without adhesion: Variation of the maximum tangential pull-out force F_x^{\max} as a function of the initial degree of osseointegration ϕ_0 and (a) the interference fit IF , (b) the trabecular Young's modulus E_{tb} , and (c) the friction coefficient μ_b . The reference case is marked with *. Adopted from [Immel et al. \(2021c\)](#).

7.3.2.3 Mode III: Torsional Debonding Test

Figure 7.19 (a) shows the debonding torque M_z^* as a function of the rotation angle for different values of ϕ_0 and the reference case. The torque increases, reaches a peak at an angle of about 3° and then decreases to reach a constant torque of 47 Nm at about 4.5° due to the present compressive normal force. The degree of osseointegration starts to decrease at an angle of about 2.6° and becomes zero at about 4.5° (see Figure 7.19 (b)). As for the normal and the tangential pull-out cases, only the magnitude of the peak of the load-displacement curve is affected when increasing the degree of osseointegration ϕ_0 .

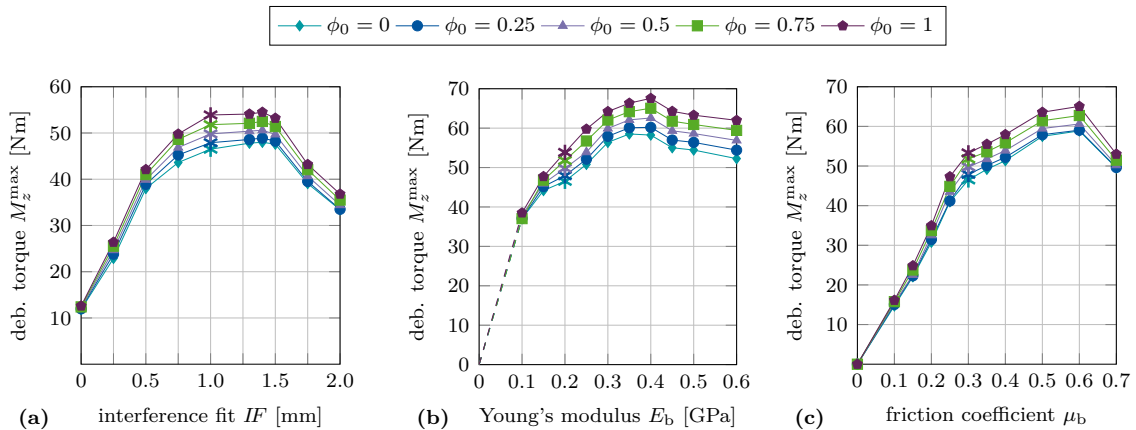


Figure 7.18 – Torsional debonding without adhesion: Variation of the maximum debonding torque M_z^{\max} as a function of the initial degree of osseointegration ϕ_0 and (a) the interference fit IF , (b) the trabecular Young's modulus E_{tb} , and (c) the friction coefficient μ_b . The reference case is marked with *. Adopted from [Immel et al. \(2021c\)](#).

Figures 7.18 (a)–(c) show the variation of the maximum debonding torque M_z^{\max} as a function of the parameters IF , E_{tb} , μ_b , and ϕ_0 . First, the torque increases with increasing parameter

IF , E_{tb} , μ_b , reaches a peak, and then decreases. The maximum values of the torque are obtained around $IF = 1.4$ mm, $E_{tb} = 0.4$ GPa, and $\mu_b = 0.6$, which correspond to the same parameters as for the pull-out tests. For the interference fit IF , a larger plateau for $IF = 1.0 - 1.5$ mm as compared to the pull-out tests is obtained. The maximum torque obtained for $\phi_0 = 1$ is 55 Nm, 68 Nm, and 65 Nm, respectively.

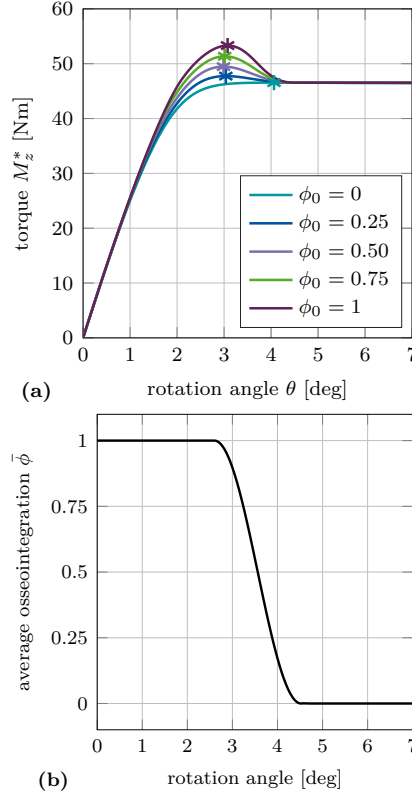


Figure 7.19 – Torsional debonding without adhesion for the reference case: (a) Variation of the debonding torque M_z^* as a function of the initial degree of osseointegration ϕ_0 . The maximum debonding torque $M_z^{\max*}$ is marked with *. (b) Average degree of osseointegration of the bone-implant interface $\bar{\phi}$ for an initial degree of osseointegration $\phi_0 = 1$. Adopted from [Immel et al. \(2021c\)](#).

7.3.3 Debonding with Adhesion in Normal Direction and Adhesive Friction

The results corresponding to the load-displacement curves and pull-out force/ debonding torque obtained with the three removal tests and with the EMC are presented below. In addition to the modified Coulomb's friction law (6.3), the EMC includes a CZM in normal direction (7.1) and adhesive friction (7.2).

7.3.3.1 Mixed Mode I: Normal Pull-out Test

Figure 7.20 shows the variation of the normal reaction force F_z^* as a function of the tangential displacement and the initial degree of osseointegration ϕ_0 for the reference case. The normal reaction force increases, reaches a peak at a displacement of about 0.25 mm and then decreases. The effect of osseointegration and adhesive friction on the load-displacement curve is more pronounced than for the MC. This can be seen as the magnitude increase of the pull-out forces

is higher and the peaks are wider (compare Figures 7.13 (a) and 7.20). In contrast to the MC, here, F_z^* depends on ϕ_0 throughout the whole debonding process, which is due to the adhesion in normal direction. However, the initial slope of the normal reaction force curves does not change significantly when increasing ϕ_0 . Compared to the results obtained when considering only tangential debonding (see Fig. 7.13 (a)), some small oscillations after the peak are visible.

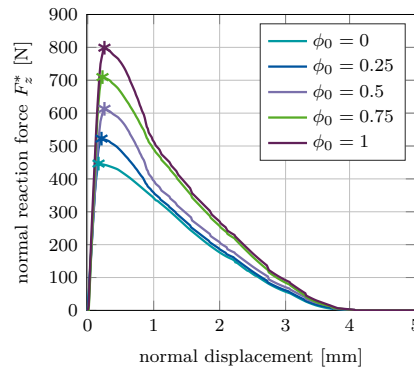


Figure 7.20 – Normal debonding with adhesive friction: Variation of the normal force F_z^* as a function of the initial degree of osseointegration ϕ_0 for the reference case. The maximum pull-out force $F_z^{\max*}$ is marked with *. Adopted from [Immel et al. \(2021c\)](#).

Figures 7.21 (a)–(c) show the maximum normal pull-out force F_z^{\max} as a function of the parameters IF , E_{tb} , μ_b , and ϕ_0 . The slopes of the different curves of pull-out forces are similar to the ones obtained with the MC (cf. Section 7.3.2.1), with the peak values obtained for the same values of IF , E_{tb} , and μ . For $\mu_b \leq 0.15$ the pull-out force remains equal to zero, regardless of the degree of osseointegration.

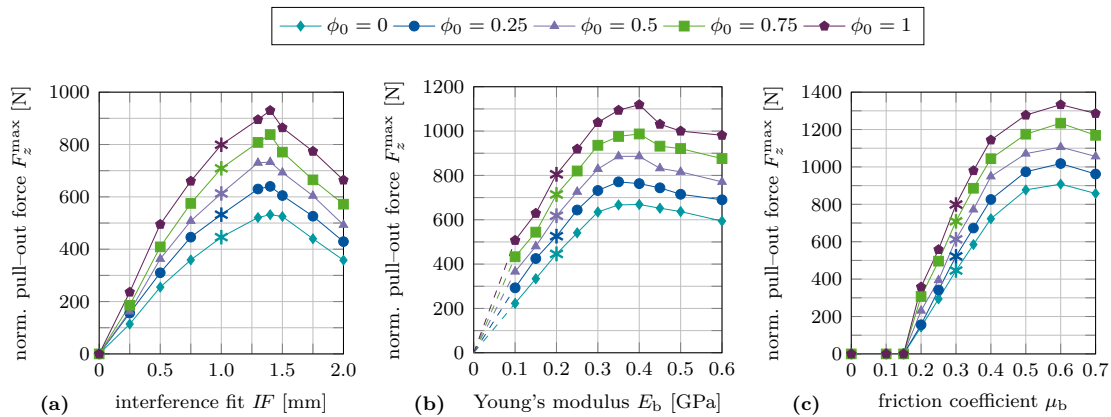


Figure 7.21 – Normal debonding with adhesive friction: Variation of the maximum normal pull-out force F_z^{\max} as a function of the initial degree of osseointegration ϕ_0 and (a) the interference fit IF , (b) the trabecular Young's modulus E_{tb} , and (c) the friction coefficient μ_b . The reference case is marked with *. Adopted from [Immel et al. \(2021c\)](#).

7.3.3.2 Mixed Mode II: Tangential Pull-Out Test

Figure 7.22 shows the tangential reaction force F_x^* as a function of the tangential displacement for different values of ϕ_0 . The effect of osseointegration and adhesive friction on the load-displacement curve is more pronounced with the EMC than with the MC. As for the normal

pull-out test, F_x^* remains dependent on ϕ_0 throughout the whole debonding process. The peak in tangential reaction force is reached at a displacement of about 0.08 mm. Furthermore, the increase in magnitude is considerably larger than for the MC, while remaining roughly one magnitude lower than the results for the normal pull-out case with adhesive friction. Here, larger oscillations are visible, which are discussed in Section 7.4.3.

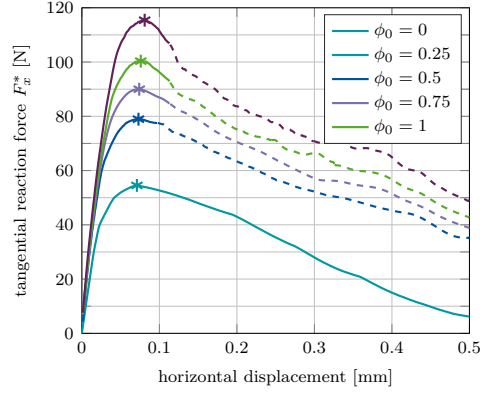


Figure 7.22 – Tangential debonding with adhesive friction: Variation of the tangential force F_x^* a function of the initial degree of osseointegration ϕ_0 for the reference case. The maximum pull-out force $F_x^{\max*}$ is marked with *. Adopted from [Immel et al. \(2021c\)](#).

Figures 7.23 (a)–(c) show the variation of the maximum tangential pull-out force F_x^{\max} as a function of the parameters IF , E_{tb} , μ_b , and ϕ_0 . While the peaks in tangential pull-out force are obtained for the same parameters as before, the slope of F_x^{\max} as a function of all parameters (IF , E_{tb} , μ_b) depends on the initial degree of osseointegration. As before, for $\mu_b \leq 0.15$ the tangential pull-out force remains zero independent of the degree of osseointegration.

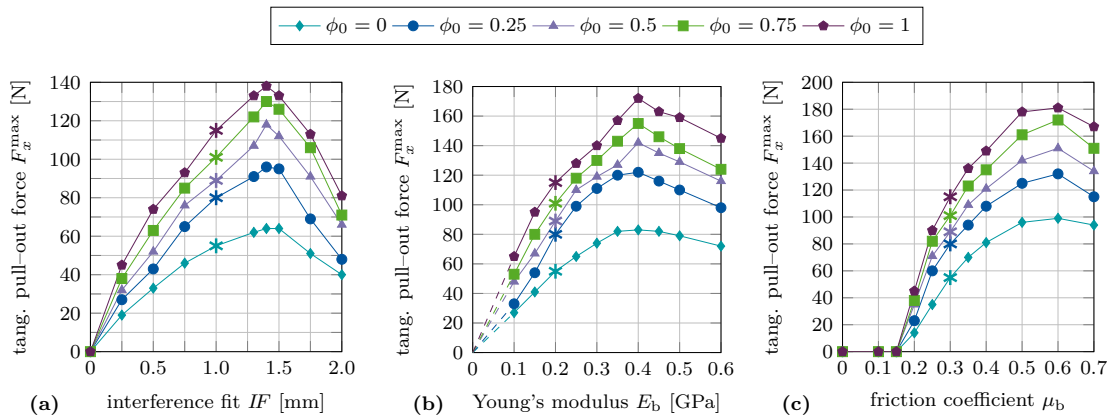


Figure 7.23 – Tangential debonding with adhesive friction: Variation of the maximum tangential pull-out force F_x^{\max} as a function of the initial degree of osseointegration ϕ_0 and (a) the interference fit IF , (b) the trabecular Young's modulus E_{tb} , and (c) the friction coefficient μ_b . The reference case is marked with *. Adopted from [Immel et al. \(2021c\)](#).

7.3.3.3 Mode III: Torsional Debonding Test

Figure 7.24 shows the variation of the debonding torque M_z^* as a function of the rotation angle and the initial degree of osseointegration ϕ_0 for the reference case. In contrast to the results

obtained with the MC, the peak in torque is obtained at a rotation angle of approximately $\theta = 3.5^\circ$. Then the torque decreases to a constant value due to the present compressive normal force. When considering adhesive friction, the torque after full debonding does not reach the same constant values for each ϕ_0 due to the shift in the tangential sliding threshold (7.2), that depends on ϕ_0 .

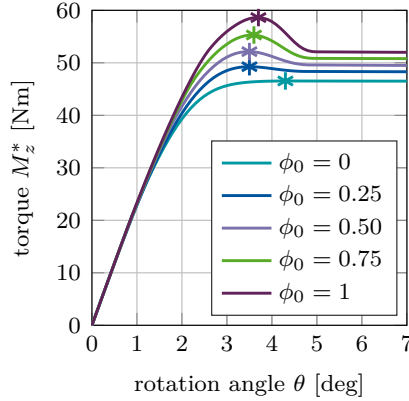


Figure 7.24 – Torsional debonding with adhesive friction: Variation of the debonding torque M_z^* as a function of the initial degree of osseointegration ϕ_0 for the reference case. The maximal torque $M_z^{\max*}$ marked with *. Adopted from [Immel et al. \(2021c\)](#).

Figures 7.25 (a)–(c) show the variation of the maximum debonding torque M_z^{\max} as a function of the parameters IF , E_{tb} , μ_b , for different values of ϕ_0 . In contrast to the pull-out test, the removal torque curves are very similar to the corresponding results obtained with the modified Coulomb’s law. Peaks in torque are obtained for the same values of IF , E_{tb} , μ_b as for the pull-out tests and the modified Coulomb’s law.

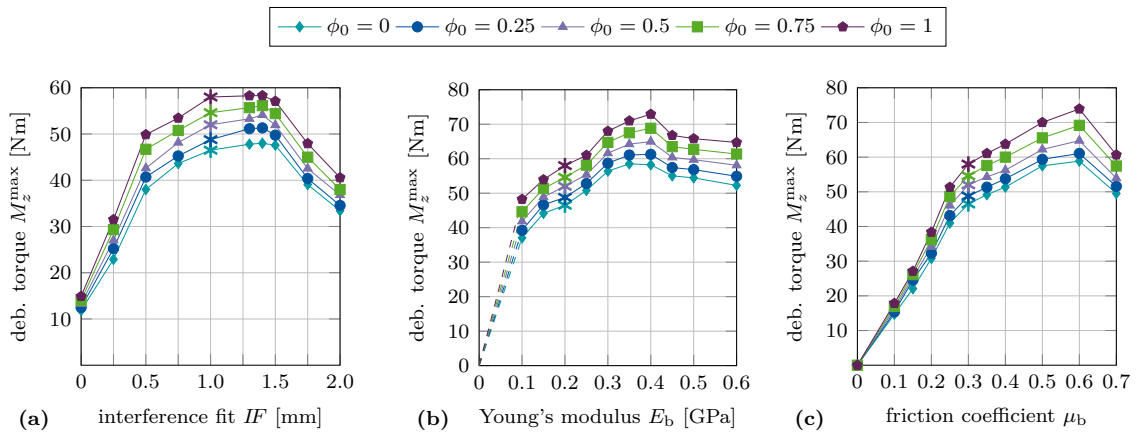


Figure 7.25 – Torsional debonding with adhesive friction: Variation of the maximal debonding torque M_z^{\max} as a function of the initial degree of osseointegration ϕ_0 and (a) the interference fit IF , (b) the trabecular Young’s modulus E_{tb} , and (c) the friction coefficient μ_b . The reference case is marked with *. Adopted from [Immel et al. \(2021c\)](#).

7.4 Discussion

This work studies the contact and debonding behavior between implant and bone using a new adhesive friction model that accounts for partial osseointegration. The new extension to adhesive friction is first demonstrated on a simple model of an osseointegrated implant, following previous studies (Rønold and Ellingsen, 2002; Rønold et al., 2003; Fraulob et al., 2020a,b,c; Immel et al., 2020). Then, both the original and the extended debonding model, are applied to the debonding of a partially osseointegrated acetabular cup implant, which corresponds to a situation of clinical interest. The effect of increasing the osseointegration level on implant stability is examined by analyzing the behavior of the maximum removal force/torque, for three patient- and implant-dependent parameters: IF , E_{tb} , and μ_b . Overall, both debonding models provide reasonable qualitative estimates of long-term stability with higher estimates of implant stability for the extension to adhesive friction.

7.4.1 Comparison of the Modified and Extended Coulomb's Law with Respect to their Biomechanical Relevance

Figure 7.26 shows the ratio between the maximum removal forces/torque obtained for perfect initial osseointegration ($\phi_0 = 1$) and no initial osseointegration ($\phi_0 = 0$) ($F^{\max}(\phi_0 = 1)/F^{\max}(\phi_0 = 0)$) for the studied parameters and removal tests when considering both proposed models. Table 7.2 shows the corresponding average percentage increase in the maximum pull-out forces/torque. The relative variation of the pull-out force/debonding torque obtained by considering the modified Coulomb's law is qualitatively similar when varying IF and E_{tb} , with values ranging between 38 and 62%, with a slightly higher increase of the reaction force for lower values of IF and E_{tb} . Concerning the friction coefficient μ_b , the modified Coulomb's law shows the largest effect on the pull-out force/torque for a value of $\mu_b = 0.2$. This effect then decreases when increasing the friction coefficient. The increase of the maximum pull-out force is much higher for the EMC compared to the MC with values ranging between 46–172%. In addition, osseointegration modeled with the EMC leads to a larger increase of the maximum removal force/torque for low parameter values, which corresponds to low initial stability but high contact area.

While the relative variation of F_x^{\max} , F_z^{\max} , M_z^{\max} produced by the two debonding models due to changes of μ_b are very similar, the slopes of the curves in Figure 7.26 for IF and E_{tb} show considerable differences between the two contact models. The MC only has a small effect on the maximum torque for all observed parameters with a total increase in torque of 7–15%. The present extension produces a higher increase in the maximum torque of 21–35%, due to the shift in the tangential traction Eq. (7.2). Overall, the effect on the maximum torque remains considerably lower compared to the pull-out tests, as no contact is lost during the torsion test. Table 3 lists the average percentage increase in the maximum pull-out forces F_x^{\max} , F_z^{\max} and debonding torque M_z^{\max} from 0 to 100% osseointegration for interference fit IF , Young's modulus E_{tb} , and friction coefficient μ_b for both contact laws.

Both presented contact models produce reasonable estimates for the long-term stability of the ACI, when compared to existing numerical results for the initial stability (Raffa et al., 2019) (see Figures 7.13 and 7.20, $\phi_0 = 0$). Overall, the maximum pull-out forces F_x^{\max} , F_z^{\max} and the debonding torque M_z^{\max} all increase nearly linearly with increasing degree of osseointegration ϕ_0

for every chosen parameter IF, μ_b, E_{tb} . In this work, osseointegration is shown to significantly increase implant stability (see Figure 7.26). However, the dependence of the maximum pull-out force/debonding torque on the different parameter sets remains essentially the same as for primary stability.

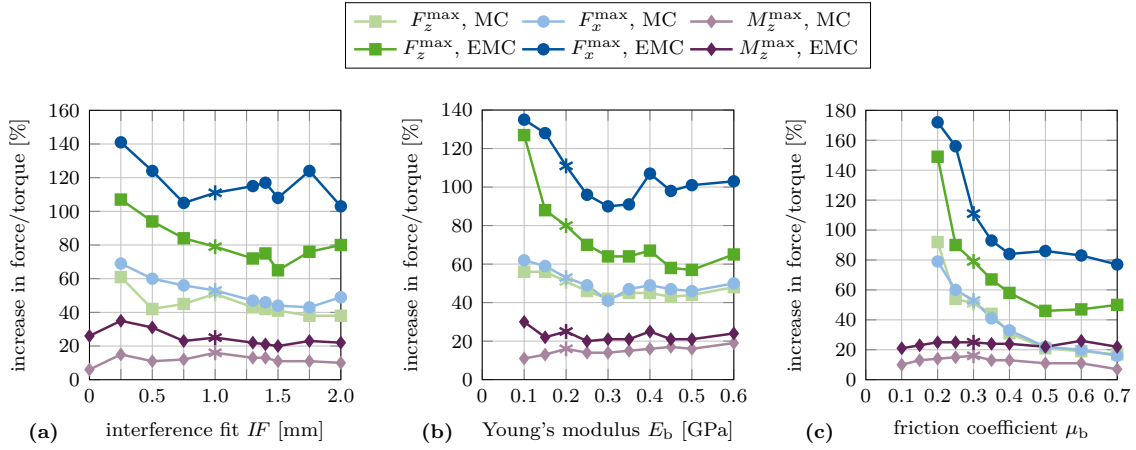


Figure 7.26 – Ratio between the maximum removal forces/torque obtained for perfect initial osseointegration ($\phi_0 = 1$) and no initial osseointegration ($\phi_0 = 0$) as a function of (a) the interference fit IF , (b) the trabecular Young's modulus E_{tb} , and (c) the friction coefficient μ_b for the different removal tests. Shown are results for the modified Coulomb's law (MC) and the new extension (EMC). The reference case is marked with *. Some results for $IF = 0$ mm, $E_{tb} = 0$, and $\mu_b = 0 - 0.15$ are omitted, as there is no measurable increase in removal force/debonding torque. Adopted from [Immel et al. \(2021c\)](#).

force/torque model	F_z^{\max}		F_x^{\max}		M_z^{\max}	
	MC	EMC	MC	EMC	MC	EMC
interference fit IF	42%	81%	50%	116%	12%	26%
Young's modulus E_{tb}	48%	74%	50%	106%	15%	24%
friction coefficient μ_b	41%	73%	41%	108%	12%	21%

Table 7.2 – Average percentage increase in the maximum pull-out forces F_z^{\max}, F_x^{\max} and debonding torque M_z^{\max} from 0 to 100% osseointegration for interference fit IF , Young's modulus E_{tb} , and friction coefficient μ_b for the modified Coulomb's law (MC) and its new extension (EMC). Adopted from [Immel et al. \(2021c\)](#).

The two presented contact models indicate that poor initial stability will lead to poor or suboptimal long-term stability, which emphasizes the crucial role of primary stability for the implant outcome. This finding is in agreement with the literature, where initial stability is determined as the governing factor of long-term stability ([Pilliar et al., 1986](#); [Engh et al., 1992, 2004](#); [Rittel et al., 2018](#)), as the mechanical conditions at the bone-implant interface have a significant effect on bone growth and remodeling. Furthermore, the present extension has a higher effect on poor initial stability, stressing the importance of adhesion for low initial stability.

Both presented debonding models also allow the assessment of how loading that does not result in complete debonding affects the remaining osseointegration state ϕ of the bone-implant interface (see e.g. Figure 7.13 (b)). Future studies that couple the EMC with cyclic loading

and bone growth and remodeling could e.g. provide answers on how daily loading affects the bonding state of the interface during and after healing.

7.4.2 Comparison with Similar Studies

Since most numerical studies that model osseointegrated interfaces assume perfectly bonded surfaces and thus, do not simulate the actual debonding of the interface, only few comparisons with existing work can be made. One comparable work is the study of [Rittel et al. \(2018\)](#), where the influence of partial osseointegration on dental implant stability and cohesive failure was studied. There, a tie constraint was applied to parts of the bone-implant interface throughout the simulation, such that bone-implant debonding occurred as cohesive failure in the bone around the bone-implant interface. Partial osseointegration was modeled by defining a relative osseointegrated area with a random distribution and restricting non-integrated areas to frictional contact. One key finding of the study of [Rittel et al. \(2018\)](#) was that none of their removal tests was able to distinguish osseointegration above 20% and that the torque test was more accurate than a pull-out test in determining the degree of osseointegration. Based on these findings, it was concluded that osseointegration of only 20% of the bone-implant interface provides sufficient long-term stability. In the present study, opposite findings are obtained. Here, all considered debonding tests show consistent increase in stability for increasing initial degree of osseointegration. Furthermore, osseointegration showed the least effect on the debonding torque and the highest for mode II debonding. The difference between the two studies might stem from the difference between the cohesive failure model of [Rittel et al. \(2018\)](#) and the adhesive failure models presented here, and/or the difference in geometry and contact conditions.

Further studies and especially experimental testing, as proposed in Section 7.2, are necessary in order to calibrate and validate the proposed contact models.

7.4.3 Numerical Stability

Mesh convergence was investigated for the reference case and the modified Coulomb's friction law (see Appendix B.3). The load-displacement curves obtained when considering adhesive friction (see Figures 7.20 and 7.22 (a)) show oscillations in the reaction force after the peak and require an increased number of Newton-Raphson iterations and thus, increased computing (see Appendix A). In the cases of normal and tangential debonding, the added adhesion in normal direction results in alternating sticking and sliding (so called stick-slip motion), producing oscillations in the results. The quasi-static assumption used in this work is not suitable in those cases and a dynamic simulation should be performed instead to account for the inertia in the system.

Due to the lack of experimental data and comparable numerical results, the *a priori* assessment of the choice of mesh, boundary conditions and relevance of inertia, remains difficult and thus the results can only provide a qualitative statement of the relevance of the analyzed parameters on implant stability.

7.4.4 Perspectives and Guidelines for Future Work

In the following, perspectives for future extensions and applications of the proposed bone and contact models are discussed. Furthermore, we state guidelines for future experimental

testing, in order to obtain relevant data to calibrate and validate the proposed models.

7.4.4.1 Modeling Perspectives

Bone Modeling

This work uses idealized bone geometries. This was done in order to use results from [Raffa et al. \(2019\)](#) as calibration for cases with $\phi_0 = 0$. Further, our work focuses on the contact behavior of the osseointegrated bone-implant interface. The contact geometry and contact conditions of the hemispherical cavity are very similar to a generic pelvis. While the simplified bone geometry is a justified simplification in this work, an analysis of e.g. different pelvis shapes and defects on the contact behavior of the bone-implant interface would be of clinical relevance.

The bone block was modeled with trabecular bone without a cortical layer and the bone was rigidly fixed at the entire bottom surface. The absence of cortical bone in the contact area is in accordance with a previous study ([Immel et al., 2021a](#)) and findings in the literature ([Anderson et al., 2005](#); [Phillips et al., 2007](#); [Watson et al., 2017](#)), that indicate that the reaming performed during surgery may completely remove cortical bone tissue from the contact area. Due to the simplified setup, the influence of muscle tissue and ligaments on the deformation behavior and load response was neglected as well, which is in agreement with what is commonly done in the literature ([Hao et al., 2011](#); [Clarke et al., 2013](#)). However, it has been shown that muscles and ligaments have to be taken into account when analyzing the stress distribution inside the acetabulum ([Shirazi-Adl et al., 1993](#)), which is beyond the scope of the present study. Future studies should consider more realistic and physiological geometries and boundary conditions to improve the accuracy of the numerical results and provide more reliable estimations of implant stability.

No actual bone ingrowth or bone remodeling was modeled and homogeneous osseointegration over the whole bone-implant interface was assumed. In reality, only certain parts of the bone-implant interface are osseointegrated depending on the contact conditions, such as contact stress, micromotion, and initial gap. In addition, initial gaps after surgery might be filled with bone tissue during the healing phase and thus increase the contact area and bonding strength over time. In future works, the presented debonding models should be coupled with suitable osseointegration models and bone remodeling algorithms ([Caouette et al., 2013](#); [Mukherjee and Gupta, 2016](#); [Chanda et al., 2020](#); [Martin et al., 2020](#)), to achieve a more reliable assessment of implant long-term stability. These models should account for pressure- and micromotion-dependent bone apposition and resorption, as well as changes in the contact gap and the maturation of new bone tissue, e.g. by changing the bone's elastic properties with respect to healing time. Furthermore, due to bone growth and the change in elastic properties of the bone during osseointegration and remodeling, the stress inside the bone changes during the healing process and might be significantly different after healing compared to the state directly after surgery. As the change in stress can significantly affect secondary stability, remodeling related effects should be considered in future works.

Contact Modeling

This work neglects the roughness of the implant surface and of the reamed bone cavity. While a simple modeling of rough surfaces by adjusting μ_b, μ_{ub}, t_0 is possible, the explicit modeling of

rough surfaces should be considered in future works, as surface roughness affects initial stability and osseointegration and thus also long-term stability. Furthermore, due to the rise of additive manufacturing in implantology, complex implant surface topologies become more and more relevant and should be studied.

The CZM in Eq. (7.1) is modeled with a sharp drop in t_n at $g_n = g_b$. Future studies should explore CZM models that depend on ϕ instead of ϕ_0 and have a smooth decline in t_n for $g_n > g_b$.

The removal force/debonding torque were chosen as determinants of long-term stability. The stress distribution could be used as another determinant, as is done in other works (Janssen et al., 2010; Rourke and Taylor, 2020). However, the stress distribution inside the bone changes during healing and osseointegration, as the mechanical properties of the bone tissue change when the new bone tissue mineralizes. This makes comparisons of stress fields of initial stability and secondary stability scenarios difficult, when this temporal change is not accounted for.

As in previous studies by our group (Raffa et al., 2019; Immel et al., 2020, 2021a), a quasi-static configuration was considered, and all dynamic aspects were neglected, similarly to what was done in comparable works (Spears et al., 2001; Le Cann et al., 2014; Raffa et al., 2019). Note that a previous study focuses on the insertion process of an acetabular cup implant by considering dynamic modeling (Michel et al., 2017), which is important when modeling the insertion by hammer impacts. Furthermore, the stick-slip results with the present extended contact model (see Figures 7.20 and 7.22) indicate that dynamic simulations become necessary when considering high frictional and adhesive forces.

7.4.4.2 Experimental Perspectives

Model EMC depends on two additional physiological parameters t_0, g_0 that can be determined based on some of the few experimental results available in the literature (Rønold and Ellingsen, 2002). However, to the best of our knowledge, no suitable measurements have been obtained for osseointegrated acetabular cup implants yet, which is why we calibrated our models with measurements for coin-shaped implants instead. Future experimental tests of osseointegrated implants under mixed mode or mode III debonding under constant tension (as presented in Section 7.2) can provide important insight on the adhesive behavior of the osseointegrated interface to calibrate and validate the proposed debonding models.

Last, the strong influence of biological as well as mechanical factors and the bone geometry on the long-term stability make validation of the presented numerical models difficult. At present, experimental studies that provide sufficient information on the behavior and stability of the partially osseointegrated bone-implant interface, are lacking in the literature (Helgason et al., 2008). We suggest to perform mixed mode debonding and mode III debonding under constant tension, as demonstrated in Section 7.2. These results would provide important information on the debonding behavior of osseointegrated interfaces and allow to further calibrate and validate the extension of the modified Coulomb's law. Further computational studies cannot reliably provide more insight on the *in vivo* behavior, as the level of sophistication of the models is beyond the point of verification with current *in vivo*, *ex vivo*, and even some *in vitro* measurement techniques (Taylor and Prendergast, 2015). Therefore, it becomes more and more difficult to reliably assess the performance of numerical models for the bone-implant interface. If FE models are to be trusted and accepted by clinicians, they need to demonstrate that they are capable of predicting realistic *in vivo* behavior. Thus, further development of experimental

measurement techniques and quantification of relevant biomechanical metrics (e.g., stress-strain behavior, micromotion, friction, adhesion, debonding under tension) is essential to provide the data necessary to develop and improve numerical models. However, the development of new and more accurate experimental machinery and techniques that are able to provide the necessary data is difficult and time consuming and provides a constant challenge. While experimental and numerical methods keep improving, a certain acceptance that FE studies may not be representative of the *in vivo* conditions yet but are an approximate model, needs to be established.

7.5 Conclusion

This work presents a new extended debonding model for the bone-implant interface, which can describe the debonding behavior of osseointegrated acetabular cup implants and thus assess their stability. In addition to the modified Coulomb's law in Chapter 6, it includes a cohesive zone model in normal direction and adhesive friction in tangential direction.

The modified Coulomb's law and its extension show that friction and adhesion increase the pull-out force/debonding torque of osseointegrated implants, and thus are relevant for long-term stability. Furthermore it is shown that, while osseointegration increases implant secondary stability, a sufficient primary stability remains crucial for long-term stability, which is in agreement with the literature. These findings underline the importance of the development of surgical decision support systems such as the surgical hammer instrumented with a force sensor to measure the displacement of an osteotome or implant and determine when full insertion has taken place (Michel et al., 2016a,b; Dubory et al., 2020; Lomami et al., 2020) or contactless vibro-acoustic measurement devices that can monitor implant seating (Goossens et al., 2021). Furthermore, a future detailed study would be able to answer how cyclic loading affects the bonding state of the interface during and after healing. Last, this work provides directions for important experimental testing of osseointegrated coin-shaped implants. Mixed mode debonding and mode III debonding under constant tension could provide important information on the debonding behavior of osseointegrated interfaces and allow for further calibration and validation of the proposed contact models. Furthermore, osseointegration algorithms based on, e.g., the contact state, should be considered instead of pre-defined or homogeneous osseointegration as has been done in this and the previous chapter. Coupling simulations of initial stability, subsequent osseointegration and bone remodeling, and long-term stability and debonding can provide more reliable assessments of implant stability and aid in implant conception and individual patient treatment. A simple example of coupling the developed debonding models from Chapters 6 and 7 with an osseointegration algorithm instead of using pre-defined osseointegration is presented in the next chapter. There, three simple evolution laws for osseointegration, based on the primary stability of the implant are introduced and demonstrated on a CSI.

Chapter 8

Evolution Laws for Osseointegration Based on Initial Stability

In the previous chapters, numerical models for the secondary stability of partially osseointegrated implants with pre-defined osseointegration patterns or homogeneous distribution were presented. To complete the workflow of the numerical modeling of implant stability and the implant life cycle presented in this thesis, this chapter provides an outlook on how to model osseointegration and healing, and how to incorporate it into the workflow of simulating implant stability. Therefore, three simple evolution laws for osseointegration are outlined. These models depend on the contact gap and the contact pressure of the BII after insertion, and the healing time. Thus, the pressure and displacement fields created during the simulation of implant insertion, such as presented in Chapter 5 can be used as input for the modeling of bone apposition and the creation of osseointegration patterns. This computed osseointegration setting can then be used instead of the pre-defined patterns presented in Chapter 6 or the homogeneous approach used in Chapter 7. This procedure provides a more accurate representation of osseointegration and thus, a more realistic assessment of long-term stability. Furthermore, this allows to have one streamlined workflow for the whole life cycle of an implant, where all three steps of implant stability analysis (insertion, osseointegration, debonding) are governed by the same key parameters and macroscopic contact phenomena. A summary of existing osseointegration and bone remodeling algorithms is given in Section 2.3.3.2.

Parts of this chapter are in preparation for publication as [Sauer and Immel \(2022\)](#).

8.1 Simple Evolution Laws for Osseointegration

To model osseointegration over time, the formulation of chemical contact reactions is utilized. Here, $\hat{\phi} = \hat{\phi}(t, p_c, g_n)$ is defined as the degree of osseointegration during healing¹. Then, ϕ_0 introduced in Chapter 6 becomes equivalent to $\hat{\phi}$ after a certain healing time t and $\hat{\phi}_0 = 0$ represents the initial state before healing. To define increasing bonding due to osseointegration,

1. Overall, a unified model where $\phi \in [0, 1]$ represents both the increasing degree of osseointegration during healing and the (de)bonding state of the BII after healing and during loading can be established. Then, ϕ_0 corresponds to the initial state before healing (usually $\phi_0 = 0$). ϕ increases and/or decreases during the osseointegration process (due to bone apposition and bone resorption) and decreases during debonding. In order to emphasize the difference between modeling the osseointegration and the debonding processes, a different notation $\hat{\phi}$ for osseointegration is chosen here.

an evolution law for a chemical contact state (Sauer et al., 2022) is used:

$$\dot{\hat{\phi}} = \hat{\phi}(p_c, g_n, \hat{\phi}) \quad \forall \mathbf{x}_c \in \partial_c \mathcal{B}_k, \quad (8.1)$$

e.g. depending on the contact pressure $p_c(\mathbf{x})$, the normal contact gap $g_n(\mathbf{x})$, and the current state of osseointegration $\hat{\phi}(\mathbf{x})$ of each Gauss-point. The simplest reaction model is the linear reaction model

$$\dot{\hat{\phi}} = k_r \overrightarrow{k} (1 - \hat{\phi}), \quad (8.2)$$

where \overrightarrow{k} describes a forward reaction (bone apposition) and k_r represents the reaction velocity, providing a simple time-dependent osseointegration and bone remodeling law. k_r can be dependent on e.g., the healing time t but also the contact state g_n, p_c . Here, for simplicity it is considered to be $k_r = \text{const}$. In order to consider not only bone apposition but also bone resorption, which is part of the processes of osseointegration and bone remodeling (see Section 2.2.3.2), the extended linear reaction model is used, where \overleftarrow{k} describes a backward reaction (bone resorption). The overall reaction rate is then defined as

$$k = \overrightarrow{k} - \overleftarrow{k}, \quad (8.3)$$

and the evolution law becomes

$$\dot{\hat{\phi}} = k_r k (1 - \hat{\phi}), \quad (8.4)$$

In this work, three simple osseointegration models based on the extended linear model are introduced.

8.1.1 Model A

First, a simple phenomenological model is derived. Here, for simplicity,

$$\overleftarrow{k}_A = 1 - \overrightarrow{k}_A, \quad (8.5)$$

is assumed. When an uncemented implant has been inserted into the host bone cavity, an initial gap g_n between bone and implant can remain, e.g. as seen in Chapter 5. Therefore, some parts of the implant can be under pressure, while other areas have no contact at all. Therefore, a distinction between truly touching contact ($g_n \leq 0$, denoted "C") and short range reactions ($g_n > 0$, denoted "SR") has to be made. For touching contact, $\overrightarrow{k}_A = \overrightarrow{k}_c^A(p_c)$, with a reaction rate based on the contact pressure is defined. The reaction rate is designed within the limits of compressive stress p_c^{\min} and tensile stress p_c^{\max} for osseointegration (Kaneko et al., 2004; Viceconti et al., 2004). Both can be assumed as constants or to evolve with bone maturation. In this work, they are assumed to be constant. From p_c^{\min} the reaction rate \overrightarrow{k}_c^A first increases from 0 to 1, reaches a plateau from $p_c^{\text{opt},1}$ to $p_c^{\text{opt},2}$, and then decreases back to 0 at p_c^{\max} , i.e.

$$\overrightarrow{k}_c^A(p_c) = \begin{cases} 1 & p_c^{\text{opt},1} < p_c < p_c^{\text{opt},2}, \\ \frac{3}{4} - \frac{1}{4} \sin\left(\frac{\pi}{2b_1} \left(\frac{p_c}{p_c^{\text{opt},1}} - b_1 - 1\right)\right) & p_c^{\min} \leq p_c \leq p_c^{\text{opt},1}, \\ \frac{3}{4} - \frac{1}{4} \sin\left(\frac{\pi}{2b_2} \left(\frac{p_c}{p_c^{\text{opt},2}} - b_2 - 1\right)\right) & p_c^{\text{opt},2} \leq p_c \leq p_c^{\max}, \\ 0 & p_c < p_c^{\min} \vee p_c > p_c^{\max}, \end{cases}, \quad (8.6)$$

with

$$b_1 = \frac{p_c^{\min} - p_c^{\text{opt},1}}{2 p_c^{\text{opt},1}}, \quad b_2 = \frac{p_c^{\max} - p_c^{\text{opt},2}}{2 p_c^{\text{opt},2}}, \quad (8.7)$$

and

$$p_c^{\text{opt},1} = p_c^{\min} + \frac{|p_c^{\min}| + |p_c^{\max}|}{4}, \quad p_c^{\text{opt},2} = p_c^{\max} - \frac{|p_c^{\min}| + |p_c^{\max}|}{4}. \quad (8.8)$$

The overall reaction rate for truly touching contact $k_c^A = \vec{k}_c^A - \overleftarrow{k}_c^A$ is then

$$k_c^A(p_c) = \begin{cases} 1 & p_c^{\text{opt},1} < p_c < p_c^{\text{opt},2}, \\ \frac{1}{2} - \frac{1}{2} \sin\left(\frac{\pi}{2b_1} \left(\frac{p_c}{p_c^{\text{opt},1}} - b_1 - 1\right)\right) & p_c^{\min} \leq p_c \leq p_c^{\text{opt},1}, \\ \frac{1}{2} - \frac{1}{2} \sin\left(\frac{\pi}{2b_2} \left(\frac{p_c}{p_c^{\text{opt},2}} - b_2 - 1\right)\right) & p_c^{\text{opt},2} \leq p_c \leq p_c^{\max}, \\ 0 & p_c < p_c^{\min} \vee p_c > p_c^{\max}. \end{cases} \quad (8.9)$$

This model corresponds with observations from the literature where excessive stress or pressure can inhibit bone growth (Sotto-Maior et al., 2010).

The reaction rate for short range contact, namely $\vec{k} = \vec{k}_{\text{SR}}^A(g_n)$, is designed within the limits for the contact gap g_n , $g_{\text{opt}} = 500 \mu\text{m}$ and $g_{\text{lim}} = 1000 \mu\text{m}$, as introduced in Chapter 5. For $g_n < g_{\text{opt}}$ the reaction rate is 1. For $g_n \geq g_{\text{opt}}$ the reaction rate decreases until it reaches 0 at $g_n = g_{\text{lim}}$, i.e.

$$\vec{k}_{\text{SR}}^A(g_n) = \begin{cases} 1 & g_n < g_{\text{opt}}, \\ \frac{3}{4} - \frac{1}{4} \sin\left(\frac{\pi}{2b_3} \left(\frac{g_n}{g_{\text{opt}}} - b_3 - 1\right)\right) & g_{\text{opt}} \leq g_n \leq g_{\text{lim}}, \\ 0 & g_n > g_{\text{lim}}, \end{cases} \quad (8.10)$$

$$\text{with } b_3 = \frac{g_{\text{lim}} - g_{\text{opt}}}{2 g_{\text{opt}}}. \quad (8.11)$$

The gap limit g_{lim} defines the maximal gap where contact reactions can occur, and thus osseointegration, and g_{opt} is the gap until which full osseointegration ($\hat{\phi} = 1$) is possible, and corresponds to observations from clinical trials and experiments (Fernandes et al., 2002; Jasty et al., 1988; MacKenzie et al., 1994; Schmalzried et al., 1992; Spears et al., 2000; Udomkiat et al., 2002). The overall reaction rate for short range contact $k_{\text{SR}}^A = \vec{k}_{\text{SR}}^A - \overleftarrow{k}_{\text{SR}}^A$ is then

$$k_{\text{SR}}^A(g_n) = \begin{cases} 1 & g_n < g_{\text{opt}}, \\ \frac{1}{2} - \frac{1}{2} \sin\left(\frac{\pi}{2b_3} \left(\frac{g_n}{g_{\text{opt}}} - b_3 - 1\right)\right) & g_{\text{opt}} \leq g_n \leq g_{\text{lim}}, \\ 0 & g_n > g_{\text{lim}}. \end{cases} \quad (8.12)$$

The reaction rates k_c^A and k_{SR}^A are shown in Figure 8.1.

The analytical solution of Eq. (8.4) for model A is given by

$$\hat{\phi}_A(t) = \vec{k}_A \left(1 - e^{-k_r t}\right), \quad (8.13)$$

and the corresponding numerical solution obtained with the implicit backward Euler method is

$$\hat{\phi}_A^{n+1} = \frac{\Delta t k_r \vec{k}_A + \hat{\phi}_A^n}{1 + \Delta t k_r}. \quad (8.14)$$

For model A, the maximal degree of initial osseointegration reduces to $\hat{\phi}_A^{\max} = \vec{k}_A$.

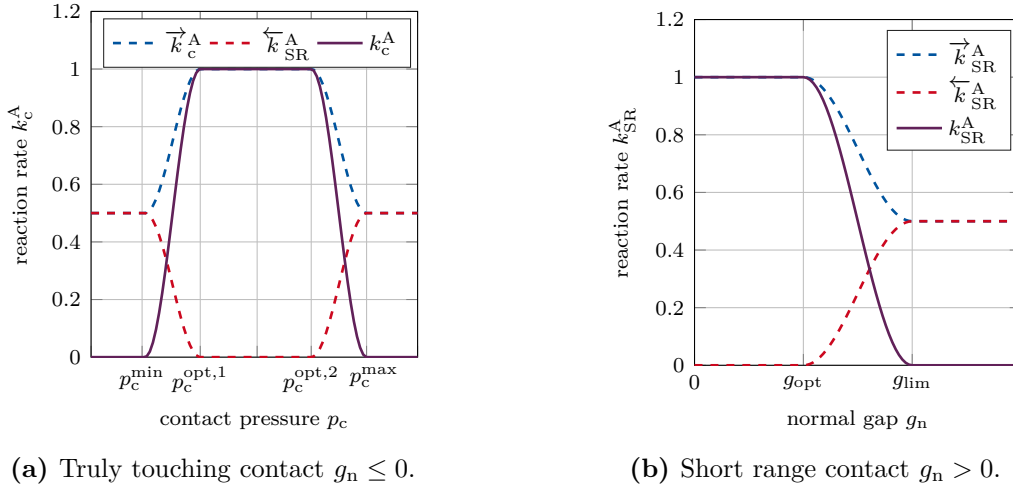


Figure 8.1 – Illustration of the reaction rates for truly touching contact k_c^A and short range contact k_{SR}^A for model A.

8.1.2 Model B

The second evolution law models the bone apposition reaction (forward) and the bone resorption reaction (backward) explicitly. The forward and backward reaction rates for touching surfaces $\vec{k}_B = \vec{k}_c^B$ and $\overleftarrow{k}_B = \overleftarrow{k}_c^B$ are defined as

$$\vec{k}_c^B(p_c) = 1, \quad (8.15)$$

$$\overleftarrow{k}_c^B(p_c) = \begin{cases} \frac{2}{3(p_{\min} + p_{\max})} \left(p_c - \frac{p_{\min} + p_{\max}}{2} \right)^2 & p_{\min} \leq p_c \leq p_{\max}, \\ 1 & \text{elsewhere.} \end{cases} \quad (8.16)$$

Here, it is assumed that due to contact, the forward reaction rate \vec{k}_c^B is always 1. However, with increasing pressure or tension, the backward reaction rate \overleftarrow{k}_c^B increases. The reaction rates cancel each other out at the pressure limits p_{\min} and p_{\max} and the overall reaction rate becomes zero.

For short range contact, it is assumed that the forward reaction rate $\vec{k}_B = \vec{k}_{SR}^B$ decreases linearly from 1 to zero for an increasing contact gap, while the backward reaction rate for short range contact $\overleftarrow{k}_B = \overleftarrow{k}_{SR}^B$ increases quadratically from 0 to 1. The reaction rates cancel each other out at $g_n = g_{\lim}$, i.e.

$$\vec{k}_{SR}^B(g_n) = 1 - \frac{g_n}{g_{\text{opt}} + g_{\lim}}, \quad \overleftarrow{k}_{SR}^B(g_n) = \frac{g_{\text{opt}} g_n^2}{(g_{\text{opt}} + g_{\lim}) g_{\lim}^2}. \quad (8.17)$$

The different reaction rates of model B are shown in Figure 8.2.

The analytical solution of Eq. (8.4) for model B is then given by

$$\hat{\phi}_B(t) = \frac{1}{1 - \frac{\overleftarrow{k}_B}{\vec{k}_B}} \left(1 - e^{-k_r k_B t} \right), \quad (8.18)$$

and the numerical solution obtained with the implicit backward Euler method is

$$\hat{\phi}_B^{n+1} = \frac{\Delta t k_r \vec{k}_B + \hat{\phi}_B^n}{1 + \Delta t k_r k_B}. \quad (8.19)$$

Here, the maximal degree of initial osseointegration is $\hat{\phi}_B^{\max} = \vec{k}_B / k_B$.

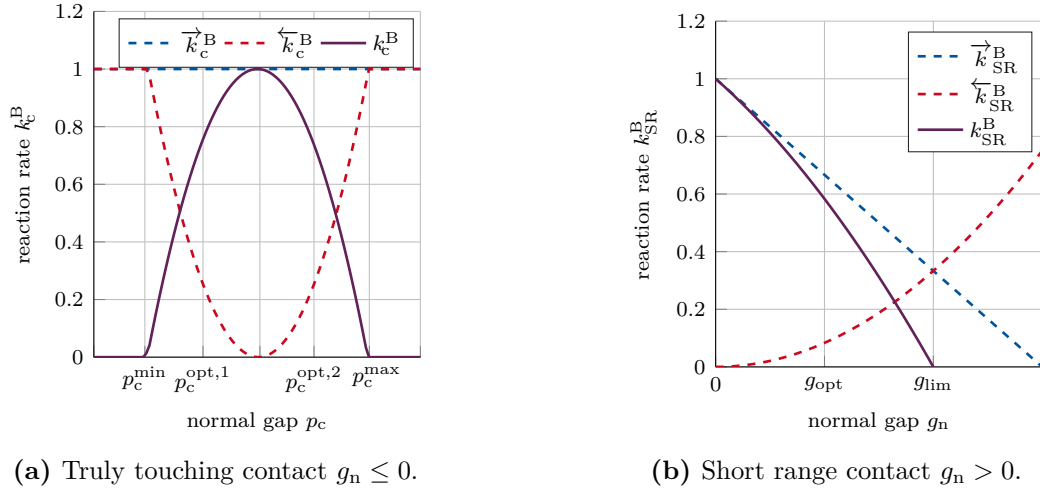


Figure 8.2 – Illustration of the reaction rates for truly touching contact k_c^B and short range contact k_{SR}^B for model B.

8.1.3 Model C

An even simpler but continuous model can be derived by modeling truly touching and short-range contact based on the contact gap alone. The forward reaction is modeled as

$$\overrightarrow{k}_C = \begin{cases} 0 & \text{if } g_n < (g_{\text{opt}} - \Delta g) \vee g_c > g_{\text{lim}}, \\ \frac{\overrightarrow{k}_0}{2} \cdot \left[\cos\left(\frac{g_c - g_{\text{lim}}}{g_{\text{lim}} - g_{\text{opt}}}\right) \right] & \text{if } (g_{\text{opt}} - \Delta g) \leq g_c \leq g_{\text{lim}}. \end{cases} \quad (8.20)$$

The backward reaction is modeled as

$$\overleftarrow{k}_C = \begin{cases} \overleftarrow{k}_0 (g_c + g_{\text{lim}} + \Delta g)^2 & g_n < (g_{\text{opt}} - \Delta g), \\ 0 & (g_{\text{opt}} - \Delta g) \leq g_c \leq g_{\text{lim}}, \\ \overleftarrow{k}_0 (g_c - g_{\text{lim}})^2 & g_c > g_{\text{lim}}, \end{cases} \quad (8.21)$$

which allows to model actual bone resorption, when k_C becomes negative. Here, $\overrightarrow{k}_0 = \overleftarrow{k}_0 = 1$, for simplicity. The different reaction rates of model C are shown in Figure 8.3. The analytical solution for Eq. (8.4) for model C is given by

$$\hat{\phi}_C(t) = \frac{1}{1 - \frac{\overleftarrow{k}_C}{\overrightarrow{k}_C}} + \left(1 - e^{-k_r k_C t}\right), \quad (8.22)$$

and the numerical solution is given by

$$\hat{\phi}_C^{n+1} = \frac{\Delta t k_r \overrightarrow{k}_C + \hat{\phi}_C^n}{\Delta t k_r k_C + 1}. \quad (8.23)$$

The maximal degree of osseointegration is given by $\phi_C^{\max} = \overrightarrow{k}_C / k_C$. An example for the evolution of $\hat{\phi}$ at a certain point on the BII over time is given in Figure 8.4.

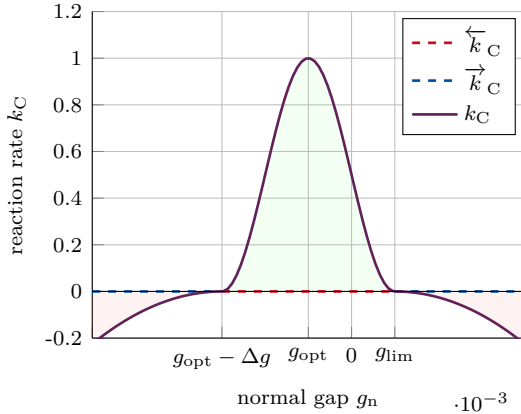


Figure 8.3 – Illustration of the reaction rate for model C. The green area represents condition which induce bone growth, while red areas represent condition that induce bone resorption.

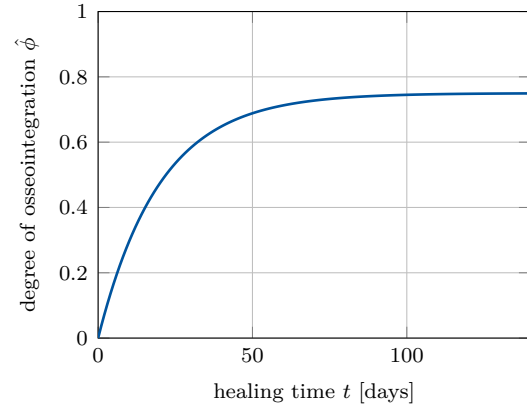


Figure 8.4 – Example of the evolution of osseointegration $\hat{\phi}$ at a certain point on the BII over healing time t .

8.2 Application to Coin-Shaped Implants

To demonstrate the new osseointegration laws and the complete workflow from initial stability, over osseointegration, to long-term stability and debonding, the CSI model introduced in Chapter 6 is used.

8.2.1 Setup

Unless stated otherwise, the same geometry, boundary conditions, material parameters, and solver parameters as in Section 6.4.1 are used.

To adequately demonstrate the pressure- and contact gap-dependent osseointegration law, the bone block is modeled with a rough upper surface by modifying the z -coordinate of the upper bone surface according to

$$z(x, y) = \gamma \left[\sin \left(\frac{0.1\pi}{\lambda} x \right) + \sin \left(\frac{0.1\pi}{\lambda} y \right) \right], \quad (8.24)$$

where $\gamma = 500 \mu\text{m}$ is the peak-to-peak amplitude and $\lambda = 10 \mu\text{m}$ is the wave period. The implant surface remains perfectly flat.

The bodies are meshed according to the parameters given in Table 8.1, where n_e denotes the number of elements of the body/surface and n_{gp} denotes the number of Gauss-points per element. While the bulk is discretized with linear Lagrangian shape functions, the contact surfaces are discretized with quadratic NURBS (Corbett and Sauer, 2014, 2015). The mesh of the complete setup and an enlargement of the bone surface profile are shown in Figure 8.5.

The parameters from the evolution laws introduced in Sections 8.1.1-8.1.3 and the parameters for the EMC from Section 7.1 are listed in Table 8.2 with values chosen based on previous works and from the literature.

The simulation is divided into three steps:

body	n_e	type of shape fcts.	n_{gp}
implant bulk	800	linear Lagrange	$2 \times 2 \times 2$
bone bulk	5000	linear Lagrange	$2 \times 2 \times 2$
implant contact surface	400	quadratic NURBS	5×5
bone contact surface	2500	quadratic NURBS	5×5

Table 8.1 – Parameters of the finite element mesh: Number of elements n_e , type of shape functions and number of Gauss-points per element n_{gp} for the two bodies and their contact surfaces.

1. insertion: the upper implant surface is pushed downward into the bone block with the displacement d_0 ;
2. osseointegration: the evolution laws A, B, and C from Section 8.1 are applied for the healing time t and the degree of osseointegration $\hat{\phi}$ is computed for every Gauss-point;
3. debonding: after the healing time t , the upper surface of the implant is rotated for 10° around its z -axis, until the implant is fully debonded.

Three different healing times are considered: $t = 14, 30, 100$ days.

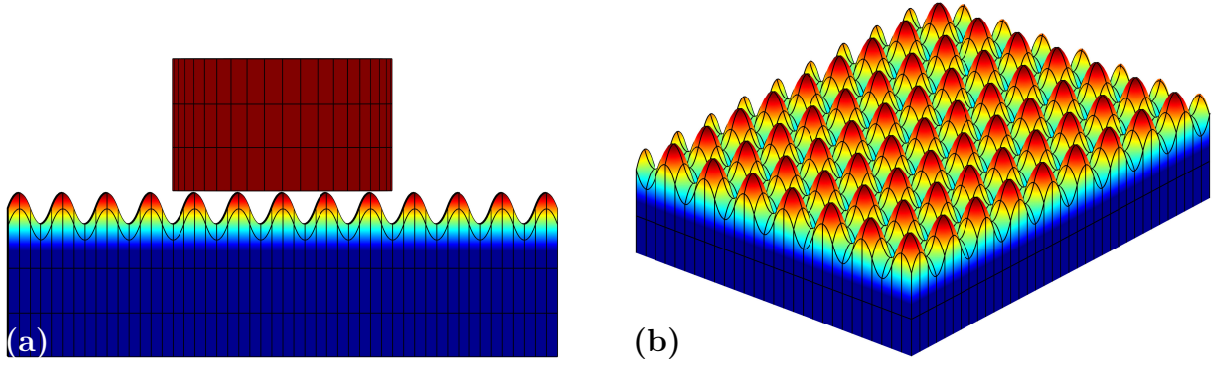


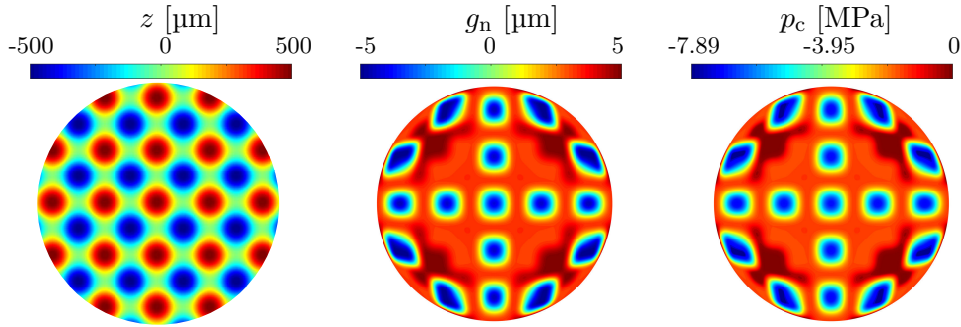
Figure 8.5 – (a) NURBS-enriched FE mesh of the rough bone block and the implant. (b) Enlargement of the bone surface profile with coloring based on the z -coordinate.

parameter	symbol	value
compressive stress limit	p_c^{\min}	-7.89 MPa (2004)
tensile stress limit	p_c^{\max}	0.8 MPa (2004)
optimal gap	g_{opt}	500 μm (2002; 1988; 1994; 1992; 2000; 2002)
gap limit	g_{lim}	1000 μm (1988; 1994)
reaction velocity	k_r	0.05 1/d
unbroken BII friction coeff.	μ_{ub}	0.44 (2020)
broken BII friction coeff.	μ_b	0.3 (1997a; 2020)
sliding threshold	a_s	22 μm (2020)
transition factor	b_s	0.74 (2020)
adhesive traction	t_0	1.8 MPa (2021b; 2021c; 2002)
adhesive gap limit	g_0	22 μm (2021b)
initial displacement	d_0	6.5 μm (2020)

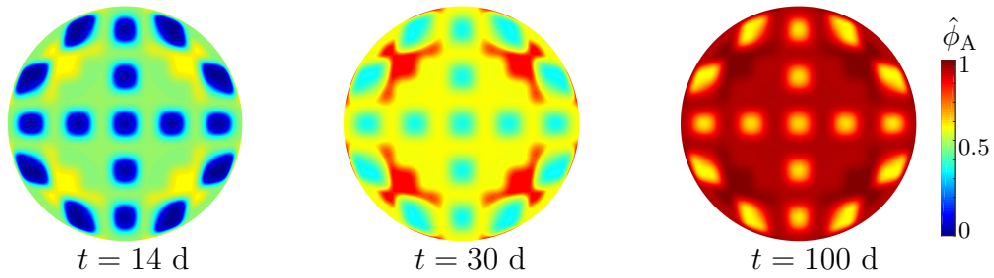
Table 8.2 – Parameters of the evolution laws for osseointegration and the EMC with corresponding values from the literature.

8.2.2 Results

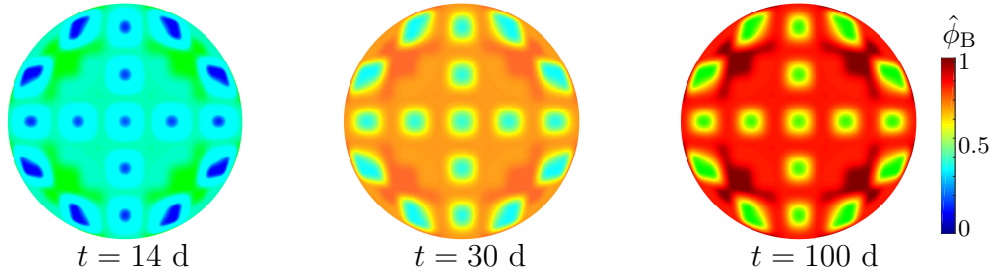
Figure 8.6(a) shows the surface profile of the bone block z under the CSI before insertion, the normal contact gap g_n and the contact pressure p_c at the BII after insertion, respectively. The average contact pressure is -5.55 MPa, which is within the pressure limits p_c^{\min} and p_c^{\max} of the two osseointegration models. Figures 8.6(b)- 8.6(d) show the distribution and degree of osseointegration for model A, B, and C after a healing time of 14, 30, and 100 days, respectively.



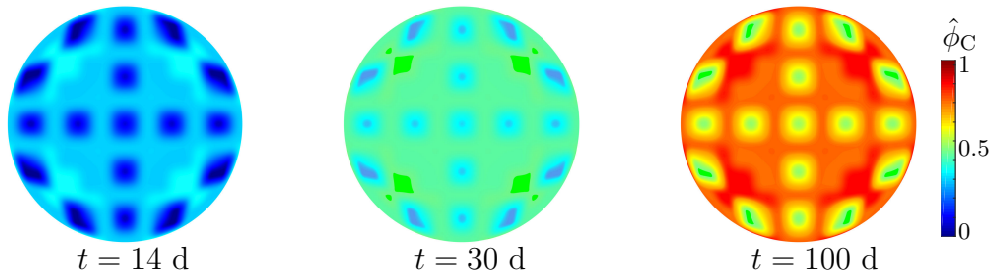
(a) Surface profile of the bone block z before insertion, normal gap g_n , and contact pressure p_c at the BII after insertion.



(b) Progression and distribution of osseointegration $\hat{\phi}_A$ at the BII for model A.



(c) Progression and distribution of osseointegration $\hat{\phi}_B$ at the BII for model B.



(d) Progression and distribution of osseointegration $\hat{\phi}_C$ at the BII for model C.

Figure 8.6 – Osseointegration of the CSI with respect to the healing time and evolution law.

While the patterns of osseointegration correspond with the gap/pressure field and do not change over time, the increase in the degree of osseointegration $\hat{\phi}$ is visible. The whole progression of the average degree of osseointegration $\hat{\phi}$ for all models over time is shown in Figure 8.7. The average degree of osseointegration is almost the same for the first two models until $t \approx 18$ days. For increasing t the model A predicts a higher average osseointegration than model B, due to the large plateau in c_c^A . The least increase in $\hat{\phi}$ is predicted by model C, due to bone resorption.

Last, the debonding of the osseointegrated implant is simulated by rotating the implant around its z -axis, as is done in Section 6.4 and 7.2. Figure 8.8 shows the torque curves for a respective healing time of 14, 30, and 100 days. As expected, only the magnitude of the maximal torque is affected, while the rest of the torque curve remains independent of $\hat{\phi}$ and t .

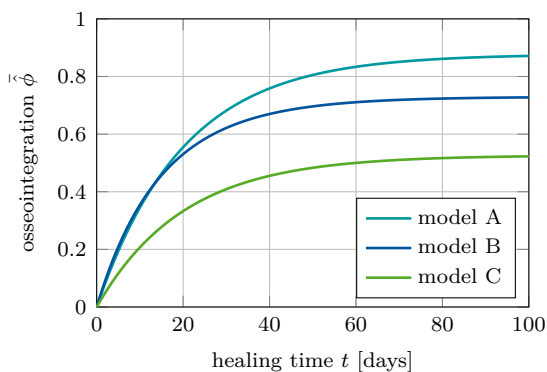


Figure 8.7 – Average degree of osseointegration $\hat{\phi}$ over time t for model A, B, and C.

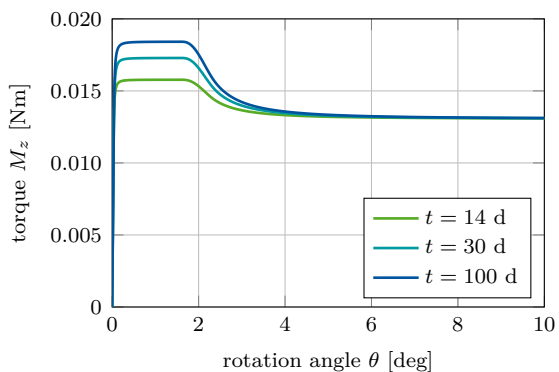


Figure 8.8 – Variation of the torque M_z as a function of the imposed rotation angle θ for model A.

8.2.3 Discussion and Limitations

This work aims to provide an outlook on (i) how to couple osseointegration laws with simulations of initial and long-term stability and (ii) how simple osseointegration laws can be designed based on the same mechanical parameters that govern models for primary and secondary stability. Furthermore, due to the use of a state variable as the representation of osseointegration, the presented approach is suitable for explicitly modeling the subsequent debonding of the (partially) osseointegrated interface, in contrast to common osseointegration and bone remodeling algorithms that result in fully bonded surfaces (Andreykiv et al., 2005; Chanda et al., 2020; Fernandes et al., 2002; Spears et al., 2000; Viceconti et al., 2004). Due to the inclusion of reverse reaction rates, bone resorption and bone remodeling can simply be integrated into the model. Full coupling would then allow to model the effect of applied loads during healing on the osseointegration of the implant. The average degree of osseointegration predicted by the models and shown in Figure 8.7 corresponds well to the results of other more complex, numerical approaches (Caouette et al., 2013; Chanda et al., 2020; Tarala et al., 2013).

Due to the idealized contact conditions and the lack of experimental results to adequately choose the parameters of the evolution laws, the calculated osseointegration of over 70% after complete healing (here, $t = 100$ days) is rather high. In reality, usually only 30-70% of the implant surface is osseointegrated (Brånemark, 1977; Brånemark et al., 1997; Marin et al.,

2010). Thus, more experimental results are needed to derive more realistic parameters for the evolution laws.

Although, a rough surface profile was used to investigate osseointegration under truly touching and short range contact conditions, no contact gap remained. Therefore, the models should be applied to rougher surface profiles and different pressure conditions (e.g. tension), to assess if the models generally overestimate the degree of osseointegration. Especially the behavior for mainly short range contact, as is the case for, e.g. acetabular cup implants (Jasty et al., 1997; MacKenzie et al., 1994; Schmalzried et al., 1992; Udomkiat et al., 2002) would be of interest.

The presented evolution laws are simplified significantly and leave room for improvement and extension. They were created mainly for illustrative purposes and are phenomenological at best. Some limitations and possible extensions for future work need to be addressed nonetheless, apart from the limitations introduced by the usage of the models from Chapters 6 and 7 (and discussed in their respective sections).

First, in the presented example, it is assumed that no change in contact and loading condition during the healing phase takes place. For a more realistic approach, a full coupling between mechanical and chemical contact should be established, see, e.g. Sauer et al. (2022). Based on this coupling, an explicit model of bone apposition and resorption based on, e.g. excessive micromotion at the BII, could be established, as is done in Caouette et al. (2013); Chanda et al. (2020); Tarala et al. (2013).

Second, not only the bonding state but also the maturation of bone tissue should be considered, by e.g., time-dependent change of material parameters such as bone stiffness, as is done in Andreykiv et al. (2005); Dickinson et al. (2012); Mukherjee and Gupta (2017); Tarala et al. (2013). Another approach would be to use evolution laws with focus on the biochemical processes, as presented by Andreykiv et al. (2005); Chanda et al. (2020); Dickinson et al. (2012); Mukherjee and Gupta (2017).

Third, these evolution laws do not model actual bone growth and thus no change in geometry at the BII takes place. However, bone growth changes the geometry (e.g. contact gaps are filled over time) and mechanical conditions (e.g. change in stress distribution, bone stiffness, and material symmetry) at the BII, which needs to be accounted for.

Last, instead of using smooth or artificially rough surfaces, this model can also be used with actual rough or porous implant surfaces, as well as geometries obtained from topology optimization. Similarly, measurements or geometries obtained from μ CT can be used for the bone block.

8.2.4 Conclusion

Overall it is shown that simple evolution laws based on macroscopic parameters such as the contact gap and contact pressure can provide reasonable initial estimations of osseointegration over time and that a simulation workflow and analysis of the implant life cycle, where each step is based on the same mechanical factors, is possible and easy to establish. While providing room for improvements and the ability to be coupled with different models, the presented modeling approach poses an initial step to a holistic approach towards modeling implant behavior inside the patients body.

Chapter 9

Conclusion

This chapter concludes this thesis by summarizing the most important aspects of the presented models of primary and secondary stability, and osseointegration. Furthermore, a perspective for future challenges and work is given.

9.1 Summary

The aim of this thesis was to develop adhesive and frictional contact models that can characterize the contact behavior of the bone-implant interface during and after surgery, as well as after osseointegration. Therefore, critical reviews of the current state of the art of numerical models for primary and secondary stability, as well as osseointegration and bone remodeling were given first.

The first project dealt with the determinants of initial stability of an uncemented ACI in a 3D hemi-pelvis. The effect of variations of the bone stiffness, interfacial friction coefficient, and diametric interference fit on stability in terms of pull-out force and polar gap was presented and discussed. The data suggested, that increasing the interference fit and friction coefficient excessively does not improve stability and a careful choice is more beneficial. Maximal initial stability can be achieved by optimal combination of the friction coefficient and interference fit based on the bone stiffness. Furthermore, it was shown that the pull-out force cannot be taken as the sole quantification of initial stability (as is done in the clinic), as high pull-out forces coincide with large polar gaps that can compromise long-term stability. This encourages the development of guiding tools for surgeons to help achieving and quantifying initial stability better.

To approach long-term stability and debonding of osseointegrated implants, a modified Coulomb's friction law was developed. This law utilizes a variable friction function, based on the current bonding and deformation state of the BII, thus allowing to describe bonded, debonding, and debonded interface behavior. Before debonding, a high friction coefficient is used to mimic the effects of bonding and adhesion. During deformation and debonding of the BII, the friction coefficient decreases to allow for complete debonding of the interface. This model poses a contrast to common approaches that utilize perfectly bonded or fully sliding elements. Case studies with simple geometries and homogeneous osseointegration can be solved analytically, while complex contact conditions and inhomogeneous osseointegration require numerical analysis. The model was applied to debonding, partially osseointegrated CSI and proved to be a good

characterization of the debonding behavior when compared to experimental data. Furthermore, both the analytical and the numerical model allowed for the estimation of the shear stiffness and friction coefficient of the BIL.

This new contact model was then applied to the debonding of osseointegrated ACI, to determine the importance of osseointegration on long-term stability, but also the relevance of initial stability. Three different loading scenarios were considered: normal pull-out, tangential pull-out and torsion. Stability increased almost linearly for increasing osseointegration for all studied parameters. The same parameter values of the interference fit, the bone stiffness, and the friction coefficient as for initial stability produced peak values for pull-out force and torque.

To improve the modified Coulomb's friction model and to account for adhesion in normal direction, it was extended by an exponential cohesive zone model. Furthermore, the tangential contact traction was shifted to allow for adhesive friction for positive contact stress (tension). The models capabilities were first demonstrated on a CSI and then applied to the debonding of osseointegrated ACI. While having only small impact on the overall load-displacement behavior of the system, the addition of normal adhesion lead to a significant increase in predicted pull-out force and torque, especially for cases with low initial stability, i.e. case with a larger contact surface. While osseointegration increased stability up to 116% compared to the initial stability, even perfect osseointegration could not overcome poor initial stability, further stressing the importance of adequate primary stability and the development of corresponding measurement and guiding techniques.

The two models for long-term stability presented in this thesis used either pre-defined osseointegration patterns or a homogeneous distribution of osseointegration of the contact surface. To complete the workflow of the numerical modeling of implant stability and the implant life cycle presented in this thesis, two simple evolution models for osseointegration were introduced and coupled with simulating initial and long-term stability. The three evolution laws incorporate bone apposition as well as bone resorption, based on the contact state after insertion in terms of contact gap and contact pressure. The three laws were then applied to CSI and the resulting osseointegration was used as input for debonding tests. Although the presented evolution laws are very simple, they produce similar results as more complex osseointegration and bone remodeling laws. As the predicted osseointegration does not result in fully bonded elements, as is the more common approach in the literature, the predicted osseointegration can be used as a more accurate input for simulating long-term implant stability and debonding.

Overall, this thesis provides consecutive, numerical models of implant primary stability, osseointegration, and secondary stability. The presented models provide insight on the behavior of the bone-implant interface and help in understanding the phenomena of implant debonding. They can also be used to help develop methods and guidelines for surgeons to support their choice of implant and surgical technique for a specific patient. Furthermore, they enable a holistic approach to model the *in vivo* behavior of bone implants during the surgery, osseointegration, and cyclic loading after healing. Thus, the suggested models can be used as a tool in implant conception, design, optimization, and evaluation. Last, the explicit modeling of the adhesive and macroscopic debonding of the bone-implant interface in normal and tangential direction poses a novel approach in modeling debonding of the osseointegrated bone-implant interface. Although specifically designed for this purpose, the (extended) modified Coulomb's friction law can also be applied to simulation the debonding of all kinds of imperfectly bonded interfaces.

9.2 Perspective

The presented formulations can be extended in different aspects apart from the limitations and extensions already discussed in the respective chapters and above.

9.2.1 Coupled Models

FE models of orthopedic devices can be used to assess if new implant designs (or subtle changes in design) can lead to significant improvements compared to existing implants and if they are robust to patient and surgical variability. Furthermore, they can be used to develop decision support tools for planing orthopedic surgery, such as computer assisted surgery, customized patient implants and surgical techniques, and quantification of initial stability during surgery, by providing additional information about the potential risk of failure on a patient-specific basis. However, no single model will be able to address all relevant factors due to the multi-scale, multi-time, and multi-body biomechanical problem of artificial joint replacements. Therefore, the coupling of different models to simulate the complete life cycle of an implant from the surgery, over osseointegration and bone remodeling, to long-term behavior and stability will be necessary to make realistic predictions of the performance of new implants and surgical techniques. In the case of this work, the deformation and stress data from the primary stability model discussed in Chapter 5 can be used as input for stress- or micromotion-based prediction of osseointegration and remodeling as demonstrated in Chapter 8. Then, the osseointegration patterns and conditions provided by these models can in turn be used as input for secondary stability models, as discussed in Chapters 6 and 7. Models of secondary stability can also be combined with models that incorporate complex cyclic loading conditions and boundary conditions that account for, e.g., muscle movement, tendons, and other soft tissues. Due to the general nature of the models presented in Chapter 6 and 7 they can also be used to characterize the behavior of other (imperfectly) bonded interfaces that exhibit tangential and normal bonding and debonding.

9.2.2 Additive Manufacturing and Shape Optimization

With the rise of additive manufacturing in implantology and the improvement of medical imaging methods, numerical models will need to consider realistic and complex implant and bone geometries. In the long-term, homogeneous material models will have to give way to the non-homogeneous, anisotropic bone properties mapped from μ CT and other measurement techniques. Furthermore, a coupling of shape optimization algorithms, which are more and more used to design implants, with osseointegration and debonding models could improve the performance and life expectancy of implants as well allow for full customization based on the patients complete physiological condition.

9.2.3 Experimental Measurement Techniques

Another factor is the amount of limitations and unknowns in the modeling of the BII, due to the lack of experimental data to populate the numerical models or the need to better understand the fundamentals of the biomechanics of the BII over time. Compared to other engineering disciplines like automotive or aerospace engineering, the knowledge of loading conditions acting on

orthopedic devices, including the interaction of muscles, tendons and soft tissue, is still quite limited. To the author's knowledge there still exist no *in vivo* studies to, e.g., measure the full stress-strain distribution at the BII of joint implants for different patient and loading scenarios over time, due to the difficulties in obtaining that data. Further computational studies cannot reliably provide more insight on *in vivo* behavior, as the level of sophistication of the models is beyond the point of verification with current *in vivo*, *ex vivo*, and even some *in vitro* measurement techniques. Especially, contact mechanics require experiments with a wide range of loading and interface conditions to generate enough data to formulate, populate, and verify new contact models. Therefore, it becomes more and more difficult to reliably assess the performance of implants and surgical techniques with numerical models. If FE models are to be trusted and accepted by clinicians, they need to demonstrate that they are capable of predicting realistic *in vivo* behavior. Thus, further development of experimental measurement techniques and quantification of relevant biomechanical metrics (e.g., stress-strain behavior, micromotion, friction, adhesion, debonding under tension) is essential to provide the data necessary to develop and improve numerical models. However, the development of new and more accurate experimental machinery and techniques that are able to provide the necessary data is difficult and time consuming and provides a constant challenge. Until then, a certain acceptance that FE studies may not be representative of the *in vivo* conditions but an idealized model, needs to be established.

Résumé substantiel

Les implants osseux permettent le remplacement ou la réparation partiels ou complets de structures ostéoarticulaires, et constituent actuellement l'approche thérapeutique la plus utilisée pour soigner les articulations et les os endommagés. Du fait de la hausse continue de l'espérance de vie, on assiste à une augmentation rapide du nombre de patients atteints d'affections et de maladies musculosquelettiques telles que les fractures, l'ostéoporose et les métastases osseuses, qui nécessitent un remplacement partiel ou total des articulations. Certains cas relativement courants nécessitent le remplacement total de l'articulation, comme c'est le cas lors d'une arthroplastie totale de la hanche ou du genou. Bien que ces interventions soient les plus fréquentes en chirurgie orthopédique, on constate de nombreux cas de descellements aseptiques entraînant souvent des échecs implantaires difficiles à anticiper, car les phénomènes responsables du remodelage osseux et de l'apposition osseuse sont complexes et restent mal connus.

L'un des facteurs les plus importants pour assurer le succès d'un implant osseux est sa stabilité mécanique. Un bon contact initial entre l'os et l'implant, une bonne qualité osseuse et une quantité appropriée de micromouvements à l'interface os-implant sont autant de facteurs qui garantissent une bonne croissance de l'os néoformé et donc l'intégration de l'implant à l'intérieur du corps du patient. Une mauvaise stabilité initiale, une mauvaise répartition de la charge et des micromouvements importants peuvent au contraire entraîner une mauvaise intégration de l'implant, puis un descellement et un échec chirurgical. Ces situations peuvent augmenter le frottement au niveau de l'interface os-implant, ce qui peut également entraîner des échecs implantaires.

On distingue deux types de stabilité implantaire : 1. la stabilité primaire (ou initiale) pendant l'opération chirurgicale, qui est principalement régie par des facteurs mécaniques tels que des phénomènes d'imbrication et la qualité osseuse du patient, et 2. la stabilité secondaire (ou à long terme), qui est atteinte plusieurs semaines ou mois après l'opération par la formation et la maturation de tissu osseux au niveau de l'interface os-implant, un processus appelé ostéointégration. Alors que l'évolution de la stabilité secondaire de l'implant est régie par des processus biomécaniques complexes, le comportement mécanique de l'interface os-implant reste crucial pour le résultat chirurgical. Par conséquent, les modèles présentés dans cette thèse sont basés sur la biomécanique.

Dans le domaine du génie mécanique et de la mécanique des structures, la modélisation et la simulation numérique sont des approches déjà bien établies pour concevoir, simuler et optimiser les procédures, les machines et les procédés mécaniques, biologiques et chimiques. Cependant, le contact adhésif entre les os et les implants est un problème multi-physique et multi-échelle complexe, qu'il reste difficile de modéliser finement en prenant en compte tous les phénomènes pertinents. Il est donc encore difficile de comprendre et de prédire les phénomènes

se déroulant lors de l'ensemble du cycle de vie d'un implant. Comme la stabilité de l'implant implique des phénomènes à différentes échelles spatio-temporelles, la biomécanique de l'implant, qui comprend la mécanique tissulaire, structurale et du contact ainsi que la biochimie, présente un certain nombre de défis uniques et absents des applications de modélisation informatique plus traditionnelles. De plus, en raison de la taille et de la forme des prothèses articulaires usuelles et de l'importance des phénomènes de remodelage osseux, les données expérimentales concernant la stabilité à long terme sont rares, ce qui rend la validation des modèles numériques difficile.

L'objectif des modèles numériques en lien avec l'implantologie est de modéliser le remodelage osseux et l'ostéointégration, d'acquérir une compréhension fondamentale du comportement mécanique de l'interface os-implant, d'aider à la conception de nouveaux implants et à leurs tests précliniques, et de comparer leurs performances avec celle des implants existants. Bien qu'il existe de nombreuses études numériques concernant ces aspects, la modélisation et la prédiction spécifiques au descellement dû à une ostéointégration imparfaite font encore défaut dans la littérature. L'objectif de ce travail est de proposer plusieurs modélisations complémentaires du contact adhésif à l'interface os-implant pendant et après l'opération chirurgicale. Les modèles de contact développés prennent en compte le comportement non linéaire du matériau, les grandes déformations, le frottement adhésif, l'ostéointégration et le décollement de l'interface os-implant. L'os et l'implant sont modélisés comme des solides déformables. Ces modèles sont d'abord appliqués à des implants de forme cylindrique pour vérification et validation, puis à une cupule acétabulaire utilisée dans le cadre des prothèses de hanche pour en simuler la stabilité primaire et secondaire. Trois approches complémentaires sont proposées.

Dans un premier temps, les déterminants biomécaniques de la stabilité primaire d'une cupule acétabulaire non-cimentée sont présentés. Pour quantifier la stabilité primaire, l'insertion d'une cupule acétabulaire dans un héli-bassin humain et son retrait ultérieur sont simulés. La stabilité primaire est quantifiée par l'espace restant entre la cavité de la hanche et l'implant après insertion et par la force d'arrachement maximale. L'influence d'un ajustement serré lors de l'insertion de la cupule, du coefficient de frottement à l'interface et de la rigidité du tissu osseux cortical et trabéculaire sur la stabilité primaire est discutée. Sur la base de la rigidité osseuse d'un patient, des combinaisons optimales de l'ajustement serré et du coefficient de frottement peuvent être identifiées pour assurer une stabilité initiale optimale. Tous les paramètres étudiés influencent significativement la stabilité primaire de la cupule acétabulaire. Une combinaison optimale de coefficient de frottement et de l'ajustement serré a été déterminée. La forte corrélation entre les paramètres susmentionnés nécessite donc une attention particulière de la part des fabricants d'implants et des chirurgiens afin de maximiser la stabilité primaire de la cupule acétabulaire. Les résultats numériques sont cohérents avec les études expérimentales et numériques précédentes et aideront les chirurgiens à choisir l'ajustement serré optimal d'une manière spécifique au patient, en fonction de sa qualité osseuse et de l'implant choisi. Les résultats montrent également qu'une différence supérieure à 1,4 mm entre le diamètre de la cavité osseuse et celui de la cupule ainsi qu'un coefficient de frottement supérieur à 0,6 ne permettent pas d'améliorer la stabilité primaire de la cupule acétabulaire. Ces résultats peuvent aider à la conception des implants et au choix des traitements de surface appropriés. De plus, cette étude fournit des informations détaillées sur l'état de contact local et sur l'influence des paramètres spécifiques à l'implant et au patient, et constitue donc une étape importante vers la modélisation et la compréhension de la stabilité implantaire. Cependant, cette première partie ne prend pas en compte les phénomènes d'adhésion à l'interface os-implant.

Dans un second temps, un modèle phénoménologique du comportement de contact frictionnel relatif aux implants ostéointégrés est développé. La loi de Coulomb est étendue en considérant un coefficient de frottement variable modélisant la transition d'un état intact (interface ostéointégrée) à un état décollé. Le coefficient de friction est déterminé sur la base d'une variable d'état dépendant du glissement total à l'interface os-implant. Alors que l'état intact correspond à une interface ostéointégrée, donc à la présence de liaisons adhésives et à un plus grand coefficient de frottement, l'état décollé dénote un comportement en frottement pur à l'interface avec un coefficient de frottement plus faible. Ainsi, ce modèle peut rendre compte des forces de cisaillement tangentielles plus élevées observées dans les implants ostéointégrés par rapport aux implants non-ostéointégrés. Ce modèle est appliqué au décollement en torsion d'un implant cylindrique et les résultats sont comparés aux données expérimentales ainsi qu'à un modèle analytique développé précédemment. L'hypothèse d'une transition en douceur d'un état intact à un état cassé, caractérisée par un coefficient de frottement décroissant pendant le processus de décollement, permet d'obtenir un bon accord entre les données expérimentales et les approches analytique et numérique. Bien que le modèle analytique soit relativement simple, il s'agit d'un moyen efficace de fournir des estimations rapides pour ce type d'expérience. Les résultats numériques, en revanche, sont plus précis et permettent de modéliser plus finement un comportement du matériau, une distribution des contraintes et une ostéointégration partielle plus complexes. Les deux approches permettent d'estimer plusieurs paramètres importants de l'interface os-implant. Le modèle de frottement proposé permet de comprendre les phénomènes de décollement à l'interface os-implant.

Dans un troisième temps, la loi de Coulomb modifiée développée précédemment pour le décollement tangentiel est appliquée pour simuler et estimer les déterminants de la stabilité à long-terme d'une cupule acétabulaire. De plus, le modèle est complété en considérant l'adhésion dans la direction normale via l'utilisation d'un modèle de zone cohésive afin de tenir compte du décollement dans la direction normale et de permettre la prise en compte du frottement adhésif. Ce modèle de contact est appliqué pour simuler en 3D le descellement d'une cupule acétabulaire ostéointégrée à travers différents tests d'arrachement. La stabilité de l'implant est quantifiée par la force et le couple d'arrachement, et les déterminants biomécaniques de la stabilité à long terme, tels que la stabilité primaire et le degré d'ostéointégration, sont évalués. Les résultats sont comparés au modèle purement tangentiel pour identifier la pertinence de l'adhérence normale dans le descellement de la cupule acétabulaire. Tout en n'ayant qu'un faible impact sur le comportement global charge-déplacement du système, l'ajout d'une adhérence normale conduit à une augmentation significative de la force d'arrachement et du couple prédits, en particulier pour les cas ayant une faible stabilité initiale, et donc une plus grande surface de contact. Bien que le processus d'ostéointégration permette d'augmenter la stabilité d'un implant d'une valeur pouvant aller jusqu'à 116% de sa stabilité primaire, même une ostéointégration parfaite ne suffit pas à compenser une mauvaise stabilité primaire. Cela souligne en outre l'importance d'une bonne stabilité primaire et le développement de techniques de mesure et de guidage adéquates pour les chirurgiens.

Les modèles présentés jusqu'à présent portaient sur la stabilité initiale et à long terme et s'appuyaient sur des distributions d'ostéo-intégration prédéfinies. Pour compléter le workflow de la modélisation numérique de la stabilité des implants présenté dans cette thèse et pour modéliser le cycle de vie complet de l'implant, l'ostéointégration de l'implant doit également être modélisée. C'est pourquoi trois modèles simples d'évolution pour l'ostéointégration, basés

sur l'état de contact après l'insertion de l'implant, sont introduits.

Les trois lois d'évolution intègrent l'apposition ainsi que la résorption osseuse, en fonction de l'état de contact après insertion en termes d'intervalles et de pression de contact. Les trois lois sont ensuite appliquées aux implants cylindriques. Bien que les lois d'évolution présentées soient très simples, elles produisent des résultats similaires à des lois plus complexes d'ostéointégration et de remodelage osseux. Comme l'ostéointégration prédite par ces lois n'aboutit pas à des éléments entièrement collés, ce qui constitue l'approche la plus courante dans la littérature, cette ostéointégration prédite peut-être utilisée comme entrée plus précise pour simuler la stabilité et le décollement de l'implant à long terme.

Dans l'ensemble, cette thèse fournit des modèles numériques complémentaires de stabilité primaire, d'ostéointégration et de stabilité secondaire de l'implant. Les modèles présentés donnent un aperçu du comportement de l'interface os-implant et aident à comprendre les phénomènes mis en jeu lors du descellement de l'implant. Ils peuvent également être utilisés pour aider à définir des méthodes et des lignes directrices pour les chirurgiens afin de les appuyer dans leur choix d'implant et de technique chirurgicale spécifiquement à chaque patient. En outre, ils permettent une approche holistique pour modéliser le comportement *in vivo* d'un implant osseux pendant l'opération chirurgicale, l'ostéointégration et la mise en charge cyclique après cicatrisation et peuvent donc être utilisés comme outil de conception, d'optimisation et d'évaluation d'implants. En raison de leur caractère non-spécifique, les modèles présentés dans ce travail peuvent être appliqués à toutes sortes d'implants osseux ou plus généralement d'interfaces imparfaitement collées. De plus, les modèles peuvent être couplés à des algorithmes de remodelage ou à des données de chargement réalistes pour mener à bien des simulations et des pronostics pour tout le cycle de vie d'un implant, depuis l'opération chirurgicale jusqu'à sa stabilité à long terme sous chargement cyclique en passant par les phases de remodelage osseux et d'ostéointégration.

Appendix A

Linearization

The linearization of the internal mechanical contribution w.r.t. the deformation is given by

$$\Delta_x \delta \Pi_{\text{int}}^e = \mathbf{v}_e^T \mathbf{k}_{\text{int}}^e \Delta \mathbf{u}_k^e, \quad (\text{A.1})$$

with

$$\mathbf{k}_{\text{int}}^e = \int_{\mathcal{B}_k} \mathbf{N}_{k,\alpha}^T \sigma_{\alpha\beta} \mathbf{N}_{k,\beta} dv + \int_{\mathcal{B}_k} \mathbf{B}^T \mathbb{c} \mathbf{B} dv, \quad (\text{A.2})$$

with the derivatives of the shape functions $\mathbf{N}_{k,\alpha}$, the tensor components $\sigma_{\alpha\beta}$, and the spatial elasticity tensor \mathbb{c} in the reference configuration, which depend on the chosen material model. A detailed derivation is given in e.g. [Wriggers \(2008\)](#).

The linearization of the mechanical contact contribution w.r.t. the deformation is given by

$$\Delta_x \delta \Pi_{\text{int}}^e = \mathbf{v}_e^T \mathbf{k}_c^e \Delta \mathbf{u}_k^e. \quad (\text{A.3})$$

When using the classical full-pass approach, \mathbf{k}_c^e is given by

$$\mathbf{k}_c^e = \begin{bmatrix} \mathbf{k}_{c,kk}^e & \mathbf{k}_{c,k\ell}^e \\ \mathbf{k}_{c,\ell k}^e & \mathbf{k}_{c,\ell\ell}^e \end{bmatrix}, \quad k, \ell = 1, 2 \wedge k \neq \ell, \quad (\text{A.4})$$

A.1 Tangent Matrix for the Modified Coulomb's Friction Law

For the MCFL, the unified model of [Duong and Sauer \(2019\)](#) (see Section 4.5.2) is used. During tangential sticking, \mathbf{k}_c^e is evaluated for the previous interacting point $\hat{\boldsymbol{\xi}}^n(\bar{\ell})$ (see Section 4.5.2), i.e.

$$\mathbf{t}_{ck} = \epsilon \mathbf{g}_c, \quad \mathbf{g}_c = \hat{\mathbf{g}}^n, \quad \epsilon_n = \epsilon_t = \epsilon, \quad (\text{A.5})$$

and thus

$$\mathbf{k}_c^e = \begin{bmatrix} \mathbf{k}_{c,kk}^e & \mathbf{k}_{c,k\bar{\ell}}^e \\ \mathbf{k}_{c,\bar{\ell}k}^e & \mathbf{k}_{c,\bar{\ell}\bar{\ell}}^e \end{bmatrix}, \quad k, \bar{\ell} = 1, 2 \wedge k \neq \bar{\ell}. \quad (\text{A.6})$$

The components of \mathbf{k}_c^e are the given by

$$\begin{aligned}
\mathbf{k}_{c,kk}^e &= \int_{\Gamma_k^e} \mathbf{N}_k^T \frac{\partial \mathbf{t}_{ck}}{\partial \mathbf{u}_k^e} da + \int_{\Gamma_k^e} \mathbf{N}_k^T \mathbf{t}_{ck} \otimes \mathbf{a}_k^\alpha \mathbf{N}_{k,\alpha} da \\
\mathbf{k}_{c,k\bar{\ell}}^e &= - \int_{\Gamma_k^e} \mathbf{N}_k^T \frac{\partial \mathbf{t}_{ck}}{\partial \mathbf{u}_{\bar{\ell}}^e} da \\
\mathbf{k}_{c,\bar{\ell}k}^e &= - \int_{\Gamma_k^e} \mathbf{N}_{\bar{\ell}}^T \frac{\partial \mathbf{t}_{ck}}{\partial \mathbf{u}_k^e} da - \int_{\Gamma_k^e} \mathbf{N}_{\bar{\ell}}^T \mathbf{t}_{ck} \otimes \mathbf{a}_k^\alpha \mathbf{N}_{k,\alpha} da \\
\mathbf{k}_{c,\bar{\ell}\bar{\ell}}^e &= \int_{\Gamma_k^e} \mathbf{N}_{\bar{\ell}}^T \frac{\partial \mathbf{t}_{ck}}{\partial \mathbf{u}_{\bar{\ell}}^e},
\end{aligned} \tag{A.7}$$

with

$$\frac{\partial \mathbf{t}_{ck}}{\partial \mathbf{u}_k^e} = \epsilon \mathbf{N}_k, \quad \frac{\partial \mathbf{t}_{ck}}{\partial \mathbf{u}_{\bar{\ell}}^e} = \epsilon \mathbf{N}_{\bar{\ell}}. \tag{A.8}$$

During tangential sliding, \mathbf{k}_c^e has to be evaluated for the current interacting point $\hat{\boldsymbol{\xi}}(\hat{\ell})$ and the previous interacting point $\hat{\boldsymbol{\xi}}^n(\bar{\ell})$, i.e.

$$\mathbf{t}_{ck} = \epsilon \mathbf{g}_c, \quad \mathbf{g}_c = \hat{\mathbf{g}}^{n+1}, \tag{A.9}$$

and thus

$$\mathbf{k}_c^e = \begin{bmatrix} \mathbf{k}_{c,kk}^e & \mathbf{k}_{c,k\hat{\ell}}^e & \mathbf{k}_{c,k\bar{\ell}}^e \\ \mathbf{k}_{c,\hat{\ell}k}^e & \mathbf{k}_{c,\hat{\ell}\hat{\ell}}^e & \mathbf{k}_{c,\hat{\ell}\bar{\ell}}^e \end{bmatrix}, \quad k, \hat{\ell}, \bar{\ell} = 1, 2 \wedge k \neq \ell. \tag{A.10}$$

The components are defined by

$$\begin{aligned}
\mathbf{k}_{c,kk}^e &= \int_{\Gamma_k^e} \mathbf{N}_k^T \frac{\partial \mathbf{t}_{ck}}{\partial \mathbf{u}_k^e} da + \int_{\Gamma_k^e} \mathbf{N}_k^T \mathbf{t}_{ck} \otimes \mathbf{a}_k^\alpha \mathbf{N}_{k,\alpha} da \\
\mathbf{k}_{c,k\hat{\ell}}^e &= - \int_{\Gamma_k^e} \mathbf{N}_k^T \frac{\partial \mathbf{t}_{ck}}{\partial \mathbf{u}_{\hat{\ell}}^e} da \\
\mathbf{k}_{c,k\bar{\ell}}^e &= - \int_{\Gamma_k^e} \mathbf{N}_k^T \frac{\partial \mathbf{t}_{ck}}{\partial \mathbf{u}_{\bar{\ell}}^e} da \\
\mathbf{k}_{c,\hat{\ell}k}^e &= - \int_{\Gamma_k^e} \mathbf{N}_{\hat{\ell},\alpha}^T \mathbf{t}_{ck} \mathbf{M}_k^\alpha da - \int_{\Gamma_k^e} \mathbf{N}_{\hat{\ell}}^T \frac{\partial \mathbf{t}_{ck}}{\partial \mathbf{u}_k^e} da - \int_{\Gamma_k^e} \mathbf{N}_{\hat{\ell}}^T \mathbf{t}_{ck} \otimes \mathbf{a}_k^\alpha \mathbf{N}_{k,\alpha} da \\
\mathbf{k}_{c,\hat{\ell}\hat{\ell}}^e &= - \int_{\Gamma_k^e} \mathbf{N}_{\hat{\ell},\alpha}^T \mathbf{t}_{ck} \mathbf{M}_{\hat{\ell}}^\alpha da - \int_{\Gamma_k^e} \mathbf{N}_{\hat{\ell}}^T \frac{\partial \mathbf{t}_{ck}}{\partial \mathbf{u}_{\hat{\ell}}^e}, \\
\mathbf{k}_{c,\hat{\ell}\bar{\ell}}^e &= - \int_{\Gamma_k^e} \mathbf{N}_{\hat{\ell},\alpha}^T \mathbf{t}_{ck} \mathbf{M}_{\bar{\ell}}^\alpha da + \int_{\Gamma_k^e} \mathbf{N}_{\hat{\ell}}^T \frac{\partial \mathbf{t}_{ck}}{\partial \mathbf{u}_{\bar{\ell}}^e} da,
\end{aligned} \tag{A.11}$$

with

$$\frac{\partial \mathbf{t}_{ck}}{\partial \mathbf{u}_k^e} = \epsilon (\mathbf{N}_k - \mathbf{a}_\alpha \mathbf{M}_k^\alpha), \quad \mathbf{M}_{\bar{\ell}}^\alpha := -c^{\alpha\beta} (\mathbf{c}_\beta - \mathbf{m}_\beta) \cdot \mathbf{N}_{\bar{\ell}}, \tag{A.12}$$

$$\frac{\partial \mathbf{t}_{ck}}{\partial \mathbf{u}_{\hat{\ell}}^e} = \epsilon (\mathbf{N}_{\hat{\ell}} + \mathbf{a}_\alpha \mathbf{M}_{\hat{\ell}}^\alpha), \quad \mathbf{M}_{\hat{\ell}}^\alpha := -c^{\alpha\beta} [(\mathbf{g}_c - \mathbf{g}_\tau^{\max}) \cdot \mathbf{N}_{\hat{\ell},\beta} - \mathbf{c}_\beta \cdot \mathbf{N}_{\hat{\ell}} - \mathbf{d}_\beta^\gamma \cdot \mathbf{N}_{\hat{\ell},\gamma}], \tag{A.13}$$

$$\frac{\partial \mathbf{t}_{ck}}{\partial \mathbf{u}_{\bar{\ell}}^e} = \epsilon \mathbf{a}_\alpha \mathbf{M}_{\bar{\ell}}^\alpha, \quad \mathbf{M}_{\bar{\ell}}^\alpha := -c^{\alpha\beta} \mathbf{m}_\beta \cdot \mathbf{N}_{\bar{\ell}}, \tag{A.14}$$

and

$$\mathbf{c}_\alpha := \mathbf{a}_\alpha - \mu \operatorname{sign}(g_n) \tau_\alpha \mathbf{n}, \quad (\text{A.15})$$

$$\mathbf{d}_\alpha^\beta := \mu \frac{\|\mathbf{g}_n\|}{\|\hat{\mathbf{g}}_\tau^n\|} (\delta_\alpha^\beta - \tau_\alpha^\beta) \hat{\mathbf{g}}_n^n - \mu \operatorname{sign}(g_n) \tau_\alpha \mathbf{n} g^\beta, \quad (\text{A.16})$$

$$\mathbf{m}_\alpha := \mu \frac{\|\mathbf{g}_n\|}{\|\hat{\mathbf{g}}_\tau^n\|} (\mathbf{a}_\alpha - \tau_{\alpha\beta} \mathbf{a}^\beta). \quad (\text{A.17})$$

Appendix B

Convergence Studies

B.1 Acetabular Cup Implant in Human Hemi-Pelvis

To analyze the convergence behavior of the hemi-pelvis mesh, three different finite element meshes were constructed, denoted *coarse*, *medium*, and *fine* with approximately 92,500, 125,000, and 250,000 elements, respectively. In addition, different numbers of load steps $l_1 \in [100, 200, 400]$ were investigated. The reference case ($E_{tb}^* = 0.2$ GPa, $E_{cb}^* = 18$ GPa, $\mu^* = 0.3$, $IF^* = 1.0$ mm) was chosen as the parameter set and the normal pull-out force F_z^* was chosen as the target value.

Figure B.1 shows the convergence behavior of the different meshes. Computations with $l_1 = 100$ did not converge. The estimated exact value of $F_z^{\max*}(\phi = 1) = 181.91$ N.

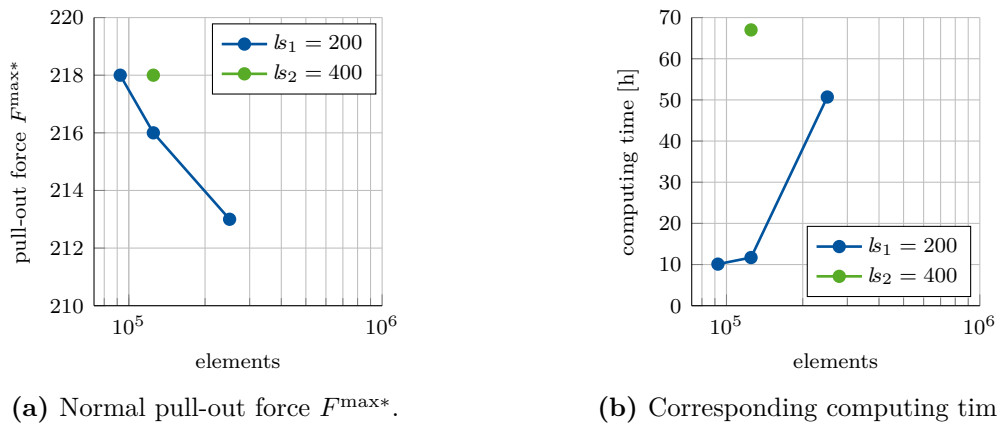


Figure B.1 – Normal pull-out force F_z^* and corresponding computing time with respect to number of contact elements on the bone block.

The corresponding error of the coarse, medium, and fine mesh for $l_1 = 200$ is 1.9, 0.6, and 0.2%, respectively. Due to the considerable difference in computing time while having a very low error, the medium mesh was chosen over the fine mesh. The coarse mesh has a coarse resolution especially at the contact surface in the bone cavity. Although having a small error for the reference case, it was assumed that the mesh might be too coarse for parameter combinations that result in stiffer systems. Therefore, the coarse mesh was discarded as well. The error for the medium mesh with $l_1 = 400$ is 0.2% while the computing time is 67 hours. As the decrease

in error was negligible compared to the increase in computing time, the number of time steps $l_1 = 200$ ($\Delta l = d_0/200$) was chosen as a basis for all computations.

It should be noted, that the chosen parameter set has an influence on the computing time and the accuracy. Parameter combinations that produce high pull-out forces also require more computing time. Furthermore, Newton-Raphson convergence could not be achieved for all parameter combinations with $\Delta l = d_0/200$. In those cases, the load step size had to be decreased to $\Delta l = d_0/5000$ to ensure convergence.

B.2 Modified Coulomb's Friction Law on Coin-Shaped Implants

To analyze the convergence behavior of the MC applied to the CSI, three different finite element meshes were constructed, denoted *coarse*, *medium*, and *fine* with 3,390, 12,354, and 47,130 degrees of freedom, respectively. In addition, different load step sizes $[0.1^\circ, 0.05^\circ, 0.02^\circ, 0.01^\circ, 0.005^\circ, 0.004^\circ]$ were investigated, corresponding to a number of load steps of $[100, 200, 500, 1,000, 2,000, 2,500]$, respectively. For the parameters, data set 1 with $\mu_b = 0.4$ was chosen. To compare the different setups, we define the mean relative torque error

$$e_{M_z}^{\text{rel}} = \text{mean}_{\theta \in [0, 10^\circ]} \left(\left\| \frac{M_z^{\text{exp}}(\theta) - M_z(\theta)}{M_z^{\text{max}}} \right\| \right), \quad (\text{B.1})$$

where here M_z^{max} is the maximum torque obtained by the numerical solution.

Load step	Coarse	Medium	Fine
0.10°	0.02233	0.02195	0.02186
0.05°	0.02242	0.02197	0.02185
0.02°	0.02239	0.02191	0.02177
0.01°	0.02240	0.02190	0.02176
0.005°	0.02241	0.02190	0.02176
0.004°	0.02241	0.02190	0.02176

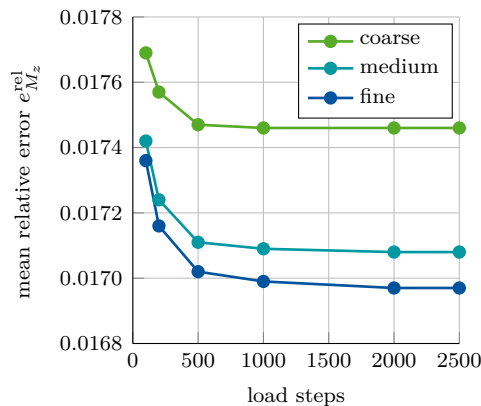


Table B.1 – Mesh sensitivity: mean per-centage error $e_{M_z}^{\text{mp}}$ according to Eq. (6.24) for different configurations of data set 1 ($\mu_b = 0.4$). Adopted from [Immel et al. \(2020\)](#). **Figure B.2** – Mesh sensitivity: mean relative error $e_{M_z}^{\text{rel}}$ according to Eq. (B.1) for different configurations of data set 1 ($\mu_b = 0.4$). Adopted from [Immel et al. \(2020\)](#).

Figure B.2 shows the convergence behavior of the different meshes. It can be seen that $e_{M_z}^{\text{mp}}$ reaches its limit for all meshes after 1,000 load steps to 0.0175, 0.0171, and 0.017, respectively. This is also the case for the mean percentage error shown in Table B.1, with its lowest value of 2.176 % for the fine mesh and the highest value of 2.241 % for the coarse mesh. In addition, the error is increasing with the number of load steps for the coarse mesh. This stems from the coarse resolution of the peak for larger load steps and thus leading to the torque values to be closer to the experimental data. It should be noted, that the mesh size has a small effect on

the outcome of the parameter study and thus, both $e_{M_z}^{\text{mp}}$ and $e_{M_z}^{\text{rel}}$ can be further minimized by performing a separate parameter estimation for each mesh.

B.3 Modified Coulomb's Friction Law on Acetabular Cup Implants

To analyze the convergence behavior of the MC applied to the acetabular cup implant, five different finite element meshes for the bone block were constructed with increasing refinement of the elements in x - and y -direction. The number of elements for each mesh are shown in Table B.2. The reference case ($E_{\text{tb}}^* = 0.2$ GPa, $\mu_{\text{b}}^* = 0.3$, $IF^* = 1.0$ mm) was chosen as the parameter set, and the maximum normal pull-out force $F_z^{\text{max}*}(\phi_0 = 1)$ was chosen as the target value.

body	mesh 1	mesh 2	mesh 3	mesh 4	mesh 5
contact elements bone	1000	2000	4000	8000	16000
contact elements implant	49	81	169	361	676
bulk elements	5188	10252	20588	40972	81602
total elements	6237	12333	24757	49333	98278

Table B.2 – Number of elements of the finite element meshes. Adopted from [Immel et al. \(2021c\)](#).

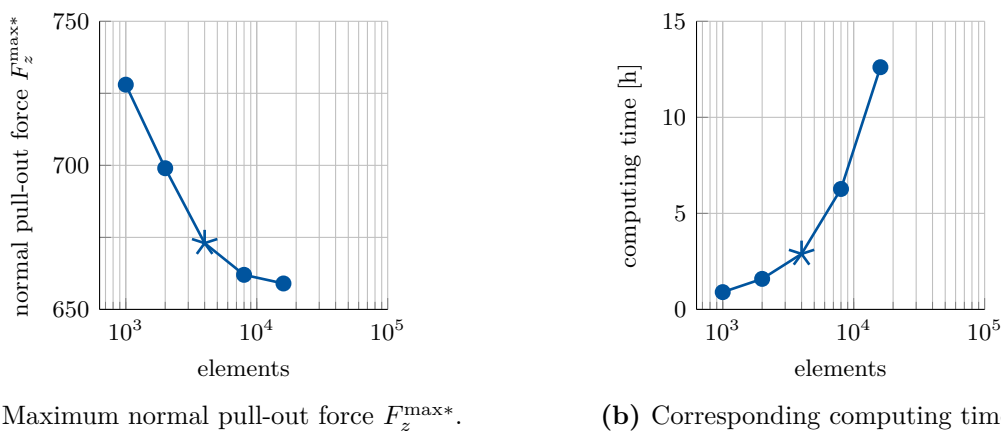


Figure B.3 – Maximum normal pull-out force $F_z^{\text{max}*}$ and corresponding computing time with respect to number of contact elements on the bone block. Mesh 3, which is used for the computations in this work, is marked with \star . Adopted from [Immel et al. \(2021c\)](#).

Figure B.3 shows the convergence behavior of the maximum pull-out force. It decreases with increasing number of elements, while the computing time increases exponentially. The estimated exact value of $F_z^{\text{max}*}(\phi_0 = 1) = 659$ N. The corresponding relative error of the maximum pull-out force of the meshes 1 to 4 is 10.5, 6.1, 2.1, and 0.4%, respectively. Due to the focus on contact problems, the mesh was only refined in x - and y -direction. The number of elements in z -direction remains 5, as a previous convergence study showed no measurable improvement with further refinement in z -direction. Due to the lack of comparable experimental data and the amount of computations (58 with standard Coulomb's law, 435 with each of the two contact models)

necessary for Section 7.3, mesh 3 was deemed to have a reasonable ratio between accuracy and computing time and was thus chosen for all computations in Section 7.3.

The average computing time with both contact models for the different loading cases performed with mesh 3 is listed in Table B.3. It should be noted, that the chosen parameter combination has an influence on the computing time. Parameter combinations that produce high pull-out forces also require more computing time.

load case	avg. computing time [h]	avg. # of Newton steps	# of load steps
case 1 MC	2	3	100
case 2 MC	16	4	1000
case 3 MC	2	3	100
case 1 EMC	3	4	100
case 2 EMC	30	6	1000
case 3 EMC	3	4	100

Table B.3 – Average computing time, average number of Newton-Raphson steps, and corresponding number of load steps for the simulations with the modified Coulomb’s law (MC) and its extension to adhesive friction (EMC) for the different loading cases. The results are shown for mesh 3. Adopted from [Immel et al. \(2021c\)](#).

Bibliography

- 4web medical. 4web medical posterior spine truss system – curved. <https://4webmedical.com/products/posterior-spine-truss-system-curved/>, 2021. Accessed: 16.02.2021.
- AAOS. American Academy of Orthopaedic Surgeons. Total hip replacement. <https://orthoinfo.aaos.org/globalassets/figures/a00377f03.jpg>. Accessed: 16.02.2021.
- R. Agarwal and A. García. Biomaterial strategies for engineering implants for enhanced osseointegration and bone repair. *Advanced Drug Delivery Reviews*, **94**:53–62, 2015.
- R. Ahmed, A. W. L. Law, T. W. Cheung, and C. Lau. Raman spectroscopy of bone composition during healing of subcritical calvarial defects. *Biomedical Optics Express*, **9**(4):1704–1716, 2018.
- T. Albrektsson, P. Brånemark, H. Hansson, and J. Lindström. Osseointegrated titanium implants: requirements for ensuring a long-lasting, direct bone-to-implant anchorage in man. *Acta Orthopaedica Scandinavica*, **52**(2):155–170, 1981.
- T. Albrektsson, H. Hansson, and B. Ivarsson. Interface analysis of titanium and zirconium bone implants. *Biomaterials*, **6**(2):97–101, 1985.
- T. Albrektsson, T. Jansson, and U. Lekholm. Osseointegrated dental implants. *Dental Clinics of North America*, **30**(1):151–174, 1986.
- F. Amirouche, G. Solitro, S. Broviak, M. Gonzalez, W. Goldstein, and R. Barmada. Factors influencing initial cup stability in total hip arthroplasty. *Clinical Biomechanics*, **29**(10):1177–1185, 2014.
- R. B. Anchieta, M. Baldassarri, F. Guastaldi, N. Tovar, M. N. Janal, J. Gottlow, M. Dard, R. Jimbo, and P. G. Coelho. Mechanical property assessment of bone healing around a titanium–zirconium alloy dental implant. *Clinical Implant Dentistry and Related Research*, **16**(6):913–919, 2014.
- R. B. Anchieta, M. V. Guimarães, M. Suzuki, N. Tovar, E. A. Bonfante, P. Atria, and P. G. Coelho. Nanomechanical assessment of bone surrounding implants loaded for 3 years in a canine experimental model. *Journal of Oral and Maxillofacial Surgery*, **76**(1):71–79, 2018.
- A. E. Anderson, C. L. Peters, B. D. Tuttle, and J. A. Weiss. Subject-specific finite element model of the pelvis: development, validation and sensitivity studies. *Journal of Biomechanical Engineering*, **127**(3):364–373, 2005.

- A. Andreykiv, P. Prendergast, F. Van Keulen, W. Swieszkowski, and P. Rozing. Bone ingrowth simulation for a concept glenoid component design. *Journal of Biomechanics*, **38**(5):1023–1033, 2005.
- Z. Artzi, N. Givol, M. D. Rohrer, C. E. Nemcovsky, H. S. Prasad, and H. Tal. Qualitative and quantitative expression of bovine bone mineral in experimental bone defects. Part 1: Description of a dog model and histological observations. *Journal of Periodontology*, **74**(8):1143–1152, 2003a.
- Z. Artzi, N. Givol, M. D. Rohrer, C. E. Nemcovsky, H. S. Prasad, and H. Tal. Qualitative and quantitative expression of bovine bone mineral in experimental bone defects. part 2: morphometric analysis. *Journal of Periodontology*, **74**(8):1153–1160, 2003b.
- M. Atsumi, S.-H. Park, and H.-L. Wang. Methods used to assess implant stability: current status. *International Journal of Oral & Maxillofacial Implants*, **22**(5), 2007.
- G. I. Barenblatt. The mathematical theory of equilibrium cracks in brittle fracture. In *Advances in Applied Mechanics*, volume **7**, pages 55–129. Elsevier, 1962.
- E. Baril, L. Lefebvre, and S. Hacking. Direct visualization and quantification of bone growth into porous titanium implants using micro computed tomography. *Journal of Materials Science: Materials in Medicine*, **22**(5):1321–1332, 2011.
- F. Barrere, C. V. D. Valk, G. Meijer, R. Dalmeijer, K. D. Groot, and P. Layrolle. Osteointegration of biomimetic apatite coating applied onto dense and porous metal implants in femurs of goats. *Journal of Biomedical Materials Research Part B: Applied Biomaterials*, **67**(1):655–665, 2003.
- F. Barrere, M. Snel, C. van Blitterswijk, K. de Groot, and P. Layrolle. Nano-scale study of the nucleation and growth of calcium phosphate coating on titanium implants. *Biomaterials*, **25**(14):2901–2910, 2004.
- D. Bayarchimeg, H. Namgoong, B. K. Kim, M. D. Kim, S. Kim, T.-I. Kim, Y. J. Seol, Y. M. Lee, Y. Ku, I.-C. Rhyu, et al. Evaluation of the correlation between insertion torque and primary stability of dental implants using a block bone test. *Journal of Periodontal & Implant Science*, **43**(1):30, 2013.
- H. H. Bayraktar, E. F. Morgan, G. L. Niebur, G. E. Morris, E. K. Wong, and T. M. Keaveny. Comparison of the elastic and yield properties of human femoral trabecular and cortical bone tissue. *Journal of Biomechanics*, **37**(1):27–35, 2004.
- b.braun. b.braun plasmafit acetabular cup system. <https://www.bbraun.com/en/products/b0/plasmafit-cementlessacetabularcupsystem.html>, 2021. Accessed: 16.02.2021.
- T. Belytschko, W. Liu, and B. Moran. *Nonlinear Finite Elements for Continua and Structures*. J. Wiley & Sons.–2000.–600 pp, 2000.
- S. Berahmani, D. Janssen, S. van Kessel, D. Wolfson, M. de Waal Malefijt, P. Buma, and N. Verdonschot. An experimental study to investigate biomechanical aspects of the initial stability of press-fit implants. *Journal of the Mechanical Behavior of Biomedical Materials*, **42**:177–185, 2015.

- J. E. Biemond, R. Aquarius, N. Verdonschot, and P. Buma. Frictional and bone ingrowth properties of engineered surface topographies produced by electron beam technology. *Archives of Orthopaedic and Trauma Surgery*, **131**(5):711–718, 2011.
- biotech-dental. biotech dental: The BIS dental implant. <http://www.biotech-dental.com/en/professional-health/dental-products-solutions/dental-implant/dental-implant-bis-conic/>, 2021. Accessed: 16.02.2021.
- N. E. Bishop, J.-C. Höhn, S. Rothstock, N. B. Damm, and M. M. Morlock. The influence of bone damage on press-fit mechanics. *Journal of Biomechanics*, **47**(6):1472–1478, 2014.
- M. J. Borden, M. A. Scott, J. A. Evans, and T. J. R. Hughes. Isogeometric finite element data structures based on Bezier extraction of NURBS. *International Journal of Numerical Methods in Engineering*, **85**(1):15–47, 2011.
- C. Bragdon, D. Burke, J. Lowenstein, D. O’Connor, B. Ramamurti, M. Jasty, and W. Harris. Differences in stiffness of the interface between a cementless porous implant and cancellous bone in vivo in dogs due to varying amounts of implant motion. *The Journal of Arthroplasty*, **11**(8):945–951, 1996.
- P.-I. Brånemark. Osseointegrated implants in the treatment of the edentulous jaw. experience from a 10-year period. *Scand. J. Plast. Reconstr. Surg. Suppl.*, **16**, 1977.
- R. Brånemark, L. O. Öhrnell, P. Nilsson, and P. Thomsen. Biomechanical characterization of osseointegration during healing: an experimental in vitro study in the rat. *Biomaterials*, **18**: 969–978, 1997.
- R. Brånemark, L.-O. Öhrnell, R. Skalak, L. Carlsson, and P.-I. Brånemark. Biomechanical characterization of osseointegration: an experimental in vivo investigation in the beagle dog. *Journal of Orthopaedic Research*, **16**(1):61–69, 1998.
- J. B. Brunski, D. A. Puleo, and A. Nanci. Biomaterials and biomechanics of oral and maxillo-facial implants: current status and future developments. *The International Journal of Oral & Maxillofacial Implants*, **15**(1):15–46, 2000.
- C. Caouette, M. N. Bureau, M. Lavigne, P.-A. Vendittoli, and N. Nuño. A new interface element with progressive damage and osseointegration for modeling of interfaces in hip resurfacing. *Proceedings of the Institution of Mechanical Engineers, Part H: Journal of Engineering in Medicine*, **227**(3):209–220, 2013.
- C. Castellani, R. A. Lindtner, P. Hausbrandt, E. Tschegg, S. E. Stanzl-Tschegg, G. Zanoni, S. Beck, and A.-M. Weinberg. Bone-implant interface strength and osseointegration: Biodegradable magnesium alloy versus standard titanium control. *Acta Biomaterialia*, **7**(1): 432–440, 2011.
- S. Chanda, K. Mukherjee, S. Gupta, and D. K. Pratihari. A comparative assessment of two designs of hip stem using rule-based simulation of combined osseointegration and remodelling. *Proceedings of the Institution of Mechanical Engineers, Part H: Journal of Engineering in Medicine*, **234**(1):118–128, 2020.

- P.-C. Chang, Y.-J. Seol, N. Kikuchi, S. A. Goldstein, and W. V. Giannobile. Functional apparent moduli as predictors of oral implant osseointegration dynamics. *Journal of Biomedical Materials Research Part B: Applied Biomaterials*, **94**(1):118–126, 2010.
- J. Charnley. The bonding of prostheses to bone by cement. *The Journal of Bone and Joint Surgery. British Volume*, **46**(3):518–529, 1964.
- A. Chateauminos, C. Fretigny, and L. Olanier. Friction and shear fracture of an adhesive contact under torsion. *Physical Review E*, **81**(2):026106, 2010.
- D. Chong, U. Hansen, and A. Amis. Analysis of bone–prosthesis interface micromotion for cementless tibial prosthesis fixation and the influence of loading conditions. *Journal of Biomechanics*, **43**(6):1074–1080, 2010.
- I.-C. Chou, S.-Y. Lee, M.-C. Wu, C.-W. Sun, and C.-P. Jiang. Finite element modelling of implant designs and cortical bone thickness on stress distribution in maxillary type iv bone. *Computer Methods in Biomechanics and Biomedical Engineering*, **17**(5):516–526, 2014.
- P. Cignoni, M. Callieri, M. Corsini, M. Dellepiane, F. Ganovelli, and G. Ranzuglia. Meshlab: an open-source mesh processing tool. In *Eurographics Italian Chapter Conference*, volume **2008**, pages 129–136. Salerno, Italy, 2008.
- A. C. Cilingir, V. Ucar, and R. Kazan. Three–dimensional anatomic finite element modelling of hemi–arthroplasty of human hip joint. *Trends in Biomaterials and Artificial Organs*, **21**(1):63–72, 2007.
- S. Clarke, A. Phillips, and A. Bull. Evaluating a suitable level of model complexity for finite element analysis of the intact acetabulum. *Computer Methods in Biomechanics and Biomedical Engineering*, **16**(7):717–724, 2013.
- D. Cochran, R. Schenk, A. Lussi, F. Higginbottom, and D. Buser. Bone response to unloaded and loaded titanium implants with a sandblasted and acid–etched surface: A histometric study in the canine mandible. *Journal of Biomedical Materials Research: An Official Journal of The Society for Biomaterials, The Japanese Society for Biomaterials, and the Australian Society for Biomaterials*, **40**(1):1–11, 1998.
- S. Cook, K. Thomas, J. Delton, T. Volkman, T. Whitecloud, and J. Key. Hydroxylapatite coating of porous implants improves bone ingrowth and interface attachment strength. *Journal of Biomedical Materials Research Part A*, **26**(8):989–1001, 1992.
- C. J. Corbett and R. A. Sauer. NURBS–enriched contact finite elements. *Computer Methods in Applied Mechanics and Engineering*, **275**:55–75, 2014.
- C. J. Corbett and R. A. Sauer. Three–dimensional isogeometrically enriched finite elements for frictional contact and mixed–mode debonding. *Computer Methods in Applied Mechanics and Engineering*, **284**:781–806, 2015.
- J. A. Cottrell, T. J. Hughes, and Y. Bazilevs. *Isogeometric analysis: Toward integration of CAD and FEA*. John Wiley & Sons, 2009.

-
- M. G. Cox. The numerical evaluation of b-splines. *IMA Journal of Applied Mathematics*, 10(2): 134–149, 1972.
- P. Cram, X. Lu, S. L. Kates, J. A. Singh, Y. Li, and B. R. Wolf. Total knee arthroplasty volume, utilization, and outcomes among medicare beneficiaries, 1991-2010. *Journal of the American Medical Association*, **308**(12):1227–1236, 2012.
- R. W. Crawford and D. Murray. Total hip replacement: indications for surgery and risk factors for failure. *Annals of the Rheumatic Diseases*, **56**(8):455–457, 1997.
- M. Curtis, R. Jinnah, V. Wilson, and D. Hungerford. The initial stability of uncemented acetabular components. *The Journal of Bone and Joint Surgery. British volume*, **74**(3):372–376, 1992.
- N. Damm, M. Morlock, and N. Bishop. Friction coefficient and effective interference at the implant–bone interface. *Journal of Biomechanics*, **48**(12):3517–3521, 2015.
- M. Dammak, A. Shirazi-Adl, M. Schwartz, and L. Gustavson. Friction properties at the bone-metal interface: Comparison of four different porous metal surfaces. *Journal of Biomedical Materials Research Part A*, **35**(3):329–336, 1997a.
- M. Dammak, A. Shirazi-Adl, and D. Zukor. Analysis of cementless implants using interface nonlinear friction–experimental and finite element studies. *Journal of Biomechanics*, **30**(2): 121–129, 1997b.
- C. De Boor. On calculating with b-splines. *Journal of Approximation Theory*, 6(1):50–62, 1972.
- H. De Bruyn, V. Christiaens, R. Doornewaard, M. Jacobsson, J. Cosyn, W. Jacquet, and S. Vervaeke. Implant surface roughness and patient factors on long-term peri-implant bone loss. *Periodontology 2000*, **73**(1):218–227, 2017.
- V. Demenko, I. Linetskiy, L. Linetska, V. Nesvit, A. Shevchenko, O. Yefremov, and H.-W. Weisskircher. Prognosis of implant longevity in terms of annual bone loss: a methodological finite element study. *Computer Methods in Biomechanics and Biomedical Engineering*, **19**(2): 180–187, 2016.
- A. Dickinson, A. Taylor, and M. Browne. Implant–bone interface healing and adaptation in resurfacing hip replacement. *Computer Methods in Biomechanics and Biomedical Engineering*, **15**(9):935–947, 2012.
- J. H. Dieterich. Time-dependent friction and the mechanics of stick-slip. In *Rock Friction and Earthquake Prediction*, pages 790–806. Springer, 1978.
- J. H. Dieterich. Modeling of rock friction: 1. experimental results and constitutive equations. *Journal of Geophysical Research: Solid Earth*, **84**(B5):2161–2168, 1979a.
- M. Doblaré and J. García. Anisotropic bone remodelling model based on a continuum damage-repair theory. *Journal of Biomechanics*, **35**(1):1–17, 2002.

- M. Drexler, T. Dwyer, M. Marmor, M. Abolghasemian, A. Sternheim, and H. Cameron. Cementless fixation in total knee arthroplasty: down the boulevard of broken dreams—opposes. *The Journal of Bone and Joint Surgery. British Volume*, **94**(11_Supple_A):85–89, 2012.
- A. Dubory, G. Rosi, A. Tijou, H. A. Lomami, C.-H. Flouzat-Lachaniette, and G. Haiat. A cadaveric validation of a method based on impact analysis to monitor the femoral stem insertion. *Journal of the Mechanical Behavior of Biomedical Materials*, **103**:103535, 2020.
- D. S. Dugdale. Yielding of steel sheets containing slits. *Journal of the Mechanics and Physics of Solids*, **8**(2):100–104, 1960.
- T. X. Duong and R. A. Sauer. A concise frictional contact formulation based on surface potentials and isogeometric discretization. *Computational Mechanics*, **64**(4):951–970, 2019.
- C. A. Engh, D. O’Connor, M. Jasty, T. F. McGovern, J. D. Bobyn, and W. H. Harris. Quantification of implant micromotion, strain shielding, and bone resorption with porous-coated anatomic medullary locking femoral prostheses. *Clinical Orthopaedics and Related Research*, (285):13–29, 1992.
- C. A. Engh, R. H. Hopper Jr, and C. A. Engh Jr. Long-term porous-coated cup survivorship using spikes, screws, and press-fitting for initial fixation. *The Journal of Arthroplasty*, **19**(7):54–60, 2004.
- P. Fernandes, J. Folgado, C. Jacobs, and V. Pellegrini. A contact model with ingrowth control for bone remodelling around cementless stems. *Journal of Biomechanics*, **35**(2):167–176, 2002.
- C. Fitzpatrick, P. Hemelaar, and M. Taylor. Computationally efficient prediction of bone–implant interface micromotion of a cementless tibial tray during gait. *Journal of Biomechanics*, **47**(7):1718–1726, 2014.
- M. Fraulob, S. Le Cann, B. Voumard, H. Yasui, K. Yano, R. Vayron, M. Matsukawa, P. Zysset, and G. Haiat. Multimodal evaluation of the spatiotemporal variations of periprosthetic bone properties. *Journal of Biomechanical Engineering*, **142**(12), 2020a.
- M. Fraulob, S. Pang, S. Le Cann, R. Vayron, M. Laurent-Brocq, S. Todatry, J. A. Soares, I. Jasiuk, and G. Haiat. Multimodal characterization of the bone–implant interface using raman spectroscopy and nanoindentation. *Medical Engineering & Physics*, **84**:60–67, 2020b.
- M. Fraulob, R. Vayron, S. Le Cann, B. Lecuelle, Y. Hériveaux, H. A. Lomami, C. F. Lachaniette, and G. Haiat. Quantitative ultrasound assessment of the influence of roughness and healing time on osseointegration phenomena. *Scientific Reports*, **10**(1):1–12, 2020c.
- B. Friberg, L. Sennerby, J. Roos, P. Johansson, C. Strid, and U. Lekholm. Evaluation of bone density using cutting resistance measurements and microradiography. an in vitro study in pig ribs. *Clinical Oral Implants Research*, **6**(3):164–171, 1995.
- B. Friberg, L. Sennerby, K. Gröndahl, C. Bergström, T. Bäck, and U. Lekholm. On cutting torque measurements during implant placement: a 3–year clinical prospective study. *Clinical Implant Dentistry and Related research*, **1**(2):75–83, 1999.

- O. Galasso, M. Mariconda, G. Calonego, and G. Gasparini. Physical, mechanical and pharmacological properties of coloured bone cement with and without antibiotics. *The Journal of Bone and Joint Surgery. British Volume*, **93**(11):1529–1536, 2011.
- F. Galloway, M. Kahnt, H. Ramm, P. Worsley, S. Zachow, P. Nair, and M. Taylor. A large scale finite element study of a cementless osseointegrated tibial tray. *Journal of Biomechanics*, **46**(11):1900–1906, 2013.
- X. Gao and I. Sevostianov. Connection between elastic and electrical properties of cortical bone. *Journal of Biomechanics*, **49**(5):765–772, 2016.
- X. Gao, M. Fraulob, and G. Haiat. Biomechanical behaviours of the bone–implant interface: a review. *Journal of the Royal Society Interface*, **16**(156):20190259, 2019.
- R. Ghosh and S. Gupta. Bone remodelling around cementless composite acetabular components: The effects of implant geometry and implant–bone interfacial conditions. *Journal of the Mechanical Behavior of Biomedical materials*, **32**:257–269, 2014.
- A. H. Goldman, L. C. Armstrong, J. R. Owen, J. S. Wayne, and W. A. Jiranek. Does increased coefficient of friction of highly porous metal increase initial stability at the acetabular interface? *The Journal of Arthroplasty*, **31**(3):721–726, 2016.
- S. A. Goldstein. The mechanical properties of trabecular bone: dependence on anatomic location and function. *Journal of Biomechanics*, **20**(11-12):1055–1061, 1987.
- Q. Goossens, L. Pastrav, J. Roosen, M. Mulier, W. Desmet, J. Vander Sloten, and K. Denis. Acoustic analysis to monitor implant seating and early detect fractures in cementless tha: An in vivo study. *Journal of Orthopaedic Research*, **39**(6):1164–1173, 2021.
- K. Grandfield. Bone, implants, and their interfaces. *Physics Today*, **68**(4):40, 2015.
- J. A. Grant, N. E. Bishop, N. Götzen, C. Sprecher, M. Honl, and M. M. Morlock. Artificial composite bone as a model of human trabecular bone: the implant–bone interface. *Journal of Bomechanics*, **40**(5):1158–1164, 2007.
- A. Grimberg, V. Jansson, O. Melsheimer, and A. Steinbrück. Endoprothesenregister deutschland: Jahresbericht 2019. *EPRD Deutsche Endoprothesenregister GmbH: Berlin, Germany*, 2019.
- S. Gupta, B. Pal, and A. M. New. The effects of interfacial conditions and stem length on potential failure mechanisms in the uncemented resurfaced femur. *Annals of Biomedical Engineering*, **38**(6):2107–2120, 2010.
- M. H. Hadjari, J. M. Hollis, O. E. Hofmann, C. M. Flahiff, and C. L. Nelson. Initial stability of porous coated acetabular implants. the effect of screw placement, screw tightness, defect type, and oversize implants. *Clinical Orthopaedics and Related Research*, (**307**):117–123, 1994.
- G. Haiat, H.-L. Wang, and J. Brunski. Effects of biomechanical properties of the bone–implant interface on dental implant stability: from in silico approaches to the patient’s mouth. *Annual Review of Biomedical Engineering*, **16**:187–213, 2014.

- N. P. Hailer, G. Garellick, and J. Kärrholm. Uncemented and cemented primary total hip arthroplasty in the swedish hip arthroplasty register: evaluation of 170,413 operations. *Acta Orthopaedica*, **81**(1):34–41, 2010.
- H. Hamaker. The london-van der waals attraction between spherical particles. *Physica*, **4**(10):1058–1072, 1937.
- Z. Hao, C. Wan, X. Gao, and T. Ji. The effect of boundary condition on the biomechanics of a human pelvic joint under an axial compressive load: a three-dimensional finite element model. *Journal of Biomechanical Engineering*, **133**(10):101006, 2011.
- B. Helgason, M. Viceconti, T. P. Rúnarsson, and S. Brynjólfsson. On the mechanical stability of porous coated press fit titanium implants: a finite element study of a pushout test. *Journal of Biomechanics*, **41**(8):1675–1681, 2008.
- B. Helgason, H. Pálsson, T. P. Rúnarsson, L. Frossard, and M. Viceconti. Risk of failure during gait for direct skeletal attachment of a femoral prosthesis: A finite element study. *Medical Engineering & Physics*, **31**(5):595–600, 2009.
- P. Henyš and L. Čapek. Material model of pelvic bone based on modal analysis: a study on the composite bone. *Biomechanics and Modeling in Mechanobiology*, **6**(1):363–373, 2017.
- P. Herberts and H. Malchau. How outcome studies have changed total hip arthroplasty practices in sweden. *Clinical Orthopaedics and Related Research*, (**344**):44–60, 1997.
- P. Herberts and H. Malchau. Long-term registration has improved the quality of hip replacement: a review of the swedish thr register comparing 160,000 cases. *Acta Orthopaedica Scandinavica*, **71**(2):111–121, 2000.
- hipSTL. Lincoln 3D scans. <https://www.lincoln3dscans.co.uk/lincoln-3d-scans/2018/7/3/human-pelvis-bone>. Accessed: 11.06.2019.
- G. Holzapfel. *Nonlinear solid mechanics*, volume **24**. Wiley Chichester, 2000.
- H. Hothi, J. Busfield, and J. Shelton. Explicit finite element modelling of the impaction of metal press-fit acetabular components. *Proceedings of the Institution of Mechanical Engineers, Part H: Journal of Engineering in Medicine*, **225**(3):303–314, 2011.
- J.-T. Hsu, K.-A. Lai, Q. Chen, M. E. Zobitz, H.-L. Huang, K.-N. An, and C.-H. Chang. The relation between micromotion and screw fixation in acetabular cup. *Computer Methods and Programs in Biomedicine*, **84**(1):34–41, 2006.
- J.-T. Hsu, C.-H. Chang, H.-L. Huang, M. E. Zobitz, W.-P. Chen, K.-A. Lai, and K.-N. An. The number of screws, bone quality, and friction coefficient affect acetabular cup stability. *Medical Engineering & Physics*, **29**(10):1089–1095, 2007.
- T. J. R. Hughes, J. A. Cottrell, and Y. Bazilevs. Isogeometric analysis: CAD, finite elements, NURBS, exact geometry and mesh refinement. *Computer Methods in Applied Mechanics and Engineering*, **194**(1):4135–4195, 2005.

- R. Huiskes. Failed innovation in total hip replacement: diagnosis and proposals for a cure. *Acta Orthopaedica Scandinavica*, **64**(6):699–716, 1993.
- R. Huiskes, H. Weinans, H. Grootenboer, M. Dalstra, B. Fudala, and T. Slooff. Adaptive bone-remodeling theory applied to prosthetic-design analysis. *Journal of Biomechanics*, **20**(11-12): 1135–1150, 1987.
- R. Huiskes, W. D. van Driel, P. J. Prendergast, and K. Søballe. A biomechanical regulatory model for periprosthetic fibrous-tissue differentiation. *Journal of Materials Science: Materials in Medicine*, **8**(12):785–788, 1997.
- S. Huja, T. Katona, D. Burr, L. Garetto, and W. Roberts. Microdamage adjacent to endosseous implants. *Bone*, **25**(2):217–222, 1999.
- K. Immel, T. X. Duong, V.-H. Nguyen, G. Haiat, and R. A. Sauer. A frictional and adhesive contact model for debonding of the bone–implant interface based on state variable friction laws. In T. Gleim and S. Lange, editors, *Proceedings of 8th GACM Colloquium on Computational Mechanics*, pages 393–396. kassel university GmbH, 2019.
- K. Immel, T. X. Duong, V.-H. Nguyen, G. Haiat, and R. A. Sauer. A modified coulomb’s law for the tangential debonding of osseointegrated implants. *Biomechanics and Modeling in Mechanobiology*, **19**:1–18, 2020.
- K. Immel, V.-H. Nguyen, A. Dubory, C.-H. Flouzat-Lachaniette, R. A. Sauer, and G. Haiat. Determinants of the primary stability of cementless acetabular cup implants: A 3D finite element study. *Computers in Biology and Medicine*, **135**:104607, 2021a.
- K. Immel, V.-H. Nguyen, G. Haiat, and R. A. Sauer. Long-term stability and debonding of cementless implants. In *Proceedings in Applied Mathematics and Mechanics*, volume 21, page e202100118, 2021b. doi: <https://doi.org/10.1002/pamm.202100118>.
- K. Immel, V.-H. Nguyen, G. Haiat, and R. A. Sauer. Modeling the debonding process of osseointegrated implants due to coupled adhesion and friction. *arXiv preprint arXiv:2112.06793*, 2021c.
- D. Janssen, R. E. Zwartelé, H. C. Doets, and N. Verdonschot. Computational assessment of press–fit acetabular implant fixation: the effect of implant design, interference fit, bone quality, and frictional properties. *Proceedings of the Institution of Mechanical Engineers, Part H: Journal of Engineering in Medicine*, **224**(1):67–75, 2010.
- M. Jasty, R. Summer, J. O. Galante, C. R. Bragdon, E. A. Cargill, and W. H. Harris. Bone ingrowth into porous–surfaced harris/galante prosthesis acetabular components retrieved from human patients. In *Presented at the 55th Annual Meeting of the American Academy of Orthopaedic Surgeons. Atlanta, Georgia*, volume **102**, 1988.
- M. Jasty, C. Bragdon, D. Burke, D. O’connor, J. Lowenstein, and W. Harris. In vivo skeletal responses to porous-surfaced implants subjected to small induced motions. *Journal of Bone and Joint Surgery*, **79**(5):707–14, 1997.

- A. Jemat, M. J. Ghazali, M. Razali, and Y. Otsuka. Surface modifications and their effects on titanium dental implants. *Biomedical Research International*, 2015, 2015.
- C. Johansson and T. Albrektsson. A removal torque and histomorphometric study of commercially pure niobium and titanium implants in rabbit bone. *Clinical Oral Implants Research*, **2**(1):24–29, 1991.
- J. E. Jones. On the determination of molecular fields.—i. from the variation of the viscosity of a gas with temperature. *Proceedings of the Royal Society of London. Series A, Containing Papers of a Mathematical and Physical Character*, 106(738):441–462, 1924a.
- J. E. Jones. On the determination of molecular fields.—ii. from the equation of state of a gas. *Proceedings of the Royal Society of London. Series A, Containing Papers of a Mathematical and Physical Character*, 106(738):463–477, 1924b.
- T. S. Kaneko, J. S. Bell, M. R. Pejcic, J. Tehranzadeh, and J. H. Keyak. Mechanical properties, density and quantitative ct scan data of trabecular bone with and without metastases. *Journal of Biomechanics*, **37**(4):523–530, 2004.
- D.-G. Kim, K. L. Elias, Y.-H. Jeong, H.-J. Kwon, M. Clements, W. A. Brantley, D. J. Lee, and J.-S. Han. Differences between buccal and lingual bone quality and quantity of peri-implant regions. *Journal of the Mechanical Behavior of Biomedical Materials*, **60**:48–55, 2016a.
- D.-G. Kim, H.-J. Kwon, Y.-H. Jeong, E. Kosel, D. J. Lee, J.-S. Han, H.-L. Kim, and D.-J. Kim. Mechanical properties of bone tissues surrounding dental implant systems with different treatments and healing periods. *Clinical Oral Investigations*, **20**(8):2211–2220, 2016b.
- Y. Kim, T. Brown, D. Pedersen, and J. Callaghan. Reamed surface topography and component seating in press-fit cementless acetabular fixation. *The Journal of Arthroplasty*, **10**:S14–S21, 1995.
- P. T. Knott, S. M. Mardjetko, R. H. Kim, T. M. Cotter, M. M. Dunn, S. T. Patel, M. J. Spencer, A. S. Wilson, and D. S. Tager. A comparison of magnetic and radiographic imaging artifact after using three types of metal rods: stainless steel, titanium, and vitallium. *The Spine Journal*, **10**(9):789–794, 2010.
- R. Korabi, K. Shemtov-Yona, A. Dorogoy, and D. Rittel. The failure envelope concept applied to the bone-dental implant system. *Scientific Reports*, **7**(1):1–11, 2017.
- D. Kurniawan, F. Nor, H. Lee, and J. Lim. Finite element analysis of bone-implant biomechanics: refinement through featuring various osseointegration conditions. *International Journal of Oral and Maxillofacial Surgery*, **41**(9):1090–1096, 2012.
- S. M. Kurtz, K. Ong, E. Lau, F. Mowat, and M. Halpern. Projections of primary and revision hip and knee arthroplasty in the united states from 2005 to 2030. *The Journal of Bone & Joint Surgery*, **89**(4):780–785, 2007.
- S. M. Kurtz, K. L. Ong, E. Lau, and K. J. Bozic. Impact of the economic downturn on total joint replacement demand in the united states: updated projections to 2021. *The Journal of Bone & Joint Surgery*, **96**(8):624–630, 2014.

-
- I. Kutzner, B. Heinlein, F. Graichen, A. Bender, A. Rohlmann, A. Halder, A. Beier, and G. Bergmann. Loading of the knee joint during activities of daily living measured in vivo in five subjects. *Journal of Biomechanics*, **43**(11):2164–2173, 2010.
- L. Kwong, D. O’Connor, R. Sedlacek, R. Krushell, W. Maloney, and W. Harris. A quantitative in vitro assessment of fit and screw fixation on the stability of a cementless hemispherical acetabular component. *The Journal of Arthroplasty*, **9**(2):163–170, 1994.
- P. Laugier and G. Haiat. *Bone quantitative ultrasound*, volume **576**. Springer, 2011.
- T. A. Laursen. *Computational contact and impact mechanics: fundamentals of modeling interfacial phenomena in nonlinear finite element analysis*. Springer Science & Business Media, 2013.
- S. Le Cann, A. Galland, B. Rosa, T. Le Corroller, M. Pithioux, J.-N. Argenson, P. Chabrand, and S. Parratte. Does surface roughness influence the primary stability of acetabular cups? a numerical and experimental biomechanical evaluation. *Medical Engineering & Physics*, **36**(9):1185–1190, 2014.
- L. Le Guéhennec, A. Soueidan, P. Layrolle, and Y. Amouriq. Surface treatments of titanium dental implants for rapid osseointegration. *Dental Materials*, **23**(7):844–854, 2007.
- I. D. Learmonth, C. Young, and C. Rorabeck. The operation of the century: total hip replacement. *The Lancet*, **370**(9597):1508–1519, 2007.
- K. Lee and S. Goodman. Current state and future of joint replacements in the hip and knee. *Expert Review of Medical Devices*, **5**(3):383–393, 2008.
- H. A. Lomami, C. Damour, G. Rosi, A.-S. Poudrel, A. Dubory, C.-H. Flouzat-Lachaniette, and G. Haiat. Ex vivo estimation of cementless femoral stem stability using an instrumented hammer. *Clinical Biomechanics*, **76**:105006, 2020.
- C. B. Lopes, A. L. Pinheiro, S. Sathaiyah, N. S. D. Silva, and M. A. Salgado. Infrared laser photobiomodulation (λ 830 nm) on bone tissue around dental implants: a raman spectroscopy and scanning electronic microscopy study in rabbits. *Photomedicine and Laser Surgery*, **25**(2):96–101, 2007.
- A. Lutz and U. Nackenhorst. Numerical investigations on the osseointegration of uncemented endoprostheses based on bio-active interface theory. *Computational Mechanics*, **50**(3):367–381, 2012.
- W. Macdonald, L. Carlsson, G. Charnley, and C. Jacobsson. Press-fit acetabular cup fixation: principles and testing. *Proceedings of the Institution of Mechanical Engineers, Part H: Journal of Engineering in Medicine*, **213**(1):33–39, 1999.
- J. R. MacKenzie, J. J. Callaghan, D. R. Pedersen, and T. D. Brown. Areas of contact and extent of gaps with implantation of oversized acetabular components in total hip arthroplasty. *Clinical Orthopaedics and Related Research*, (298):127–136, 1994.

- C. Marin, R. Granato, M. Suzuki, M. N. Janal, et al. Biomechanical and histomorphometric analysis of etched and non-etched resorbable blasting media processed implant surfaces: an experimental study in dogs. *Journal of the Mechanical Behavior of Biomedical Materials*, **3**(5):382–391, 2010.
- D. C. Markel, N. Hora, and M. Grimm. Press-fit stability of uncemented hemispheric acetabular components: a comparison of three porous coating systems. *International Orthopaedics*, **26**(2):72–75, 2002.
- M. Martin, T. Lemaire, G. Haiat, P. Pivonka, and V. Sansalone. Bone orthotropic remodeling as a thermodynamically-driven evolution. *Journal of Mechanics in Medicine and Biology*, **20**(04):1950084, 2020.
- V. Mathieu, F. Anagnostou, E. Soffer, and G. Haiat. Ultrasonic evaluation of dental implant biomechanical stability: an in vitro study. *Ultrasound in Medicine & Biology*, **37**(2):262–270, 2011a.
- V. Mathieu, K. Fukui, M. Matsukawa, M. Kawabe, R. Vayron, E. Soffer, F. Anagnostou, and G. Haiat. Micro-brillouin scattering measurements in mature and newly formed bone tissue surrounding an implant. *Journal of Biomechanical Engineering*, 133(2), 2011b.
- V. Mathieu, K. Fukui, M. Matsukawa, M. Kawabe, R. Vayron, E. Soffer, F. Anagnostou, and G. Haiat. Micro-brillouin scattering measurements in mature and newly formed bone tissue surrounding an implant. *Journal of Biomechanical Engineering*, **133**(2):021006, 2011c.
- V. Mathieu, R. Vayron, E. Barthel, D. Dalmas, E. Soffer, F. Anagnostou, and G. Haiat. Mode III cleavage of a coin-shaped titanium implant in bone: Effect of friction and crack propagation. *Journal of the Mechanical Behavior of Biomedical Materials*, **8**(1):194–203, 2012a.
- V. Mathieu, R. Vayron, E. Soffer, F. Anagnostou, and G. Haiat. Influence of healing time on the ultrasonic response of the bone-implant interface. *Ultrasound in Medicine & Biology*, **38**(4):611–618, 2012b.
- J. C. Mergel, R. Sahli, J. Scheibert, and R. A. Sauer. Continuum contact models for coupled adhesion and friction. *The Journal of Adhesion*, **95**(12):1101–1133, 2019.
- J. C. Mergel, J. Scheibert, and R. A. Sauer. Contact with coupled adhesion and friction: Computational framework, applications, and new insights. *Journal of the Mechanics and Physics of Solids*, 146:104194, 2021.
- A. Michel, R. Bosc, V. Mathieu, P. Hernigou, and G. Haiat. Monitoring the press-fit insertion of an acetabular cup by impact measurements: Influence of bone abrasion. *Proceedings of the Institution of Mechanical Engineers, Part H: Journal of Engineering in Medicine*, **228**(10):1027–1034, 2014.
- A. Michel, R. Bosc, J. Meningaud, P. Hernigou, and G. Haiat. Assessing the acetabular cup implant primary stability by impact analyses: A cadaveric study. *PloS one*, **11**(11):e0166778, 2016a.

- A. Michel, R. Bosc, F. Sailhan, R. Vayron, and G. Haiat. Ex vivo estimation of cementless acetabular cup stability using an impact hammer. *Medical Engineering & Physics*, **38**(2): 80–86, 2016b.
- A. Michel, V.-H. Nguyen, R. Bosc, R. Vayron, P. Hernigou, S. Naili, and G. Haiat. Finite element model of the impaction of a press-fitted acetabular cup. *Medical & Biological Engineering & Computing*, **55**(5):781–791, 2017.
- S. Mondal and R. Ghosh. The effects of implant orientations and implant–bone interfacial conditions on potential causes of failure of tibial component due to total ankle replacement. *Journal of Medical and Biological Engineering*, **39**(4):541–551, 2019.
- P. Moreo, M. Pérez, J. García-Aznar, and M. Doblaré. Modelling the mechanical behaviour of living bony interfaces. *Computer Methods in Applied Mechanics and Engineering*, **196**(35-36): 3300–3314, 2007.
- E. F. Morgan, G. U. Unnikrisnan, and A. I. Hussein. Bone mechanical properties in healthy and diseased states. *Annual Review of Biomedical Engineering*, **20**:119–143, 2018.
- K. Mukherjee and S. Gupta. Simulation of tissue differentiation around acetabular cups: the effects of implant–bone relative displacement and polar gap. *Advanced Biomechanical Applications*, **1**(2):95–109, 2014.
- K. Mukherjee and S. Gupta. Bone ingrowth around porous-coated acetabular implant: a three-dimensional finite element study using mechanoregulatory algorithm. *Biomechanics and Modeling in Mechanobiology*, **15**(2):389–403, 2016.
- K. Mukherjee and S. Gupta. Influence of implant surface texture design on peri-acetabular bone ingrowth: a mechanobiology based finite element analysis. *Journal of Biomechanical Engineering*, **139**(3), 2017.
- N. Murakami and N. Wakabayashi. Finite element contact analysis as a critical technique in dental biomechanics: a review. *Journal of Prosthodontic Research*, **58**(2):92–101, 2014.
- V.-H. Nguyen, G. Rosi, S. Naili, A. Michel, M.-L. Raffa, R. Bosc, J.-P. Meningaud, C. Chappard, N. Takano, and G. Haiat. Influence of anisotropic bone properties on the biomechanical behavior of the acetabular cup implant: a multiscale finite element study. *Computer Methods in Biomechanics and Biomedical Engineering*, **20**(12):1312–1325, 2017.
- J. Nonhoff, T. Moest, C. M. Schmitt, T. Weisel, S. Bauer, and K. Schlegel. Establishment of a new pull-out strength testing method to quantify early osseointegration—an experimental pilot study. *Journal of Cranio-Maxillofacial Surgery*, **43**(10):1966–1973, 2015.
- A. Novaes, S. de Souzae, R. de Barros, K. Pereira, G. Iezzi, and A. Piattelli. Influence of implant surfaces on osseointegration. *Brazilian Dental Journal*, **21**(6):471–481, 2010.
- E. Novitskaya, P. Chen, E. Hamed, L. Jun, V. A. Lubarda, I. Jasiuk, and J. McKittrick. Recent advances on the measurement and calculation of the elastic moduli of cortical and trabecular bone: a review. *Theoretical and Applied Mechanics*, **38**(3):209–297, 2011.

- B. Olory, E. Havet, A. Gabrion, J. Vernois, and P. Mertl. Comparative in vitro assessment of the primary stability of cementless press-fit acetabular cups. *Acta Orthopædica Belgica*, **70**(1):31–37, 2004.
- M. J. Olszta, X. Cheng, S. S. Jee, R. Kumar, Y.-Y. Kim, M. J. Kaufman, E. P. Douglas, and L. B. Gower. Bone structure and formation: A new perspective. *Materials Science and Engineering: R: Reports*, **58**(3-5):77–116, 2007.
- M. Ovesy, M. Aeschlimann, and P. K. Zysset. Explicit finite element analysis can predict the mechanical response of conical implant press-fit in homogenized trabecular bone. *Journal of Biomechanics*, page 109844, 2020.
- A. Palmquist, F. Lindberg, L. Emanuelsson, R. Brånemark, H. Engqvist, and P. Thomsen. Biomechanical, histological, and ultrastructural analyses of laser micro- and nano-structured titanium alloy implants: A study in rabbit. *Journal of Biomedical Materials Research Part A*, **92**(4):1476–1486, 2010.
- P. Pankaj. Patient-specific modelling of bone and bone-implant systems: the challenges. *International Journal for Numerical Methods in Biomedical Engineering*, **29**(2):233–249, 2013.
- E. Paschalis, K. Verdellis, S. Doty, A. Boskey, R. Mendelsohn, and M. Yamauchi. Spectroscopic characterization of collagen cross-links in bone. *Journal of Bone and Mineral Research*, **16**(10):1821–1828, 2001.
- S. H. Pettersen, T. S. Wik, and B. Skallerud. Subject specific finite element analysis of implant stability for a cementless femoral stem. *Clinical Biomechanics*, **24**(6):480–487, 2009.
- A. Phillips, P. Pankaj, C. Howie, A. Usmani, and A. Simpson. Finite element modelling of the pelvis: inclusion of muscular and ligamentous boundary conditions. *Medical Engineering & Physics*, **29**(7):739–748, 2007.
- R. Pilliar, J. Lee, and C. Maniopoulos. Observations on the effect of movement on bone ingrowth into porous-surfaced implants. *Clinical Orthopaedics and Related Research*, **208**:108–113, 1986.
- P. Prendergast. Finite element models in tissue mechanics and orthopaedic implant design. *Clinical Biomechanics*, **12**(6):343–366, 1997.
- P. Prendergast and D. Taylor. Prediction of bone adaptation using damage accumulation. *Journal of Biomechanics*, **27**(8):1067–1076, 1994.
- M. L. Raffa, V.-H. Nguyen, E. Tabor, K. Immel, V. Housset, C.-H. Flouzat-Lachaniette, and G. Haiat. Dependence of the primary stability of cementless acetabular cup implants on the biomechanical environment. *Proceedings of the Institution of Mechanical Engineers, Part H: Journal of Engineering in Medicine*, **233**(12):1237–1249, 2019.
- D. Rancourt, A. Shirazi-Adl, G. Drouin, and G. Paiement. Friction properties of the interface between porous-surfaced metals and tibial cancellous bone. *Journal of Biomedical Materials Research Part A*, **24**(11):1503–1519, 1990.

- J. Y. Rho, R. B. Ashman, and C. H. Turner. Young's modulus of trabecular and cortical bone material: ultrasonic and microtensile measurements. *Journal of Biomechanics*, **26**(2):111–119, 1993.
- J. Rice and A. L. Ruina. Stability of steady frictional slipping. *Journal of Applied Mechanics*, **50**(2):343–349, 1983.
- M. D. Ries, M. Harbaugh, J. Shea, and R. Lambert. Effect of cementless acetabular cup geometry on strain distribution and press–fit stability. *The Journal of Arthroplasty*, **12**(2):207–212, 1997.
- D. Rittel, A. Dorogoy, and K. Shemtov-Yona. Modelling dental implant extraction by pullout and torque procedures. *Journal of the Mechanical Behavior of Biomedical Materials*, **71**:416–427, 2017.
- D. Rittel, A. Dorogoy, and K. Shemtov-Yona. Modeling the effect of osseointegration on dental implant pullout and torque removal tests. *Clinical Implant Dentistry and Related Research*, **20**(5):683–691, 2018.
- W. E. Roberts, K. E. Simmons, L. P. Garetto, and R. DeCastro. Bone physiology and metabolism in dental implantology: risk factors for osteoporosis and other metabolic bone diseases. *Implant Dentistry*, **1**(1):11–21, 1992.
- O. Robertsson, J. Ranstam, M. Sundberg, A. W-Dahl, and L. Lidgren. The swedish knee arthroplasty register: a review. *Bone & Joint Research*, **3**(7):217–222, 2014.
- H. J. Rønold and J. E. Ellingsen. Effect of micro-roughness produced by tio2 blasting—tensile testing of bone attachment by using coin-shaped implants. *Biomaterials*, **23**(21):4211–4219, 2002.
- H. J. Rønold, S. P. Lyngstadaas, and J. E. Ellingsen. Analysing the optimal value for titanium implant roughness in bone attachment using a tensile test. *Biomaterials*, **24**(25):4559–4564, 2003.
- D. O. Rourke and M. Taylor. Patient and surgical variability in the primary stability of cementless acetabular cups: a finite element study. *Journal of Orthopaedic Research*, **38**(7):1515–1522, 2020.
- A. Ruina. Slip instability and state variable friction laws. *Journal of Geophysical Research: Solid Earth*, **88**(B12):10359–10370, 1983.
- G. E. Salvi and N. P. Lang. Diagnostic parameters for monitoring peri-implant conditions. *International Journal of Oral & Maxillofacial Implants*, **19**(7), 2004.
- P. M. Sandborn, S. D. Cook, W. P. Spires, and M. A. Kester. Tissue response to porous-coated implants lacking initial bone apposition. *The Journal of Arthroplasty*, **3**(4):337–346, 1988.
- V. Sansalone, S. Naili, V. Bousson, C. Bergot, F. Peyrin, J. Zarka, J. Laredo, and G. Haiat. Determination of the heterogeneous anisotropic elastic properties of human femoral bone: from nanoscopic to organ scale. *Journal of Biomechanics*, **43**(10):1857–1863, 2010.

- R. A. Sauer. Enriched contact finite elements for stable peeling computations. *International Journal for Numerical Methods in Engineering*, **87**(6):593–616, 2011.
- R. A. Sauer. A survey of computational models for adhesion. *The Journal of Adhesion*, **92**(2):81–120, 2016.
- R. A. Sauer and L. De Lorenzis. A computational contact formulation based on surface potentials. *Computer Methods in Applied Mechanics and Engineering*, **253**:369–395, 2013.
- R. A. Sauer and L. De Lorenzis. An unbiased computational contact formulation for 3D friction. *International Journal for Numerical Methods in Engineering*, **101**(4):251–280, 2015.
- R. A. Sauer and K. Immel. A fully coupled chemo–thermo–mechanical contact model and its application to bonding and debonding. *in preparation*, 2022.
- R. A. Sauer, R. Ghaffari, and A. Gupta. The multiplicative deformation split for shells with application to growth, chemical swelling, thermoelasticity, viscoelasticity and elastoplasticity. *International Journal of Solids and Structures*, **174**:53–68, 2019.
- R. A. Sauer, T. X. Duong, and K. K. Mandadapu. A chemo-mechano-thermodynamical contact theory for adhesion, friction, and (de) bonding reactions. *Mathematics and Mechanics of Solids*, **27**(4):711–745, 2022.
- T. P. Schmalzried, L. M. Kwong, M. Jasty, R. C. Sedlacek, T. C. Haire, D. O. O’Connor, C. R. Bragdon, J. M. Kabo, A. J. Malcolm, and W. H. Harris. The mechanism of loosening of cemented acetabular components in total hip arthroplasty. analysis of specimens retrieved at autopsy. *Clinical Orthopaedics and Related Research*, (**274**):60–78, 1992.
- M. L. Schwarz, M. Kowarsch, S. Rose, K. Becker, T. Lenz, and L. Jani. Effect of surface roughness, porosity, and a resorbable calcium phosphate coating on osseointegration of titanium in a minipig model. *Journal of Biomedical Materials Research Part A*, **89**(3):667–678, 2009.
- F. A. Shah, A. Snis, A. Matic, P. Thomsen, and A. Palmquist. 3D printed Ti6Al4V implant surface promotes bone maturation and retains a higher density of less aged osteocytes at the bone–implant interface. *Acta Biomaterialia*, **30**:357–367, 2016.
- F. A. Shah, S. Sayardoust, P. Thomsen, and A. Palmquist. Extracellular matrix composition during bone regeneration in the human dental alveolar socket. *Bone*, **127**:244–249, 2019.
- M. Shalabi, A. Gortemaker, M. Hof, J. Jansen, and N. Creugers. Implant surface roughness and bone healing: a systematic review. *Journal of Dental Research*, **85**(6):496–500, 2006.
- N. K. Sharma, D. K. Sehgal, and R. K. Pandey. Comparative study of locational variation in shear and transverse elastic modulus of buffalo cortical bone. *IERI Procedia*, **1**:205–210, 2012.
- A. Shirazi-Adl. Finite element stress analysis of a push–out test part 1: fixed interface using stress compatible elements. *Journal of Biomechanical Engineering*, **114**(1):111–118, 1992.
- A. Shirazi-Adl, M. Dammak, and G. Paiement. Experimental determination of friction characteristics at the trabecular bone and porous–coated metal interface in cementless implants. *Journal of Biomedical Materials Research Part A*, **27**(2):167–175, 1993.

- R. Skripitz and P. Aspenberg. Attachment of PMMA cement to bone: force measurements in rats. *Biomaterials*, **20**(4):351–356, 1999.
- K. Søballe. Hydroxyapatite ceramic coating for bone implant fixation: mechanical and histological studies in dogs. *Acta Orthopaedica Scandinavica*, **64**(sup255):1–58, 1993.
- B. S. Sotto-Maior, E. P. Rocha, E. O. d. Almeida, A. C. Freitas-Júnior, R. B. Anchieta, and A. A. D. B. Cury. Influence of high insertion torque on implant placement: an anisotropic bone stress analysis. *Brazilian Dental Journal*, **21**(6):508–514, 2010.
- R. Souffrant, C. Zietz, A. Fritsche, D. Kluess, W. Mittelmeier, and R. Bader. Advanced material modelling in numerical simulation of primary acetabular press-fit cup stability. *Computer Methods in Biomechanics and Biomedical Engineering*, **15**(8):787–793, 2012.
- I. R. Spears, M. M. Morlock, M. Pfeiderer, E. Schneider, and E. Hille. The influence of friction and interference on the seating of a hemispherical press-fit cup: a finite element investigation. *Journal of Biomechanics*, **32**(11):1183–1189, 1999.
- I. R. Spears, M. Pfeiderer, E. Schneider, E. Hille, G. Bergmann, and M. M. Morlock. Interfacial conditions between a press-fit acetabular cup and bone during daily activities: implications for achieving bone in-growth. *Journal of Biomechanics*, **33**(11):1471–1477, 2000.
- I. R. Spears, M. Pfeiderer, E. Schneider, E. Hille, and M. M. Morlock. The effect of interfacial parameters on cup–bone relative micromotions: A finite element investigation. *Journal of Biomechanics*, **34**(1):113–120, 2001.
- strykerCTKS. stryker Triathlon Tritanium cementless total knee system. <https://www.stryker.com/us/en/joint-replacement/products/triathlon-tritanium.html>, 2021. Accessed: 16.02.2021.
- strykerTridentII. stryker Trident II acetabular system. <https://www.stryker.com/us/en/joint-replacement/products/trident-ii.html>, 2021. Accessed: 16.02.2021.
- Y. Sul, D. Kwon, B. Kang, S. Oh, and C. Johansson. Experimental evidence for interfacial biochemical bonding in osseointegrated titanium implants. *Clinical Oral Implants Research*, **24**(A100):8–19, 2013.
- M. Sütpideler, S. E. Eckert, M. Zobitz, and K.-N. An. Finite element analysis of effect of prosthesis height, angle of force application, and implant offset on supporting bone. *International Journal of Oral & Maxillofacial Implants*, **19**(6), 2004.
- V. Swami, V. Vijayaraghavan, and V. Swami. Current trends to measure implant stability. *The Journal of the Indian Prosthodontic Society*, **16**(2):124, 2016.
- T. Tang, V. Ebacher, P. Cripton, P. Guy, H. McKay, and R. Wang. Shear deformation and fracture of human cortical bone. *Bone*, **71**:25–35, 2015.
- M. Tarala, D. Janssen, and N. Verdonshot. Toward a method to simulate the process of bone ingrowth in cementless tha using finite element method. *Medical Engineering & Physics*, **35**(4):543–548, 2013.

- M. Taylor and P. J. Prendergast. Four decades of finite element analysis of orthopaedic devices: where are we now and what are the opportunities? *Journal of Biomechanics*, **48**(5):767–778, 2015.
- M. Taylor, R. Bryan, and F. Galloway. Accounting for patient variability in finite element analysis of the intact and implanted hip and knee: a review. *International Journal for Numerical Methods in Biomedical Engineering*, **29**(2):273–292, 2013.
- P. Tomaszewski, N. Verdonschot, S. Bulstra, and G. J. Verkerke. A comparative finite–element analysis of bone failure and load transfer of osseointegrated prostheses fixations. *Annals of Biomedical Engineering*, **38**(7):2418–2427, 2010.
- N. Toossi, B. Adeli, A. J. Timperley, F. S. Haddad, M. Maltenfort, and J. Parvizi. Acetabular components in total hip arthroplasty: is there evidence that cementless fixation is better? *The Journal of Bone and Joint Surgery*, **95**(2):168–174, 2013.
- P. Trisi and W. Rao. Bone classification: clinical–histomorphometric comparison. *Clinical Oral Implants Research*, **10**(1):1–7, 1999.
- P. Trisi, S. De Benedittis, G. Perfetti, and D. Berardi. Primary stability, insertion torque and bone density of cylindrical implant ad modum branemark: is there a relationship? an in vitro study. *Clinical Oral Implants Research*, **22**(5):567–570, 2011.
- E. Tschegg, R. Lindtner, V. Doblhoff-Dier, S. Stanzl-Tschegg, G. Holzlechner, C. Castellani, T. Imwinkelried, and A. Weinberg. Characterization methods of bone–implant–interfaces of bioresorbable and titanium implants by fracture mechanical means. *Journal of the Mechanical Behavior of Biomedical Materials*, **4**(5):766–775, 2011.
- P. Udomkiat, L. D. Dorr, and Z. Wan. Cementless hemispheric porous–coated sockets implanted with press–fit technique without screws: average ten-year follow-up. *The Journal of Bone and Joint Surgery*, **84**(7):1195–1200, 2002.
- S. D. Ulrich, T. M. Seyler, D. Bennett, R. E. Delanois, K. J. Saleh, I. Thongtrangan, M. Kuskowski, E. Y. Cheng, P. F. Sharkey, J. Parvizi, et al. Total hip arthroplasties: what are the reasons for revision? *International Orthopaedics*, **32**(5):597–604, 2008.
- R. Vayron, E. Barthel, V. Mathieu, E. Soffer, F. Anagnostou, and G. Haiat. Variation of biomechanical properties of newly formed bone tissue determined by nanoindentation as a function of healing time. *Computer Methods in Biomechanics and Biomedical Engineering*, **14**(sup1):139–140, 2011.
- R. Vayron, E. Barthel, V. Mathieu, E. Soffer, F. Anagnostou, and G. Haiat. Nanoindentation measurements of biomechanical properties in mature and newly formed bone tissue surrounding an implant. *Journal of Biomechanical Engineering*, **134**(2):021007, 2012.
- R. Vayron, M. Matsukawa, R. Tsubota, V. Mathieu, E. Barthel, and G. Haiat. Evolution of bone biomechanical properties at the micrometer scale around titanium implant as a function of healing time. *Physics in Medicine & Biology*, **59**(6):1389, 2014.

-
- R. Vayron, V.-H. Nguyen, B. Lecuelle, H. Albini Lomami, J.-P. Meningaud, R. Bosc, and G. Haiat. Comparison of resonance frequency analysis and of quantitative ultrasound to assess dental implant osseointegration. *Sensors*, **18**(5):1397, 2018a.
- R. Vayron, V.-H. Nguyen, B. Lecuelle, and G. Haiat. Evaluation of dental implant stability in bone phantoms: Comparison between a quantitative ultrasound technique and resonance frequency analysis. *Clinical Implant Dentistry and Related Research*, **20**(4):470–478, 2018b.
- M. Viceconti, R. Muccini, M. Bernakiewicz, M. Baleani, and L. Cristofolini. Large-sliding contact elements accurately predict levels of bone-implant micromotion relevant to osseointegration. *Journal of Biomechanics*, **33**(12):1611–1618, 2000.
- M. Viceconti, A. Pancanti, M. Dotti, F. Traina, and L. Cristofolini. Effect of the initial implant fitting on the predicted secondary stability of a cementless stem. *Medical and Biological Engineering and Computing*, **42**(2):222–229, 2004.
- M. Viceconti, S. Affatato, M. Baleani, B. Bordini, L. Cristofolini, and F. Taddei. Pre-clinical validation of joint prostheses: a systematic approach. *Journal of the Mechanical Behavior of Biomedical Materials*, **2**(1):120–127, 2009.
- P. J. Watson, A. Dostanpor, M. J. Fagan, and C. A. Dobson. The effect of boundary constraints on finite element modelling of the human pelvis. *Medical Engineering & Physics*, **43**:48–57, 2017.
- H. Weinans, R. Huiskes, and H. Grootenboer. The behavior of adaptive bone-remodeling simulation models. *Journal of Biomechanics*, **25**(12):1425–1441, 1992.
- H. Weinans, R. Huiskes, B. Van Rietbergen, D. Sumner, T. Turner, and J. Galante. Adaptive bone remodeling around bonded noncemented total hip arthroplasty: a comparison between animal experiments and computer simulation. *Journal of Orthopaedic Research*, **11**(4):500–513, 1993.
- A. Wengler, U. Nimptsch, and T. Mansky. Hip and knee replacement in germany and the usa: analysis of individual inpatient data from german and us hospitals for the years 2005 to 2011. *Deutsches Ärzteblatt International*, **111**(23-24):407, 2014.
- A. Wennerberg, R. Jimbo, S. Stübinger, M. Obrecht, M. Dard, and S. Berner. Nanostructures and hydrophilicity influence osseointegration: a biomechanical study in the rabbit tibia. *Clinical Oral Implants Research*, **25**(9):1041–1050, 2014.
- W. Whitehouse and E. Dyson. Scanning electron microscope studies of trabecular bone in the proximal end of the human femur. *Journal of Anatomy*, **118**(Pt 3):417, 1974.
- K.-H. Widmer, B. Zurfluh, and E. Morscher. Load transfer and fixation mode of press-fit acetabular sockets. *The Journal of Arthroplasty*, **17**(7):926–935, 2002.
- J. Wolff. Das Gesetz der Transformation der Knochen. *Berlin, Hirschwald*, 1:1–152, 1892.
- P. Wriggers. *Computational contact mechanics*. Springer Science & Business Media, 2006.
- P. Wriggers. *Nonlinear finite element methods*. Springer Science & Business Media, 2008.

- M. Wyatt, G. Hooper, C. Frampton, and A. Rothwell. Survival outcomes of cemented compared to uncemented stems in primary total hip replacement. *World Journal of Orthopedics*, **5**(5): 591, 2014.
- X.-P. Xu and A. Needleman. The influence of nucleation criterion on shear localization in rate-sensitive porous plastic solids. *International Journal of Plasticity*, **8**(3):315–330, 1992.
- X.-P. Xu and A. Needleman. Void nucleation by inclusion debonding in a crystal matrix. *Modelling and Simulation in Materials Science and Engineering*, **1**(2):111, 1993.
- A. Yew, Z. Jin, A. Donn, M. Morlock, and G. Isaac. Deformation of press-fitted metallic resurfacing cups. part 2: finite element simulation. *Proceedings of the Institution of Mechanical Engineers, Part H: Journal of Engineering in Medicine*, **220**(2):311–319, 2006.
- Y. Zhang, P. B. Ahn, D. C. Fitzpatrick, A. D. Heiner, R. A. Poggie, and T. D. Brown. Interfacial frictional behavior: cancellous bone, cortical bone, and a novel porous tantalum biomaterial. *Journal of Musculoskeletal Research*, **3**(04):245–251, 1999.
- O. Zienkiewicz and R. Taylor. *The finite element method for solid and structural mechanics*. Butterworth–Heinemann, 2005.